Synthesis, Structure, and Catalytic Activity of Bimetallic Rhodium Complexes in the Hydroformylation and Allylic Oxidation of Alkenes

Sinethemba Mkhize

University of Cape Town

2021

Synthesis, Structure, and Catalytic Activity of Bimetallic Rhodium Complexes in the Hydroformylation and Allylic Oxidation of Alkenes

Sinethemba Mkhize

A dissertation submitted in fulfilment of the requirements of the degree

Master of Science in Chemistry

University of Cape Town

Department of Chemistry

Supervisors:

Dr. S. Ngubane

Dr. J. van Wyk

July 2021

Declaration

I know the meaning of Plagiarism and declare that all of the work in the document "**Synthesis, Structure, and Catalytic Activity of Bimetallic Rhodium Complexes in the Hydroformylation and Allylic Oxidation of Alkenes**" is my own, save for that which is properly acknowledged by means of referencing. It is to the best of my knowledge that this work has never been reported or submitted for any degree or examination by any university.

Dedication

This dissertation is dedicated my mother, father, sister, two brothers and three nephews. To my twin sister, you may have passed but you will forever be in my heart.

Acknowledgements

In opening, I would like to give my sincere gratitude to my supervisors Dr S. Ngubane for synthesis and Dr J. van Wyk for catalysis. Their expertise is unmeasurable, and for their patience, support and understanding, I am very grateful.

I would like to thank Organometallic Research Group led by Assoc. Prof G. S. Smith for always giving me advice whenever I gave progress presentations. It is wonderful to have colleagues who can assist at any moment of time. Mostly to Dr S. Siangwata, thank you for assisting me in the laboratory whenever my knowledge was limited or when you would proof-read my report. To Mr T. Medupe, it has been a pleasure to work besides you for the past three year. I will cherish our discussions.

Special thanks to Dr M. Rylands for recording the NMR experiments to all my compounds and doing it diligently. Special thanks also go to Dr H. Su who collected and analysed the crystallographic data for my complexes. To the workshop team, I appreciate your time in assisting with fixing any broken equipment so I can go one to using it.

I want to thank the support team from the central office of the Chemistry department; namely Deirdre, Joanne, Martina, Crystal and Leeta for keeping their doors open for us and making sue things run smoothly in the department. To Monique, thank you for ensuring that we are working in a safe environment. I thank the funding that I received from the Sasol Scholarships and the National Research Foundation through my supervisor Dr S. Ngubane.

Finally, I would like to give all my love to my parents Mrs Nomthandazo and Mr Mfana Mkhize, as well as my sibling Mantombi, Thulani and Sbonela Mkhize for providing me with their support and allowances that I needed throughout this stressful period. My nephews Philani, Lubanzi and Amkelo Mkhize, I love you kids. Thank you to my church for also supporting me with spiritual guidance. All these mentioned above is through the blessings of the Almighty God, for His continuous protection and provision of all my needs, I pray to Thee.

Table of Contents

Publications

Structural and Electrochemical Characterization of Bimetallic-Univalence Rh(I) Complexes Bridging Arylamidines, Hydroformylation Activity and Selectivity Evaluations. (*In preparation*)

Structural and Electrochemical Characterization of Homoleptic and Mixed Ligand Heteroleptic Rh(II) Complexes Bearing Bridging Formamidine Ligands, and Catalytic Evaluation in the Allylic Oxidation of Cyclohexene. (*In preparation*)

Conference/Symposium Contributions

29 June 2019: Poster presentation

Synthesis of Bimetallic Rhodium(II) Complexes for the Homogeneously Catalysed Hydroformylation of 1-Octene. Cape Organometallics Symposium, Cape Town.

14 – 19 June 2020: Virtual Poster presentation

Dirhodium(II) Complexes: Synthesis, Structure and Application in Allylic Oxidation of Cyclohexene. The 17th International Congress on Catalysis, San Diego.

Abstract

Synthesis, Structure, and Catalytic Activity of Bimetallic Rhodium Complexes in the Hydroformylation and Allylic Oxidation of Alkenes

Four *N,N'*-bridging diphenylformamidine (dpf) ligands **L1 – L4** were synthesised and characterised to ascertain purity. These known ligands were further reacted with the dimeric rhodium precursor $[RhCl(COD)]_2$ producing a series of diphenylformamidinato-Rh(I) bimetallic complexes **C1** – **C4**. The same ligands were also reacted with either the dirhodium trifluorotetraacetate $[Rh_2(TfOAc)_4]$ or the traditional acetate $[Rh_2(OAc)_4]$ dimers. Thes reactions yield a series of diphenylformamidinato-Rh(II) homoleptic bimetallic complexes **C5** – **C7** of the type $[Rh_2(R\text{-}dpf)_4]$ (where R = H, CH_3 or F) as well as the novel mixed ligand heteroleptic dirhodium complexes **C8** – **C11** of the type $[Rh_2(R\text{-}dpf)_x(OAc)_{4-x}]$ with x = 2 or 3 (where R = H, CH_3 or F), respectively (Figure 1).

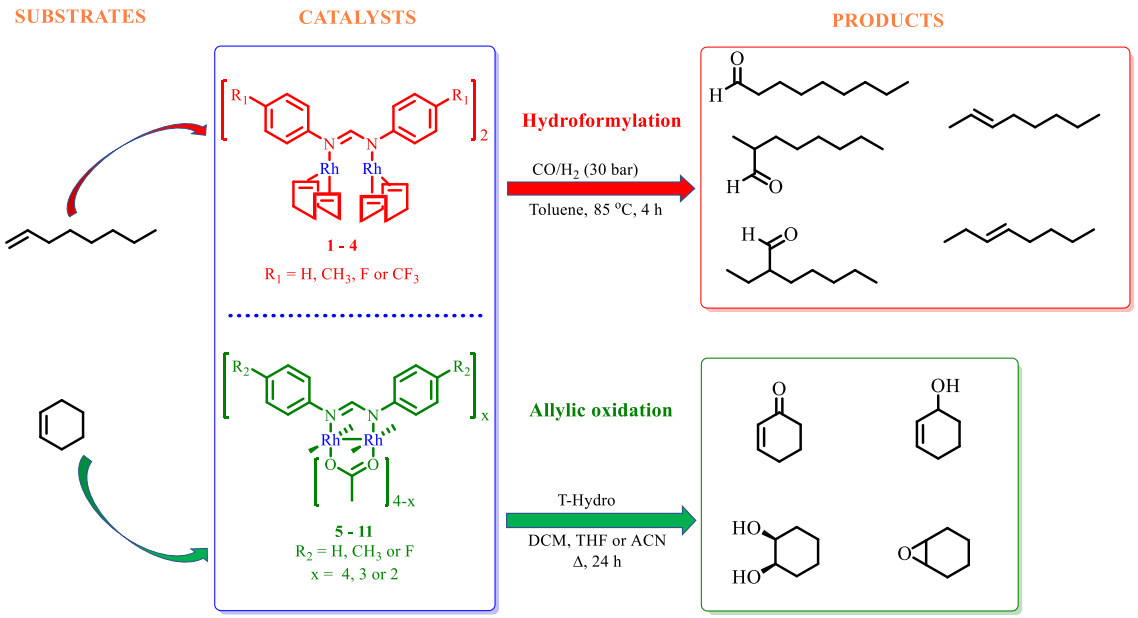

Figure 1. Hydroformylation and allylic oxidation of 1-octene and 1-cyclohexene, respectively.

The complexes were fully characterised using various spectroscopic and analytical techniques inclusive of the melting points, ^{1}H NMR, ^{13}C NMR, ^{19}F NMR and FT-IR spectroscopy as well as high resolution mass spectrometry. Furthermore, UV-visible spectroscopy and cyclic voltammetry were carried out in various coordinating and none or poorly coordinating solvents to elucidate the absorption spectroscopy and electrochemical properties of the complexes.

The Rh(I) bimetallic complexes **C1** – **C4** were evaluated as possible catalyst precursors in the hydroformylation of 1-octene, optimized at 85 ^{o}C and 30 bar of syngas (1:1 H_2/CO). Facile and quantitative conversions were obtained within 4 hours under these conditions. All complexes have near quantitative conversion, with complete conversion for complex **C4** (R = CF_3). There is equal amount of both nonanal and branched aldehydes with **C4**, indicating the rate of isomerisation is equal to the rate of aldehyde formation from the *iso*-octenes.

Homoleptic (**C5** – **C7)** and mixed ligand heteroleptic (**C8** – **C11)** dirhodium complexes were evaluated as potential catalysts towards the allylic oxidation of cyclohexene. At 0.1 mol% catalyst loading and 3 eq. of TBHP, a near quantitative substrate conversion was observed in the presence of a coordinating solvent, acetonitrile at 82 ^{o}C. Under such conditions, the heteroleptic complexes **C8** – **C11** demonstrate superior catalytic activity compared to the homoleptic complexes **C5** – **C7**. The desired 2-cyclohexen-1-one is the dominant product over the 2-cyclohexen-1-ol and cyclohexene oxide which are also produced in this catalytic reaction.

List of Abbreviations and Symbols

°	Degrees
°C	Degrees Celsius
%	Percent
Å	Angstrom
δ	Chemical shift
ρ	Reactivity constant
σ	Hammett's constant
ν	Wavenumber
ν_{max}	Maximum wavelength
A	Amperes
ACN	Acetonitrile
Ar	Aromatic
ATR-IR	Attenuated total reflectance infreared spectroscopy
ax	Axial coordination
br	Broad
^{13}C NMR	Carbon-13 nuclear magnetic resonance
calcd.	Calculated
cat	Catalyst
$CDCl_3$	Deuterated chloroform
$CHCl_3$	Chloroform
cm^{-1}	Reciprocal centimetres
COD	1,5-cyclooctadience
COSY	Correlation spectroscopy
d	Doublet
dd	Doublet of doublets
DCM	Dichloromethane
DMF	*N*,*N*-dimethylformamide
DMSO	Dimethyl sulfoxide
DMSO-d_6	Deuterated dimethyl sulfoxide
DN	Donor number
dpf	Diphenylformamidine ligand

$E_{1/2}$	Half wave poterntial
eq	Equatorial coordination
ESI-MS	Electrospray ionisation mass spectrometry
$E_T(30)$	Dimroth-Reichardt
EtOH	Ethanol
F	Faraday's constant
^{19}F NMR	Florine-19 nuclear magnetic resonace
Fc/Fc^+	Ferrocene/Ferrocenium
FT-IR	Fourier transform infrared spectrometry
g	Grams
GC	Gas chromatography
h	Hours (unit of time)
^{1}H NMR	Proton nuclear magnetic resonance
HSQC	Heteronuclear single quantum correlation
Hz	Hertz
i_{pa}	Anodic current
i_{pc}	Cathodic current
IR	Infrared
J	Coupling constant
Kcom	Comproportion constant
m	Metres for length or multiplrt for nuclear magnetic resonance
mg	Milligram
MHz	Megahertz
mL	Millilitre
MLCT	Metal to ligand charge transfer
mol	Moles
mmol	Millimoles
M.P.	Melting point
MS	Mass spectrometry
m/z	Mass to charge ratio
nm	Nanometres
NMR	Nuclear magnetic resonance
π^*	Solvent polarity

PGM	Platinum group metals
PhCl	Chlorobenzene
ppm	Parts per million
q	Quartet
r.t.	Room temperature
$Rh_2(OAc)_4$	Dirhodium(II) tetraacetate
$Rh_2(TfOAc)_4$	Dirhodium(II) tetrakis(trfluoroacetate)
s	Singlet
Syngas	Synthesis gas
t	Triplet
TBHP	Tert-butyl hydroperoxide
THF	Tetrahydrofuran
TOF	Turnover frequency
TON	Turnover number
UV-Vis	Ultraviolet Visible light spectroscopy
V	Volts

Chapter 1

Review on the Design and Synthesis of Homobimetallic Rhodium Complexes and their Applications in Catalysis

1.1 Brief History

Over the past two decades, scientific researchers have adapted to conduct their experiments on a more conservative approach, as urged by agencies such as the Environmental Protection Agency.[1] In the field of chemistry, this approach is introduced in the form of Green Chemistry.[2] This is defined as the "design of new chemical processes and chemical products that seeks to reduce or eliminate the use or generation of substances hazardous to living organisms (humans, animals and plants)".[3] Thanks to the intensive work done by John Warner and Paul Anastas, a formulation of policies now known as the 12 Principles of Green Chemistry, serve as guidelines and basis of conducting chemical experiments to protect the environment.[2] Figure 1.1 shows this 12 principles of green chemistry.

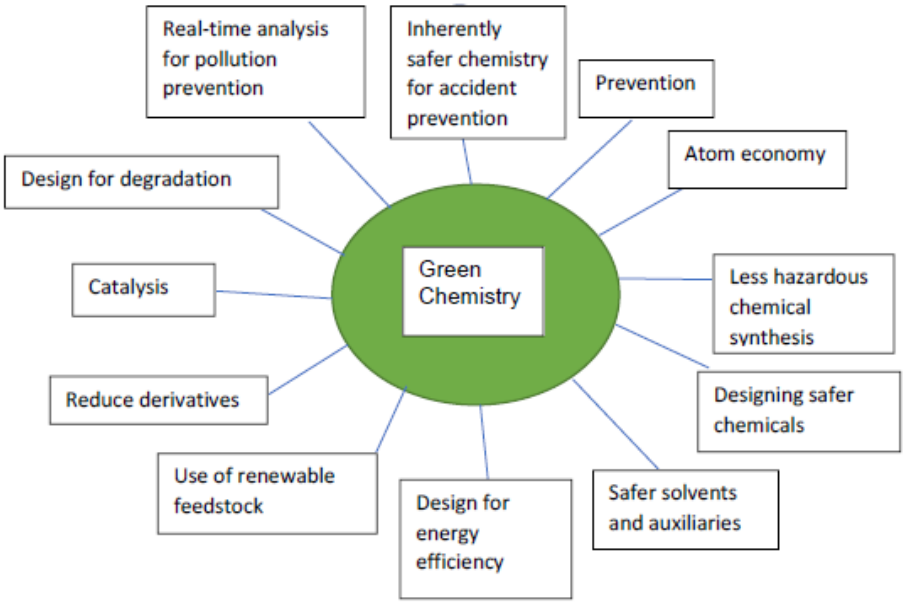

Figure 1.1 Principles of Green Chemistry Green Chemistry Design.

Included in Figure 1.1 of green chemistry is the incorporation of catalysis. A catalyst is defined as a compound that provides an alternative path that goes *via* a lower activation energy in a chemical reaction that is thermodynamically favoured, to form products much faster than

without the catalyst. The catalyst is regenerated once the reaction has reached its completion (Figure 1.2).

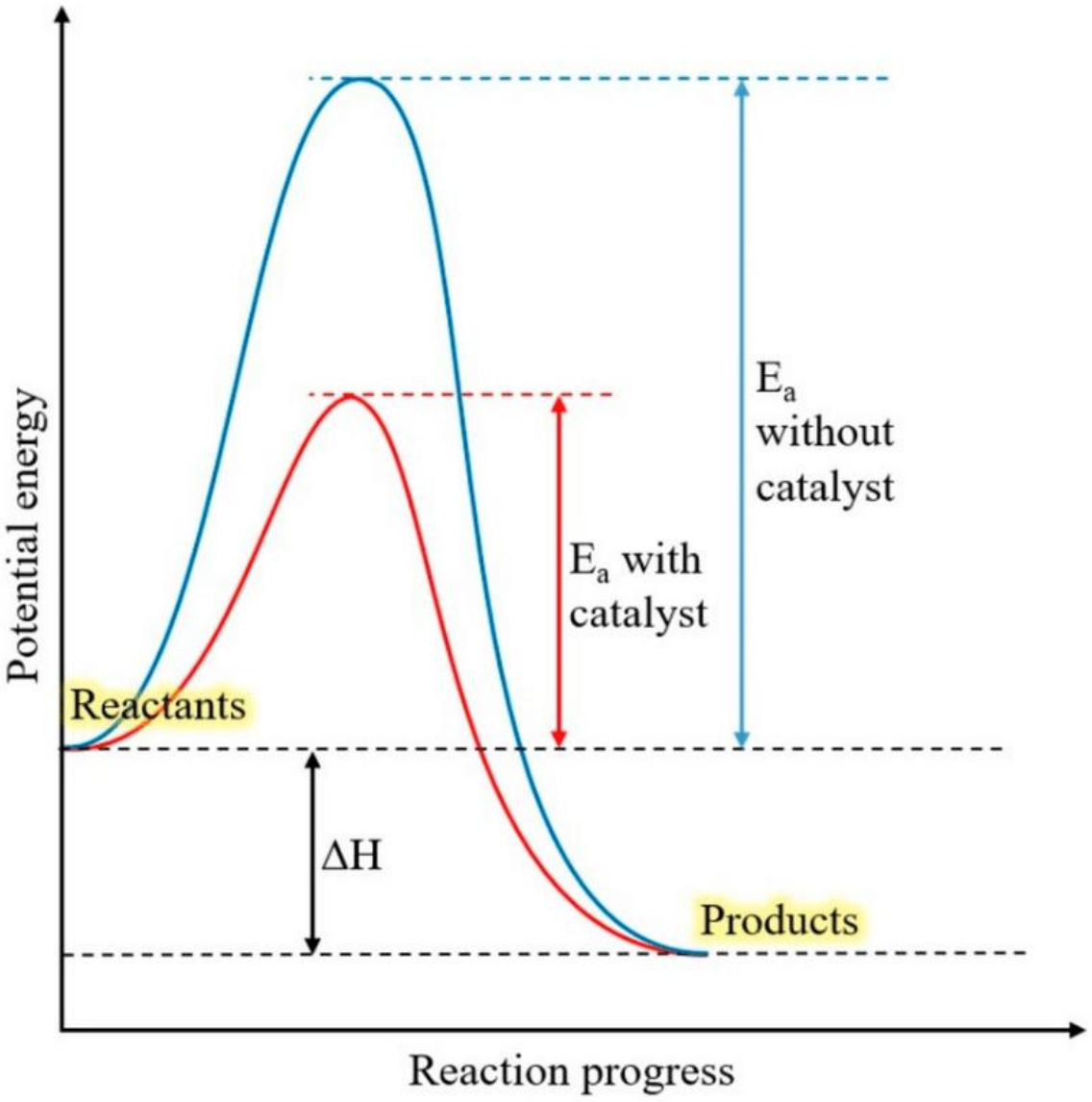

Figure 1.2 Reaction energy profile showing catalyst effect in lowering activation energy.[4]

If a catalyst is in a similar phase to the reactants and products, it is said to be homogeneous. A catalyst with a different from the reactants or products is then said to be heterogeneous.[5] There are both advantages and disadvantages in both forms of catalysts.[6] In heterogenous catalysis, it is easier to separate the catalytic species due to having a distinguishable phase, and are generally cheaper and more robust. However, their selectivities are much poor, while they are also not easily modified. Contrary to this, homogeneous catalysts are comparatively more expensive and more difficult to isolate due to the same phase relationship.[7] They are often sensitive to moisture and thermal conditions, but provide good activity and selectivity in the

reaction.[8–10] The advantages and disadvantages of homogeneous and heterogeneous catalysis are summarised in Table 1.1.

Table 1.1 Differences between homogeneous and heterogeneous catalysis

	Homogeneous catalysis	Heterogeneous catalysis
Activity	High	Variable
Catalyst recycling	Expensive	Easier and cheaper
Diffusion issues	None	Very important
Mechanistic understanding	Plausible and possible to ascertain in random conditions	Very uncertain and difficult to understand
Selectivity	High	Variable
Sensitivity towards catalysts poisons	Low	High
Service life of catalyst	Variable	Long
Reaction conditions	Low to mild	Harsh

Generally, catalysis applies to broad topics, including acid-base catalysis, enzyme catalysis and organometallic catalysis.[11] Organometallic catalysis utilises organometallic compounds as catalysts for chemical reactions.[12] Since catalysts lower the activation energy of a chemical reactions, they are designed for energy efficiency. The use of catalysts can also reduce the amount of starting material, resulting in less feedstock as there is no need for stoichiometric amounts. Catalysts tend to improve the selectivity of reactions, and thereby reducing the waste and this corresponds to another major policy of green chemistry. They also consist of renewable feedstock since catalysts are regenerated with the products upon completion of the reaction. Other catalysts allow for unfavorable (thermodynamically) reactions to be carried out. Green chemistry has a growing impact; however, it is believed that it has not yet reached its full potential. Hence, there is still a lot to be explored in this diverse field. Due to such reasons, catalysis is a major area of research in laboratory, as it will not only beneficial to laboratory research but to all industries that perform organic reactions. Some of these reactions are hydroformylation and allylic oxidation of alkenes.

1.2 Bimetallic Rhodium Complexes

1.2.1 Homobimetallic Rh complexes without a metal-metal bond

Synthetic chemists continue to explore the design of catalysts in attempts to mimic naturally occurring metal-containing enzymes (bearing two or more active sites).[13-14] These synthetic catalysts are designed to imitate the characteristics of biocatalysts, having synergistic and cooperative effects between the active metal sites contained therein. Park and Hong reported a detailed structural review on the classification of bimetallic catalysts (Figure 1.6).[15] The cooperative effects of the metal centres are realised as most efficiently when the two metal sites are in close proximity (optimum separation of 3.5 – 6 Å), with one metal acting as a Lewis acid for activating electrophiles, while the other metal serves as the counterion of nucleophiles.[16] At this optimum separation, even without direct interactions between the metal centres, their close proximity permits for interactions of the substrate with both metal centres or the close binding of two reactants to the adjoining metal centres.

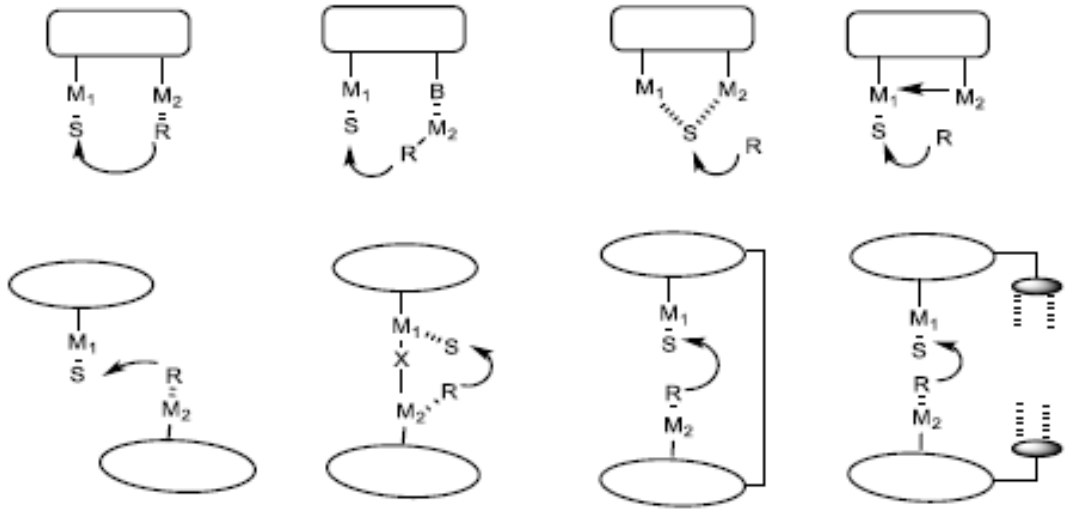

Figure 1.3 Bonding modes of ligands to metals in bimetallic complexes.

The combination of multiple catalytic sites to a single ligand structure can enhance the reactivity of a catalytic system through an induced cooperative activation and selective substrate binding to improved catalytic efficiency. The compounds can either be homobimetallic or heterobimetallic, with respect to the metals.[16–19] Stanley and co-workers have reported on the hydroformylation of 1-hexene with a *racemic* bimetallic rhodium complex *rac*- $[Rh_2(nbd)_2(et,ph\text{-}P_4)](BF_4)_2$ (nbd = norbonadiene, et = ethyl, ph = phenyl). This gave a higher rate of reaction and regioselectivity for linear aldehydes, in comparison to the same reaction with the Rh/PPh_3 which is considerably slower and less selective.[18] They proposed a

catalytic cycle that involves an intramolecular transfer of a hydride from one rhodium centre to another which contains an acyl chain, resulting in the aldehyde. This charge transfer is dependent on the close proximity of the two metal centres. In the case of heterobimetallics where different metals are used, it is often expected that the two metals will perform different functions. This allows for a more selective functionalisation of the substrate.

1.2.2 Homobimetallic Rh complexes containing a metal-metal bond

Dirhodium complexes have fascinating properties that span different including antitumour metallopharmaceuticals, phototherapeutic agents, design of supramolecular arrays and more importantly catalysis.[20,21] These compounds are said to be 'paddlewheel' with two types of ligands (Figure 1.4). The Rh atoms are connected by four bridging ligands located at the equatorial positions and other coordinating ligands including solvents at the axial positions, with the Rh–Rh bond insensitive to σ-donating axial ligands.

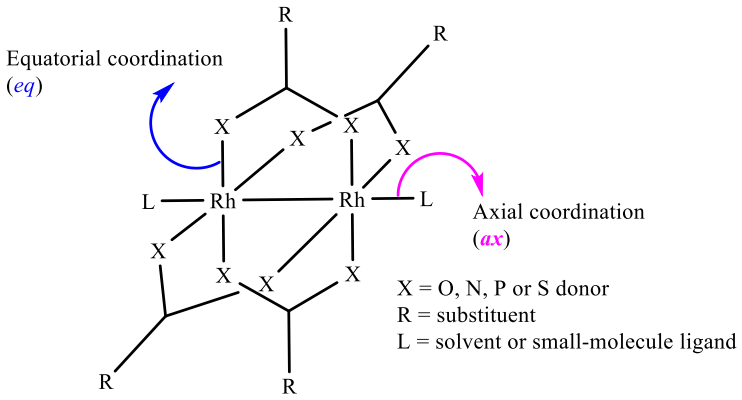

Figure 1.4 General structure of dirhodium(II) complexes showing equatorial and axial bonding.

The key in the stabilisation of the Rh_2^{4+} dirhodium core is the formation of the Rh–Rh bond. The molecular bonding orbital construction, (Figure 1.5) has fourteen electrons with eight distributed among the σ, π and δ bonding orbitals. The remaining six are distributed among the δ* and π* antibonding orbitals.[22] This gives a configuration with all electrons paired, hence diamagnetic.

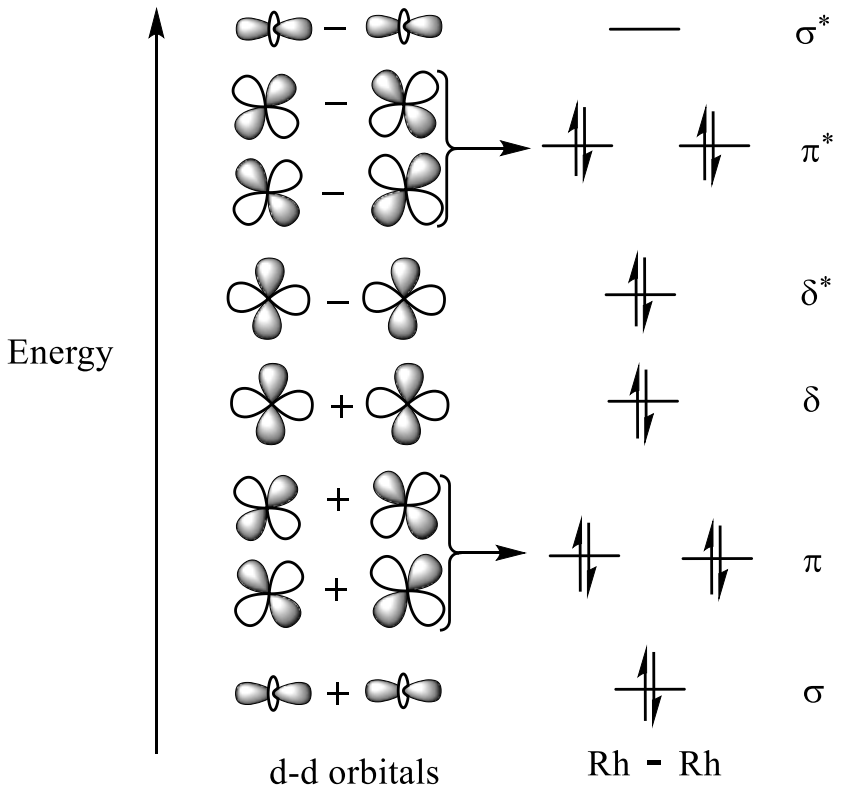

Figure 1.5 Molecular orbital construction of the Rh-Rh bond showing electron distribution.

Dirhodium carboxylate complexes are obtained from the reduction of Rh(III) compounds in alcohols media which act as reducing agent. Other preparative methods include the reflux of salts of $[RhCl_6]^{3+}$ in aqueous formic acid, refluxing $[Rh(OH)_3.H_2O]$ in a carboxylic acid or mixture of carboxylic acid and alcohol.[23] However, the yields are low by these methods. A more efficient is the reflux of $[RhCl_3.3H_2O]$ under nitrogen in a mixture of sodium acetate, acetic acid and ethanol.[24] The reduction of $[RhCl_3]$ by dimethylformamide in dimethylammonium acetate has been suggested as an alternative method.[25]

Dirhodium formamidinate complexes can be prepared by the reaction of $[Rh_2(O_2CCH_3)_4]$ with the molten formamidine ligand. Furthermore, replacing the $[Rh_2(O_2CCH_3)_4]$ with $[Rh_2(O_2CCF_3)_4]$, the yield is improved significantly.[26] An alternative method is the reflux $[RhCl_3]$ with a neutral formamidine in a mixture of ethanol and triethylamime, however, the yields are lower. The properties of the dirhodium complexes vary based on the nature of the ligands. The formamidinate bridging ligands introduce a chemical and structural diversity to these complexes which results in rich electrochemistry and improving their biological activity. Since N atoms are better σ-donors than O atoms, the formamidinate groups form more stable complexes as they render the Rh_2^{4+} core more electron rich. This is evidenced by Rh-Rh and

Rh-Oeq/Rh-Neq bond lengths, $Rh_2(O_2CCH_3)_4$ has a bond length of 2.38 Å and $Rh_2(DPhF)_4$ has a bond length of 2.457(11) Å.[27] In the latter, the antibonding orbitals of Rh_2^{4+} core are more populated with electron density in combination of the 'bite'. This also accounts for the observed electrochemical process, whereby the carboxylate complexes stabilize the Rh_2^{5+} state and the formamidinate complexes stabilize the Rh_2^{5+} much easier as well as the higher Rh_2^{6+}.

1.3 Homogeneous Catalysis

A number of factors should be considered whenever choosing a catalyst. These include the selectivity of the catalyst, its lifetime, ease in recycling the catalyst as well as the amount of the catalyst required. A catalyst with good selectivity will yield a larger quantity of the desired product with minimum side product. Homogeneous catalysts tend to possess good chemoselectivity as well as good regioselectivity. The high selectivity of such homogeneous catalysts makes them ideal for wide applications in industry and academia. This has contributed to increased interests in homogeneous catalysts, and they have been applied in classical organic processes such as carbonylation (in the Monsanto process),[8-9] hydrogenation (with the Wilkinson catalyst)[10] and hydroformylation reactions[28].

Some drawbacks of homogeneous systems such as the recovery of the often-expensive organometallic catalysts has propelled researchers to consider a combination of the two systems. This is aimed at subduing the disadvantages of a homogeneous system with the advantages of a heterogeneous system. The goal is to bridge the gap between the two systems through a more selective system which can operate under mild conditions and offer a more simplified procedure for catalyst separation from the product. Several approaches that have been developed are based on the immobilisation of the catalyst onto organic or inorganic support and immobilisation in biphasic systems. Employing the former comes with the possibility of leaching by the metal from the catalyst-support matrix into the product, degradation of the support system as well as a constrained catalyst which impacts negatively on its mobility for effectiveness. In contrast, biphasic catalysis not only counteracts the disadvantage of catalyst recovery associated with homogeneous systems but creates a balance between heterogeneous and homogeneous processes.

1.4 Hydroformylation

Hydroformylation, which is widely known as the "oxo process", is a metal catalysed addition reaction of hydrogen gas (H_2) and carbon monoxide (CO) across an alkene functionality, to produce a mixture of linear and branched aldehydes with an extra carbon on the original chain, Scheme 1.1. This homogeneously process was accidently discovered by Otto Roelen in 1938 at Ruhrchemie AG, during his time investigating the Fischer-Tropsch reaction.[13-14] Initially, cobalt-based catalysts were employed, whereby a Co(I) complex, $HCo(CO)_4$ is the unmodified active catalyst precursor. The hydroformylation is usually carried out under high pressure conditions to prevent dissociation of the CO ligands, with the production aldehyde and alcohol products.[31] The product ratio of linear and branched products *n:iso* is found to be typically 4:1, with a small formation of the alcohol products.[32] At higher reaction temperatures, there is a competition between the formation of the aldehyde and a subsequent reduction of the aldehyde, so alcohols are observed as major products. As of recently, the focus has been on the design of rhodium-based catalysed due to higher reactivity of Rh centres.

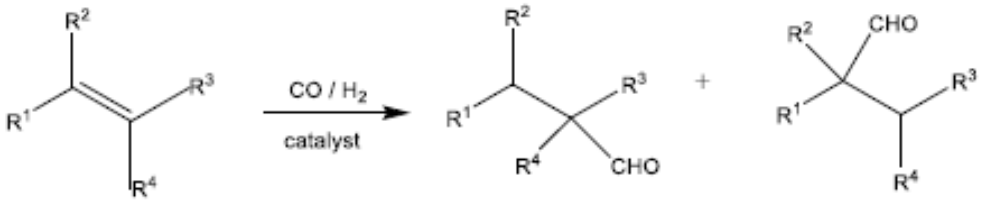

Scheme 1.1 A general reaction scheme for the hydroformylation of alkenes. Here, R1 – R4 is an alkyl, aryl or H.

1.4.1 Mechanism for the rhodium catalysed hydroformylation

A possible mechanism for the Rh catalysed hydroformylation is proposed in Scheme 1.2.[33] The first step is the dissociation of CO from the five-coordinate precursor to generate the active four-coordinate catalyst [$HRh(CO)_3$] (Rh(I) complex **1.21**, ($16e^-$) with a vacant site for coordination. The alkene substrate can then coordinate to the vacant site in the second step, to a Rh(I) complex **1.22** ($18e^-$). From here, the reaction can go via a path that leads to the linear products and the other leading to branched products. For the linear pathway, there is a hydride migration of the hydride *cis* to the alkyl ligand, inserting itself to the more internal carbon to form the four-coordinate complex **1.23b**. To this species, a CO molecule is coordinated leading to five-coordinate complex **1.24b**. The coordinated CO which is *cis* to the σ-bound alkyl migrates to insert itself between the C–Rh bond to make a s-bound acyl Rh(I) complex **1.25b**. To this complex, the hydrogen molecule coordinates to yield a six-coordinate Rh(III) complex,

which then undergoes reductive elimination to regenerate the active species **1.21** while dissociating the aldehyde product. In the branched pathway, the hydride migration occurs at the terminal carbon of the alkyl chain to form the σ-bound alkyl complex **1.23a**. To this complex, an incoming CO molecule coordinates to generate the five-coordinate complex **1.24a**. A similar ligand migratory insertion of the CO to the alkyl leads to the formation of the σ-bound acyl complex **1.25a**. The hydrogen molecule oxidises the complexes to the six-coordinate Rh(III) species which is followed by a subsequent reductive elimination. The oxidation state and coordination number both decrease by two, regenerating the active species.

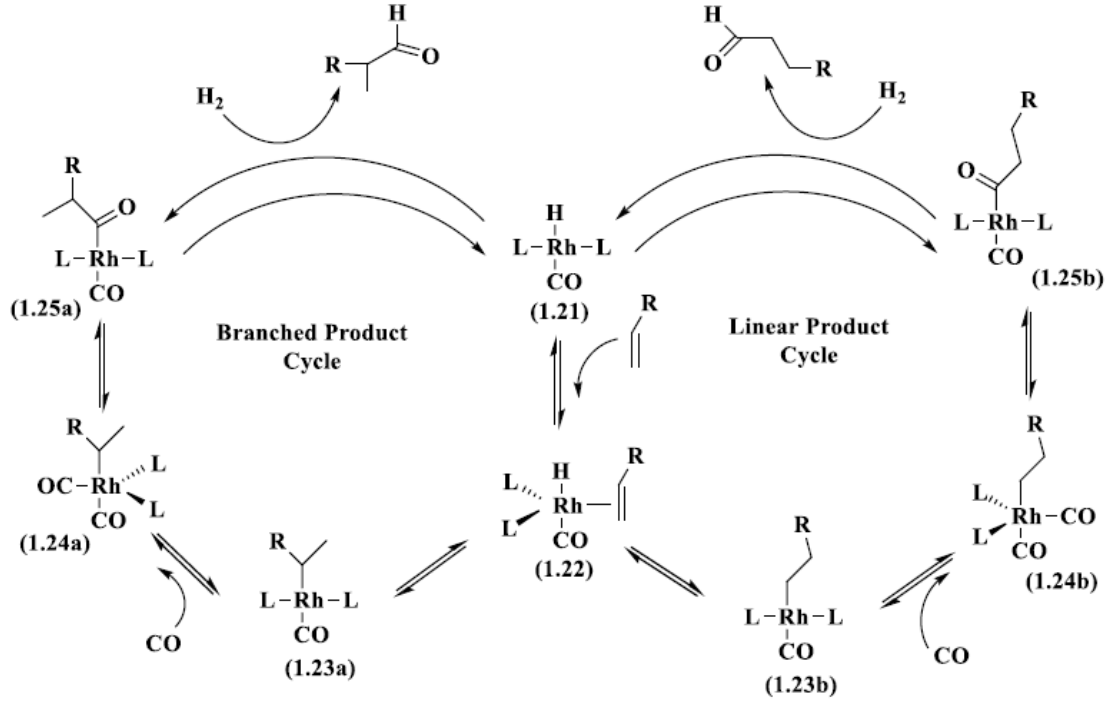

Scheme 1.2 A catalytic cycle of an unmodified Rh catalysed hydroformylation.

The rhodium catalyst precursor is usually modified to an isoelectronic and isostructural catalyst precursor by replacing one of the CO ligands with a phosphine ligand (PR_3), [$HRh(CO)_3(PR_3)$] (Figure 1.6). The modified species is generally stable compared to the unmodified and requires low pressure. The bulky PR_3 has a large cone angle and high steric bulk, so its introduction permits for the hydride migration step to favour the linear products.[34] The *n:iso* ratio would then change to 8:1, with more linear products.[34] Further scrutiny reveals that there is greater hydrogenation activity. This is rationalised from the reduction of the aldehyde to the alcohol, leading to more alcohol products rather than the aldehydes. The mechanism is similar with that of unmodified Rh catalyst with the third step with the introduced steric bulk favouring the

terminal alkyl ligand and another H_2 molecule introduced on the C=O bond of complexes **1.24a** and **1.24b** to CH–OH, followed by a reductive elimination to regenerate the active species.[35]

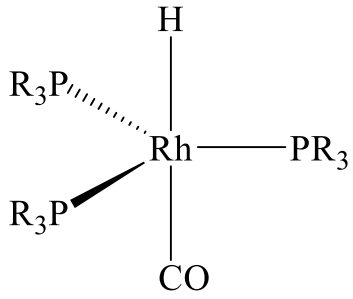

Figure 1.6 Structure of phosphine modified Rh(I) complexes used in hydroformylation.

There has been a wide usage of hydroformylation of alkenes in industrial processes, most specifically in pharmaceuticals, perfumery and agrochemical.[35] Most specifically is the use of rhodium catalysts. Due of the high cost of rhodium, much of literature has attempted to develop techniques which will use rhodium catalysts in hydroformylation to produce targets with a margin of higher profits. This still proves to be difficult because aldehydes are difficult to remove from the expensive rhodium catalyst, but products of lower olefins are easily separated by distillation techniques. Biphasic systems and immobilised catalysts are just a few separation methods currently in use.[36] In immobilised catalysis, the catalyst is bound to a solid support like silica and the activity is improved by this binding. In both cases, it is easier to isolate the catalyst due to the different phases. As such, these separation techniques are currently in use.[35] This is slightly different from systems whereby the catalyst is active in its solid state, where the activity is caused by the presence of the nanoparticles.

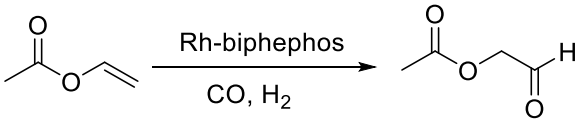

Scheme 1.3 Preparation of 2-oxoethyl acetate under hydroformylation conditions.

A Rh-biphephos catalyst has been used for the hydroformylation of vinyl acetate (Scheme 1.3), with a molar substrate to catalyst loading ratio of 4000:1 at 80 °C, 3 bar.[37] The *n:iso* ratio was reported to be 15:1, attributed to high steric demand of the biphephos ligand, which inhibit the hydride migration to branched product. The same catalyst was used in the hydroformylation of *N*-allyl phthalimide to afford an aldehyde with a ratio of 11.5:1 (Scheme 1.4).

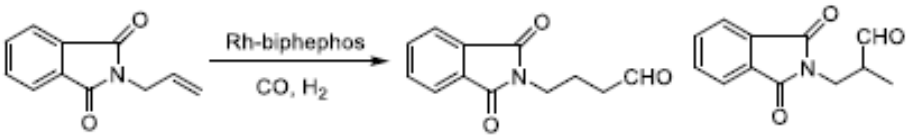

Scheme 1.4 Hydroformylation of N-allyl phthalimide.

Rh-diazaphospholane was employed as a catalyst for the hydroformylation of vinyl acetate to the aldehyde 2-(acetoxy)propanal, with reports of a 96.8*%ee* enantiomeric selectivity and a large *n:iso* ratio of 139:1.[38] An aldehyde Florhydral is prepared by the selective hydroformylation of 1,3-propylenebenzene with Rh-PPh_3 (Scheme 1.5) . The Florhydral is reduced with a hydrogen molecule and a Pd/C catalyst to afford its respective saturated form.

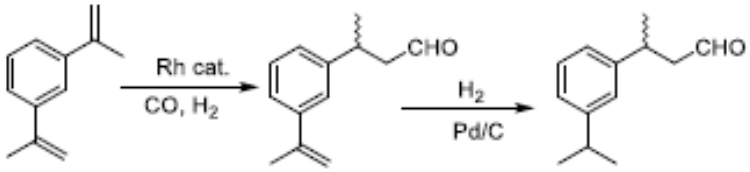

Scheme 1.5 Preparation of Florhydral by hydroformylation and reduction sequences.

There has also been attempts to prepare the enantiomerically pure Florhydral by asymmetric hydroformylation methods, but this has only led to low enantioselectivities compared to the far more enantioselective asymmetric hydrogenation route with a 97*%ee*.[20] Using Rh-(*S,R*)-Binaphos in the asymmetric hydroformylation of aryl vinly ethers, the chiral aldehyde 2,4-DCPPA is produced with a 72*%ee* and a 2:1 *n:iso* ratio.[7]

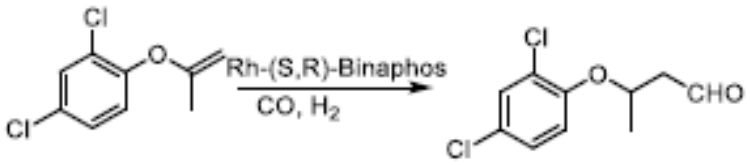

Scheme 1.6 Asymmetric hydroformylation of aryl vinyl ethers.

Finally, a Rh-xantphos is used in the preparation of an insecticidal sulfoximine, by the hydroformylation of 3-methylenetetrahydrothiophene to an aldehyde intermediate.[39] The linear aldehyde is the only regioisomer formed. The intermediate can be aminated sequentially, followed by cyclisation to form a pyridine ring and oxidation of the sulphur.

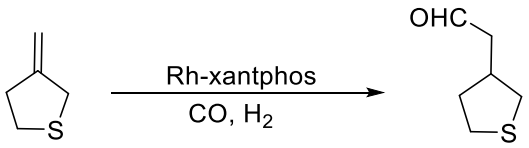

Scheme 1.7 Preparation of an insecticidal sulfoximine by hydroformylation.

1.5 Allylic oxidation

The allylic oxidation of an alkene is one of the simplest cases that proceeds via C–H bond functionalization.[40] This eco-friendly process aims to functionalise C–H bonds, making synthetic scheme shorter, cleaner and more efficient, without use of protection-deprotection sequences. As mentioned above, the reaction requires harsh conditions due to the high dissociation bond of the carbon-hydrogen bond.[41] Investigations have been placed in similar reactions that will enable the use of mild conditions. Of these is weak coordination by directing functional group in Pd, Rh and Ru. It has been reported that with Pd(II), strongly coordinated palladacycles form thermodynamically stable intermediates that are unreactive with functionalizing reagents under mild conditions. However, the presence of a strong acid is needed to activate the intermediate. In contrast, cyclopalladation intermediates containing weakly coordinating directing groups are thermodynamically disfavoured, however, these are more reactive towards functionalization reagents to give desired products controlled by kinetics. This observation is similar to that reported by Halpern in asymmetric hydrogenation.

For Rh(III), relatively high yields are obtained for the synthesis of isoquinolone natural products from pivaloyl hydroximates and vinyl acetate in methanol using a $[Cp^*RhCl_2]_2$ (**6**) catalyst with CsOAc, Scheme 1.8.[42] Webb *et. al.* postulate that the mechanism involves a rearrangement of N-metalated hydroxamic acid intermediate since the reaction occurs only in the presence of $[Cp^*RhCl_2]_2$.

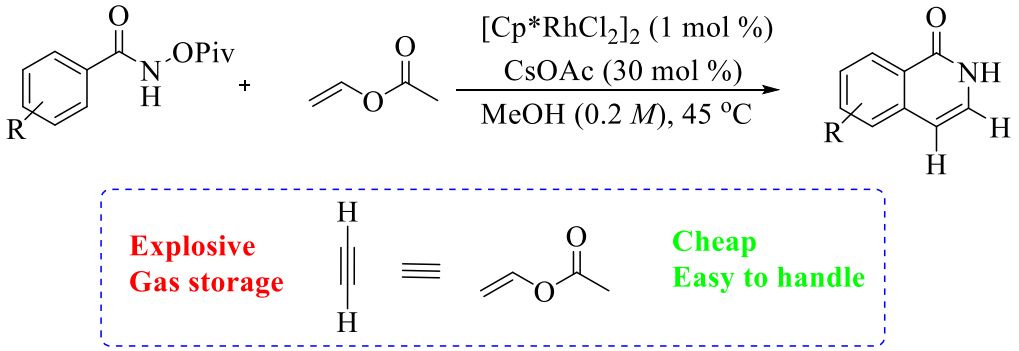

Scheme 1.8 Allylic oxidation of vinyl acetate with pivaloyl hydroximates with a Rh(III) catalyst **6**.

In allylic oxidation, the olefin substrate either linear or cyclic is reacted with an oxidizing agent as an oxygen source with a metal catalyst present. As seen on Scheme 1.6, alkenone (enone) and alkenol (enol) products can be obtained, which gives the problem in chemoselectivity.

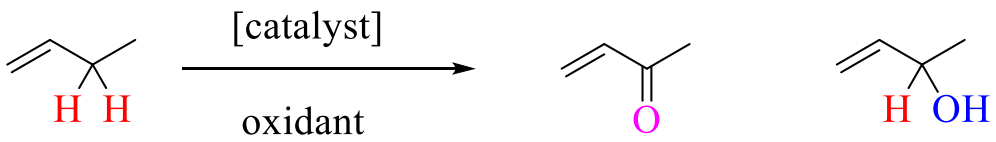

Scheme 1.9 Allylic oxidation of a linear alkene.

There has also been reports of epoxide products and other side products.[43,44] In the case of the enone and enol products, the allylic C–H bond is activated with a lower bond dissociation energy due to the possible resonance with the C=C double bong to stabilize the transition state. As a result of this, the allylic hydrogens are more susceptible to radical abstraction than proton abstraction provided no basic reagent is involved in the reaction. Products derived from allylic oxidation have wide applications ranging from intermediates for total synthesis of natural products, anticancer reagents and flavouring constituents. Strategies that have been adopted in the past lack regioselectivity, stereoselectivity and usually have overoxidation issues. Moreover, the assisting reagents were mainly based on Se or Cr oxides in stoichiometric amounts. Fortunately, eco-friendly alternative methods based on the chemistry of Cu, Pd and Rh have been reported. The key is the ability for the metal complexes to undergo a 1-electron oxidation.[45]

In the case of Cu, Garcia-Cabeza *et. al.* have reported the preparation of a copper-aluminium mixed oxide (Cu-Al Ox) that catalyses the allylic hydroxylation of enones.[46] They observed that the electron-deficient C=C double bond is oxidized with good yields, when employing Cu-

Al Ox with potassium tert-butoxide (^{t}BuOK) and molecular oxygen (O_2) from air as the oxidant. They proceeded to investigating the allylic oxidation of electron-rich alkenes, using tert-butylhydroperoxide (TBHP) as the oxidant. The reaction was observed as sensitive to the nature of the solvent and is quantitative when acetonitrile is used. Furthermore, the Cu–Al Ox catalyst is essential since the yields are significantly low in its absence. Cycloalkenes substrates and aromatic carboxylic acids bearing different functional groups as oxidants were also evaluated. The presence of either electron-withdrawing or electron-donating group in the aromatic ring of the acid does not affect the outcome of the reaction.[46] They were able to propose a mechanism, Scheme 1.10, based on the work of Beckwith and Savitzas[47] and Mayoral *et. al.*[48]. This was supported by whereby the Cu–Al Ox provides a surface for coordination, thus reducing the activation energy for the O–O bond cleavage of TBHP or C–H of cyclohexene. The cyclohexenyl radical carbon at C3 is stabilised by the shift of the double to C2 and C3, with coordination at C1. The cyclohexenyl radical is locked by the Cu or Al atoms. This is followed by a pericyclic rearrangement around the plane containing the metallic surface, which leads to the formation of the corresponding ester.

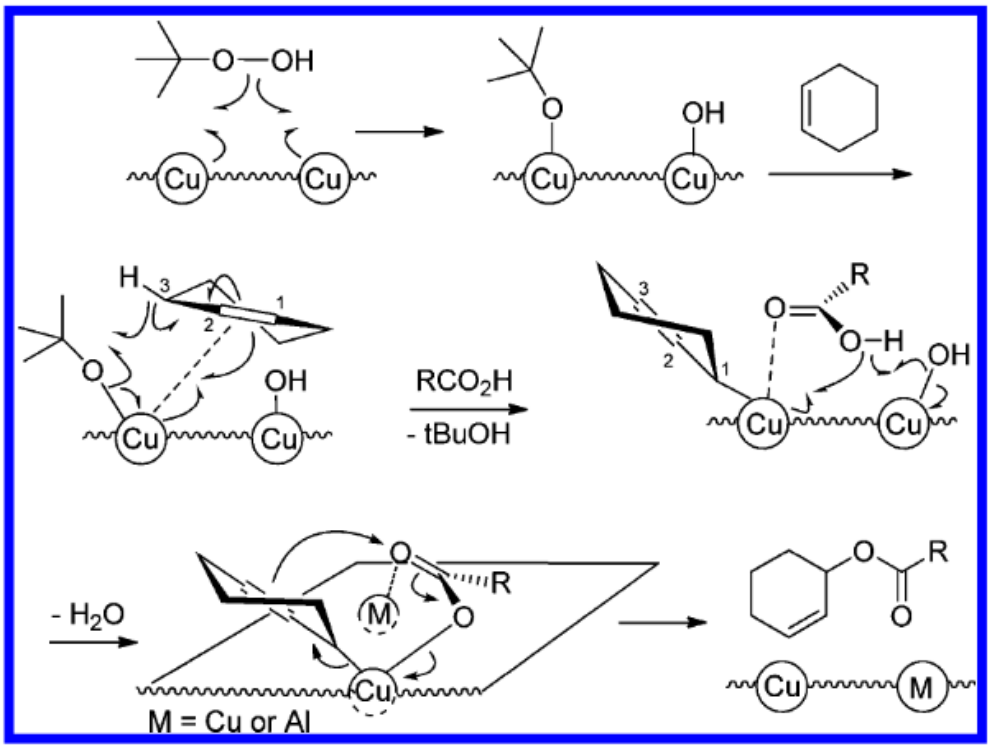

Scheme 1.10 Mechanism for the allylic oxidation of cyclohexene with TBHP.

Surprisingly, when the carboxylic acid is replaced with L-proline, instead of an ester, the corresponding enol or enone are obtained, Scheme 1.11. A possible explanation would involve a formation of a complex between L-proline and copper atom of Cu-Al Ox as reported by Ding

and Stahl.[49,50] Statistical analysis on the reaction found that the highest yield is obtained with at 60 mg/mmol catalyst loading of Cu–Al Ox and 4.5 eq. of TBHP, increasing the reaction yield from 40 to 64 %. This could be due slow reactivity of the Cu metal centre.

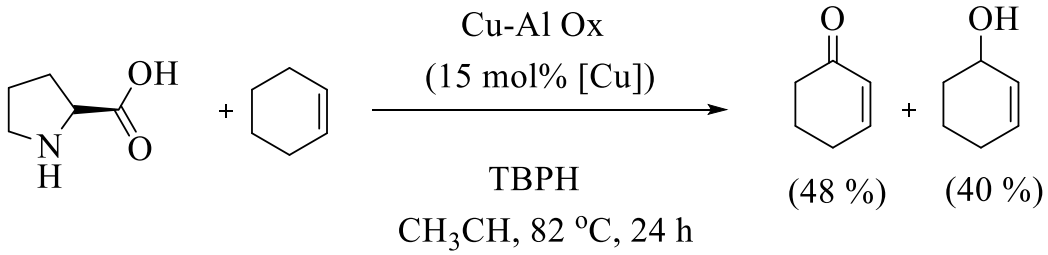

Scheme 1.11 Synthesis of cyclohexenol and cyclohexanone from L-proline and cyclohexene.

1.5.1 Metal-free allylic oxidation of linear and cyclic substrates

Recently, selective oxidation strategies which require synergistic effects of fundamental parameters that will achieve optimal efficiency. This includes oxidants, catalysts, feedstock, reaction solvents and mechanisms of the optimised reactions.[51] These complexes result to an improvement of the oxidation systems to fulfil the important reactions.[52] The focus has been placed on environmental issues to minimise toxic chemicals, energy consumption and waste production on the basis of atom efficiency and sustainability of the chemical transformation.[3-4] In this case, the traditional stochiometric amounts of toxic oxidants is replaced with molecular oxygen O_2.[5-6] This is an ideal oxidant due to water being its sole by-product. However, the direct use requires activation processes that rise from the Wigner spin conservation rule[57] in its triplet ground state and challenges of selective oxo-functionalisation.[6,8-9] The metal-free organocatalytic strategies have gained momentum in many oxidation processes with molecular oxygen,[56,58,59] with advantages in green chemistry for long-term considerations.[60] In context of metal-free catalysis, use of photocatalytic oxidation is quiet appealing as it can afford good conversion and selectivity under mild reaction conditions.[61–64] Allylic and benzylic oxidation are of special interest due to their products from raw materials found as key intermediates with commercial applications including pharmaceuticals, flavourants, polyester fibres, and agrochemical (Figure 1.6)[15-17,24–30]

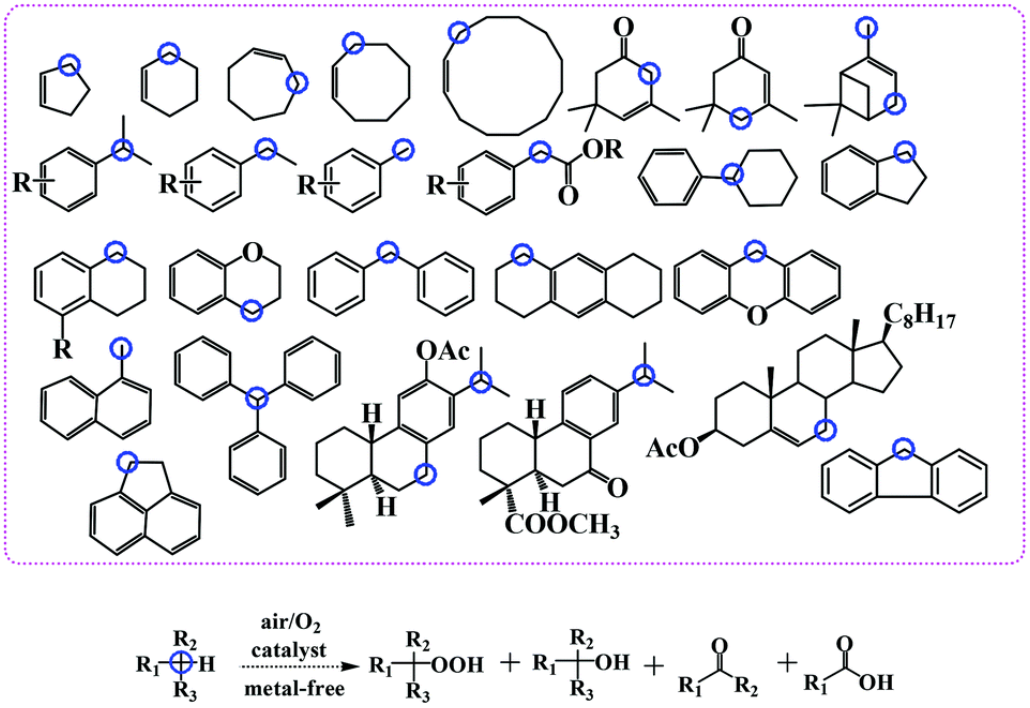

Figure 1.7 Metal-free allylic oxidation of cyclic alkenes with O_2.

Innovative oxidation strategies that involve the relatively cheap and non-toxic N-hydroxyphthalimide (NHPI)[81,82] have emerged as tools for organocatalysts for the selective oxo-functionalisation of various organic substrates at mild reaction conditions. Several reviews have summarised these striking applications.[56,58,59] Mechanistic investigations have reached the following consensus (Scheme 1.12); the hydrogen abstraction from alkene substrates by phthalimide-N-oxyl radical (PINO•) (route b), *in situ* that is generated by NHPI (route a), serves as a crucial step.[83] The resulting carbon-centred radicals are easily trapped by a molecular oxygen (route c) leading to peroxyl radicals which then generates PINO and yield hydroperoxides *via* a near-perfect equilibrium reaction (route d).[84] Hydroperoxides are ultimately converted into oxygenated molecules through radical α-H abstraction routes or redox decomposition.[65,84–88]

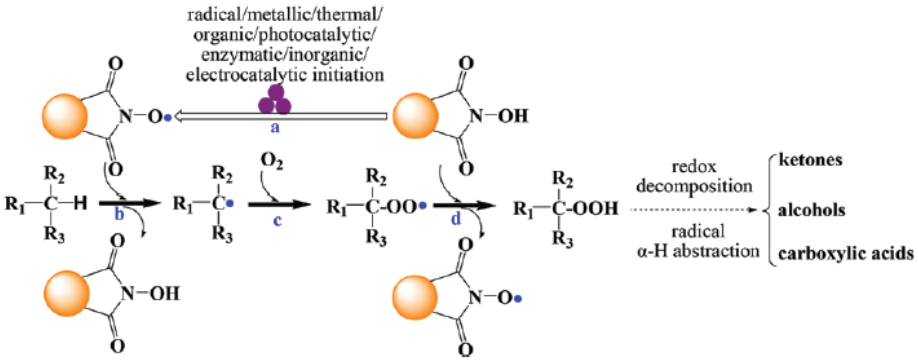

Scheme 1.12 Literature mechanism of allylic oxidation with NHPI is an initiator.

There are quite a few organic substrates that utilise the electron-transfer and oxidation processes. Xu and co-workers attempted to develop similar organocatalytic systems.[77] The performances of the combination of *o*-phenanthroline (*o*-Phen) or bipyridine (and its analogues) with NHPI were assessed in the oxidation of ethylbenzene with a presence of molecular bromine (Br_2).[77] *o*-Phen was found to be the most efficient mediator, followed by 2,2-bipyridine and bathophenanthroline. The lower modulated behaviours of other analogues are reported to be related to the steric hindrance of the substituents around the active sites of nitrogen atoms which hinder their contact with NHPI. These oxidation reactions undergo free radical pathways with no induction periods, while Br_2 functions as a single-electron initiator for the conversion of *o*-Phen derivatives to the corresponding cation radicals, thus promoting the generation of PINO• from NHPI (Scheme 1.13).

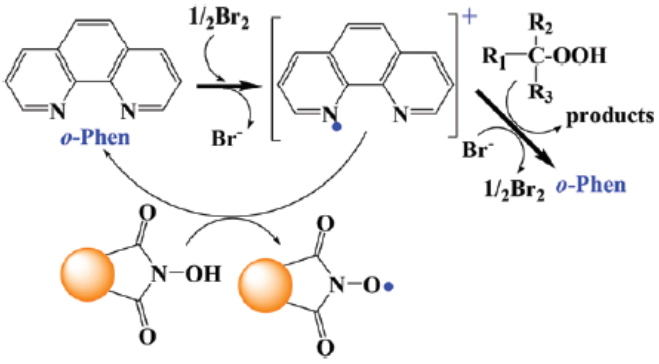

Scheme 1.13 Allylic oxidation with NHPI and *o*-Phen in the presence of Br_2.

Peroxides are commonly used as oxidising agents, radical initiators, and precursors in preparation of phenols. Dibenzoyl peoxide (DBP) (ref 79, 111),[83,89] cyclohexenebenzene-1-hydroperoxide (CHBHP),[90] tert-butylperoxypivalate (BPP)[74,91] and m-chloroperobenzoic acid (m-CPBA)[76] have been utilise as initiators in the NHPI-catalysed allylic and benzylic oxidation. These peroxides induce PINO• from NPIH through heat or light induced self-

decomposition (Scheme 1.14) Foricher *et. al.* reported on the oxidation of allylic isoprenoids by the NHPI/BPO system and its analogous systems, which affords an acceptable conversion (ca. 62–100%) and selectivity (ca. 65–91%) of allylic ketones.[83] The catalysts were used in stoichiometric amounts, and could be recovered at the end.

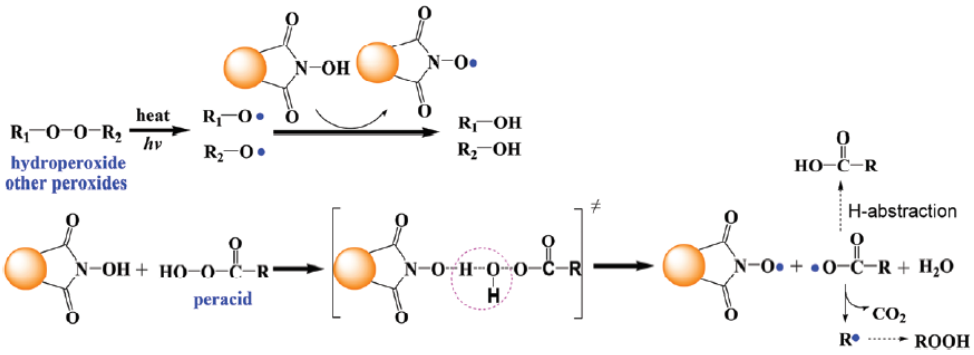

Scheme 1.14 Allylic oxidation with NHPI and hydroperoxide.

1.5.2 Metal catalysed allylic oxidation of linear and cyclic substrates

Classically, allylic oxidation was mainly based on selenium (SeO_2),[73-74] manganese (MnO_2),[94] and potassium ($KMnO_4$) compounds. However, these were found to lack in stereo- and regioselectivity, and frequently encountered toxicity. This prompted researchers to shift their focus to transition metal, as this are easily oxidised and favour the generation of radicals.[95] Zhang *et. al.* reported on the allylic oxidation of cyclic alkenes with molecular oxygen and tert-butyl hydroperoxide with a copper-manganese oxide catalyst (Scheme 1.15).[96] They found that in acetonitrile, total conversion is obtained with unhindered cycloalkenes and is chemoselective to only the ketone product with excellent regioselectivity. The ketone product could be oxidised to the oxide product with a yield of 92.8 %.

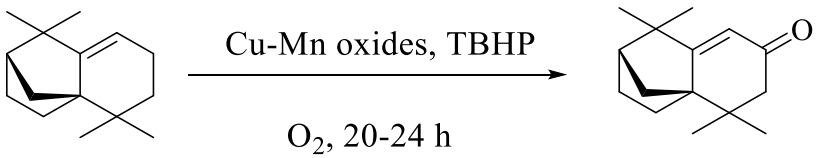

Scheme 1.15 Allylic oxidation of cyclic alkene with Cu-Mn oxides.

On the other hand, Garcia-Cabeza designed a copper-aluminium mixed oxide used as a catalyst in the allylic oxidation of internal olefins (Scheme 1.16).[97] With L-proline and TBHP, yields a 50/50 mixture of the ketone and alcohol products. The reaction of the internal olefine with a carboxylic acid and TBHP, esters are obtained with moderate to excellent yields (40 – 80 %).

Similar products are obtained from the Kharasch-Sosnovsky reaction, where an alkene is reacted with a peroxide with CuBr in benzene.[48,98–100]

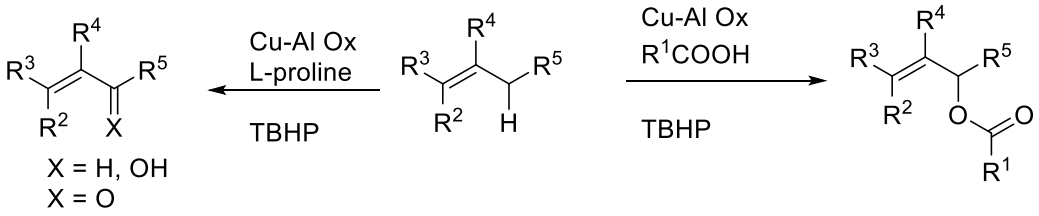

Scheme 1.16 Oxidation of internal olefins with Cu-Al oxide catalysts.

As of recent, the focus has shifted to transition metals and the platinum-group metals (PGM), namely Rh as a potential catalyst for allylic oxidation, as shown by White[101] and Doyle[102]. Certainly, Catino *et. al.* showed that the dirhodium(II) caprolactamate complex $[Rh_2(cap)_4]$ is more active than the dirhodium(II) acetate complex $[Rh_2(OAc)_4]$ and the pentafluoro acetate complex $[Rh_2(pfb)_4]$ with 1 mol% of catalyst in the oxidation carbon 1 substituted cyclohexenes.[103,104] This is accounted for by the easier access to the Rh_2^{5+} species since $[Rh_2(cap)_4]$ readily undergoes a one electron oxidation (with $E_{1/2}$ = 11 mV). The addition of 50 mol% K_2CO_3 significantly reduces reaction time to 1 h and catalyst loading to 0.1 mol% while increasing the yield. The reaction is regioselective towards unhindered α-H. Withdrawing groups at carbon 1 cause the alkene to be electron deficient, giving lower yield.

Du bois' dirhodium(II) complex $[Rh_2(esp)_2]$ was found to be a robust, efficient and recyclable catalyst for solvent-free allylic and benzylic oxidation.[105] With 1 mol% catalyst loading and T-Hydro in *n*-heptane could oxidise the Δ^5-steroid with excellent yields (> 80 %) in 6 h. Su et. al. found that the $[Rh_2(cap)_4]$ complex is able to oxidise styrenes with TBHP, giving complete conversion when water is the solvent, however, the reaction lacks any chemoselectivity.[87-88] Finally, Anderson et. al. designed a tethered, axially coordinated heteroleptic dirhodium(II) complex $[Rh_2(OAc)_3(PhTCB)]$, which was used in the cyclopropanation of styrenes, good yields (> 70 %) and chemoselectivity towards the cyclopropane over the diester.[108]

1.6 Motivation and Rationale of the Study

Owing to the differences in binding strength, electrochemical and spectroscopic properties of O donor and N donor atoms at the equatorial position in dirhodium complexes, the synthesis of ligands with these donor atoms; acetates (O donors) and formamidinates (N donors) with electron-releasing or electron-withdrawing substituents at designated position and the preparation of fully substituted and mixed-ligand complexes could lead to a series of

compounds with fascinating properties, including electronic and steric properties of the dirhodium complexes. The availability of two Rh(II) metal centres could afford easier access to the catalytically active Rh(III) species for both allylic oxidation and hydroformylation. Finally, the applications of these bimetallic Rh(I) and Rh(II) complexes as catalysts in the above-mentioned organic transformations, namely hydroformylation and allylic oxidation will broaden the scope of available methods in the laboratory to installing oxidized functionality.

1.7 Research Aims and Objectives

1.7.1 General aims

The aim of the study is to design, synthesise and characterise bimetallic rhodium(I) and dirhodium(II) paddlewheel complexes containing bridging diphenylformamidinate ligands. The complexes will be evaluated for their catalytic activity: the bimetallic rhodium(I) complexes are to be evaluated in the hydroformylation of 1-octene and the dirhodium(II) complexes are to be evaluated in the allylic oxidation of cyclohexene.

1.7.2 Specific objectives

- Synthesis and characterisation of diphenylformamidine ligands.

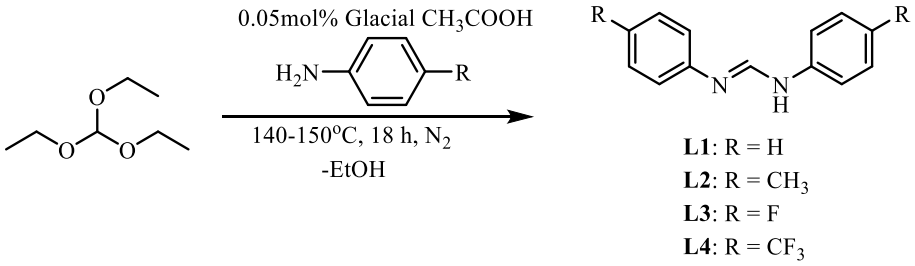

Scheme 1.17 Synthesis of diphenylformamidine ligands L1 – L4.

- Synthesis and characterisation of bimetallic rhodium(I) complexes.

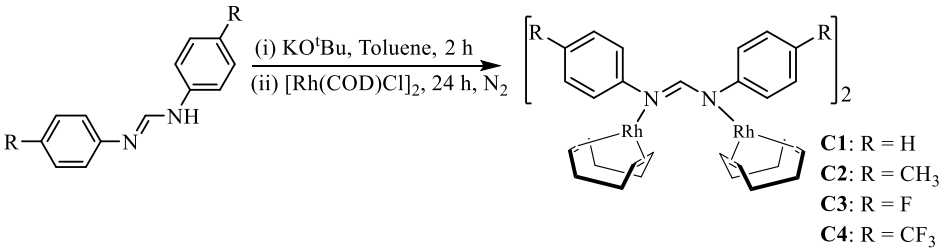

Scheme 1.18 Synthesis of bimetallic rhodium(I) complexes **C1** – **C4**.

- Synthesis and characterisation of homoleptic dirhodium(II) paddlewheel complexes.

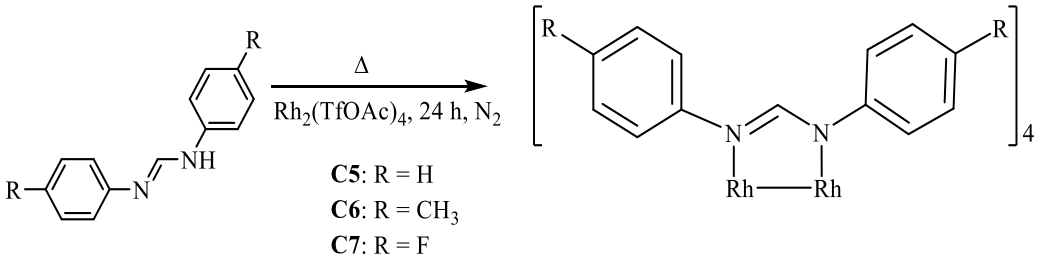

Scheme 1.19 Synthesis of homoleptic dirhodium(II) complexes **C5** – **C7**.

- Synthesis and characterisation of dirhodium(II) paddlewheel complexes.

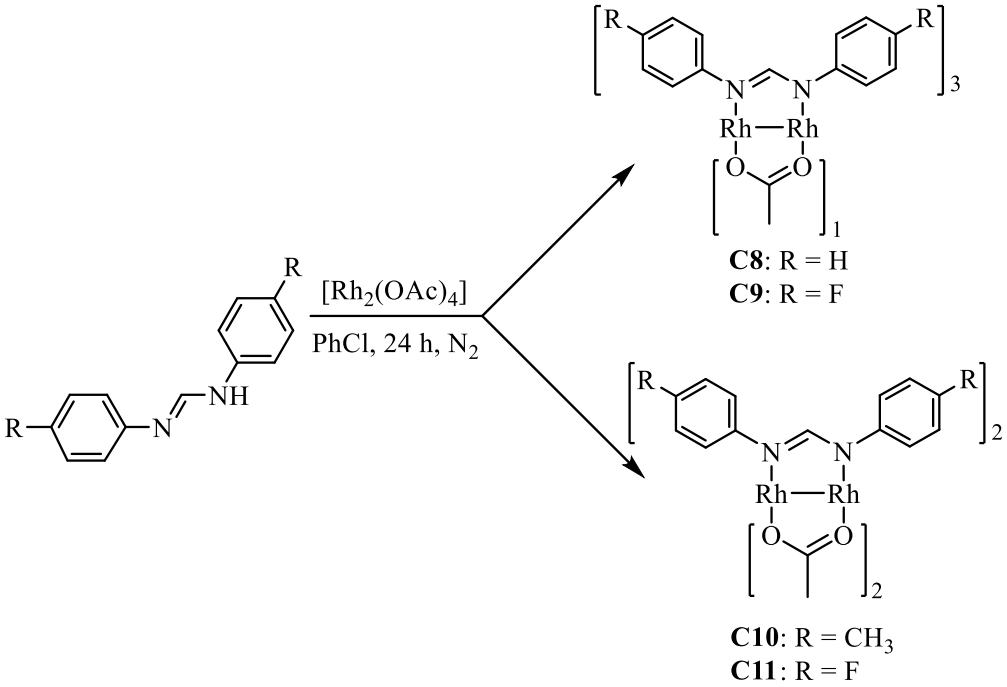

Scheme 1.20 Synthesis of mixed ligand heteroleptic dirhodium(II) complexes **C8** – **C11**.

- Evaluation of the bimetallic rhodium(I) complexes as potential catalysts for the hydroformylation of 1-octene.
- Evaluation of the dirhodium(II) paddlewheel complexes as potential catalysts for the allylic oxidation of cyclohexene.

1.8 References

1 M. L. Burnett, *Environ. Manage.*, 1998, **22**, 213–224.

2 P. T. Anastas and J. C. Warner, *Green Chemistry: Theory and Practice*, Oxford University Press, New York, 1998.

3 P. T. Anastas, L. B. Bartlett, M. M. Kirchhoff and T. C. Williamson, *Catal. Today*, 2000, **55**, 11–22.

4 S. I. S. Mashuri, M. L. Ibrahim, M. F. Kasim, M. S. Mastuli, U. Rashid, A. H. Abdullah, A. Islam, N. Asikin-Mijan, Y. H. Tan, N. Mansir, N. H. M. Kaus and T. Y. Y. Hin, *Catalysts*, 2020, **10**, 1–29.

5 P. Pino and C. Botteghi, *Org. Synth.*, 1977, **57**, 11.

6 T. Bligaard, R. M. Bullock, C. T. Campbell, J. G. Chen, B. C. Gates, R. J. Gorte, C. W. Jones, W. D. Jones, J. R. Kitchin and S. L. Scott, *ACS Catal.*, 2016, **6**, 2590–2602.

7 P. J. Harrington and E. Lodewijk, *Org. Process Res. Dev.*, 1997, **1**, 72–76.

8 T. L. Church, Y. D. Y. L. Getzler, C. M. Byrne and G. W. Coates, *Chem. Commun.*, 2007, 657–674.

9 G. J. Sunley and D. J. Watson, *Catal. Today*, 2000, **58**, 293–307.

10 R. E. Harmon, S. K. Gupta and D. J. Brown, *Chem. Rev.*, 1973, **73**, 21–52.

11 J. Halpern, *Pure Appl. Chem.*, 2001, **73**, 209–220.

12 B. Cornils, W. A. Herrmann and M. Rasch, *Angew. Chemie Int. Ed.*, 1994, **33**, 2144–2163.

13 P. J. Deuss, R. Denheeten, W. Laan and P. C. J. Kamer, *Chem. - A Eur. J.*, 2011, **17**, 4680–4698.

14 M. H. Pérez-Temprano, J. A. Casares and P. Espinet, *Chem. - A Eur. J.*, 2012, **18**, 1864–1884.

15 J. Park and S. Hong, *Chem. Soc. Rev.*, 2012, **41**, 6931–6943.

16 G. J. Rowlands, *Tetrahedron*, 2001, **57**, 1865–1882.

17 I. Bratko and M. Gómez, *Dalt. Trans.*, 2013, **42**, 10664–10681.

18 B. L. Feringa and E. K. van den Beuken, *Tetrahedron*, 1998, **54**, 12985–13011.

19 S. W. S. Choy, M. J. Page, M. Bhadbhade and B. A. Messerle, *Organometallics*, 2013, **32**, 4726–4729.

20 F. A. Cotton, C. A. Murillo, S. E. Stiriba, X. Wang and R. Yu, *Inorg. Chem.*, 2005, **44**,

8223–8233.

21 A. M. Angeles-Boza, H. T. Chifotides, J. D. Aguirre, A. Chouai, P. K. L. Fu, K. R. Dunbar and C. Turro, *J. Med. Chem.*, 2006, **49**, 6841–6847.

22 F. A. Cotton, E. A. Hillard and C. A. Murillo, *J. Am. Chem. Soc.*, 2002, **124**, 5658–5660.

23 E. B. Boyar and S. D. Robinson, *Coord. Chem. Rev.*, 1983, **50**, 109–208.

24 S. A. Johnson, H. R. Hunt and H. M. Neumann, *Inorg. Chem.*, 1963, **2**, 960–962.

25 H. Sheth, *Int. J. Psychosoc. Rehabil.*, 2016, **20**, 25–33.

26 N. A. Ezerskaya, E. S. Toropchenova, I. V. Kubrakova, S. V. Krasheninnikova, T. F. Kudinova, T. A. Fomina and I. N. Kiseleva, *J. Anal. Chem.*, 2000, **55**, 1132–1135.

27 J. L. Bear, B. Han, Z. Wu, E. Van Caemelbecke and K. M. Kadish, *Inorg. Chem.*, 2001, **40**, 2275–2281.

28 M. Beller and J. G. E. Krauter, *J. Mol. Catal. A Chem.*, 1999, 31–39.

29 A. C. J. Koeken, L. J. P. Van Den Broeke, N. E. Benes and J. T. F. Keurentjes, *J. Mol. Catal. A Chem.*, 2011, **346**, 94–101.

30 F. Hebrard and P. Kalck, *Chem. Rev.*, 2009, **109**, 4272–4282.

31 R. F. Heck and D. S. Breslow, *J. Am. Chem. Soc.*, 1961, **83**, 4023–4027.

32 G. D. Frey, *J. Organomet. Chem.*, 2014, **754**, 5–7.

33 S. Gladiali, J. Carles Bayón and C. Claver, *Tetrahedron: Asymmetry*, 1995, **6**, 1453–1474.

34 P. Meakin, J. P. Jesson and T. C. A., *J. Am. Chem. Soc.*, 1972, **2**, 3240–3242.

35 G. T. Whiteker and C. J. Cobley, in *Organometallics as Catalysts in the Fine Chemical Industry*, 2012, vol. 42, pp. 35–46.

36 P. J. Thomas, A. T. Axtell, J. Klosin, P. Wei, C. L. Rand, T. P. Clark, C. R. Landis and K. A. Abboud, *Org. Lett.*, 2007, **9**, 2665–2668.

37 S. Paganelli, A. Ciappa, M. Marchetti, A. Scrivanti and U. Matteoli, *J. Mol. Catal. A Chem.*, 2006, **247**, 138–144.

38 C. Botteghi, G. Delogu, M. Marchetti, S. Paganelli and B. Sechi, *J. Mol. Catal. A Chem.*, 1999, **143**, 311–323.

39 K. M. Kuhn and R. H. Grubbs, *Org. Lett.*, 2008, **10**, 2075–2077.

40 J. Wencel-Delord, T. Dröge, F. Liu and F. Glorius, *Chem. Soc. Rev.*, 2011, **40**, 4740–4761.

41 Z. Tian, L. Lis and S. R. Kass, *J. Org. Chem.*, 2013, **78**, 12650–12653.

42 N. J. Webb, S. P. Marsden and S. A. Raw, *Org. Lett.*, 2014, **16**, 4718–4721.

43 J. T. Groves, G. A. McClusky, R. E. White and M. J. Coon, *Biochem. Biophys. Res. Commun.*, 1978, **81**, 154–160.

44 J. T. Groves, T. E. Nemo and R. S. Myers, *J. Am. Chem. Soc.*, 1979, **101**, 1032–1033.

45 K. Srinivasan and S. Perrier, *J. Mol. Catal.*, 1986, **36**, 297–317.

46 A. L. García-Cabeza, R. Marín-Barrios, F. J. Moreno-Dorado, M. J. Ortega, G. M. Massanet and F. M. Guerra, *Org. Lett.*, 2014, **16**, 1598–1601.

47 A. L. J. Beckwith and A. A. Zavitsas, *J. Am. Chem. Soc.*, 1986, **108**, 8230–8234.

48 J. A. Mayoral, S. Rodríguez-Rodríguez and L. Salvatella, *Chem. - A Eur. J.*, 2008, **14**, 9274–9285.

49 G. Zhang, X. Han, Y. Luan, Y. Wang, X. Wen and C. Ding, *Chem. Commun.*, 2013, **49**, 7908–7910.

50 J. M. Hoover, B. L. Ryland and S. S. Stahl, *J. Am. Chem. Soc.*, 2013, **135**, 2357–2367.

51 U. Neuenschwander, N. Turrà, C. Aellig, P. Mania and I. Hermans, *Chimia (Aarau).*, 2010, **64**, 225–230.

52 M. Beller, *Adv. Synth. Catal.*, 2004, **346**, 107–108.

53 R. A. Sheldon and I. W. C. E. Arenas, *Adv. Synth. Catal.*, 2004, **346**, 1051–1071.

54 R. A. Sheldon, *Green Chem.*, 2007, **9**, 1273–1283.

55 G. J. Ten Brink, I. W. C. E. Arends and R. A. Sheldon, *Science (80-.).*, 2000, **287**, 1636–1639.

56 A. Dos Santos, L. El Kaïm and L. Grimaud, *Org. Biomol. Chem.*, 2013, **11**, 3282–

3287.

57 E. Roduner, W. Kaim, B. Sarkar, V. B. Urlacher, J. Pleiss, R. Gläser, W. D. Einicke, G. A. Sprenger, U. Beifuß, E. Klemm, C. Liebner, H. Hieronymus, S. F. Hsu, B. Plietker and S. Laschat, *ChemCatChem*, 2013, **5**, 82–112.

58 S. Wertz and A. Studer, *Green Chem.*, 2013, **15**, 3116–3134.

59 L. Melone and C. Punta, *Beilstein J. Org. Chem.*, 2013, **9**, 1296–1310.

60 P. J. Dunn, *Chem. Soc. Rev.*, 2012, **41**, 1452–1461.

61 S. P. Fritz, A. Mumtaz, M. Yar, E. M. McGarrigle and V. K. Aggarwal, *European J. Org. Chem.*, 2011, 3156–3164.

62 J. Hu, Y. Hu, J. Mao, J. Yao, Z. Chen and H. Li, *Green Chem.*, 2012, **14**, 2894–2898.

63 K. Ohkubo, K. Suga, K. Morikawa and S. Fukuzumi, *J. Am. Chem. Soc.*, 2003, **125**, 12850–12859.

64 K. Ohkubo and S. Fukuzumi, *Org. Lett.*, 2000, **2**, 3647–3650.

65 N. Hirai, N. Sawatari, N. Nakamura, S. Sakaguchi and Y. Ishii, *J. Org. Chem.*, 2003, **68**, 6587–6590.

66 R. Nakamura, Y. Obora and Y. Ishii, *Adv. Synth. Catal.*, 2009, **351**, 1677–1684.

67 T. Lu, Y. Mao, K. Yao, J. Xu and M. Lu, *Catal. Commun.*, 2012, **27**, 124–128.

68 H. L. Ding and L. P. Zeng, *Adv. Mater. Res.*, 2013, **709**, 74–79.

69 X. Yang, Y. Wang, L. Zhou, C. Chen, W. Zhang and J. Xu, *J. Chem. Technol. Biotechnol.*, 2010, **85**, 564–568.

70 K. Wang, Z. Zhou, J. Song, L. Bi, N. Shen, Y. Wu, F. Chen and H. Wen, *J. Hazard. Mater.*, 2010, **184**, 400–405.

71 R. A. F. Tomás, J. C. M. Bordado and J. F. P. Gomes, *Chem. Rev.*, 2013, **113**, 7421–7469.

72 O. Fukuda, S. Sakaguchi and Y. Ishii, *Adv. Synth. Catal.*, 2001, **343**, 809–813.

73 Y. Aoki, S. Sakaguchi and Y. Ishii, *Adv. Synth. Catal.*, 2004, **346**, 199–202.

74 Y. Aoki, N. Hirai, S. Sakaguchi and Y. Ishii, *Tetrahedron*, 2005, **61**, 10995–10999.

75 G. Zheng, C. Liu, Q. Wang, M. Wang and G. Yang, *Adv. Synth. Catal.*, 2009, **351**, 2638–2642.

76 L. Melone, S. Prosperini, C. Gambarotti, N. Pastori, F. Recupero and C. Punta, *J. Mol. Catal. A Chem.*, 2012, **355**, 155–160.

77 X. Tong, J. Xu and H. Miao, *Adv. Synth. Catal.*, 2005, **347**, 1953–1957.

78 D. Singh, M. E. Rezac and P. H. Pfromm, *J. Am. Oil Chem. Soc.*, 2009, **86**, 93–101.

79 L. Zhou, Y. Chen, X. Yang, Y. Su, W. Zhang and J. Xu, *Catal. Letters*, 2008, **125**, 154–159.

80 Z. Du, Z. Sun, W. Zhang, H. Miao, H. Ma and J. Xu, *Tetrahedron Lett.*, 2009, **50**, 1677–1680.

81 Y. Yoshino, Y. Hayashi, T. Iwahama, S. Sakaguchi and Y. Ishii, *J. Org. Chem.*, 1997, **62**, 6810–6813.

82 Y. Ishii, S. Sakaguchi and T. Iwahama, *Adv. Synth. Catal.*, 2001, **343**, 393–427.

83 K. Chen, P. Zhang, Y. Wang and H. Li, *Green Chem.*, 2014, **16**, 2344–2374.

84 I. Hermans, T. L. Nguyen, P. A. Jacobs and J. Peeters, *ChemPhysChem*, 2005, **6**, 637–645.

85 Y. Ishii and S. Sakaguchi, *Catal. Today*, 2006, **117**, 105–113.

86 K. Chen, Y. Sun, C. Wang, J. Yao, Z. Chen and H. Li, *Phys. Chem. Chem. Phys.*, 2012, **14**, 12141–12146.

87 I. Hermans, P. A. Jacobs and J. Peeters, *J. Mol. Catal. A Chem.*, 2006, **251**, 221–228.

88 L. Vereecken, T. L. Nguyen, I. Hermans and J. Peeters, *Chem. Phys. Lett.*, 2004, **393**, 432–436.

89 Z. Yao, X. Hu, J. Mao and H. Li, *Green Chem.*, 2009, **11**, 2013–2017.

90 I. W. C. E. Arends, M. Sasidharan, A. Kühnle, M. Duda, C. Jost and R. A. Sheldon, *Tetrahedron*, 2002, **58**, 9055–9061.

91 K. Matsunaka, T. Iwahama, S. Sakaguchi and Y. Ishii, *Tetrahedron Lett.*, 1999, **40**, 2165–2168.

92 R. Manktala, R. S. Dhillon and B. R. Chhabra, *Indian J. Chem. - Sect. B Org. Med. Chem.*, 2006, **45**, 1591–1594.

93 M. Haruna and K. Ito, *J. Chem. Soc. Chem. Commun.*, 1981, 483–485.

94 S. Serra, *European J. Org. Chem.*, 2015, **2015**, 6472–6478.

95 V. K. Aggarwal and C. L. Winn, *Acc. Chem. Res.*, 2004, **37**, 611–620.

96 W. Zhang, Q. Wei, L. Lan, A. Wu, X. Yin and L. Shen, *Monatshefte fur Chemie*, , DOI:10.1007/s00706-016-1742-6.

97 A. L. García-Cabeza, R. Marín-Barrios, F. J. Moreno-Dorado, M. J. Ortega, G. M. Massanet and F. M. Guerra, *Org. Lett.*, 2014, **16**, 1598–1601.

98 W. Wei, C. Zhang, Y. Xu and X. Wan, *Chem. Commun.*, 2011, **47**, 10827–10829.

99 A. I. Meyers and F. X. Tavares, *J. Org. Chem.*, 1996, **61**, 8207–8215.

100 J. Eames and M. Watkinson, *Angew. Chemie - Int. Ed.*, 2001, **40**, 3567–3571.

101 J. H. Delcamp and M. C. White, *J. Am. Chem. Soc.*, 2006, **128**, 15076–15077.

102 E. C. McLaughlin, H. Choi, K. Wang, G. Chiou and M. P. Doyle, *J. Org. Chem.*, 2009, **74**, 730–738.

103 A. J. Catino, R. E. Forslund and M. P. Doyle, *J. Am. Chem. Soc.*, 2004, **126**, 13622–13623.

104 A. J. Catino, J. M. Nichols, H. Choi, S. Gottipamula and M. P. Doyle, *Org. Lett.*, 2005, **7**, 5167–5170.

105 L. Zhao, Y. Wang, Z. Ma and Y. Wang, *Inorg. Chem.*, 2017, **56**, 8166–8174.

106 I. Wauters, W. Debrouwer and C. V. Stevens, *Beilstein J. Org. Chem.*, 2014, **10**, 1064–1096.

107 Y.-L. Su, *Org. Synth.*, 2019, **96**, 300–311.

108 B. G. Anderson, D. Cressy, J. J. Patel, C. F. Harris, G. P. A. Yap, J. F. Berry and A. Darko, *Inorg. Chem.*, 2019, **58**, 1728–173.

Chapter 2

Synthesis and Characterization of Bimetallic-Univalent Rhodium(I) and Dirhodium(II) Complexes with Bridging Diphenylformamidine Ligands

2.1 Introduction

A range of studies have been carried out on the binuclear transition metal complexes, inclusive of theoretical, spectroscopic, and magnetic studies to better understand the metal-metal interactions of these complexes.[109–112] One example is the study of rhodium ions containing bridging ligands having donor atoms such as nitrogen, oxygen, in some cases anionic halogens such as chloride atoms.[113–115] The introduction of these bridging ligands is reported to improve the stability and reactivity of the metal centre towards interaction with substrates where such complexes are used as catalysts.[116]

Formamidine compounds $[HC(NR)_2]$, where R = aromatic, are a subclass of amidine compounds $[R'C(NR)_2]$, where R' = alkyl, aryl, amido or H. These The compounds have attracted interests of chemists due to their convenient synthesis, vast tunability in their electronic and steric properties.[117] These have been synthesised by heating triethyl orthoformate with respective anilines in neat conditions.[118] An acid catalyst may be used to promote the speed of the reaction. Recently, researchers were able to use a green process in their preparation by use of sonication.[119] They have been found to be key intermediates in constructing heterocycles and functional group transformations. Furthermore, these have broad versatility in their modes of coordination to transition metals. For these, reasons, these were chosen as ligands for the purpose of the current research.

A subclass of bimetallic transition metal complexes are the bimetallic Rh(I) complexes. Early reports of such complexes include on binuclear chlorido-bridged rhodium(I) complexes $[Rh(\mu–Cl)(COD)]_2$ containing 1,5-cyclooctadiene (COD),[120] a number of analogous Rh(I) complexes such as $[Rh(L)(COD)]_2$, where (L = amidinato, triazenido and anilinopyridinato), with their applications as catalysts towards organic reaction transformations such as hydroformylation, hydrogenation, hydroamination and polymerization of alkenes.[121,122] Piraino *et al.* have reported on the characterisation and electrochemical studies of

formamidinate-bridged rhodium(I) dimers.[123] These complexes would serve as potent reducing agents, and be considered for their catalytic activity which is easily fine-tuned by the introduction of various substituents on the aromatic carbons of the bridged ligands. Furthermore, the Rh···Rh catalytic centre can be adjusted sterically and electronically by considering the nature of the ligands. Thus, the elucidation of the structural, spectroscopic, and redox properties of these complexes is paramount for the development of efficient catalysts.[124]

On the other hand, dirhodium(II) complexes have fascinating properties that span from antitumour metal pharmaceuticals, phototherapeutic agents, design of supramolecular arrays, and more importantly catalysis.[20,21] The key for such complexes is in the stabilisation of the Rh_2^{4+}, with a molecular bonding orbital construction of eight of fourteen electrons are distributed among the σ, π and δ bonding orbitals. The remaining six are distributed among the π* and δ* antibonding orbitals.[22] This results in a single bond connecting the two Rh metals and gives rise to configuration with all electrons paired, hence diamagnetic.

These dirhodium(II) compounds are said to be 'paddlewheel' complexes with two types of ligands, equatorial (*eq*) or axial (*ax*). The Rh atoms are connected by four bridging ligands via *eq* coordination, while solvent and small coordinating ligands bind via *ax* coordination. The Rh–Rh bond is reported to be insensitive to the σ-donating axial ligands. The first reported dirhodium(II) is the dirhodium(II) tetraacetate complex $[Rh_2(O_2CCH_3)_4]$ obtained from the reduction of $RhCl_3{\cdot}3H_2O$ in a mixture of sodium acetate, acetic acid, and ethanol.[125] The replacement of the acetate ligands with other bridging ligands with nitrogen, sulphur and phosphorus has also been reported.[126] However, only a few examples have been found where a degree of two or three acetate ligands are substituted for selectively.

The properties of the dirhodium(II) complexes vary based on the nature of the ligands. The carboxylate ligands allow for unhindered ligand coordination at the *ax* coordination sites. The formamidinate ligands introduce a chemical and structural diversity to these complexes which results in rich electrochemistry. A combination of the acetate and the formamidinate ligands within the Rh_2^{4+} core should improvement their biological and catalytic activity. Due to N atoms having better σ-donor ability of O donors, the formamidinate groups form more stable complexes as their render the Rh_2^{4+} core more electron rich. In this chapter, the syntheses, characterisation, structure, and electrochemistry of bimetallic Rh(I) complexes of the type

[Rh(R-dpf)(COD)]$_2$ and dirhodium(II) complexes of the type [Rh$_2$(R-dpf)$_x$(OAc)$_{4-x}$], where x = 2, 3 or 4, with bridging *N,N'*-diphenylformamidinate ligands are discussed.

2.2 Synthesis and Characterization of Diphenylformamidine Ligands (L1 - L4)

The diphenylformamidine (R-dpf) ligands **L1 – L4** were synthesised following a previously described literature procedure (Scheme 2.21).[127–130] The respective commercially available para-substituted aniline was heated to reflux with triethyl orthoformate in the presence of acetic acid *via* an acid catalysed nucleophilic substitution reaction. The R-dpf ligands were isolated as white crystalline solids with a moderate yield of 49 – 54 % and melting points ranging from 139 to 147 ^{o}C. The ligands are soluble in common polar solvents.

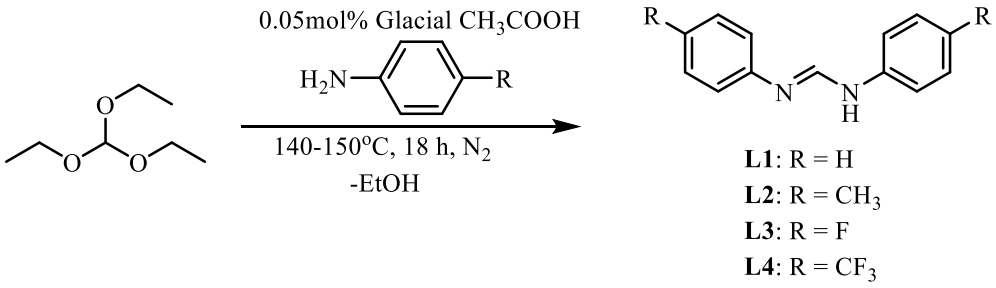

Scheme 2.21 Preparation of ligands **L1 – L4**.

In the first step of the reaction (Scheme 2.22), acetic acid protonates the triethyl orthoformate to enhance the lability of the ethoxy group. This in turn increases the electrophilicity of the electrophilic carbon by forming a carbocation. The addition of aniline leads to the elimination of ethanol. There is a proton-transfer, which is followed by an elimination of a second ethanol molecule forming an imine intermediate. The second equivalence of the aniline attacks the electrophilic carbocation of the intermediate species, followed by another proton-transfer. Subsequently, an ethanol molecule is eliminated, and acid regenerated upon the collapse of electrons from secondary amine to form a stable formamidine functionality.

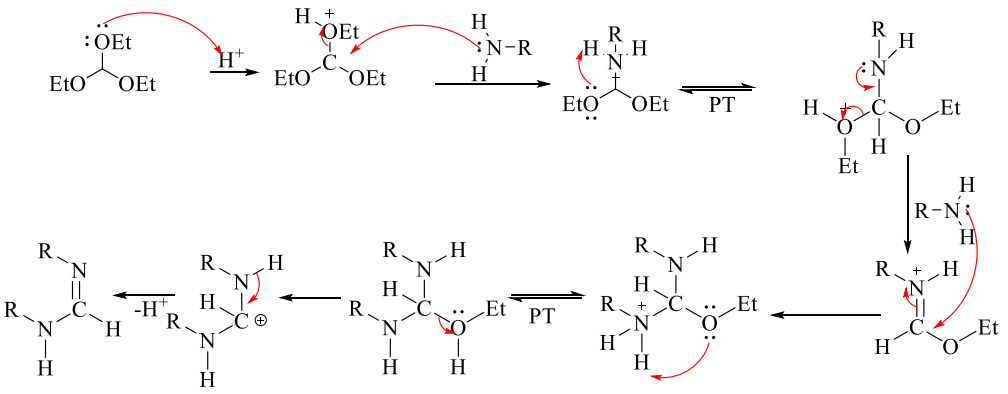

Scheme 2.22 Possible mechanism for the formation of the ligands **L1 – L4**.

The ^{1}H NMR spectrum of **L1** (Figure 2.8) indicates the successful synthesis of the reaction due to the presence of a sharp singlet appearing at $\delta = 8.24$ ppm integrating for one proton. This corresponds to the formamidinyl proton H_f.[131] A triplet integrating to four protons, resonating at 7.31 ppm belongs to the protons H_b *meta* to the nitrogen atoms. A multiplet at 7.04 – 7.11 ppm integrating for six protons is due to the overlapping signals of the H_a and H_c protons. The number of signals recorded indicates that in solution, the proton attached to the nitrogen is tautomerized by proton transfer between the two nitrogen atoms of the formamidine functionality. This dynamic behaviour is well established to analogous ligands that have been studied previously.[132] Consequently, the molecule is symmetrical as the proton is equally likely to be located on either nitrogen atom. The π-electrons are thus delocalised.

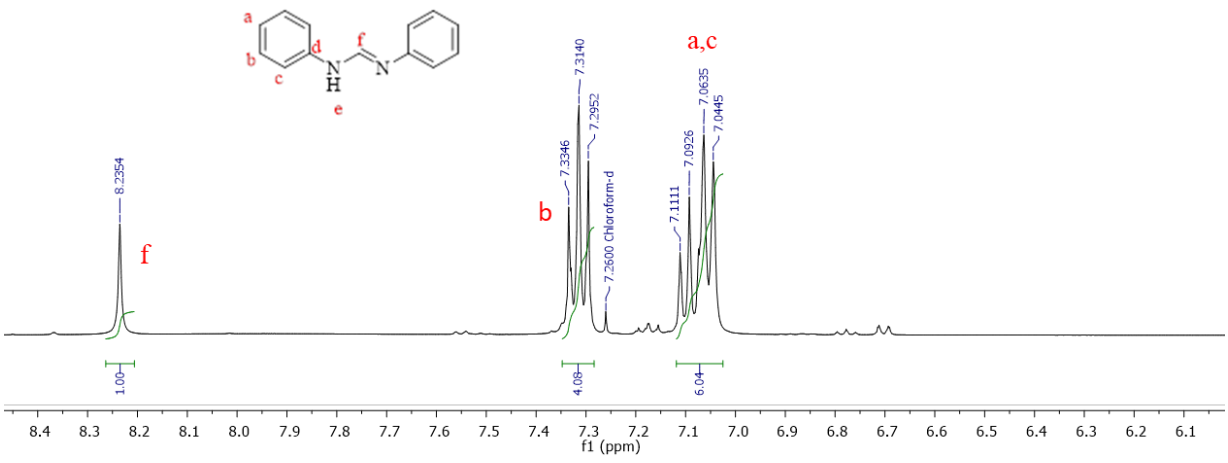

Figure 2.8 ^{1}H NMR of **L1** in $CDCl_3$.

For ligand **L2** (Figure 2.9), a singlet at 2.34 ppm integrating for six protons is assigned to the methyl protons H_a. Two doublets resonate at 6.95 ppm and 7.12 ppm each integrating to four

protons. These conform to a 1,4-disubstitution of an aromatic ring. With the aid of 2D COSY experiments, the more shielded signal is assigned to protons H_c *para* to the methyl substituent, resulting from the shielding effect of the methyl group at these positions. Consequently, the formamidinyl groups becomes more electron withdrawing due to its ability stabilise charge by delocalisation, evidenced by the shielding of the formamidinyl proton compared to **L1**. The latter signal thus belongs to protons H_d. The formamidinyl proton H_g is shifted upfield relative to that in **L1**, resonating at 8.18 ppm.

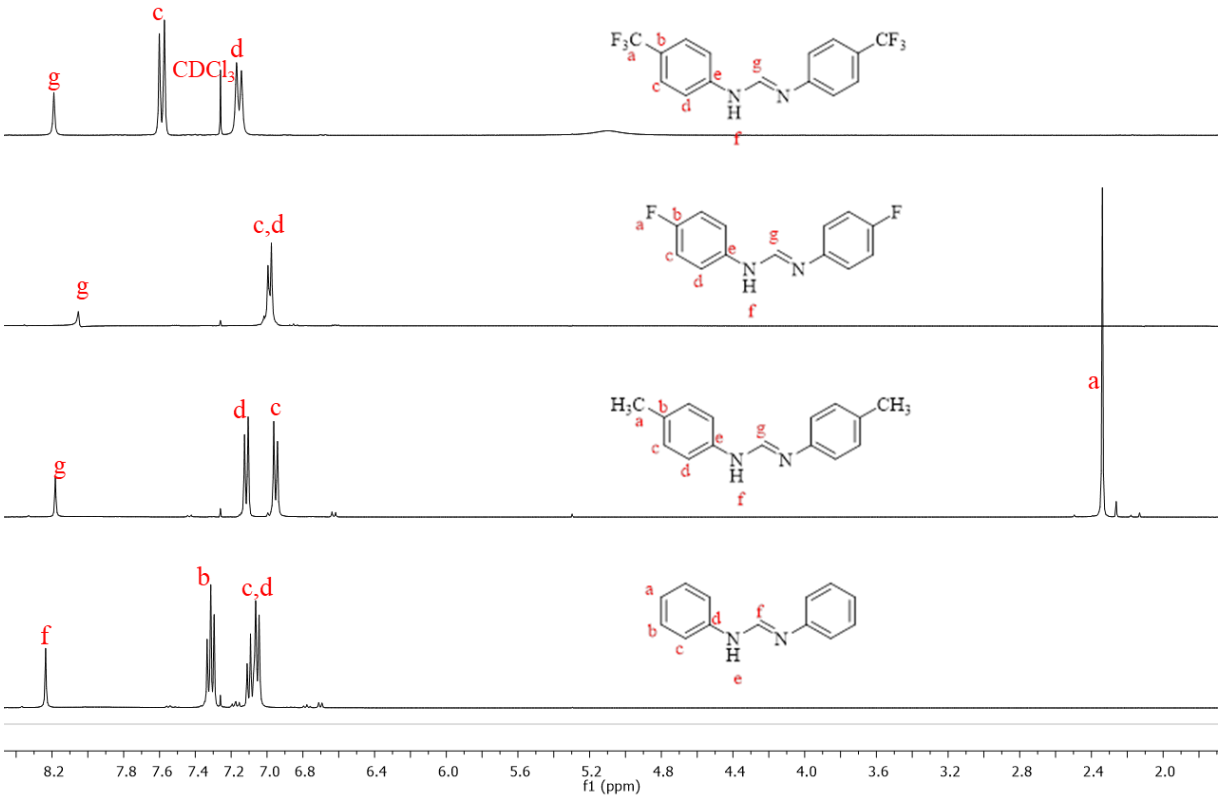

Figure 2.9 Stacked ^{1}H NMR for ligands **L1** – **L4** in $CDCl_3$.

For **L3**, upon the substitution with fluoride group, the aromatic proton signals for H_c and H_d move closer together compared to **L2** and converge to a doublet signal at δ = 6.99 – 7.01 ppm. This signifies the mesomeric effect of the fluorine substituent is dominating its counteracting inductive effect to the ring which causes an increased electron withdrawing ability of the formamidine functionality. This is further supported by the upfield shift of the formamidinyl proton H_g which resonates as a sharp singlet at 8.05 ppm integrating for one proton.

For **L4**, there are two doublets at 7.15 ppm and 7.59 ppm each integrating to four protons, which correspond to the aromatic protons with substitution at the *para* positions. In contrast to

L2, the protons directly *ortho* to the trifluoromethyl groups H_c are the more shielded doublets. This is due the withdrawing nature of the trifluoromethyl group which in turn shields the *ortho* positions. Hence, the order of the signals is reversed and proton H_d resonates as the latter signal. Furthermore, the signal for the formamidinyl proton H_g is slightly deshielded and appears as a singlet at 8.19 ppm compared to that of **L1**.

The $^{13}C\{^1H\}$ NMR together with 2-dimensional NMR was used to validate the assignments of the carbon signals. The formamidine carbon C_f resonates at 149.55 ppm for **L1**. The signal (C_g) is shifted upfield in **L2** and **L3**, to resonate at 149.50 ppm and 149.99 ppm, respectively. On the other hand, there is a upfield shift of the signal to 147.91 ppm in **L4**. The methyl signal C_a for **L2** is seen at 20.85 ppm and the trifluoromethyl signal in **L4** is seen at 114.35 ppm. For **L3**, a doublet at 116.17 ppm ($^2J_{C\text{-}F}$ = 22.6 Hz) belongs to C_c due to a two-bond coupling between C_c and F_a. In comparison, a doublet at 120.57 ppm ($^3J_{C\text{-}F}$ = 7.4 Hz) belongs to C_d due to the four-bond coupling of C_d and F_a.

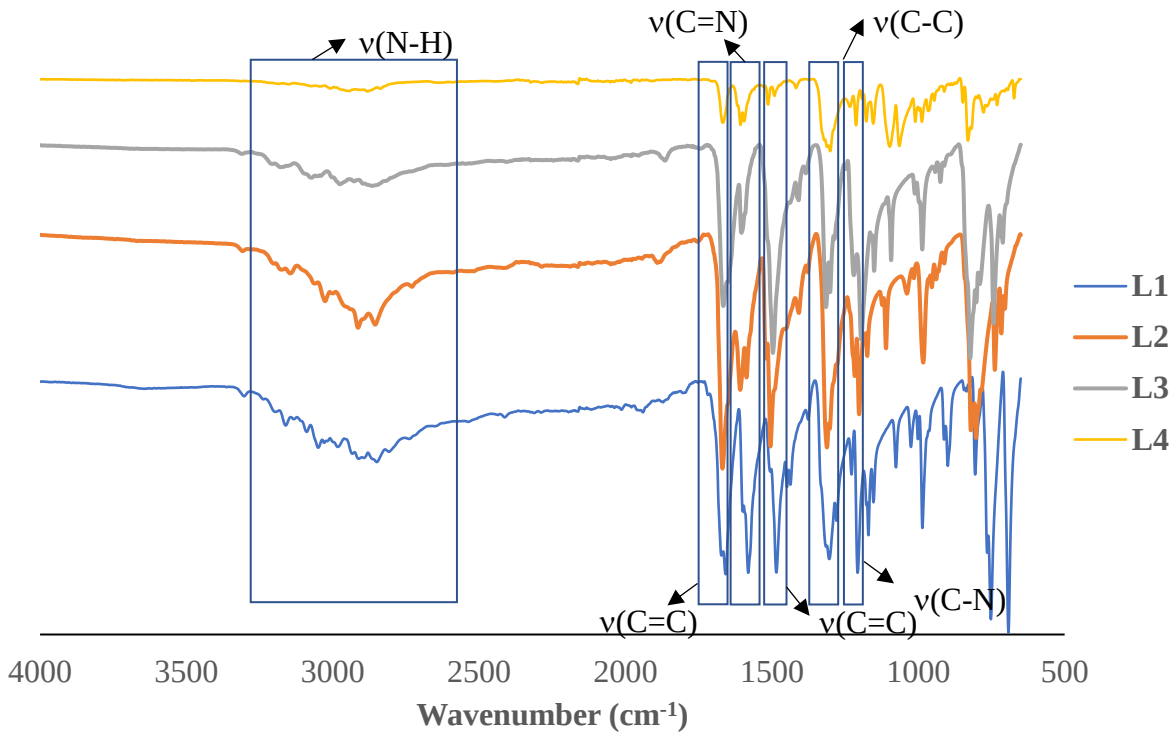

Figure 2.10 IR of ligands **L1** – **L4**.

The infrared (IR) spectra of the ligands (Figure 2.10) display broad ν(N–H) absorption bands above 3000 cm^{-1}. For **L2**, an aliphatic ν(C–H) absorption band is observed at 2850 cm^{-1}. For **L3**, a ν(C–F) absorption band appears at 1150 cm^{-1} while appearing at 1100 cm^{-1} in **L4**. The characteristic formamidine absorption band ν(C=N) resonates at 1581 cm^{-1} in **L1**. However,

this absorption band is shifted down field to 1608 in **L2**, 1601 in **L3** and 1608 in **L4**. The ESI mass spectrum was recorded in both the positive and negative ion modes. It displays a base peak for $[M + H]^+$ ion at *m/z* = 197.11 for **L1**, 225.14 for **L2**, 233.09 for **L3** and 333.27 for **L4**. These molecular weights correspond with a protonation on the more basic nitrogen of the formamidine backbone.

2.3 Synthesis of Dipenylformamidinate Rhodium(I) Homobimetallic Complexes (C1 – C4)

The new homobimetallic complexes **C1** – **C4** were synthesised by reacting two equivalents of each of the respective ligands **L1 – L4** with the rhodium(I) precursor $[Rh(COD)Cl]_2$ dimer in toluene with excess potassium tert-butoxide (Scheme 2.23).[123,133] The nucleophilic nitrogen donor ligands displace the labile chlorido ligands, while maintaining the bridging coordination mode. These rearrange in a way that the bridging ligands *cis* to each other to reduce steric interaction between the two ligands. The complexes were obtained as orange solids in moderate yields of 51 – 67 % and are thermally unstable with decomposition upon heating in the range of 210 and 218 ^oC. These are soluble in common polar solvents (DCM, EtOH, DMSO, THF and $CHCl_3$), sparingly in toluene at room temperature and become more soluble above 30 ^oC. The complexes were characterised using ^1H, $^{13}C\{^1H\}$, $^{19}F\{^1H\}$ NMR and FT-IR spectroscopy.

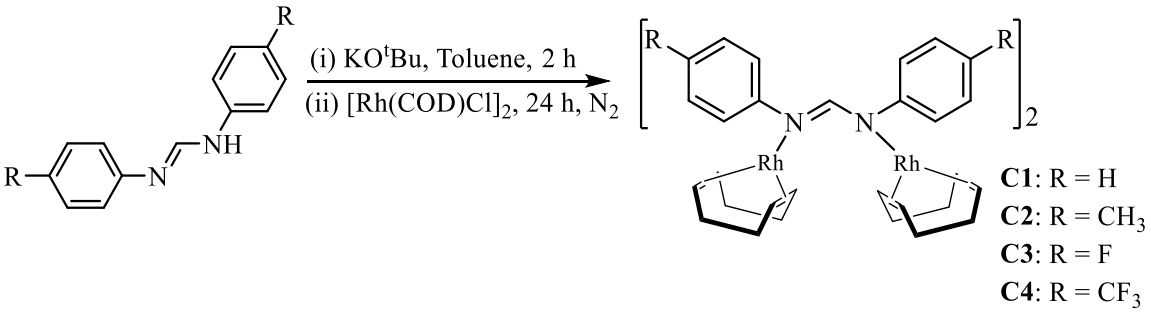

Scheme 2.23 Synthesis of the bimetallic Rh(I) complexes **C1** – **C4**.

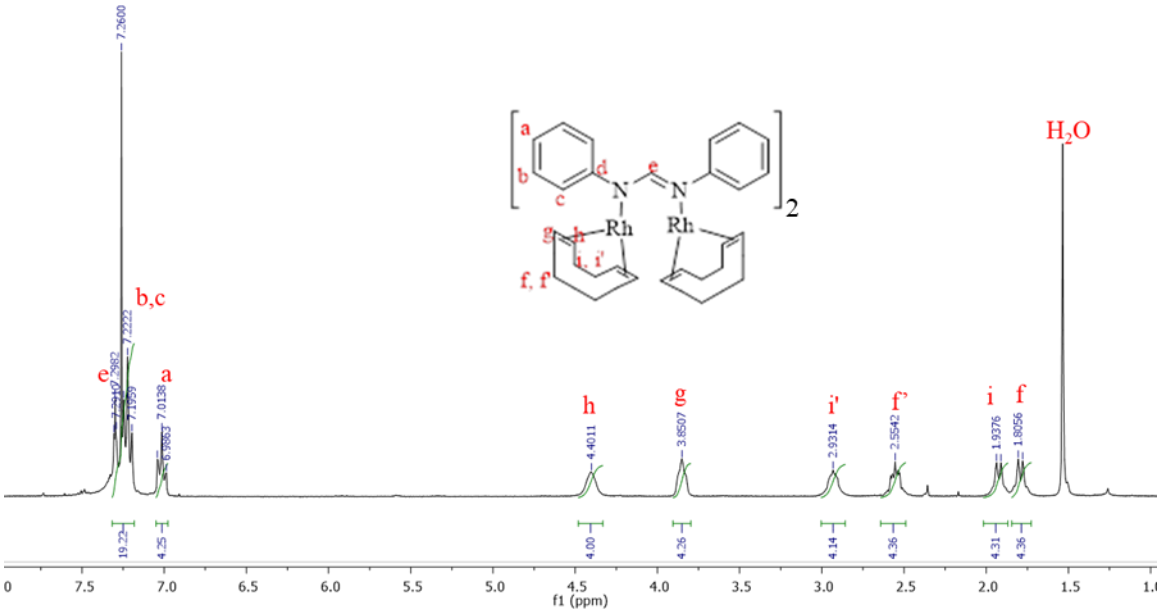

Figure 2.11 ^{1}H NMR of complex **C1** in $CDCl_3$.

The ^{1}H NMR of complex **C1** (Figure 2.11) displays a triplet at δ = 7.02 ppm integrating to four protons which correspond to the aromatic proton *para* to nitrogen H_a and a multiplet integrating for twelve protons at 7.22 ppm is assigned to the aromatic protons H_c and H_d as these signals overlap. A triplet that integrates for two protons at 7.30 ppm belongs to the formamidinyl proton H_e, with the splitting is due to proton coupling with the two equivalent, spin-active ^{103}Rh nuclei.[134] The symmetricity of the signals indicates coordination through a bidentate mode as the protons of the benzene ring on one side are in identical environment to the corresponding protons of the other aromatic ring. This is also true for the protons on the COD ligands. Six signals around the aliphatic region are observed, like other analogous compounds.[135–137]

In the aliphatic region, 2D COSY and HSQC experiments were used to validate the assignments (Figure 2.5). A pair of quartet signals each integrating to four protons resonating at 1.79 ppm and 1.92 pm is assigned to H_f and H_i, respectively. It is not clear which proton would be more shielded, so the assignments were chosen arbitrary. From the COSY spectrum (Figure 2.12), there is a cross peak between H_f and $H_{f'}$ at 2.53 ppm. Since the two signals are in different chemical shifts, the two protons are diastereotopic, so they possess a geminal coupling. This in turn indicates that upon coordination of the H-dpf ligand, the COD ligands rearrange themselves and adopt a boat conformation to reduce the strain with the phenyl rings of the ligand.

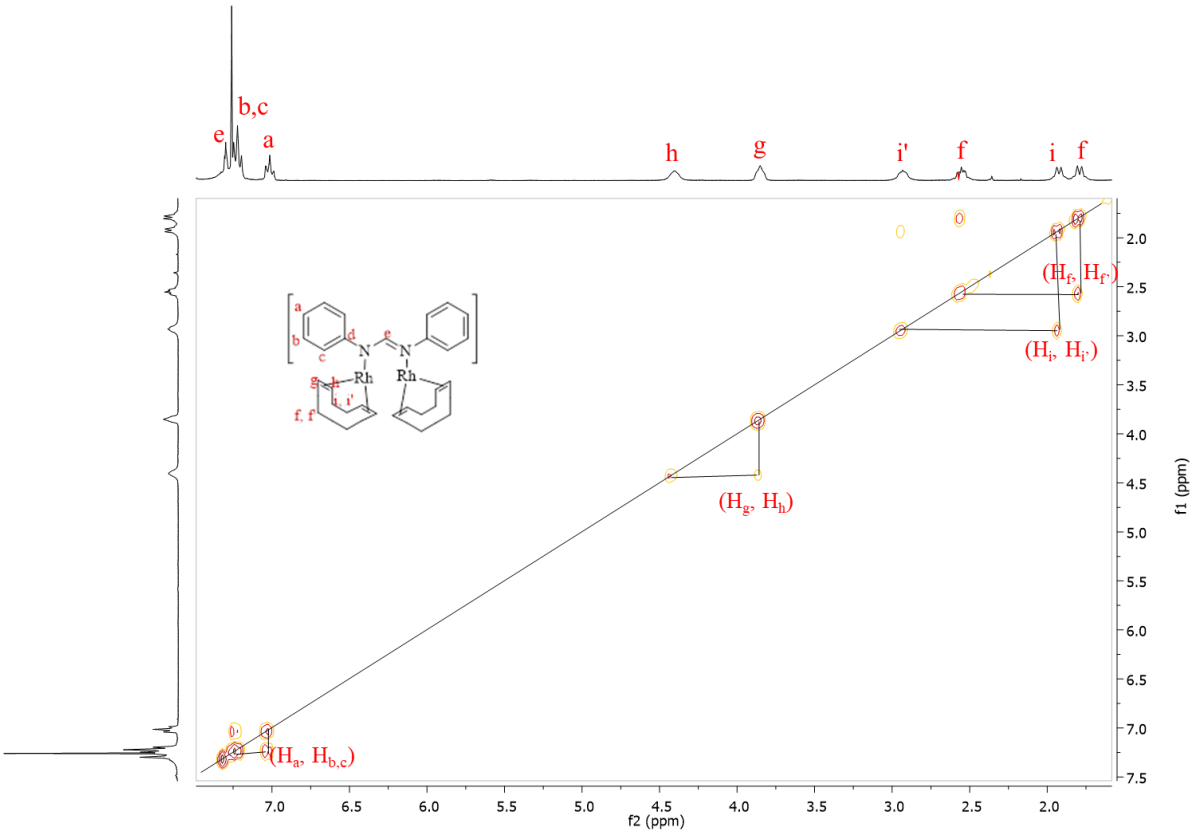

Figure 2.12 ^{1}H-^{1}H COSY NMR of complex **C1** in $CDCl_3$.

In situ, this species is the dominant species since it is the one with the lowest energy. Another cross peak is observed between H_i and $H_{i'}$ which resonates at 2.92 ppm and integrates to four protons. Similarly, the two protons H_i and $H_{i'}$ are also diastereotopic with each other as seen with the other methylene protons H_f and $H_{f'}$. The two protons H_f and H_i are more shielded than their counterparts $H_{f'}$ and $H_{i'}$ because the former pair are directly aligned and eclipse the methine protons, which results in hyperconjugation of their magnetic moments. On the other hand, $H_{f'}$ and $H_{i'}$ are antiperiplanar with a dihedral angle of ~180^{o} with the methine protons, and the two magnetic moments cancel each other out, hence less shielding. Finally, there is a cross peak between *cis*-methine protons H_g and H_h, which both appear as broad multiplets at 4.40 ppm and 6.99 ppm, each integrating to four protons, making them also diastereotopic protons of sp^2 hybridized carbons.

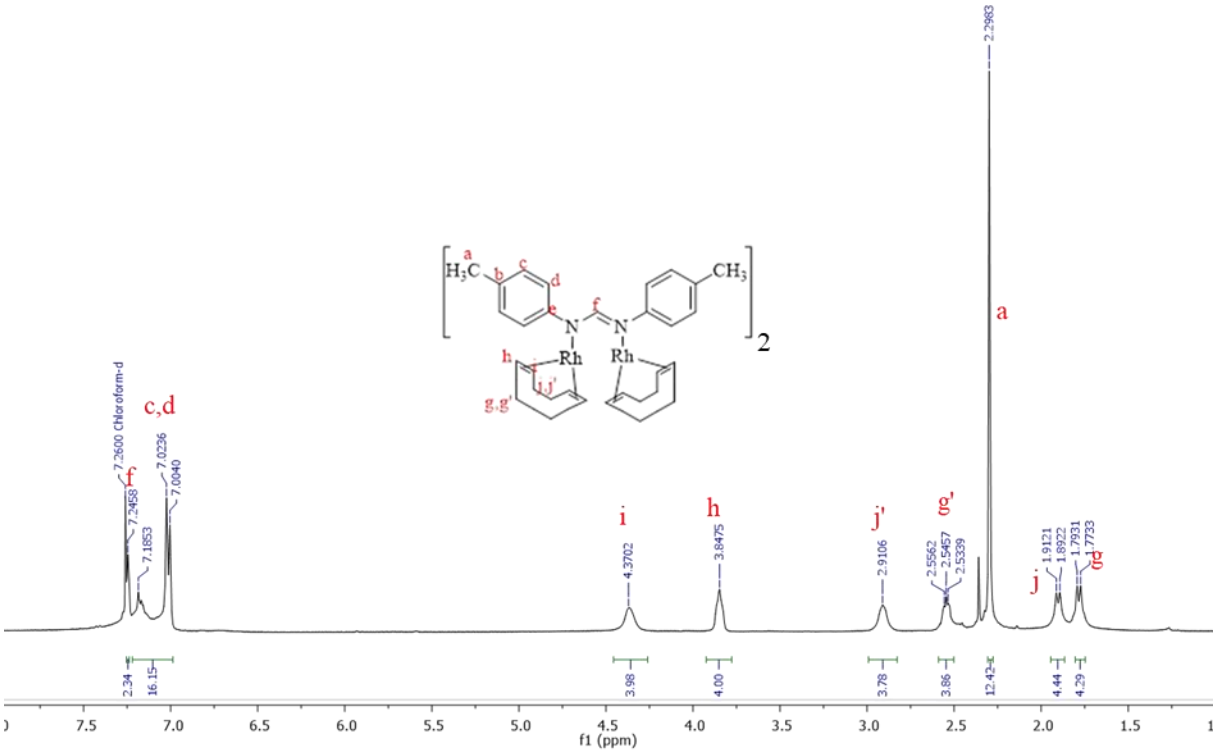

Figure 2.13 ^{1}H NMR of complex **C2** in $CDCl_3$.

For the ^{1}H NMR of complex **C2** (Figure 2.13), a singlet that integrates for twelve protons at 2.30 ppm signifies the presence of methyl protons. There is a slight upwards shift in the chemical shifts of the signals of protons on the COD ligands compared to those of **C1**. This is due to the presence of the electron donating methyl groups by conjugating its electron density to the Rh(I) metal centres through the π-electron system of the CH_3-dpf ligands. In response, more electron density is retained by the COD ligands and there is an increased overlap of the magnetic moments of the protons. The methine protons H_h and H_i of COD ligand resonate at 3.85 ppm and 4.37 ppm, respectively, while there are four methyl protons of COD each integrating to four protons for H_g, $H_{g'}$, H_j and $H_{j'}$ appear as quartets at 1.78, 1.90, 2.54 and 2.91 ppm, respectively. For the aromatic protons, H_c is shifted upfield while H_d is shifted downfield and converge to a multiplet at 7.00 – 7.18 ppm due to the competing electron effects of the methyl group and the formamidine functionality. The formamidine proton H_f appears as at triplet 7.25 ppm due the splitting by the equivalent Rh metal centres and integrates for two protons. This signal is also shifted 0.06 ppm units upfield when compared to that of **C1**, a consequence of localised charge conjugated around the formamidine group.

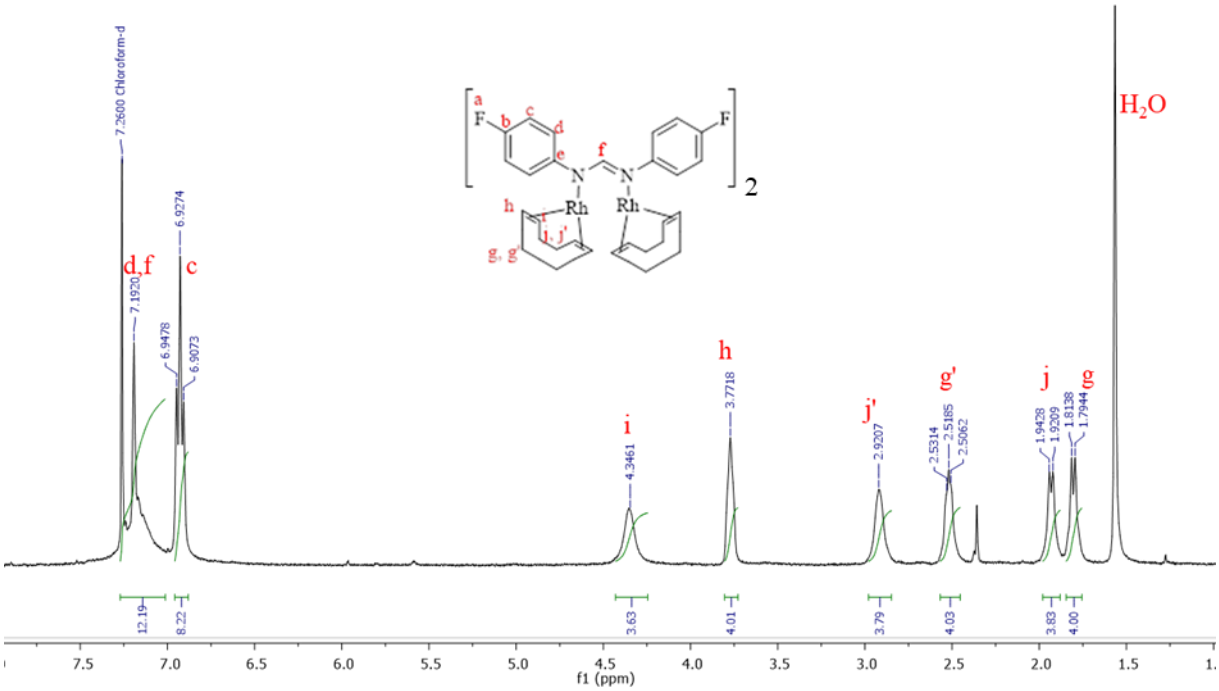

Figure 2.14 ^{1}H NMR of complex **C3** in $CDCl_3$.

For the ^{1}H NMR complex **C3** (Figure 2.14), there is a slight upfield shift in the chemical shifts in the signals of protons on the COD ligands compared to those of **C1**. This is due to the presence of the fluoride substituent having an inductive effect as the dominant electronic effect upon coordination of the ligand to the Rh(I) metal centres. This is the direct opposite effect that was observed in the free ligand **L3** where mesomeric effect was more dominant. In response, less charge is available from the ligand and more electron density comes from the COD ligands which are more bound to the Rh metal centres and hence, a decrease in the overlap of the magnetic moments of the protons of COD. The methylene protons H_h and H_i of COD ligand resonate at 3.77 ppm and 4.35 ppm, respectively, while there are four methyl protons of COD each integrating to four protons for H_g, $H_{g'}$, H_j and $H_{j'}$ appear as quartets at 1.80, 1.93, 2.52 and 2.92 ppm, respectively. For the aromatic protons, H_c appears as a triplet ($^{3}J_{H\text{-}F}$ = 6.08 Hz) at 6.93 ppm due to the splitting by the activated ^{19}F nucleus following coordination by the ligand. There is an overlap of the formamidine proton H_f and the aromatic proton H_d around 7.19 ppm.

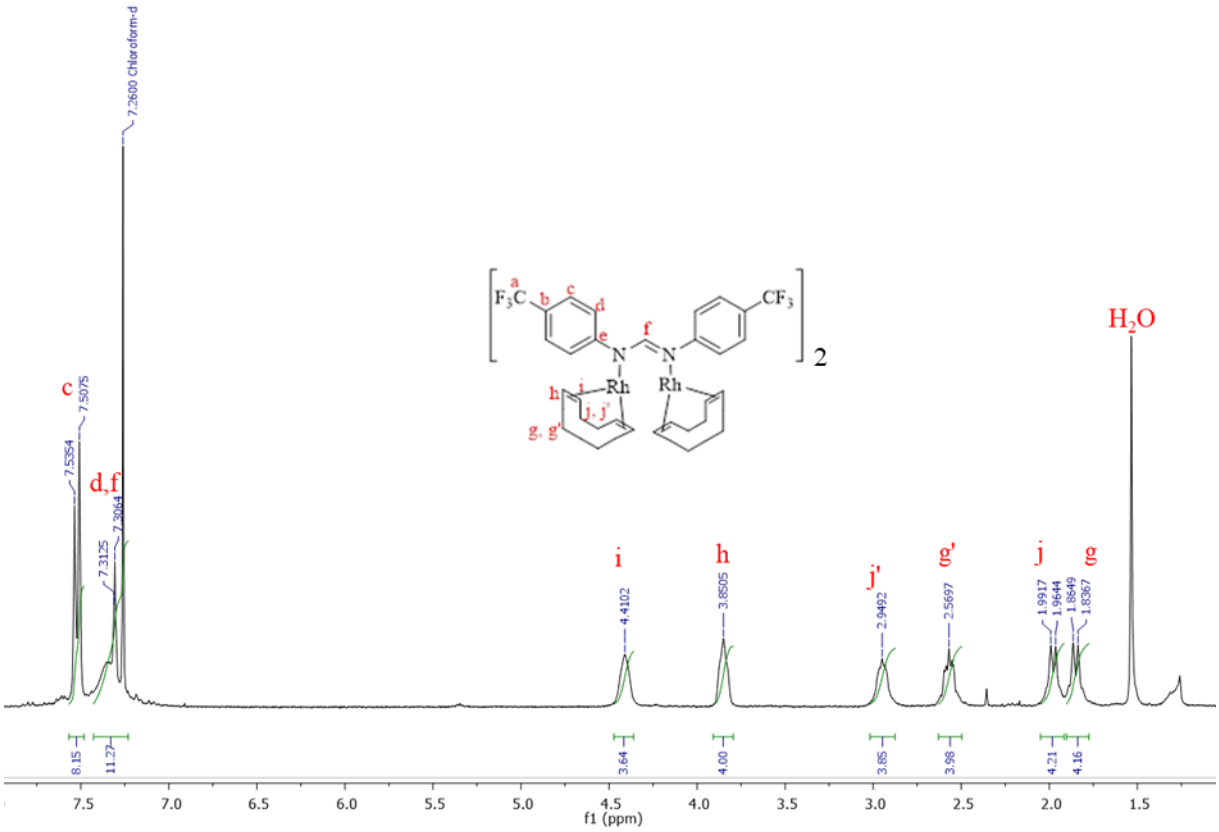

Figure 2.15 ^{1}H NMR of complex **C4** in $CDCl_3$.

For the ^{1}H NMR complex **C4** (Figure 2.15), the downward shift in the chemical shifts in the signals of protons on the COD ligands relative to those of **C1** is more pronounced, as compared to **C3**. This is due to the presence of the trifluoromethyl substituent strongly withdrawing electron density away from the aromatic ring. This results in the formamidine functionality donating its electron density to the ring to stabilise the insufficient charge. The Rh(I) metal centres then pull away more electron density from the COD ligand as the nitrogen atoms of the formamidine functionality become less electron rich. The COD ligands become more bound to the Rh metal centres and hence, a decrease in the overlap of the magnetic moments of the protons of COD. The methylene protons H_h and H_i of COD ligand resonate at 3.85 ppm and 4.41 ppm, respectively, while there are four methyl protons of COD each integrating to four protons for H_g, $H_{g'}$, H_j and $H_{j'}$ appear as quartets at 1.85, 1.97, 2.56 and 2.94 ppm, respectively. For the aromatic protons, H_c appears as a doublet at 7.52 ppm due to the splitting by H_d. This signal is the most deshielded aromatic proton due to the withdrawing nature of the

trifluoromethyl substituent which deshields the ortho positions. There is an overlap of the formamidine proton H_f and the aromatic proton H_d around 7.19 ppm.

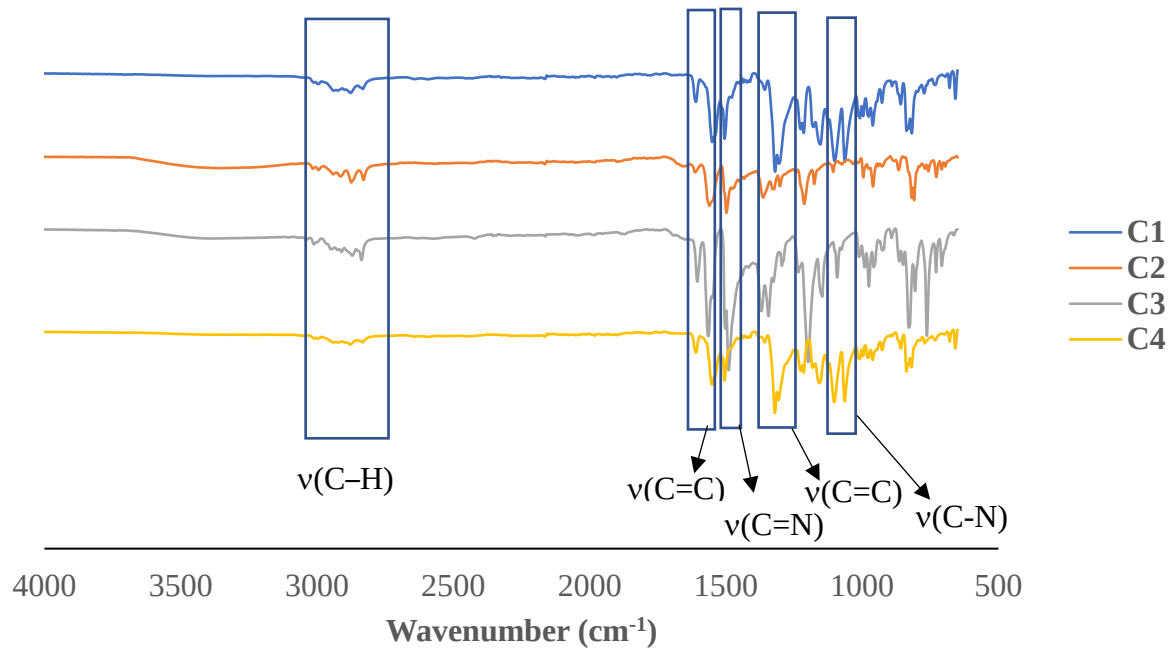

Figure 2.16 IR spectra of complexes **C1** – **C4**.

The ^{13}C NMR of the complexes displays the diagnostic formamidinyl carbon C_e signal as a singlet at 165.2 ppm in **C1**. This is more downfield compared to the free ligand. Upon substitution with a methyl group in **C2**, the signal shifts downfield to 164.9 ppm. In **C3** and **C4**, the electron withdrawing groups shift the signal to 165.1 and 165.5 ppm, respectively. The ESI-MS finds a base peak of 868.2279 (*m/z*) in **C2** and 1084.1407 (*m/z*) in **C4**, which corresponds to the $[M]^+$ cation, in agreement with literature.[138]

The ν(C=N) absorption bands resonate at to 1550 cm^{-1} in **C1**, 1560 cm^{-1} in **C2**, 1564 cm^{-1} in **C3** and 1564 cm^{-1} in **C4** (Figure 2.16). The downfield shield in the band stretches relative to their respective free ligands is due to π-backbonding from the Rh metals to the π* orbital of the formamidine functionality weaking the bond, which supports the coordination of the ligands. The decrease in the ν(C=C) absorption band frequencies to the range of 1604 and 1613 cm^{-1} on 1,5-cyclooctadiene is an indication of reduced density π-backbonding, because of a competing electron accepting group and the replacement of a π-donor ligand **C1** with a π-acceptor ligand.

2.4 Synthesis and Characterisation of Homoleptic Dirhodium(II) Complexes (C5 – C7)

The fully substituted complexes C**5 – C7** were prepared following a literature procedure.[23] These were synthesised by melting the respective ligands **L1 – L4** and adding trifluoroacetate dirhodium complex precursor [$Rh_2(TfOAc)_4$] to stir under nitrogen for 24 h, as shown in Scheme 2.24. The resulting solution was cooled to room temperature and then dissolved in hot methanol. A crude was filtered with suction and dried under vacuum to afford the desire complexes.

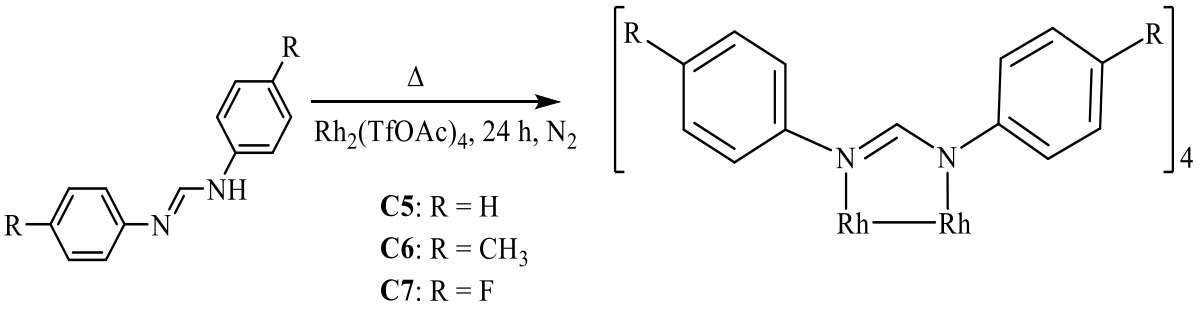

Scheme 2.24 Synthesis of the homoleptic complexes **C5** – **C7**.

The complexes are obtained from their respective ligands as dark-green solids in excellent yields of 83% (**C5**), 87% (**C6)** and 80% (**C7**). **C5** and **C7** undergo thermal decomposition in the range of 389 – 393 ^oC, slightly higher for **C6** in the range 402 – 405 ^oC. The trend observed is due to the strength of binding by the nitrogen atoms as result of the basicity. These are soluble in small molecule solvents (DCM, ACN, MeOH, DMSO and THF) and partially soluble in other common solvents due to steric crowding around the vacant axial coordination site on the rhodium metals.

The ^1H NMR of complex **C5** (Figure 2.17) shows a doublet at 6.70 ppm integrating for sixteen protons for H_c as the most shieled proton. A triplet at 6.97 ppm integrating for eight protons corresponds to H_a and a triplet at 8.08 ppm for integrates for sixteen protons is assigned to H_b. The arrangement of the signals is indicative of the formamidine functionality which conjugates its electron density towards the aromatic rings and hence shielding the protons located at the positions *ortho* and *para* to the nitrogen atoms. The signal for the formamidinyl proton H_f is now a triplet ($^3J_{Rh\text{-}H}$ = 3.1 Hz) at 7.80 ppm integrating to four protons, as compared to the sharp singlet observed in **L1**. The proton is coupling with the two Rh metals of the dirhodium(II) core, which confirms the successful complexation by chelation. The signals are at lower

chemical that those of **L1** as a resulting of the shielding backdonation by the Rh metals. This agrees with the reported chemical shifts of similar compound previously reported.[134]

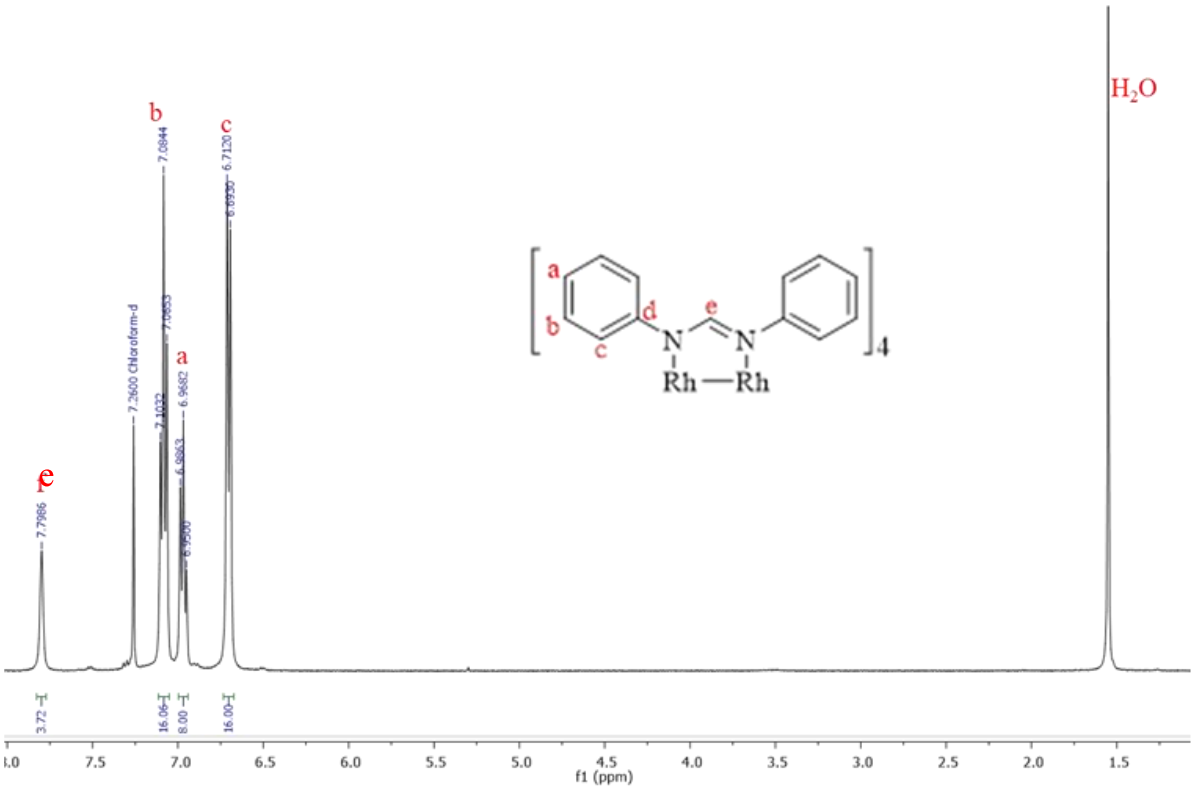

Figure 2.17 ^{1}H NMR of complex **C5** in $CDCl_3$.

The ^{1}H NMR for complex **C6** (Figure 2.18) shows a doublet resonating at 6.58 ppm which is assigned to the *ortho* proton H_c and a doublet at 6.88 ppm is assigned to *meta* proton H_d. H_c is more shielded, while H_d is more deshielded than in **C5** due to the inductive effect of the donating methyl substituent and the increasing withdrawing effect of the formamidine functionality that provides a more shielding effect for the proton. H_f appears as broad signal at 7.68 ppm integrating to four protons. The broadness is due to coupling with the spin active ^{103}Rh isotope, however, the splitting pattern for this proton due to the Rh metals could not be measured at the frequency of the NMR experiment.

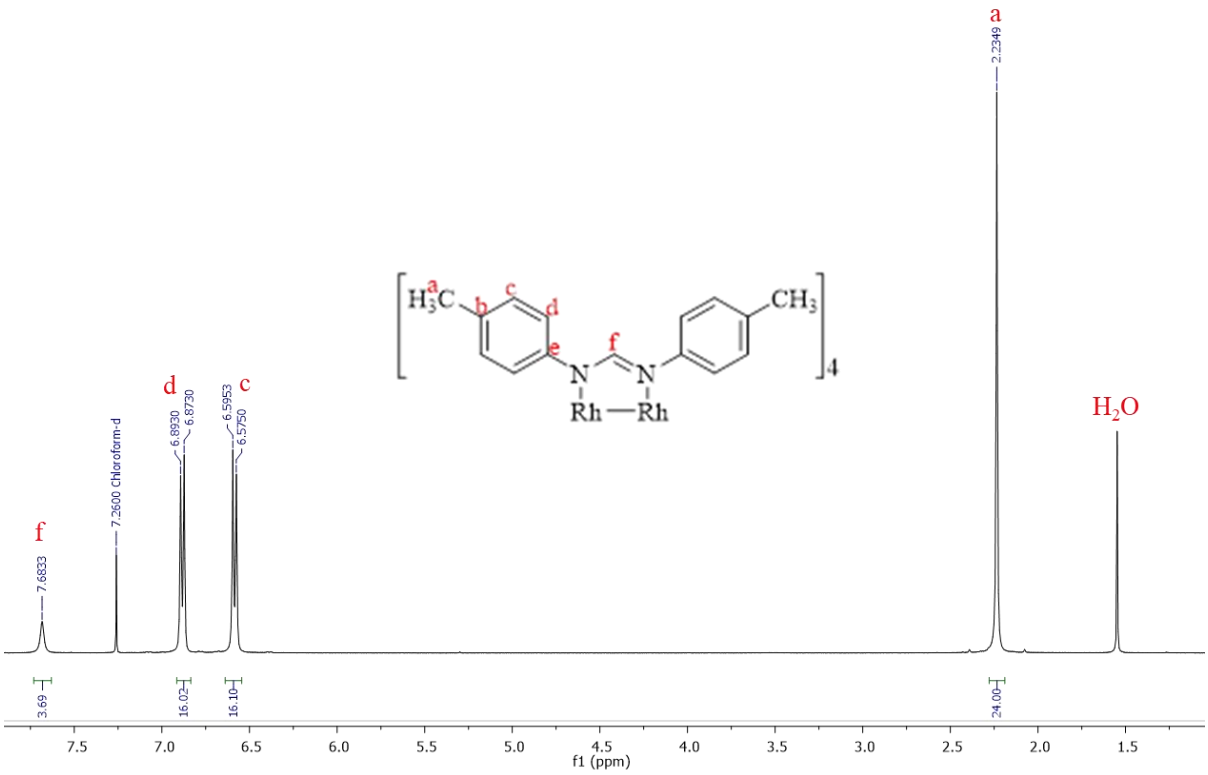

Figure 2.18 ^{1}H NMR of complex **C6** in $CDCl_3$.

The ^{1}H NMR for complex **C7**, (Figure 2.19) shows a doublet of doublet ($^{3}J_{H\text{-}H}$ = 8.8 Hz, $^{4}J_{H\text{-}F}$ = 4.7 Hz) at 6.53 ppm and a triplet with $^{3}J_{H\text{-}F}$ = 8.54 Hz appearing at 6.82 ppm. The former signal has been assigned to H_d with the large splitting caused by H_c and the small splitting caused by F through a four-bond coupling. The fluorine is activated and couples with the hydrogen after complexation. The latter signal has been assigned to H_c due to its equivalent three-bond couplings to both F and H_d. The F substituent has a dominant electron withdrawing effect after complexing, reversing the order of shielding for the aromatic protons of the unsubstituted complex **C5**, which results in the formamidinato functional group to electron release to the ring. However, this together with π-backdonation from the metals shifts H_f downfield from 7.82 ppm in complex **C7** to 6.82 ppm in complex **C5**. The ^{19}F{^{1}H} NMR for **C5** shows one singlet signal at -119.3 ppm for the F substituent.

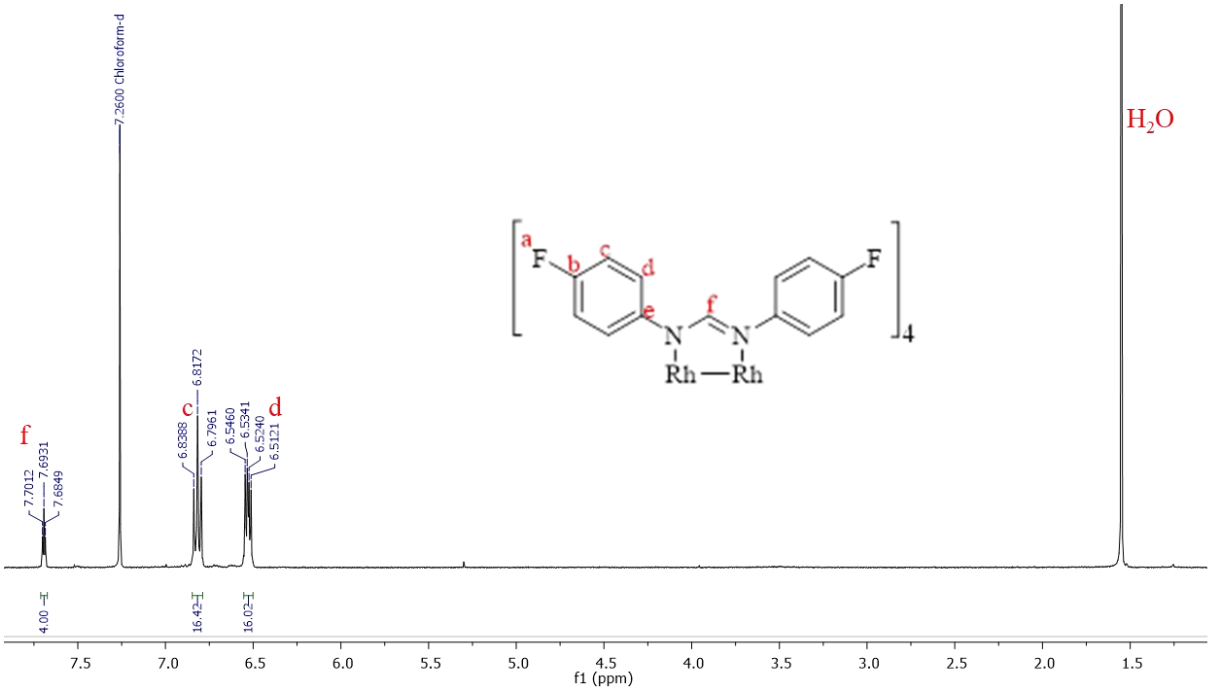

Figure 2.19 ^{1}H NMR of complex **C7** in $CDCl_3$.

The ^{13}C NMR of the complexes displays the diagnostic formamidinyl signal as a singlet at 162.9 ppm in **C5**, 162.3 ppm in **C6** and 162.7 ppm in **C7**. The methyl carbon C_a in **C6** resonates as a singlet at 20.9 ppm. Furthermore, there is a triplet at 125.3 ppm and a triplet at 115.9 ppm in **C7**. The more shielded triplet ($^{4}J_{C\text{-}F}$ = 9.75 Hz) corresponds to *meta* carbon C_d, which couples with F_a through a 4-bond coupling. The more deshielded triplet ($^{3}J_{C\text{-}F}$ = 22.83 Hz) corresponds to the *ortho* carbon C_c, that couples to F_a through a 3-bond coupling.

According ESI-MS, the $[M + H]^+$ cation is found to be the base peak in all the homoleptic complexes. **C5** has the *m/z* of 987.1862, **C6** has the *m/z* of 1099.3120 and **C7** has the *m/z* of 1130.1064.

Figure 2.20 shows the IR spectra of the complexes **C5** – **C7**. For **C5**, the formamidine absorption band ν(C=N) decreases from 1634 cm^{-1} to 1571 cm^{-1} upon complexing. This change is attributed to the π-backbonding of the Rh metals to the π*-antibonding orbitals of the formamidine. The symmetric stretching band resonates at 1621 cm^{-1}. For **C6**, the ν(C=N) absorption band decreases from 1669 cm^{-1} to 1587 cm^{-1}. The decrease is larger compared to **C5** due to the presence of methyl substituent that causes the formamidine to become withdrawing onto the π*-antibonding orbitals and thus an increase in the electron density

around the formamidine. This results in more double bond character of the conjugated N–C=N backbone in **C6** relative to **C5**.

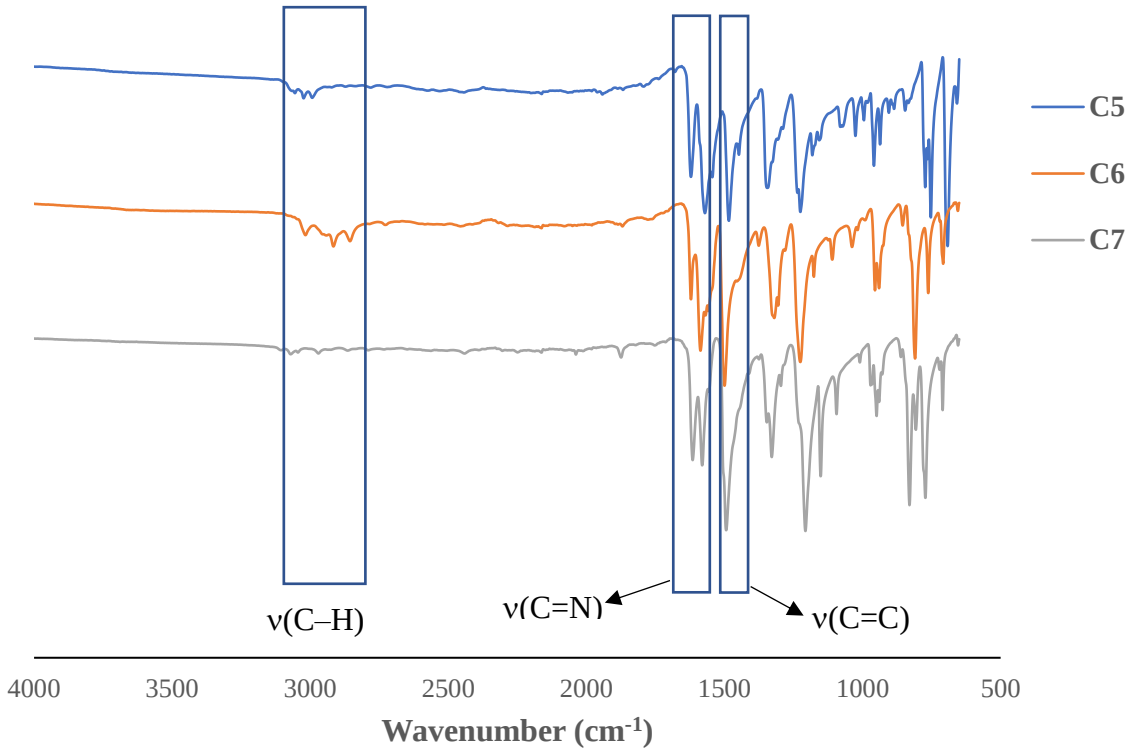

Figure 2.20 IR spectra of homoleptic complexes **C5** – **C7**.

The symmetric stretching band resonates at 1622 cm^{-1}. The ν(C=N) bond stretching frequency of **C7** decreases from 1668 cm^{-1} to 1495 cm^{-1}. This is attributed to the inductive effect fluoride substituent being more dominant than mesomeric effect upon complexing, resulting in more π-backdonation from the metals as the charge density is stabilised by the withdrawing fluoride substituents. The symmetric stretching band occurs at 1616 cm^{-1}. For the aromatic C=C bonds, the frequencies resonate at ν = 1485 in **C5**, 1510 in **C6** and 1495 cm^{-1} in **C7**. This is influenced by the electronic nature of the substituent.

2.5 Synthesis and Characterisation of Mixed ligand Dirhodium(II) Complexes (C8 – C11)

The novel mixed ligand complexes **C8** – **C11** were synthesised from the refluxing mixture of tetraacetate dirhodium(II) complex precursor [$Rh_2(OAc)_4$] and the respective ligands **L1** – **L3** in chlorobenzene, as shown in Scheme 2.25.[126] The desired products are obtained from column chromatography. In changing the amount (one, two or three equivalents) of the ligands, a mixture of the desired products is obtained.

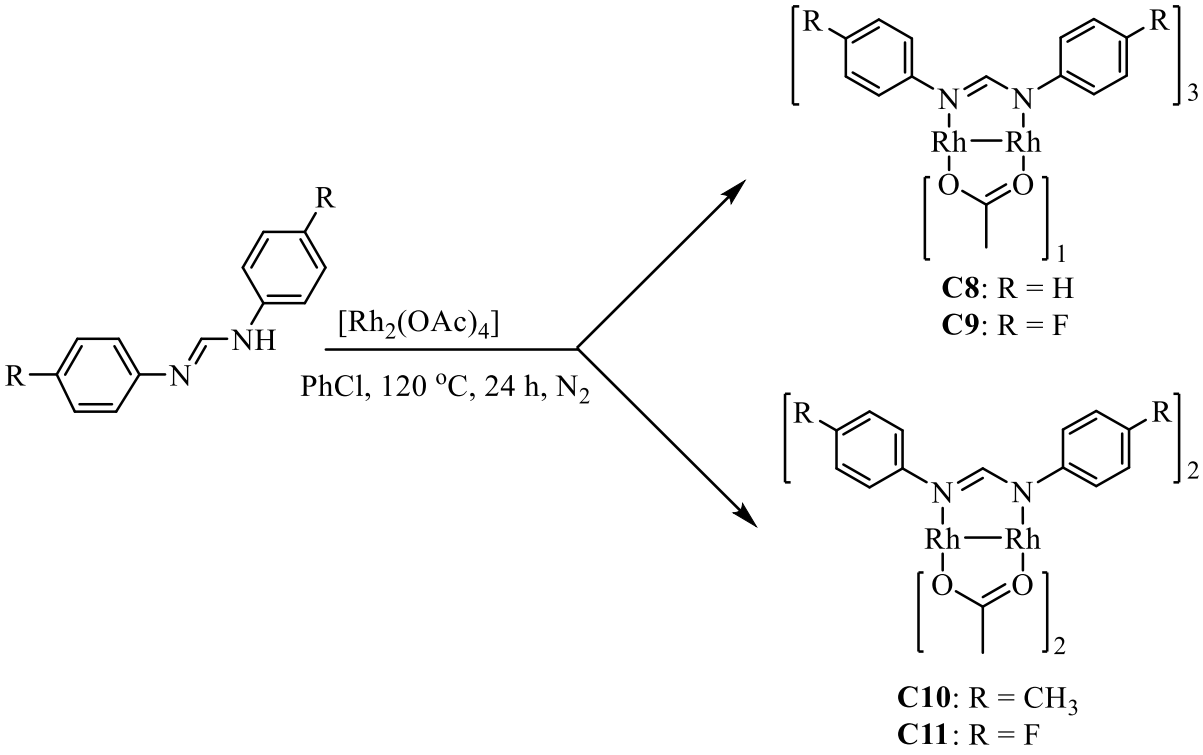

Scheme 2.25 Synthesis of the mixed ligand complexes **C8** – **C11**.

The ^{1}H NMR for complex **C8** (Figure 2.21) shows a singlet at 2.07 ppm integrating for three protons as the most shielded signal. The signal belongs to the methyl protons H_g of the acetato ligand. A triplet at 7.56 ppm integrating for one proton is assigned to the formamidinyl proton H_e from the formamidinato ligand that is *trans* to the acetato ligand. The most deshielded signal is a triplet ($^3J_{H\text{-}Rh}$ = which resonates at 8.14 ppm and integrates for two protons. This is assigned to the formamidinyl proton $H_{e'}$, from the formamidine ligands which are *cis* to the acetato ligand. The formamidinyl proton of the ligand *trans* to the acetato ligand is more shielded that the ligands that are *cis*, with this indicating that the formamidinato ligand is more electron

withdrawing than the acetato ligand. The formamidinato ligand pulls more electron density away from the acetato ligand that is directly *trans* to it and the latter signal becomes more deshielded. However, for the two formamidinato ligands directly *trans* to each other, the electron withdrawing and donating effects cancel each other out as they are equivalent since the ligands are equivalent. This is proven to be true with the aromatic proton signals as the *trans* protons appear more upfield and the *cis* protons appear more downfield. A doublet at 6.58 ppm integrating to four protons is assigned to H_c. A triplet at 6.80 ppm integrating for two protons belongs to H_a and a triplet at 6.85 ppm integrating to four protons belongs to H_b. The protons *ortho* and *para* to the nitrogen atoms are more shielded than the ones *meta*, hence the formamidine functionality has a dominant electron donating character. For the aromatic protons of the *cis* formamidinato ligands, the reversed order is observed. The *para* proton $H_{a'}$ is the more shielded and resonating as a triplet which integrates to four protons at 6.70 ppm. On the other hand, the *ortho* protons $H_{c'}$ are resonating as a doublet which integrates for eight protons at 7.07 ppm. The electron donating character of formamidine functionality localises more electron density at the *para* positions over the *ortho* positions. $H_{b'}$ resonates as a triple integrating for eight protons at 7.21 ppm.

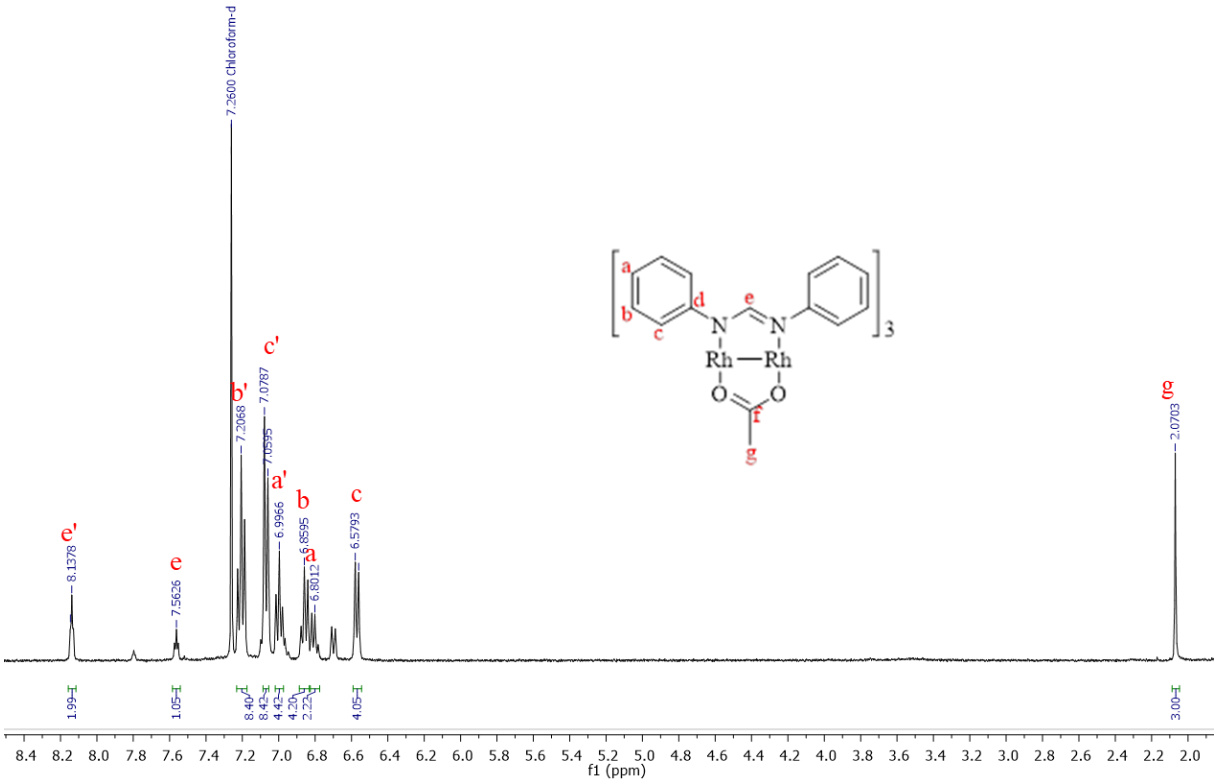

Figure 2.21 ^{1}H NMR of complex **C8** in $CDCl_3$.

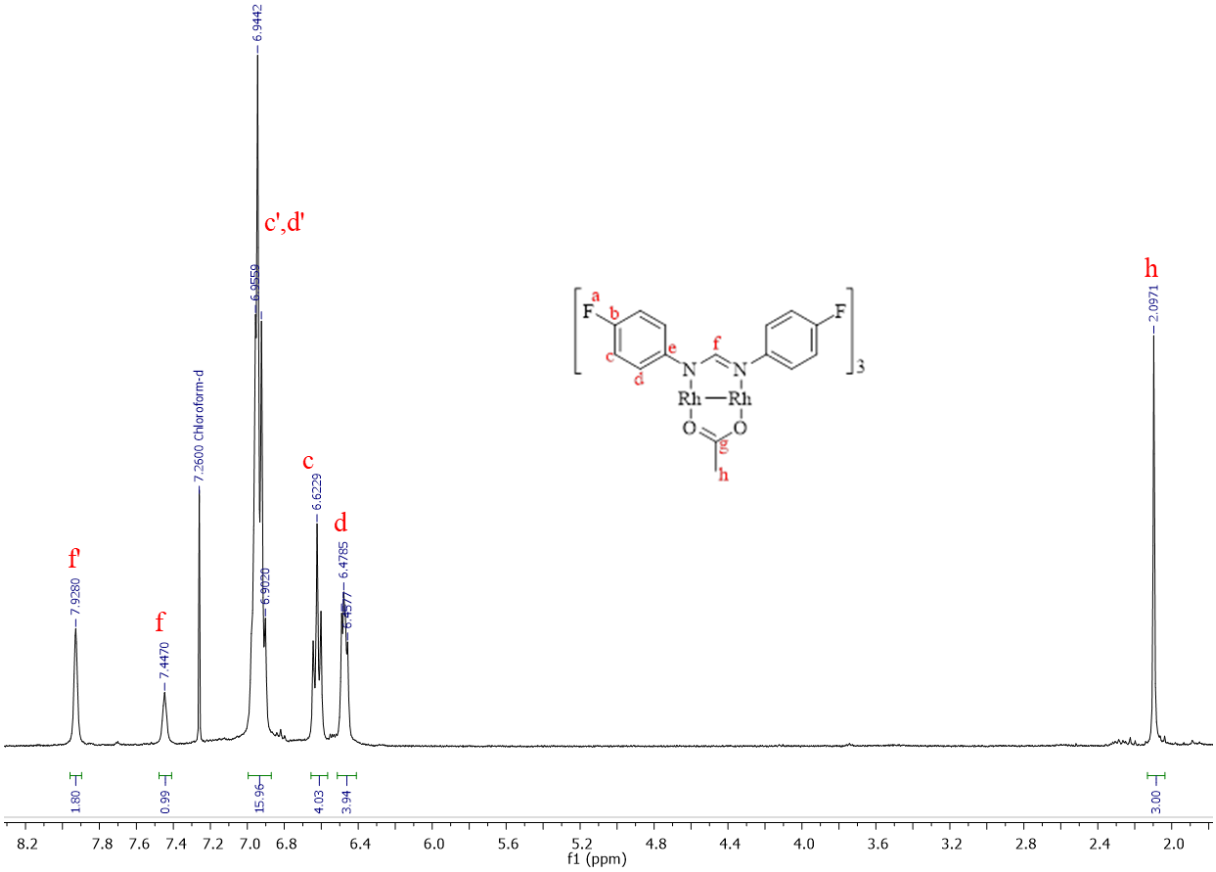

Figure 2.22 ^{1}H NMR of complex **C9** in $CDCl_3$.

The ^{1}H NMR for complex **C9** (Figure 2.22) has the methyl protons of the acetato ligand resonating 2.10 ppm integrating for three protons. For the formamidinato protons, the *trans* ligand has the formamidinyl proton H_f resonating as a multiplet at 7.45 ppm integrating for one proton and the *cis* protons $H_{f'}$ resonating as a multiplet integrating for two protons at 7.93 ppm. For the aromatic protons, H_d resonates as a doublet of doublets ($^{3}J_{H\text{-}H}$ = 8.13 Hz, $^{4}J_{H\text{-}F}$ = 4.72 Hz) at 6.47 ppm integrating to four protons. The larger splitting is a result of a 3-bond coupling to H_c and the smaller splitting is due to a 4-bond coupling to F_a. Proton H_c is seen as a triplet ($^{3}J_{H\text{-}F}$ = 8.40 Hz) at 6.62 ppm integrating to four protons. Contrary to **C8**, the *meta* protons are more shielded than the *ortho* protons, due to the increasing withdrawing nature of the fluoride group which pulls away electrons from the *ortho* and *para* positions. For the *cis* formamidinato ligands, the aromatic protons are in a similar magnetic environment and resonate as a multiplet, to which the signal integrates to sixteen protons.

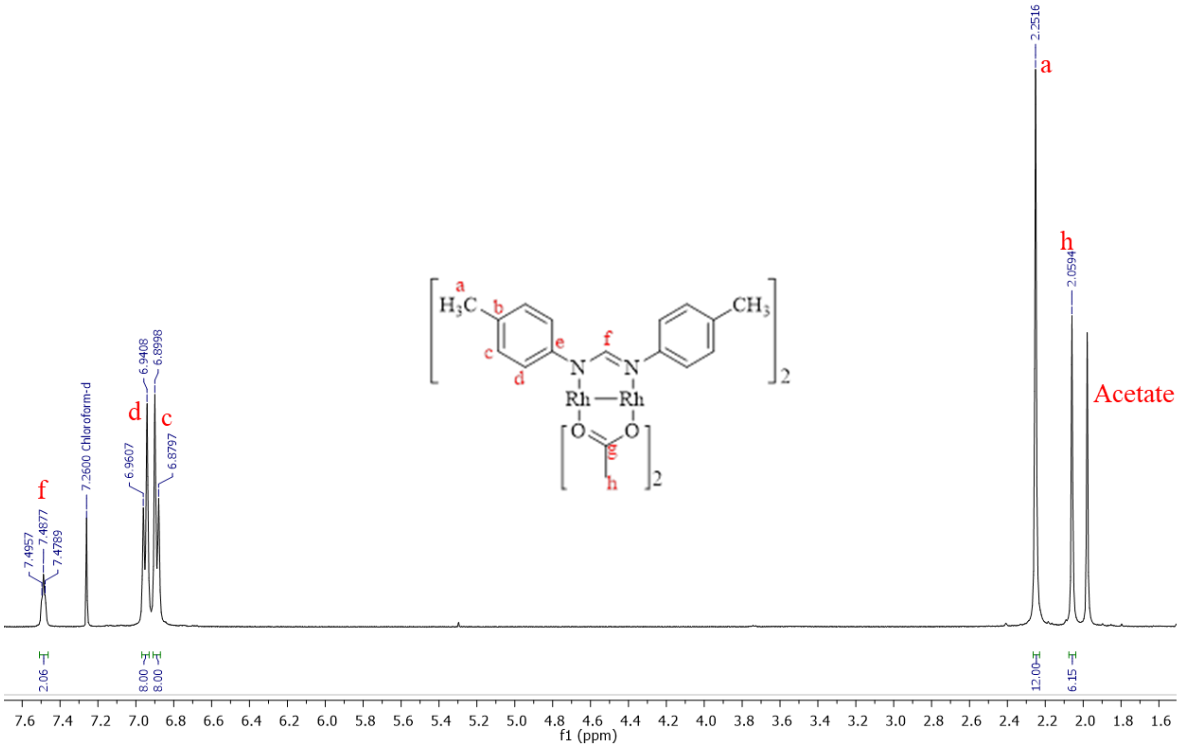

Figure 2.23 ^{1}H NMR of complex **C10** in $CDCl_3$.

The ^{1}H NMR for complex **C10** (Figure 2.23) shows two singlets at 2.06 ppm and 2.25 ppm. The more shielded signal integrating for three protons belongs to the methyl protons on the acetato ligands H_h. The less shielded aliphatic signal integrating to twelve protons is assigned to the methyl protons on the formamidinato ligands H_a. These assignments are supported by the 2:1 ratio in intensity of the signal H_a to H_h as there is twice the protons of former relative to the latter. The formamidinyl proton H_f resonates as a triplet ($^{3}J_{Rh\text{-}H}$ = 3.36 Hz) at 7.49 ppm and integrates for two protons. This signifies that the ligands are in similar chemical environment. Furthermore, since the signal is more shielded than in the free ligand **L2** (with δ = 8.12 ppm), it suffices to postulate that the each of the formamidinato are *trans* to one acetato ligand. This is supported by what is seen in **C8** and **C9**, that the formamidinato is more withdrawing if it directly opposite an acetato ligand, will have more electron density and hence more shielded. Given that the CH_3-dpf ligands are *cis* to each other, the presence of the phenyl rings induces steric interactions between the two ligands. This is the only isolated product, so the reaction favours the kinetic product. The *trans* product is the thermodynamical favoured and was not isolated. For the aromatic protons, H_c is resonating as a doublet at 6.89 ppm that integrates for eight protons. Similarly, H_d resonates as a doublet at 6.95 ppm, integrating for eight protons. The protons *ortho* to the methyl substituent is more shielded due to the electron donating ability of the methyl group.

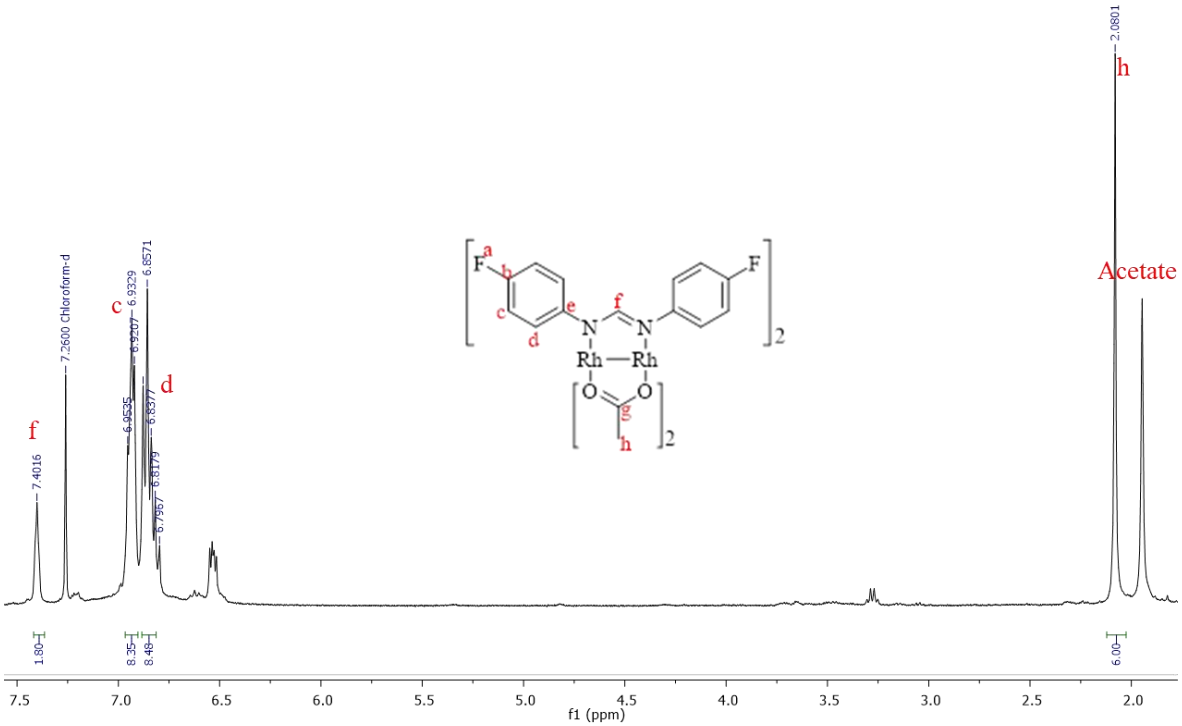

Figure 2.24 ^{1}H NMR of complex **C11** in $CDCl_3$.

The ^{1}H NMR for complex **C11** (Figure 2.24) shows a singlet at 2.08 ppm. This aliphatic signal integrates for six protons, is assigned to the methyl protons H_h of the acetato ligand. There is a slight downfield shift of the signal relative to that of **C10** (δ = 2.06 ppm) that results from the presence of the fluoride substituent at the *para* position of the aromatic rings. The fluoride has slightly dominant withdrawing strength, so it pulls away electron density of the formamidine N–C=N backbone. Since the nitrogen donor atoms become more electron deficient, the acetato ligands begin to share more of their electron density to stabilise the deficient charge. The formamidine proton H_f appears as multiplet 7.40 ppm which integrates for two protons. The slight shift compared to **C10** (δ = 7.49 ppm) also supports increased electron donating effect of the acetato ligand to the formamidinato ligand backbone which shields the proton. A multiplet at 6.80 – 6.86 ppm is assigned to aromatic protons H_d which integrates for eight protons. The triplet signal integrates for eight proton belongs to proton H_c. This reversed order of the signals compared with **C11** also supports that the fluoride substituent is withdrawing.

In the IR spectra of the complexes (Figure 2.25), **C8** – **C11** have an absorption band around 3000 cm^{-1} of a C–H stretch due to methyl group on the acetato ligands. There is a symmetric and asymmetric stretch for the delocalised carbonyl C=O stretch at 1594 – 1612 cm^{-1}. These band frequencies are slightly higher than the stretching frequency of the parent complex $[Rh_2(OAc)_4]$ which occurs at 1567 cm^{-1}. Since the acetato ligand is *trans* to the R-dpf ligand which is more withdrawing, there is less π-backbonding towards π* orbitals of the acetato ligand. This makes the bond stronger and resonate at higher frequency. For **C8**, there are two formamidine C=N stretches.

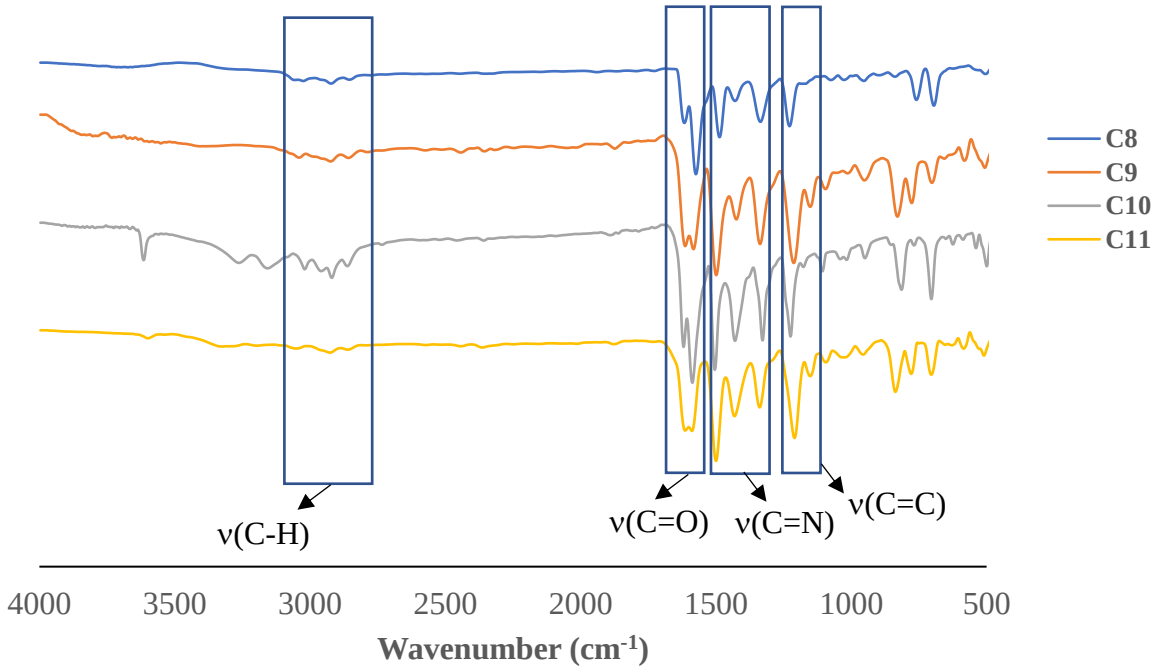

Figure 2.25 IR spectra of mixed ligand complexes **C8** – **C11**.

The higher stretching frequency at 1567 cm^{-1} is due to the two formamidinato ligands cis to the acetato ligand, while the lower stretching frequency at 1486 cm^{-1} is due to the trans formamidinato ligand. The frequencies are lower than those of the free ligand. The formamidine bond of the trans ligand is weaker due to more π-backdonation. Similarly for the other complexes, **C9** resonates at 1578 and 1494 cm^{-1} (lower than 1601 cm^{-1} found in L3), C10 resonates at 1584 and 1503 cm^{-1} (lower than 1608 cm^{-1} found in L2), and C11 resonates at 1584 and 1494 cm^{-1} (lower than 1601 cm^{-1} found in L3). The conjugated aromatic C=C stretch occurs at a frequency of 1423 – 1433 cm^{-1}.

2.6 X-ray Crystallography of Complexes

*2.6.1 Single crystals of **C1** and **C4***

To confirm the coordination of the **L1** ligand through a bridging mode, a single crystal of **C1** was obtained from layering a concentrated solution of **C1** in dichloromethane with pentane allowing for slow diffusion. Similarly, the single crystal of **C3** was also obtained by layering a dichloromethane solution of **C3** with pentane. The molecular structures for **C1** and **C3** as elucidated from single crystal X-ray diffraction are shown in Figures 2.26 and 2.27, respectively. Table 2.2 shows the crystallographic data and refinement details of the complexes.

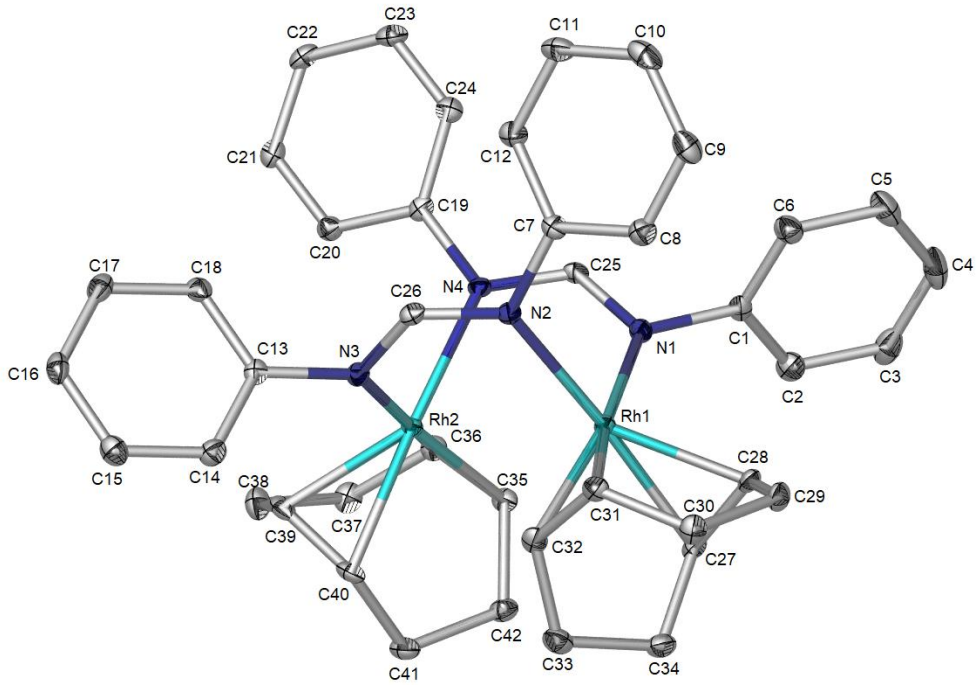

Figure 2.26 Molecular structure of **C1**. Hydrogen atoms have been omitted for clarity.

C1 crystallizes in the monoclinic $P2_1/n$ space group with four molecules in the unit cell found. Interestingly, **C2** crystallizes in the monoclinic *C2/c* space group with four molecules per unit cell, as reported by Ide and co-workers.[133,139] On the other hand, **C3** crystallizes in the $P2_1/c$ space group, with two independent molecules A and B, with eight molecules in the unit cell.

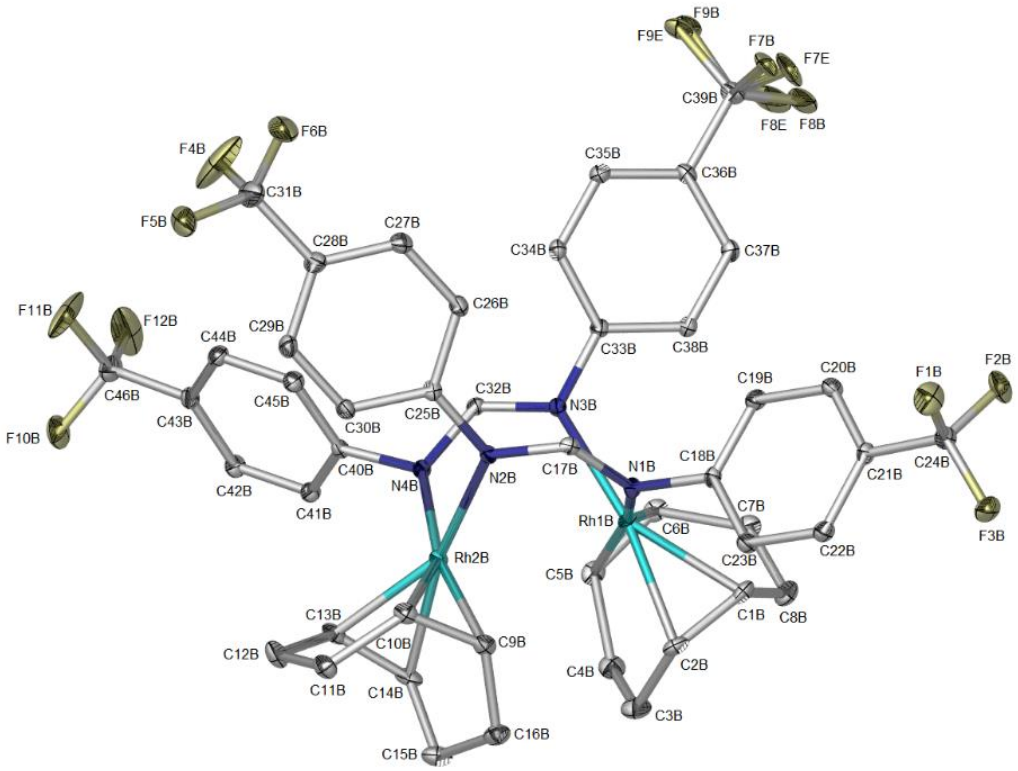

Figure 2.27 Molecular structure B of **C3**. Hydrogen atoms have been omitted for clarity.

The complexes exhibit a distorted square planar geometry around each Rh(I) centre with angles of 87 – 88 ° in **C1** and 86 ° in **C3**. An average of 2.122 Å in the Rh–N bond lengths in **C1** are slightly shorter than 2.123 Å in **C3**. This agrees with the notation of the negative charge being delocalized across the amidine N–C=N backbone.[140] Furthermore, the N–C_{Ar} average bond lengths in **C3** are 0.003 Å shorter. The presence of the withdrawing effect of the trifluoromethyl substituent from ligand **L3** stabilizes the π-backbonding of the metal centres to the π*-orbitals of the amidine group by conjugation into the aryl ring. This is further supported by the longer C=C bonds of 1.400 Å in **C1** than 1.392 Å in **C3** of the chelating COD ligands. In all the complexes, the separation of metal centres is much greater than the distances between the nitrogen atoms across. This would make it impossible to form a Rh–Rh bond, resulting in the electron-rich centres.[141] No apparent hydrogen bonding interactions are present in the packing diagrams of these complexes. The COD ligands adopt a face-down boat confirmation as the most energy stable conformer. In this case, each pair of opposite bonds are anti-parallel, which reduces the α–β proton-proton interactions. The protons are thus in different chemical environment, which is why a doubling-up of signals is identified in the NMR of the complexes. Selected parameters for **C1** and **C3** are summarized in Table 2.3.

Table 2.2 Selected crystal data and refinement details for **C1** and **C3**.

Parameters	**C1**	**C3**
Empirical formula	$C_{42}H_{46}N_4Rh_2$	$C_{46}H_{42}F_{12}N_4Rh_2$
Weight ($g.mol^{-1}$)	812.65	1084.66
Crystal system	Monoclinic	Monoclinic
Space group	$P2_1/n$	$P2_1/c$
Crystal size (mm)	0.10 x 0.11 x 0.12	0.12 x 0.17 x 0.38
a (Å)	11.6393(5)	21.9192(11)
b (Å)	22.1062(9)	25.1328(16)
c (Å)	13.4152(5)	16.0635(9)
α (º)	90	90
β (º)	98.009(10)	109.212(2)
γ (º)	90	90
Cell volume ($Å^3$)	3418.07	8354.4
Z	4	8
T (K)	173	100
D_c ($g.cm^{-3}$)	1.579	1.724
μ (mm^{-1})	1.003	0.884
R_{int}	0.048	0.031
Min, max $\Delta\rho/\varepsilon$ ($Å^3$)	-0.63, 0.63	-0.87, 0.91

Table 2.3 Selected contact distances, bond distances, bond angles for **C1** and **C3**.

Parameters	**C1**	**C3**
d(Rh–Rh) (Å)	3.239	3.270
d(Rh–N) (Å)	2.125	2.125
d(Rh–C_{COD}) (Å)	2.138	2.138
d(N=C) (Å)	1.322	1.338
d(C=C_{COD}) (Å)	1.400	1.394
Bond angle around Rh atoms (º)	N1-Rh1-N2 86.84(7)	N1B-Rh1B-N3B 86.43(6)
	N3-Rh2-N4 87.95(7)	N2B-Rh2B-N4B 85.84(6)

*2.6.2 Single crystals of [**C5**(CH$_3$CN)] adduct and **C8***

Well defined single crystals of **C5** and **C8** were obtained from acetonitrile and dichloromethane/hexane solutions, respectively. **C5** crystallizes in the tetragonal P4/ncc space group with one molecule in the unit cell found. Furthermore, this crystallizes to an adduct with one acetonitrile molecule coordinated axially to afford [**C5**(CH$_3$CN)]. The coordination of acetonitrile in the adduct causes the D_{4h} symmetry that is present in the free parent complex [Rh$_2$(dpf)$_4$] and other homoleptic dirhodium(II) complexes not be preserved.[142,143] The adduct falls in the C_{4h} symmetry point group. The asymmetric unit of [**C5**(CH$_3$CN)] in seen in Figure 2.28. One formamidinato ligand is shown for simplicity since all four equatorial ligands are equivalent.

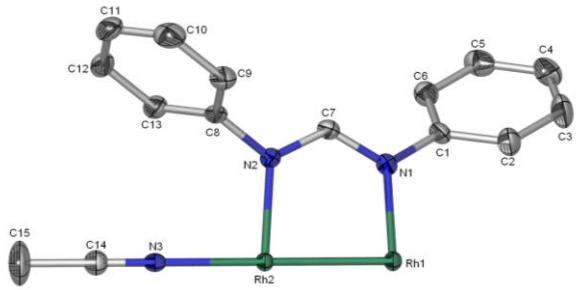

Figure 2.28 Asymmetric unit of **C5**. Hydrogen atoms have been omitted for clarity.

The complex exhibits a slightly distorted octahedral geometry around each Rh metal centre with angles of 89.88, 174.72 º N1–Rh1–N1 and 89.78, 172.98 º N2–Rh2–N2. The bonds around Rh2 slightly repel the axial coordination site to accommodate the coordination of the acetronitrile molecule. This results to smaller deviations from the expected right angles and straight lines around Rh1 as it is less affected by any interaction with the axially coordinated ACN. The equatorial Rh–N bond lengths of 2.054 Å around Rh1 are slightly shorter to those around Rh2 with 2.056 Å.[27] The axial Rh–N bond is 0.055 – 0.057 Å longer than the equatorial bonds, indicating stronger coordination at equatorial sites. The longer bond lengths around Rh2 are induced by the increased electron density from the ACN, to which is compensated by bond weakening.[144] Interestingly, axial coordination of ACN has negligible effect on π-backbonding towards equatorial ligands.

The formamidine C=N bond with a bond length of 1.316 Å is much longer than that 1.325 Å of the free ligand.[118] This double bond is more localised around Rh2 and this reduced conjugation is explained by the misalignment of the pπ-orbitals between the two benzene ring. This is due to the distortion away from the plane of the free ligand upon coordination of ACN.

The Rh–Rh bond has a length of 2.461 Å. The axial coordination of the acetonitrile molecule has a bond angle of 180 º for Rh1–Rh2–N3, with a Rh2–N3 bond length of 2.111 Å which is comparable to the analogous adduct.[144]

C8 crystallizes in the monoclinic *C2/c* space group with two independent molecules per unit cell. Interestingly, the coordination of the acetato ligand results in the loss of a horizontal mirror plane that is found in **C5**, and the principal axis of rotation is a C_2 which bisects the Rh–Rh bond, acetato and the dpf ligand directly *trans* to it. **C8** belongs to the C_{2v} symmetry point group. Figure 2.29 shows the molecular structure of **C8**.

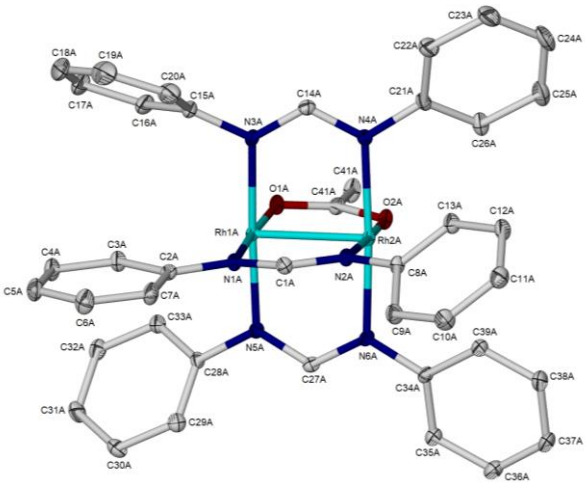

Figure 2.29 Molecular structure A of **C8**. Hydrogen atoms have been omitted for clarity.

The Rh–Rh bond has a length of 2.405 Å, which is shorter compared to **C5**. This indicates that the coordination of the acetato ligand provides more electron density to the Rh_2^{4+} core. This is supported by the results obtained from NMR where the acetato ligand is more electron donating compared to the R-dpf ligand that is directly *trans* to it. In contrast to **C5**, the complex exhibits a smaller distortion from a regular octahedral geometry around each Rh metal centre. For the *trans* equatorial bonds, N–Rh–O bond angles have an average of 176.54 º, and an average of 176.70 º is measured for the N–Rh–N. For the *cis* equatorial bonds, N–Rh–O have an average angle of 89.75 º. The N–Rh–N have bond angles of 90.16 º. These angles reveal that the H-dpf ligands *cis* to the acetato ligand are slightly distorted towards the side with the acetato ligand as there is less steric strain and more degrees of freedom for the phenyl rings. The Rh–O bonds have an average bond length of 2.057 Å which is longer than the 2.025 Å found for the Rh–N_{trans} indicating stronger coordination of the *trans* diphenylformamidinato ligand favoured by more backbonding.

For the ligands *cis* to the acetato ligand, Rh–N_{cis} bonds are slightly longer than their *trans* counterpart with an average of 2.045 Å. This due to the ligands being similar and thus having equal and competing effects on π-backbonding, making these bonds slightly weaker. This further explains the slightly longer formamidine C=N bond for the *trans* ligand with a bond length of 1.318 Å compared to the 1.316 Å bond length found for the *cis* ligands. In this case, charge conjugation of the N=C–N backbone is more favoured in comparison to **C5** and in turn, more symmetry is maintained by the molecule. As expected, no hydrogen bonding interactions are observed.

*2.6.3 Single crystals of [**C10**(H_2O)] and [**C10**($H_2O)_2$] adducts*

Two well defined and independent single crystals of **C10** were obtained from a dichloromethane/hexane solution. The blue crystal contains one water molecule coordinated to one axial site shown in Figure 2.30 and the red crystal contains two water molecules coordinated to both axial sites shown in Figure 2.31. Both structures reveal that the *cis* complex is easily isolated which agrees with the results from NMR. The *cis* isomer is a kinetical product and will be explained in Section 2.10 of the current chapter.

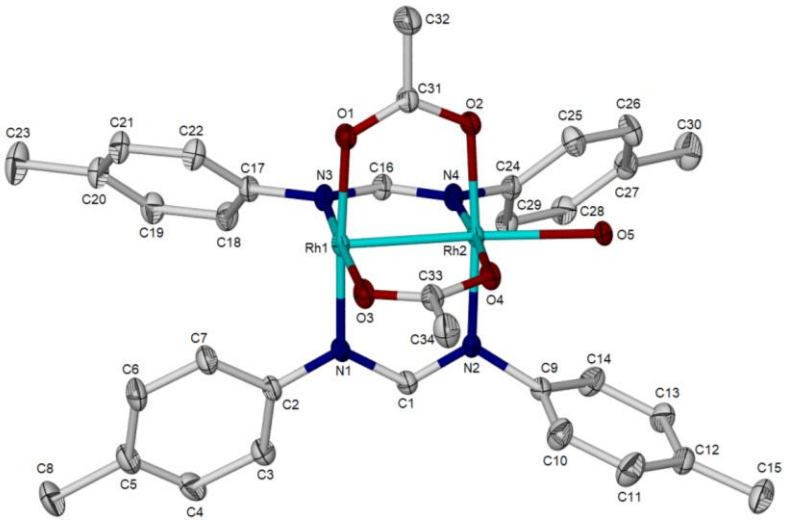

Figure 2.30 Molecular structure of the [**C10**($H_20)_2$] adduct.

The blue crystal crystallises in the triclinic P-1 space group with one molecule in the unit cell found. Furthermore, this crystallizes to an adduct with one water molecule coordinated axially to afford [**C10**(H_2O)]. The coordination of water in the adduct causes the D_{4h} symmetry that is present in the free parent complexes [$Rh_2(CH_3$-dpf$)_4$], [$Rh_2(OAc)_4$] and likewise other homoleptic dirhodium(II) complexes not be preserved.[143,144] The adduct falls in the C_1

symmetry point group which contains only the identity symmetry element only. It follows from this that the parent molecules **C10** ([$Rh_2(CH_3$-dpf$)_2(OAc)_2$]) falls in the C_s symmetry point group, as axial coordination of one solvent molecule removes the mirror plane in the molecule.

A bond length of 2.406 Å Rh–Rh bond is comparable to **C6** as reported in literature for *bis*-heteroleptic dirhodium(II) complxes.[124] In comparison, the bond is much shorter than found in the **C5** water adduct, and similar in **C8**. Like most dirhodium(II) complexes with four bridging ligands, the Rh metal centres have a slightly octahedral geometry.[145] The *trans* equatorial N–Rh1–O bonds have an average bond angle of 177.05 º, while the average bond angle of N–Rh2–O is 175.56 º. For the *cis* equatorial bonds, O–Rh1–O has an angle of 89.37 º and N–Rh1–N has an angle of 89.74 º. In comparison, bond angles of 89.22 and 90.35 º are measured for the O–Rh2–O and N–Rh2–N, respectively. Further analysis shows that the water molecule is slightly distorted towards the quadrant containing the two equatorial acetato ligands with an angle of 169.65 º for Rh1–Rh2–O5. The decrease in the number in a degree of coordination by the sterically demanding diphenylformamidinato ligands induces distortion away from the hindered side to release the strain.

For the equatorial ligands, the Rh1–N bonds have a bond length of 2.005 Å, which are slightly longer than the Rh2–N bonds with a bond length of 2.022 Å. The Rh–O bonds are longer than the Rh–N with bonds of 2.065 and 2.007 Å for Rh1–N and Rh2–N, respectively. These observations indicate that the CH_3-dpf ligands are strongly bound since they stabilise charge much better, as observed for the *trans* ligand in **C8**. Furthermore, there is more π-backbonding from Rh2 as electron density is increased by the presence of the water molecule, which makes the bonds shorter.

The axial bond Rh2–O5 has a bond length of 2.246 Å, which is much longer than the axial bond length found for **C5**, since the nitrogen atom is a better donor atom over oxygen making its coordination stronger.[133,145] The N=C and N–C bonds have similar bond lengths with an average of 1.319 Å, indicating more charge delocalization around the N=C–N. However, these conjugated N=C double bonds are longer than the conjugated C=O double bonds with a length of 1.269 Å due to the presence of the electron donating methyl group at the para position which results in a more localized charge around the formamidine backbone. The packing diagram of the complex reveals an intermolecular hydrogen bonding interaction between two molecules of [**C5**(H_2O)] involving the axial water molecule and one acetato ligand from the neighbouring molecule through O2···H5B, with an interaction distance of 1.965 Å.

The red crystal crystallises in the triclinic P-1 space group, similarly to [**C10**(H_2O)$_2$], with one molecule in the unit cell found (Figure 2.24). Furthermore, this crystallizes to an adduct with two water molecules coordinated axially to afford [**C10**(H_2O)$_2$]. The coordination of water in the adduct causes the loss of D_{4h} symmetry that is present in the free parent complexes [Rh_2(CH_3-dpf)$_4$], [Rh_2(OAc)$_4$] and likewise other homoleptic dirhodium(II) complexes.[143,144] The adduct falls in the C_s symmetry point group which contains the identity and two mirror plane symmetry elements. The adduct falls to the same symmetry group as the parent molecules **C5** as axial coordination are equivalent when similar molecules to both axial sites.

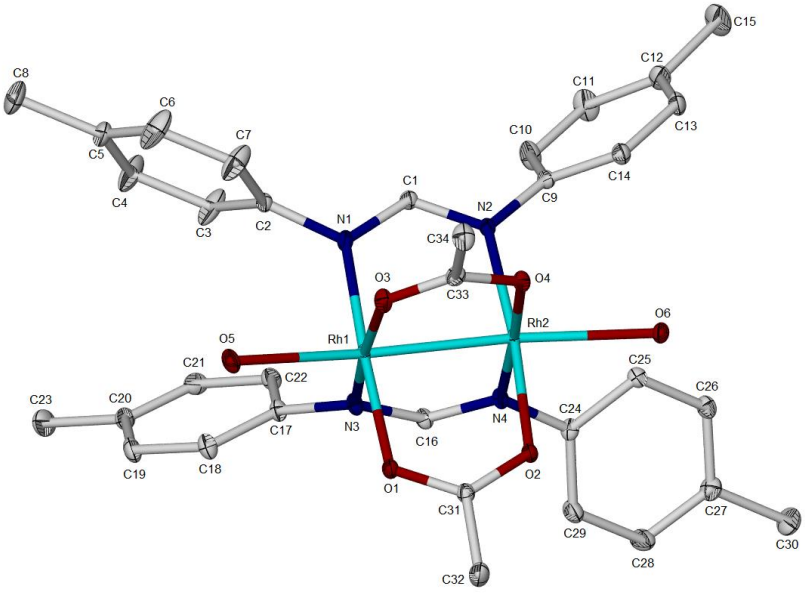

Figure 2.31 Crystal structure of a [**C10**(H_20)$_2$] adduct.

A bond length of 2.433 Å for Rh–Rh bond is much longer compared to that of [**C5**(H_2O)]. This bond lengthening results from the coordination of the second water molecule at other axial site, which increases electron density charge to the Rh_2^{4+} core. A repulsion of the two Rh metal centres is required for the molecule to stabilize the increasing charge. As observed for the [**C5**(H_2O)] adduct, the Rh metal centres have a slightly octahedral geometry. The *trans* equatorial N–Rh–O bonds have an average bond angle of 175.70 º.

For the *cis* equatorial bonds, O–Rh–O has an angle of 88.77 º and N–Rh–N with an angle of 90.67 º. The two acetato ligands move towards each other while the CH_3-dpf ligands slightly repel each other to reduce the steric strain around each Rh metal. The water molecules are slightly distorted towards the quadrant containing the two equatorial acetato ligands with an

angle of 167.45 º for Rh1–Rh2–O_{ax}. For the equatorial ligands, the Rh–N bonds have a bond length of 2.022 Å. These bonds are which are slightly shorter than the Rh–O bonds with a bond length of 2.079 Å. This is indicative of the stronger coordination of the equatorial nitrogen donor ligands over the oxygen donor ligands.

The axial bonds Rh1–O5 and Rh2–O6 have an average bond length of 2.322 Å, which is much longer than the axial bond length of 2.246 Å found for the [**C10**(H_2O)] adduct. This is explained by the increase in the electron density around the Rh_2^{4+} core. This results to a weaker axial binding, in turn the bonds lengthen. The observation is supported by the increase in the Rh–Rh bond, as previously mentioned.[124] The N=C and N–C bonds have similar bond lengths with an average of 1.320 Å, indicating more charge delocalization around the N=C–N. However, these conjugated N=C double bonds are longer than the conjugated C=O double bonds with a length of 1.268 Å due to the presence of the electron donating methyl group at the *para* position which results in a more localized charge around the formamidine backbone.

Similar observations are noticeable for the [**C10**(H_2O)] adduct. The packing diagram of the complex reveals an intermolecular hydrogen bonding interaction between two molecules of [**C10**(H_2O)$_2$] involving one axially bound water molecule with one acetato ligand from the neighbouring molecule through O1···H5A, with an interaction distance of 1.954 Å. This forms a 6-membered ring void space between the two molecules and a rod-like continuous extended network in the morphology. The selected crystal data information and refinement details are summarized below in Table 2.4.

Table 2.4 Selected crystal data and refinement details for **C5**, **C8** and **C10**

Parameter	[**C5**(CH_3CN)]	**C8**	[**C10**(H_2O)]	[**C10**$(H_2O)_2$]·$CHCl_2$
Empirical formula	$C_{54}H_{47}N_9Rh_2$	$C_{41}H_{36}N_6N_2Rh_2$	$C_{34}H_{38}N_4O_5Rh_2$	$C_{35}H_{42}N_4O_6Cl_2Rh_2$
Weight (g/mol)	1027.83	850.58	788.50	891.45
Crystal system	Tetragonal	Monoclinic	Triclinic	Triclinic
Space group	P4/ncc	C2/c	P-1	P-1
Crystal size (mm)	0.10x0.14x0.18	0.04x0.04x0.25	0.12x0.17x0.38	0.03x0.07x0.12
a (Å)	13.59(7)	67.28(5)	21.92(11)	12.51(7)
b (Å)	13.59(7)	9.89(7)	25.13(16)	13.24(7)
c (Å)	24.96(14)	22.44(17)	16.06(9)	14.02(8)
α (º)	90	90	70.97(1)	91.56(2)
β (º)	90	107.95(2)	75.16(1)	114.51(2)
γ (º)	90	90	89.17(2)	115.51(8)
Cell volume ($Å^3$)	4609.3(5)	14198.0(18)	1797.5(14)	1847.0(19)
Z	4	16	2	2
F(000)	2096	6880	800	904
T (K)	173	100	173	100
D_c (g/cm^3)	1.48	1.59	1.46	1.60
μ (1/mm)	1.003	0.976	0.961	1.087
R_{int}	0.0263	0.0361	0.0338	0.0250
Min, max $\Delta\rho/\varepsilon$ ($Å^3$)	-0.50, 0.37	-1.16, 0.74	-0.75, 1.75	-0.74, 1.12

2.7 UV-visible Spectroscopy of Complexes

*2.7.1 UV-Vis of homobimetallic rhodium complexes **C1** – **C4***

To study the electronic behaviour of the homobimetallic Rh(I) complexes, solution containing 0.10 mmol.dm^{-3} of each complex in DCM were prepared. DCM was the solvent of choice due to the high solubility of the complexes and its less interference with the complexes, which can be negligible.

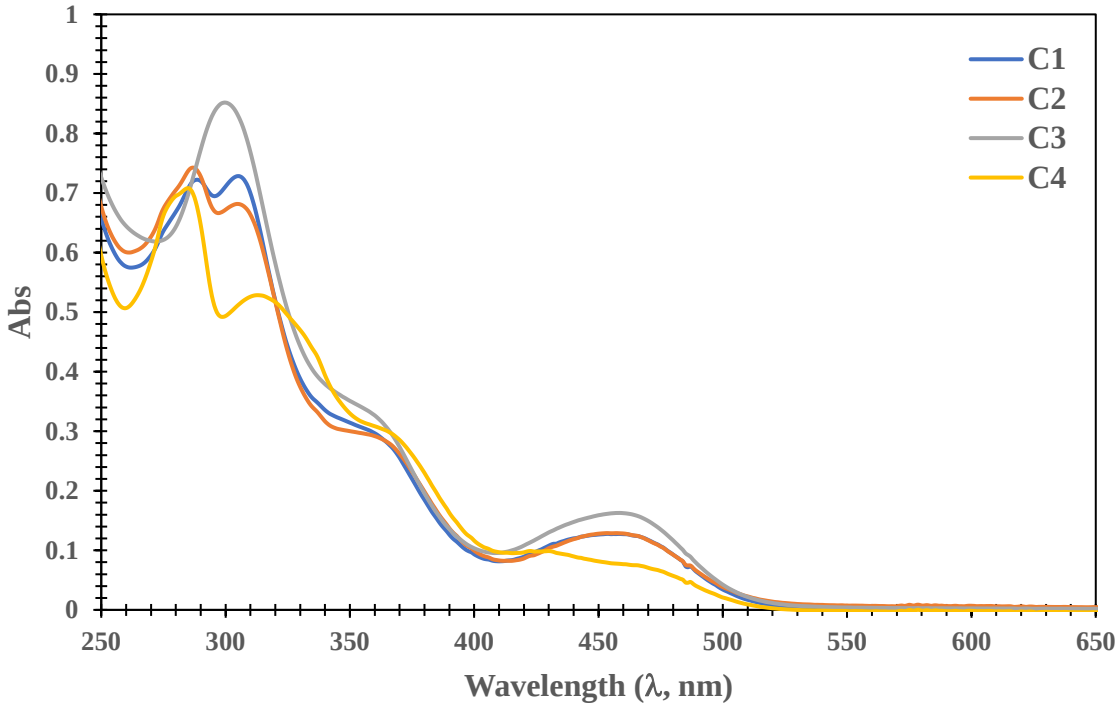

Figure 2.32 UV-Vis spectra of homobimetallic Rh(I) complexes **C1** – **C4** in DCM.

The Rh(I) complexes are d^8 low-spin metal complexes that contain a distorted square planar geometry around each metal centre, which contain orbitals that can interact with the ligand's high lying p orbitals and the low lying π* orbitals. As seen in Figure 2.32, each complex is characterised by four absorption bands. To assign these bands, previously reported examples analogous complexes found in literature were used.[27] The absorption band at 463 nm is attributed to a MLCT transition. This low energy band arise from the $d\pi$(Rh) → π*(N–C=N) transition. From this transition, the metal becomes oxidized. The energy band at 369 nm is attributed to a LMCT transition, which belongs to the charge transfer from the π(C=C$_{COD}$) → $d\pi$*(Rh) and the metal is reduced. The high energy transition band at 308 – 316 nm is attributed to the ligand centred n → π*(N–C=N), where n results from the lone pair of electrons on the

nitrogen atoms. The intense higher energy band at 287 nm results from the ligand centred π(N–C=N) → π*(N–C=N). For complex **C3**, it can be observed that the two high energy bands overlap and appear as one absorption, indicating that they result from transitions of equal energy of electron excitation. For these complexes, a general trend is observed in that there is as slight blueshift p(N–C=N) → π*(N–C=N) and a slight redshift in both the n → π*(N–C=N) and π(C=C_{COD}) → *d*π*(Rh) transitions, which is indicative of substituent dependence. The MLCT *d*π(Rh) → π*(N–C=N) transition remains unaffected by changes in the substituents.

*2.7.2 UV-Vis of dirhodium complexes **C5** – **C11** in DCM*

To study the electronic behaviour of the dirhodium Rh_2(II) complexes C5 – C11, solutions containing 10.0 mmol.dm^{-3} of each complex in DCM, THF and ACN were prepared. These solvents were used as they were solvents of choice for the catalysis. The electronic spectra will indicate the influence the interactions of the solvents, that is where the coordinating or non-coordinating solvent effect the energy transitions of electron excitations.

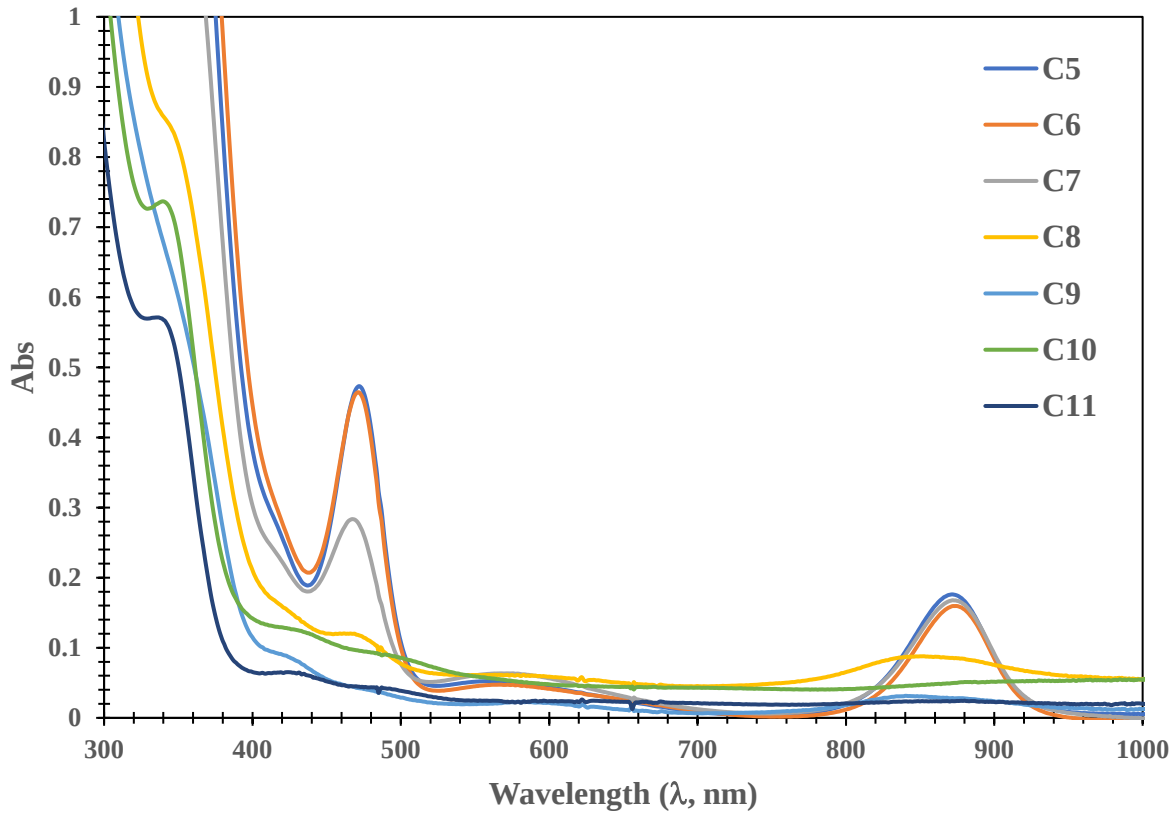

Figure 2.33 UV-Vis spectra of dirhodium(II) complexes **C5** – **C11** in DCM.

In DCM, the homoleptic complexes **C5** – **C7** have three absorption bands (Figure 2.33). The high energy band at 472 nm is attributed to the ligand $\pi \rightarrow \pi^*$ electronic transition resulting from the excitation from an electron in the π-orbital to the π^*-antibonding orbital. A weak shoulder band at 600 nm is attributed to $\pi^*(Rh_2) \rightarrow \pi^*(L)$ MLCT band. An intense, low energy band at 882 nm is assigned to the $\pi^*(Rh_2) \rightarrow \sigma^*(Rh_2)$ involving the bonding and antibonding orbitals in of the dirhodium core. For the mixed complexes **C8** – **C11**, the ligand centred $\pi \rightarrow \pi^*$ electronic transition is blue shifted 344 nm, indicating the presence of the acetate ligand populates the π-bonding orbital with more electron density more density, and the orbital is stabilised to lower energy levels. The separation between the bonding and antibonding orbitals is increased. The transition thus requires more energy. The $\pi^*(Rh_2) \rightarrow \pi^*(L)$ MLCT band is unaffected by the acetate ligand and remains at 600 nm. The $\pi^*(Rh_2) \rightarrow \sigma^*(Rh_2)$ transition is reduced as the HOMO π^* is destabilised and LUMO σ^* is stabilised for the bimetal core become less separated, hence lower energy is required for the excitation.

*2.7.3 UV-Vis of dirhodium complexes **C5** – **C11** in THF*

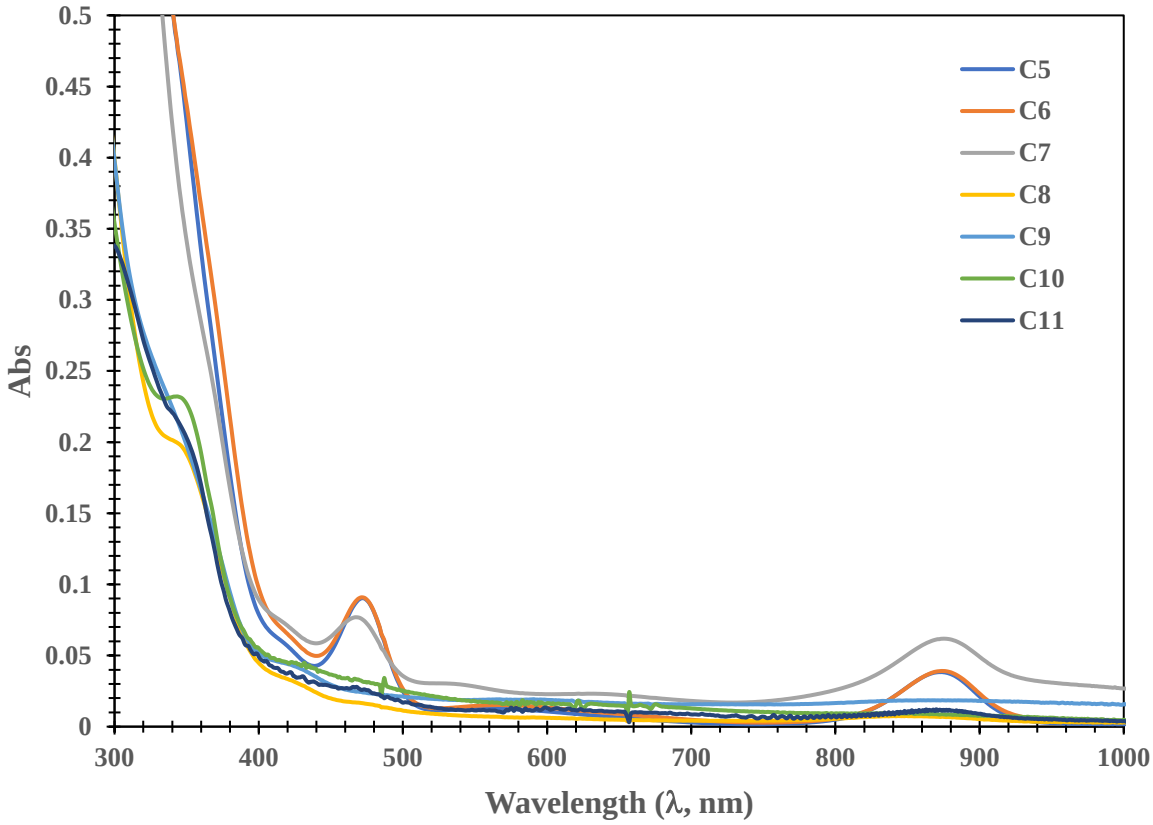

Figure 2.34 UV-Vis spectra of dirhodium(II) complexes **C5** – **C10** in THF.

In THF, the homoleptic complexes **C5** – **C7** have two absorption bands (Figure 2.34). The high energy band ligand $\pi \rightarrow \pi^*$ electronic transition resulting from the excitation of an electron in the π-orbital to the π^*-antibonding orbital is slightly red shifted to 477 nm. The $\pi^*(Rh_2) \rightarrow \pi^*(L)$ MLCT band observed in DCM is absent, indicating some interaction between the π^* orbitals of the Rh_2^{4+} core and the weakly coordinating THF. The intense, low energy band at 882 nm found observed with DCM, which is assigned to the $\pi^*(Rh_2) \rightarrow \sigma^*(Rh_2)$ involving the bonding and antibonding orbitals in of the dirhodium core remains unaffected. For the mixed complexes **C8** – **C11**, the ligand centred $\pi \rightarrow \pi^*$ electronic transition is red shifted compared to DCM and resonates at 344 nm. This also indicates that the presence of the acetate ligand populates the π-bonding orbital with more electron density more density, and the orbital is stabilised to lower energy levels. The separation between the bonding and antibonding orbitals is increased. The transition thus requires more energy. The $\pi^*(Rh_2) \rightarrow \sigma^*(Rh_2)$ transition is reduced as the HOMO π^* is destabilised to a higher energy and LUMO σ^* is stabilised to a lower energy for the bimetal core become less separated, hence lower energy is required for the excitation.

*2.7.4 UV-Vis of dirhodium complexes **C5** – **C11** in ACN*

In ACN, the homoleptic complexes **C5** – **C7** have two absorption bands (Figure 2.35). The high energy band ligand $\pi \rightarrow \pi^*$ electronic transition resulting from the excitation of an electron in the π-orbital to the π^*-antibonding orbital is slightly red shifted to 425 nm. The $\pi^*(Rh_2) \rightarrow \pi^*(L)$ MLCT band observed in DCM is absent, indicating strong interaction between the π^* orbitals of the Rh_2^{4+} core and the coordinating ACN. The intense shoulder band at 380 nm is due to the $\pi(L) \rightarrow \sigma^*(Rh_2)$ LMCT involving the bonding orbital of the ligand and the antibonding orbitals in of the dirhodium core. For the mixed complexes **C8** – **C11**, the ligand centred $\pi \rightarrow \pi^*$ electronic transition is red shifted compared to DCM and resonates at 240 nm. The acetate centred $\pi \rightarrow \pi^*$ resonates at 260 nm. This also indicates that the presence of the acetate ligand populates the π-bonding orbital with more electron density more density, and the orbital is stabilised to lower energy levels. The LMCT π (L) $\rightarrow \sigma^*(Rh_2)$ transition is appears as a shoulder at 345 nm.

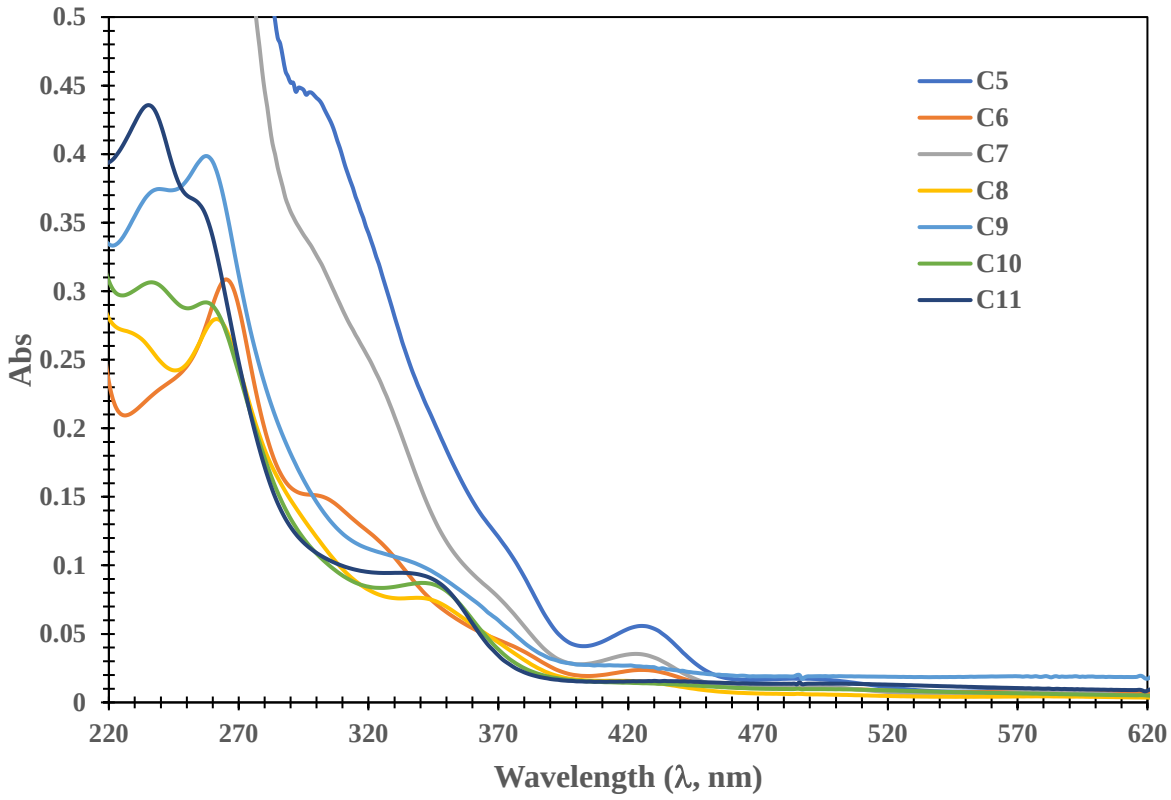

Figure 2.35 UV-Vis spectra of dirhodium(II) complexes **C5** – **C11** in ACN.

2.8 Electrochemistry

Cyclic voltammetry was used to elucidate the electrochemical properties of both series of Rh complexes to confirm the oxidation states of the complexes and understanding the product distribution in the yields obtained upon completion of catalysis. For the homobimetallic Rh(I) complexes **C1** – **C4**, the electrochemical experiments were performed in a 0.10 mol.dm^{-3} solution of TBAP in DCM containing 1.00 mmol.dm^{-3} of the analyte. For the dirhodium Rh_2(II) complexes **C5** – **C11**, the electrochemical experiments were performed in 0.20 mol.dm^{-3} solutions of TBAP in DCM, THF or ACN containing 1.00 mmol.dm^{-3} of the analyte. Measurements were taken at room temperature. A glassy carbon electrode was used as a working electrode, the reference electrode used contained 0.10 mol.dm^{-3} Ag/AgCl solution and a platinum wire used as a counter electrode. The electrochemical potentials were recorded with a scan rate of 0.10 V/s.

*2.8.1 Cyclic voltammetry of the homobimetallic rhodium complexes **C1** – **C4***

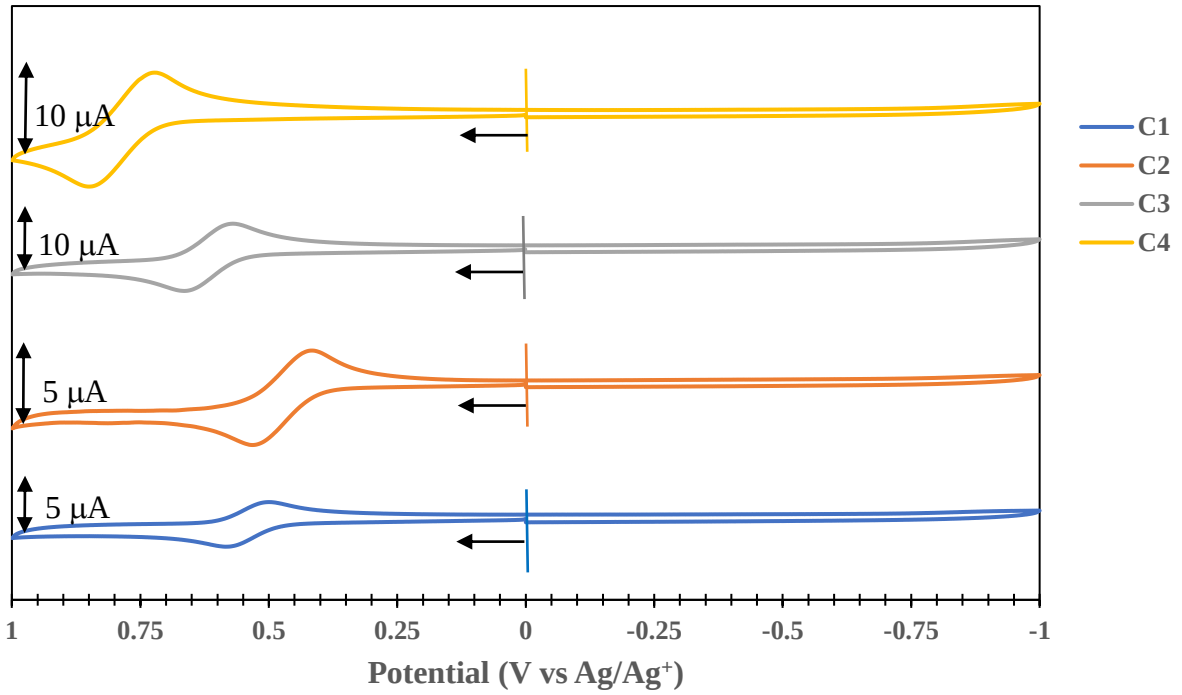

Figure 2.36 Cyclic voltammograms of **C1** – **C4** in CH_2Cl_2 containing 0.10 mol.dm^{-3} of TBAP showing the reversible Rh_2^{2+}/Rh^{3+} redox couple event. Scan rate = 100 mV/s. WE = glassy carbon, RE = Ag/AgCl and CE = Pt wire.

Figure 2.36 shows the cyclic voltammograms of the complexes **C1** – **C4**. When sweeping positively, there is a metal-centred one electron oxidation peak belonging to the redox couple at one Rh(I) centre. The Rh_2^{2+}/Rh^{3+} oxidation in **C1** occurs at a potential 0.54 V. A cathodic shift of 80 mV to 0.46 V potential upon substitution with a methyl brings about an easier oxidation in **C2** relative to **C1** as the electron donating methyl group shares more of its electron density to the Rh metal centres. This destabilises the HOMO of the metal, making it more prone to electron abstraction. In contrast, the presence of the fluoride substituent in **C3** pulls electron density away from the Rh metal centre. In turn, the HOMO of the metal is stabilised to lower energy, making the electrons occupying the orbitals less prone to abstraction. This results to an anodic shift of 70 mV to 0.61 V potential.

The trifluoromethyl substituent is more withdrawing compared to the fluoride substituent, so a larger anodic shift of 230 mV to 0.78 V potential in **C4** is observed. The electron withdrawing substituent stabilises the HOMO of the electrons to lower energy, making it harder to extract an electron. Beyond an applied potential of 1.00 V, and the 1,5-cyclooctadiene ligands

dissociated from the complexes in an irreversible process. The half-wave potentials are recorded in Table 2.5.

Table 2.5 Half-wave potentials ($E_{1/2}$, V vs Ag/AgCl) of Rh(I) complexes at room temperature in DCM containing 0.1 M TBAP at room temperature. Scan rate = 100 mV/s.

Complex	R	$E_{1/2}$[a]	i_{pa}/i_{pc}[b]	2σ
C1	H	0.54	1.04	0.00
C2	CH_3	0.47	1.03	-0.34
C3	F	0.62	1.05	0.12
C4	CF_3	0.79	1.12	1.08

[a]$E_{1/2} = \frac{1}{2}(E_{pa} + E_{pc})$. [b]$i_{pc}/i_{pa}$ = ratio of cathodic (reduction) and anodic (oxidation) peak currents.

There exists a linear-free energy relationship between the type of substituent at the para positions of the aromatic rings and the energy required for the oxidation as shown in Figure 2.37. By Hammett's equation, $E_{1/2}$ and the Hammett substituent constant are related by Equation (1), where X is the substituent, σ is the substituent constant and ρ is the reactivity constant.[146]

$$\Delta E_{1/2} = E_{1/2}(X) - E_{1/2}(H) = \rho * 2\sigma \quad (1)$$

This provides information on the reactivity of the complexes **C1** – **C4** as the substituents is changed to an electron donating methyl and electron withdrawing fluoride and trifluoromethyl groups. This further indicates the higher oxidation states species are stabilized. The complexes undergo a similar redox process mechanism, to which an electron is abstracted reversibly from the HOMO of the Rh metal centre. This process is largely dependent on the nature of the substituent as observed with similar bridging ligands.[146] The electron donating groups have an easily accessible HOMO and the electron withdrawing groups have a less accessible HOMO of the metals. The oxidation process is highly affected with reactivity constant of ρ = 0.22 by the resonance effect of the substituent.

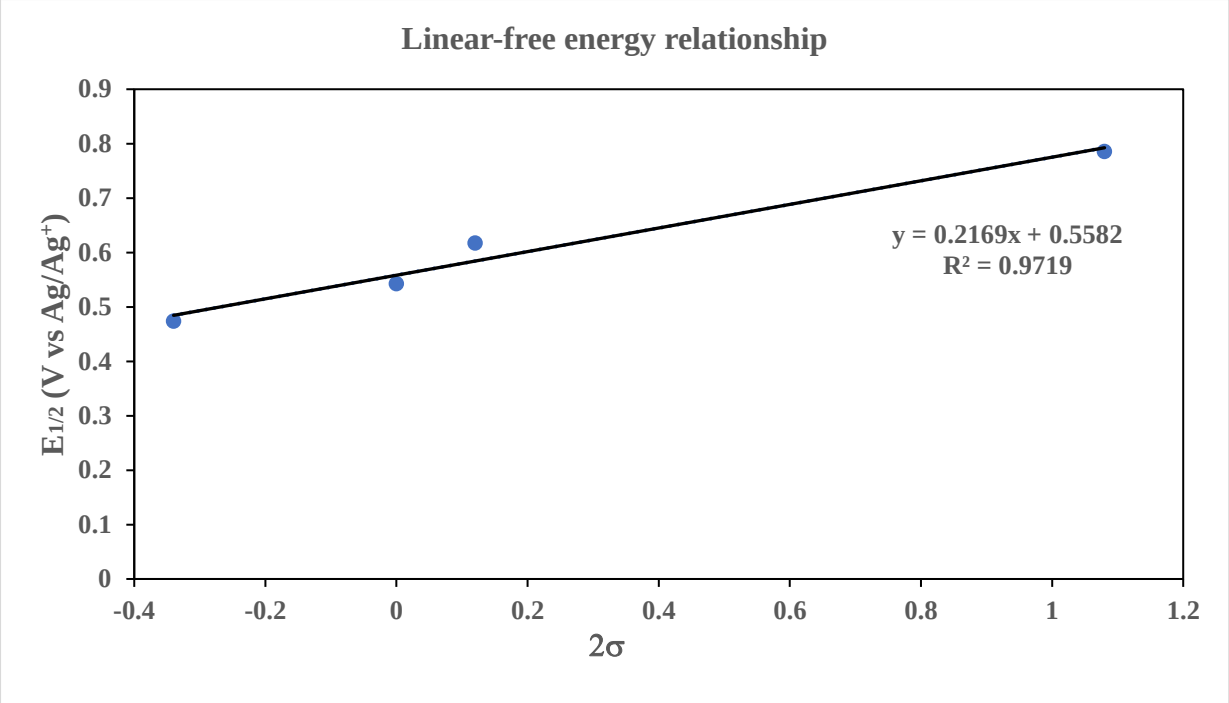

Figure 2.37 Hammett's plot in testing for a linear-free energy relationship.

*2.8.2 Cyclic voltammetry of the dirhodium(II) complexes **C5** – **C11** in DCM*

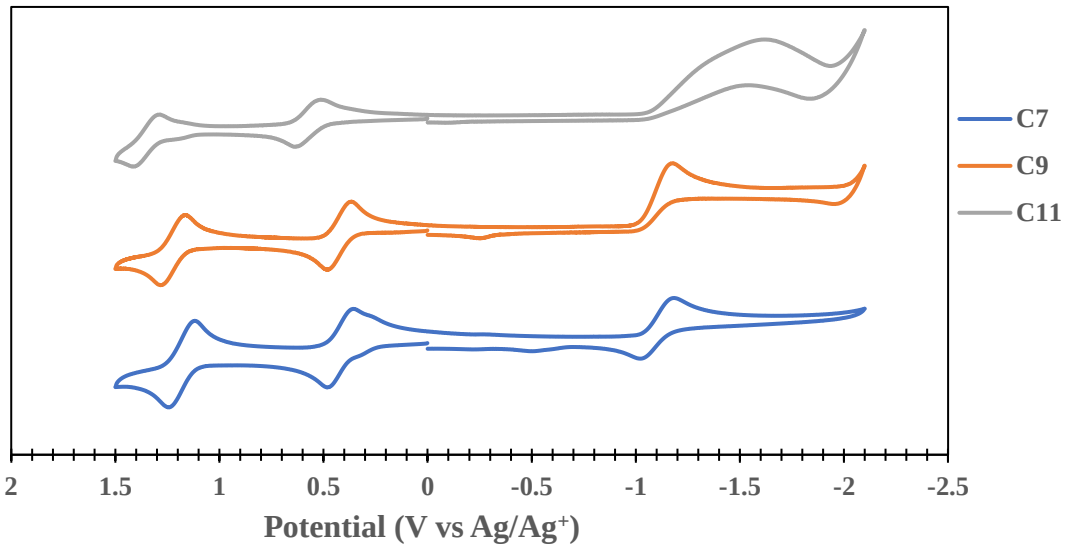

Figure 2.38 Cyclic voltammograms of **C7**, **C9** and **C11** in DCM containing 0.10 mol.dm^{-3} of TBAP showing the Rh_2^{4+}/Rh^{3+} reduction, the Rh_2^{4+}/Rh^{5+} and Rh_2^{5+}/Rh^{6+} oxidation redox couple event. Scan rate = 100 mV/s. WE = glassy carbon, RE = Ag/AgCl and CE = Pt wire.

Figure 2.38 shows the cyclic voltammograms of **C7**, **C9** and **C11** in a solution containing 0.2 mol.dm^{-3} TBAP in DCM. The homoleptic dirhodium(II) complexes **C5** – **C7** are characterised with one reversible one-electron reduction event and two reversible one-electron oxidation events. These are evidenced with the cyclic voltammogram of **C7** which was chosen as a representative for the homoleptic complexes. On the other hand, the mixed ligand dirhodium(II) complexes are characterised with one irreversible one-electron reduction event and two reversible one-electron oxidation events. These are evidenced by the cyclic voltammograms of **C9** and **C11**. Generally, in DCM, decreasing the number of R-dpf ligands coordinated to the Rh_2^{4+} core shifts the redox events to lower potentials. Furthermore, when an acetato ligands is coordinated, the reduction event becomes irreversible. It is postulated that the acetato ligand is displace by the increasing in the charge around the Rh_2^{4+} core and the compound disintegrate.

*2.8.3 Cyclic voltammetry of the dirhodium(II) complexes **C5** – **C11** in THF*

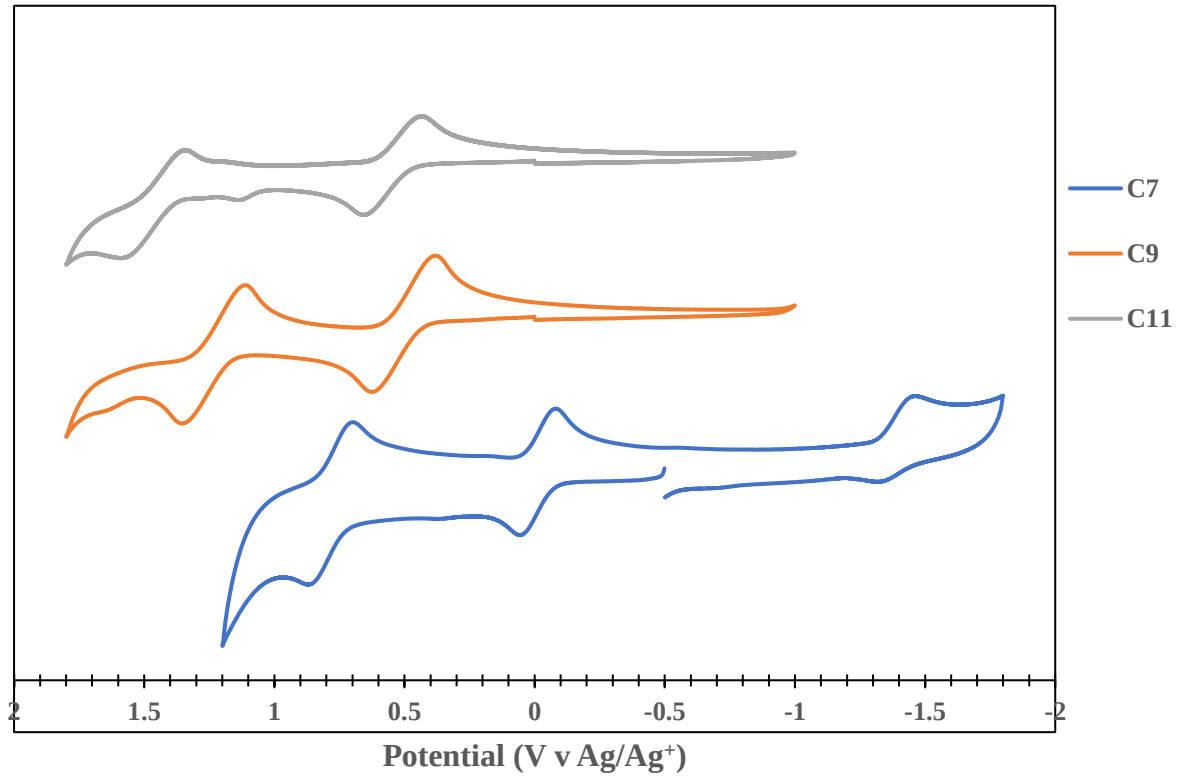

Figure 2.39 Cyclic voltammograms of **C7**, **C9** and **C11** in THF containing 0.10 mol.dm^{-3} of TBAP showing the Rh_2^{4+}/Rh^{3+} reduction, the Rh_2^{4+}/Rh^{5+} and Rh_2^{5+}/Rh^{6+} oxidation redox couple event. Scan rate = 100 mV/s. WE = glassy carbon, RE = Ag/AgCl and CE = Pt wire.

Figure 2.39 shows the cyclic voltammograms of **C7**, **C9** and **C11** in a solution containing 0.1 mol.dm^{-3} TBAP in THF. The homoleptic dirhodium(II) complexes **C5** – **C7** are characterized with one quasi-reversible one-electron reduction event and two reversible one-electron oxidation events. These are supported by the cyclic voltammogram of **C7**. The mixed ligand dirhodium(II) complexes **C8** – **C11** are characterized with two reversible one-electron oxidation events. These are evidenced by the cyclic voltammograms of **C9** and **C11**. Generally, in THF, decreasing the number of R-dpf ligands coordinated to the Rh_2^{4+} core shifts the redox events to higher potentials. The presence of a coordinated acetato ligand in combination with the weak axial coordination of a THF molecule, increases the electron density on the Rh_2^{4+} core, making it harder to reduce and easier to oxidize. Hence the disappearance of the reduction peak in the solvent window.

*2.8.4 Cyclic voltammetry of the dirhodium(II) complexes **C5**, **C7** and **C11** in ACN*

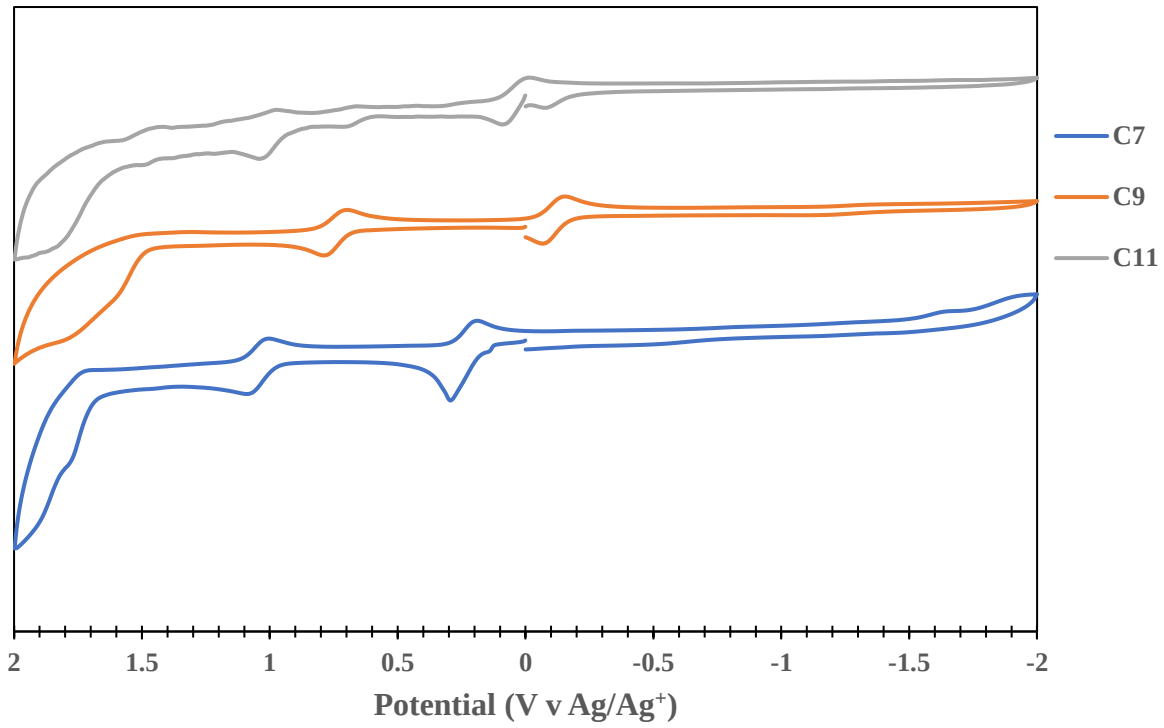

Figure 2.40 Cyclic voltammograms of **C7**, **C9** and **C11** in ACN containing 0.10 mol.dm^{-3} of TBAP showing the Rh_2^{4+}/Rh^{3+} reduction, the Rh_2^{4+}/Rh^{5+} and Rh_2^{5+}/Rh^{6+} oxidation redox couple event. Scan rate = 100 mV/s. WE = glassy carbon, RE = Ag/AgCl and CE = Pt wire.

Figure 2.40 shows the cyclic voltammograms of **C7**, **C9** and **C11** in a solution containing 0.1 mol.dm^{-3} TBAP in ACN. The homoleptic dirhodium(II) complexes **C5** – **C7** are characterised with two reversible one-electron oxidation events. These are evidenced by the cyclic

voltammogram of **C7**. Similarly, the mixed ligand dirhodium(II) complexes **C8** – **C11** are characterized with two reversible one-electron oxidation events. These supported by the cyclic voltammograms of **C9** and **C11**. Generally, in ACN, decreasing the number of R-dpf ligands coordinated to the Rh_2^{4+} core, shifts the redox events to lower potentials. The presence of a coordinated acetato ligand in combination to a strong axial coordination of and ACN molecule increases the electron density around the Rh_2^{4+} core results to harder reduction and easier oxidation, and the reduction disappears in the potential window of the solvent.

Table 2.6 shows the half-wave potentials $E_{1/2}$ of the reduction, first and second oxidation redox couple events in DCM, THF and ACN are summarised in Table 2.5. In DCM, the homoleptic complexes **C5** – **C7** have a reversible reduction event. The reduction event is related to $Rh_2^{4+/3+}$ redox couple that occurs at a potential of -1.23 V in **C5**. Upon substitution with a methyl group at the *para* position in **C6**, there is a 90 mV cathodic shift. The harder reducibility is induced by the increased electron density from the electron donating methyl group. In **C7**, a 130 mV anodic shift is brought up by the reduced electron density around the core due to the electron withdrawing fluoride group.

For the mixed ligand dirhodium(II) complexes, the one-electron reduction event is irreversible. Decreasing the R-dpf ligand coordinated by one degree, the cathodic potential E_{pc} is higher than $E_{1/2}$ of homoleptic complexes with electron rich substituents (**C8** versus **C5**) and lower for electron deficient substituents (**C9** versus **C7**). Decreasing the R-dpf ligand coordinated by two degrees, the cathodic potential E_{pc} is lower than $E_{1/2}$ of homoleptic complexes for both the electron rich (**C10** versus **C6**) and electron deficient substituents (**C11** versus **C7**). **C7** has a cathodic potential of -1.28 V, which is shifted anodically by 100 mV when substituting with the electron withdrawing fluoride substituent which pulls away electron density from the Rh_2^{4+} core, favouring the reduction. With a cathodic potential of -1.57 V in **C10**, the 20 mV anodic shift in **C11** is supported by the replacement of the electron rich methyl substituent with the electron deficient fluoride substituent.

Table 2.6 Half-wave potentials ($E_{1/2}$, V vs Ag/AgCl) reduction, first and second oxidation redox-couple events in solutions containing 0.1 M TBAP at room temperature.

Complex	x	R	$E_{1/2}(Rh_2^{4+/3+})$	$E_{1/2}(Rh_2^{4+/5+})$	$E_{1/2}(Rh_2^{5+/6+})$
DCM					
C5	4	H	-1.23	0.28	1.15
C6	4	CH_3	-1.32	0.23	1.02
C7	4	F	-1.10	0.42	1.18
C8	3	H	-1.28*	0.40	1.23
C9	3	F	-1.18*	0.42	1.22
C10	2	CH_3	-1.57*	0.48	1.27
C11	2	F	-1.55*	0.57	1.36
THF					
C5	4	H	-1.53**	-0.08	0.79
C6	4	CH_3	-1.65**	-0.17	0.69
C7	4	F	-1.39**	-0.02	0.78
C8	3	H	–	0.47	1.25
C9	3	F	–	0.51	1.23
C10	2	CH_3	–	0.48	1.37
C11	2	F	–	0.55	1.46
ACN					
C5	4	H	–	0.16	0.99
C6	4	CH_3	–	-0.07	0.85
C7	4	F	–	0.24	1.04
C8	3	H	–	-0.14	0.68
C9	3	F	–	-0.11	0.74
C10	2	CH_3	–	-0.07	0.85
C11	2	F	–	0.03	1.01

*Irreversible, E_{pa} is reported. **Quasi-reversible.

In THF, only the homoleptic dirhodium(II) complexes exhibit a reduction event. The use of THF causes a negative shift in the half-wave potentials of the reduction event. The shift is in response to the weak axial coordination interaction of the THF which increases the electron density around the core, making it harder for reduction to occur. The cathodic shifts are slightly higher in THF (120 mV in **C6** and 140 mV in **C7**) compared to DCM (90 mV in **C6** and 130

mV in **C7**). There is a stronger σ-coordination by ACN at the axial sites which is evidenced by the crystal structure of the [(**C1**)(CH_3CN)] adduct. This increases the electron density around the Rh_2^{4+} core. The LUMO σ* orbital is lowered in energy and becomes less accessible to receive an electron, hence the absence of the reduction event in the solvent window.

The first oxidation event is related to the $Rh_2^{4+/5+}$ redox couple, which occurs with the $E_{1/2}$ of 0.28 V in **C5**. A substitution with a methyl group at the *para* position causes a 50 mV cathodic shift as the core become easier to oxidise. A substitution with fluoride group causes a 140 mV anodic shift as the electrons are less accessible. In both THF and ACN, the event is shifted to lower potentials when compared to DCM, indicating an ease in oxidizing the Rh_2^{4+} core. For THF, there is cathodic shift of 36 – 44 mV, where it is higher in **C7** due to the affinity of the more electron deficient Rh_2^{4+} core to the weak axial coordination of THF to provide more electron density. For ACN, there is a cathodic shift of 0.18 – 0.44 mV, due to the strong axial coordination by the ACN increasing the electron charge density of the core and favoured stabilisation of higher charge.

For the mixed ligand complexes, the oxidation potentials are higher than those of the homoleptic complexes. The presence of the coordinated acetato ligand provides less electron density since the acetato ligand has a shorter electron π-system than the R-dpf ligands, making charge loss less favoured. The HOMO π* orbital will be low-lying in energy, leading to harder electron abstraction. A decrease in the degree of R-dpf ligands coordinated has a larger anodic shift in the potential. In THF, the mixed ligands complexes **C8** – **C11** show an anodic shift of 20 – 90 mV. In contrast, there is a cathodic shift of 510 – 550 mV when using ACN. Similar trends are observed for the second oxidation $Rh_2^{4+/5+}$ redox couple event.

*2.8.5 Cyclic voltammetry of the dirhodium(II) complexes **C5** – **C11** in DMF*

Due to its wider potential window, DMSO attempted for use to determine the presence of the reduction event that does not appear with THF and ACN, as well as in the mixed ligand complexes. However, it was found that the DMSO is strongly coordinating and forms crystals of the complexes which have limited solubility. So DMF was used since it has a slightly similar potential window to DMSO and the complexes are soluble. The half-wave potentials are summarised in Table 2.7.

Table 2.7 Half-wave potentials ($E_{1/2}$, V vs Ag/AgCl) reduction, first and second oxidation redox-couple events in DMF solution containing 0.1 M TBAP at room temperature.

Complex	x	R	$E_{1/2}(Rh_2^{4+/3+})$	$E_{1/2}(Rh_2^{4+/5+})$	$E_{1/2}(Rh_2^{5+/6+})$
C5	4	H	-1.11	0.21	0.96
C6	4	CH_3	-1.17	0.11	0.79
C7	4	F	-1.08	0.27	1.01
C8	3	H	–	0.21	0.94
C9	3	F	–	0.22	1.00
C10	2	CH_3	–	0.23	1.11
C11	2	F	–	0.32	1.22

The reduction event $Rh_2^{4+/3+}$ is present in the homoleptic complexes **C5** – **C7** and absent in the mixed ligands complexes **C8** – **C11**. It suffices to postulate that the methyl group of the acetato ligand is a strongly donating substituent, while the acetate is a poor π-acceptor ligand.[126] The coordination of the acetato ligand will cause an increase in the electron density around the Rh_2^{4+} core and stabilize the LUMO σ* orbital to lower energy. The orbital becomes less prone to accept electrons upon reduction. This is supported by the absence of the reduction event in the parent complex $[Rh_2(OAc)_4]$ as previously reported in literature.[147] However, the analogous $[Rh_2(TfOAc)_4]$ complex exhibits an irreversible one-electron reduction and no oxidation redox couple.[148] Compared to the other solvents, the DMF solvent has the reduction events occurring at slightly higher potentials than DCM and THF for the homoleptic complexes. For the first oxidation $Rh_2^{4+/5+}$ event, there is a cathodic shift compared to DCM and an anodic shift compared to THF and ACN in the homoleptic complexes. For the mixed ligands complexes, there is a cathodic shift compared to the other solvents. This is likely a result of axial coordination of DMF via the oxygen donor atom, which induces a higher dipole with the Rh_2^{4+} core.

Piraino and co-workers have reported that for such dirhodium(II) complexes, the Rh_2^{6+} complex is only stable for short times of cyclic voltammetry, which then undergoes redox changes.[124] This will modify its composition to lead to further oxidisable products. According to Gagne's suggestions,[149] one must consider the equilibrium reaction (2). From this, the relationship between the equilibrium constant of (2), known as the comproportionation

constant, K_{com}, and the difference between the potentials of the two one-electron oxidation steps should hold as shown by equation (3).[138]

$$Rh_2^{4+} + Rh_2^{6+} \rightleftharpoons 2\ Rh_2^{5+} \quad (K_{com}) \tag{2}$$

$$K_{com} = e^{nF\Delta E^o/RT} \tag{3}$$

Table 2.8 shows the calculated compropotionation constants of the homoleptic complexes for each solvent. Based on literature studies, it has been shown that the substitution of O with NH, from tetracarboxylates to tetraamidates, in the dirhodium complexes reduces the oxidation potential by about 700 mV.[138] In DCM, the unsubstituted complexes provide a shorter lived Rh_2^{6+} as evidenced by the higher K_{com} values indicating favouring the products. However, the fluoride substituted complexes have smaller K_{com} values of the methyl substituted complexes. This indicates the electron withdrawing groups gives less stable Rh_2^{6+} species, hence equilibrium is shifted towards the reactants. In the coordinating solvents, the di- and tri-substituted complexes have much larger K_{com} values. In such a case, the equilibrium is shifted towards the product side. This results from the increase of the coordinated acetato ligands, which is good electron donating ligand. So, the reaction species are easily long lived and more stabilised by the increasing electron density provided by the axially coordinated ligands. The axial coordination is much stronger with the electron deficient complexes of the electron withdrawing fluoride substituent.

Table 2.8 Comproportionation constants, K_{com} for the homoleptic complexes **C5** – **C11** in different solvents.

Complex	x	R	DCM	THF	ACN	DMF
C5	4	H	5.11×10^{14}	5.11×10^{14}	1.08×10^{14}	4.78×10^{12}
C6	4	CH_3	2.27×10^{13}	5.11×10^{14}	3.58×10^{15}	3.13×10^{11}
C7	4	F	7.06×10^{12}	3.35×10^{13}	3.35×10^{13}	3.24×10^{12}
C8	3	H	1.08×10^{14}	1.35×10^{13}	7.29×10^{13}	2.19×10^{12}
C9	3	F	3.35×10^{13}	1.49×10^{12}	2.35×10^{14}	1.54×10^{13}
C10	2	CH_3	2.27×10^{13}	1.11×10^{15}	3.58×10^{15}	7.54×10^{14}
C11	2	F	2.27×10^{13}	2.42×10^{15}	3.70×10^{16}	2.42×10^{15}

To further investigate the effect of solvent, the relationship between the half-wave potentials of the two oxidation states and the donor number of the solvent was constructed. This was done by means of Guttman's donor number, *DN* (in kcal/mol).[150] Ferrocene was used as an internal standard to eliminate variable diffusion potentials, which arise from the aqueous-nonaqueous reference electrode. So, the half-wave potentials were compensated with the ferrocene-ferrocenium redox couple.

Figure 2.41 shows the plots of relevant $E_{1/2}$(V vs Fc/Fc^+) of the $Rh_2^{4+/5+}$ and $Rh_2^{5+/6+}$ couples for **C5** as a function of *DN* formal electrode potential of **C5** in on the donor number of the solvent. In all solvents, the two processes appear as reversible charge transfers. For the $Rh_2^{4+/5+}$ oxidation, equation (4) is obtained with a regression coefficient of r = 0.99 indicating good correlation. Similarly, good correlation of equation (5) is obtained for the $Rh_2^{5+/6+}$ oxidation with r = 0.98.

$$E_{1/2}(\text{V}) = -0.3749 + 0.0075\ DN\ (R^2 = 0.9894) \quad (4)$$

$$E_{1/2}(\text{V}) = 0.4877 + 0.0070\ DN\ (R^2 = 0.9543) \quad (5)$$

However, on addition of DMF, poor correlation results for both the $Rh_2^{4+/5+}$ and $Rh_2^{5+/6+}$ couples with r = 0.58 and 0.04, respectively. This indicates that there is incomplete ability for the *DN* to account for the solvent effects. We considered linear regression analysis with multiparameters that considers the hydrogen-bonding donor (Lewis acidity) and polarity-polarizability parameters for the $Rh_2^{4+/5+}$ couple. In this case, we have chosen the Dimroth-Reichardt (E_T(30)) and solvent polarity (π^*) parameters,[151,152] together with *DN* as this have been shown to achieve better correlation than their individual regressions.

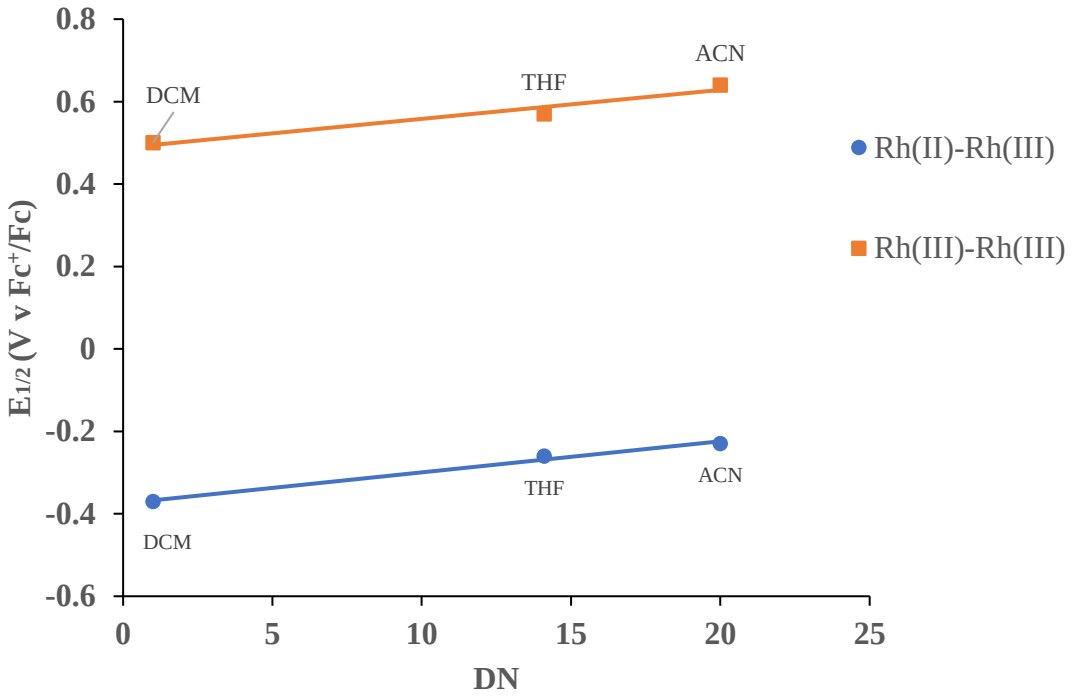

Figure 2.41 Half wave potential ($E_{1/2}$) dependence of **C5** on the solvent donor number (DN) for the $Rh_2^{4+/5+}$ (blue dots) and $Rh_2^{5+/6+}$ (orange squares).

In our case, the multiparameter regression is impossible since there are four observations, while we aim to predict four parameters. So, multiregression model with two independent parameters including *DN* would make a better predictor. Regression for *DN* and $E_T(30)$ has been found to be insignificant, with $R^2 = 0.3818$, with $E_T(30)$. A Student *t* test indicates that $E_T(30)$ is the insignificant variable. The regression for *DN* and π* is more significant, $R^2 = 0.7455$, obtaining equation (6) to describe the model. However, to determine whether DMF solvent is an outlier, more solvents would need to be evaluated to increase the sample size, which would make the conclusions drawn from each independent variable more accurate for the regression model.[138,151,153,154]

$$E_{1/2}(V) = -0.0732 + 0.0032\,DN - 0.3618\,\pi^* \quad (6)$$

2.9 Attempted Synthesis of Mono-substituted Complexes

2.9.1 Identification of isolated intermediate species

For comparative reasons, we attempted to synthesise the mono-substituted complexes of the type [Rh_2(R-dpf)$(OAc)_3$] with one diphenylformamidinato and three acetato ligands coordinated. The first attempt was to add dropwise a solution of 1.00 eq. H-dpf ligand in chlorobenzene and triethyl amine at reflux. However, the reaction leads to very low yields of the di-substituted complexes [Rh_2(R-dpf)$_2(OAc)_2$] and tri-substituted complexes [Rh_2(R-dpf)$_3$(OAc)]. These lead us to believe that it is likely this reaction is kinetically controlled reaction, and hence leads to the formation of the kinetically favoured higher substituted complexes. The second attempt was to instead add the solution of 1.00 eq. H-dpf ligand in chlorobenzene at room temperature. A purple intermediate quickly forms, and this was stirred overnight. The purple solid was isolated and upon its analysis by ^{1}H NMR, it was found that two H-dpf ligands are coordinated axially. A single crystal was obtained from DCM/Hexane.

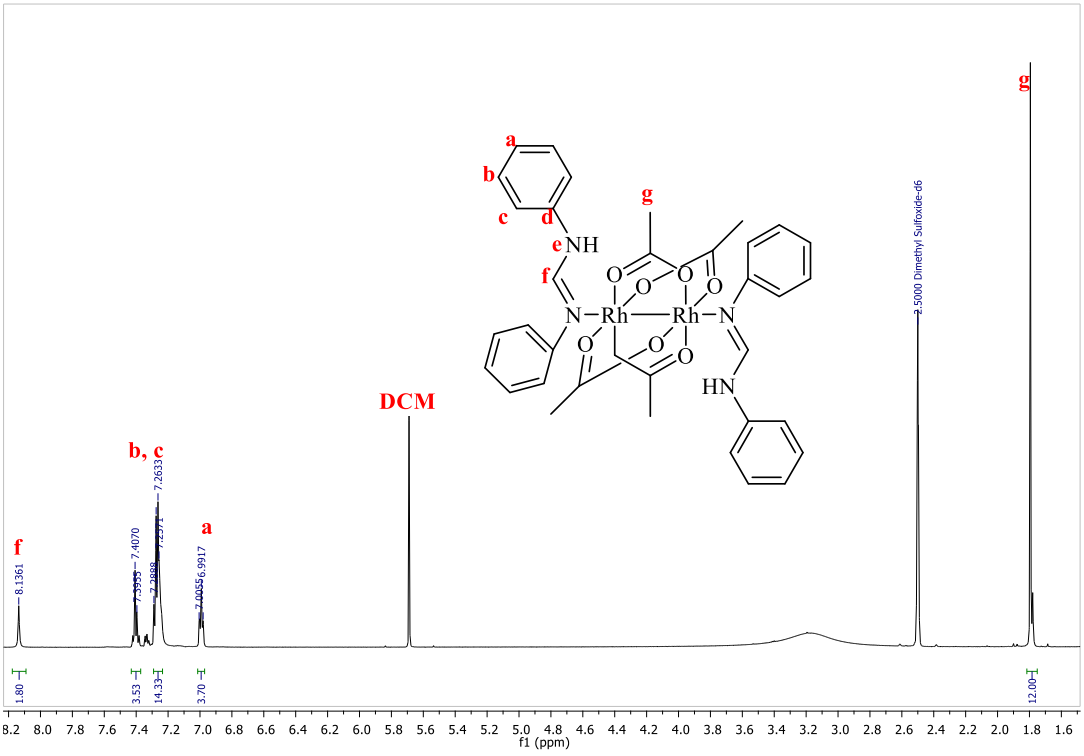

Figure 2.42 ^{1}H NMR of the isolated intermediate in DMSO-d_6.

The ^{1}H NMR (Figure 2.42) shows an aliphatic signal integrating for twelve protons. This leads us to believe that the acetato ligands still occupy all the equatorial sites like the parent complex [$Rh_2(OAc)_4$]. In the aromatic region, a triplet ($^3J_{H\text{-}H}$ = 5.06 Hz) at 6.99 ppm integrating to four

protons corresponds to the protons H_a, directly *para* to the nitrogen coordinated to the Rh centre. A multiplet at 7.26 – 7.28 ppm and the asymmetrical doublet at 7.41 ppm collectively integrate to fourteen protons. These are assigned to the overlapping aromatic protons adjacent to the non-coordinated nitrogen and the protons *meta* and *ortho* to the coordinated nitrogen. The number of the aromatic signals is an indication of some dynamical behaviour of the proton transfer between the two nitrogen atoms within the *in situ*. The two ligands will thus be identical and average out. Finally, the formamidinyl protons H_f resonate as a broad singlet at 8.14 ppm and integrate for two protons.

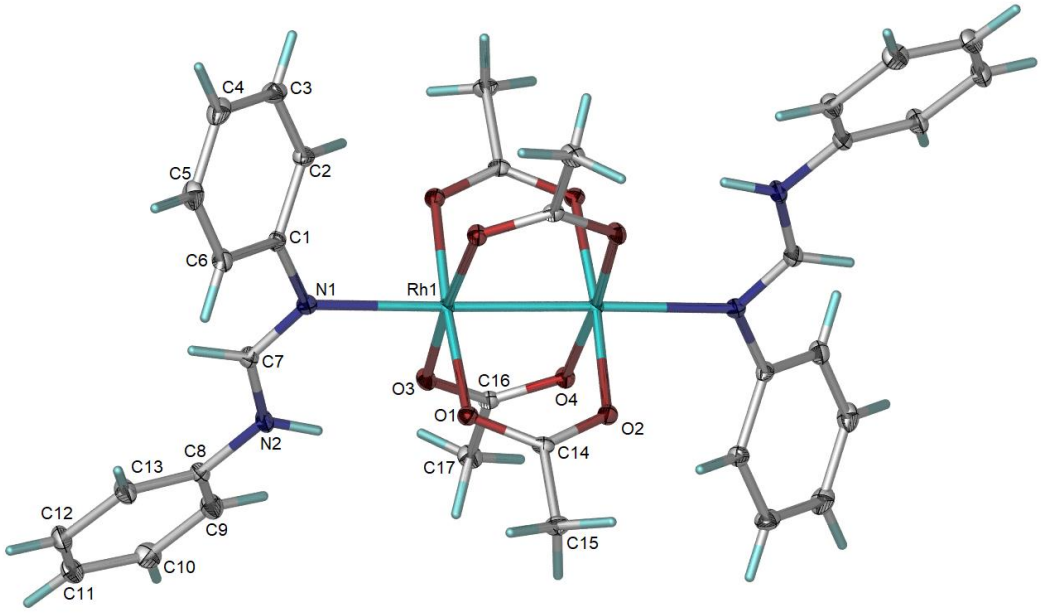

Figure 2.43 Crystal structure of isolated purple intermediate.

Figure 2.43 shows the single crystal of the isolated intermediate compound. The Rh metal centres are coordinated with the proton-free, basic nitrogen of the formamidine functionality at both axial sites. In doing so, the phenyl ring adjacent to coordinated nitrogen rotates 3.4 ^{o} about the free rotating N–C_{Ar} bonds, labelled N1–C1 and N2–C8. The phenyl rings become distorted from the plane of the free ligand molecule to minimize the strain experienced by the acetato ligands, with a distortion angle of 123.4 ^{o} around N1 for a distorted trigonal planar. This becomes the most stable form in solid-state. The coordination of the H-dpf at both axial sites changes the D_{4h} in the parent $[Rh_2(OAc)_4]$ to a C_2 symmetry point group in $[Rh_2(OAc)_4(dpf)_2]$.[142,143]

The intermediate complex crystallizes in the triclinic P-1 (No. 2) space group with two molecules in the unit cell. The complex exhibits a distorted octahedral geometry around the Rh metal centres with an average O_{eq}–Rh–N_{ax} angle of 92.26 ^{o} for both Rh1 labelled metals centres.

The O_{eq}–Rh–O_{eq} bond angle, involving two equatorial oxygen atoms directly *trans* to each other has an average of 175.46 °, of which a slight deviation from 180 ° of a straight line. The Rh1–Rh1 bond distance of 2.418(3) Å is slight shorter.[155,156] The aromatic C=C double bonds have average bond distances of 1.391 and 1.392 Å. This indicates that charge delocalization is to both rings is equal and is independent of the proximity to the N-coordinated. The N2–C7 has a bond length of 1.351(2) Å is longer than 1.293(19) Å bond length of N1–C7 bond. While these bonds are slightly, the difference in lengths indicates a stronger π-backbonding towards the π* orbitals which contains more C7=N1 bond character as delocalization around the N–C=N backbone is limited by the protonation of the non-coordinated N. The average Rh–O bond length of 2.044 Å shorter than the bond length Rh–O in the parent $[Rh_2(OAc)_4]$.[157] In comparison, the bond length is shortened upon replacing the methyl group with a trifluoromethyl group.[148] Interestingly, the Rh1–O3 has the longest bond length of 2.054 Å compared to 2.042, 2.041 and 2.039 Å for O1, O2 and O4, respectively. This is because of the existing hydrogen bonding interaction N2–H2⋯O3, which elongates the equatorial bond to overcome the energy barrier.

There have been examples from literature which report that such complexes are held by solvent or axially coordinating molecules to form continuous polymeric chains in their extended network.[131,158–160] The packing diagram has two equivalent dirhodium(II) molecules of $[Rh_2(OAc)_4(dpf)_2]$ in a unit cell. Within each molecule, there exists two intramolecular hydrogen bonding interactions which keeps the axially bound ligands intact with the Rh_2^{4+} core. The hydrogen on the non-coordinating nitrogen is hydrogen bonding to the lone pair of electrons of the closest oxygen of the acetato ligand. This interaction labelled N2–H2⋯O3 on both dpf ligands has a non-covalent bond length of 2.023 Å. Contrary to this, the interaction labelled N2–H2⋯O1 has a non-covalent bond length of 3.235 Å and is too long to form a favoured interaction, hence no hydrogen bond is present. Due to the absence of π-stacking of the phenyl rings due to the distortion, the molecule takes a discreet morphology in its network.

2.9.2 Proposed mechanism for ligand substitution

Based on the isolated intermediate $[Rh_2(OAc)_4(dpf)_2]$, a reaction mechanism for the substitution of the acetato ligands with the dpf ligands can be elucidated (shown in Scheme 2.26).[161] The first step involves the binding of the dpf ligands at both axial through the high lying σ* HOMO. This occurs independently of the equivalents of dpf ligand relative to the

[$Rh_2(OAc)_4$] starting material. This step is fast since is occurs at room temperature with no energy required, so the reaction takes a kinetic pathway.

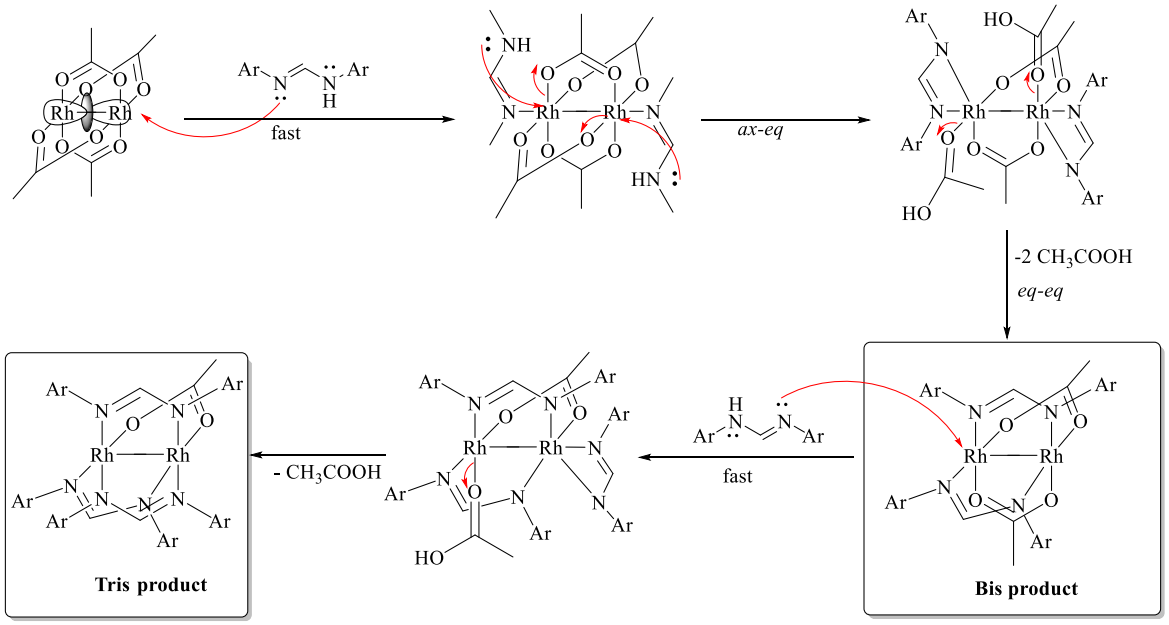

Scheme 2.26 Proposed reaction mechanism for substitution of acetato ligands with dpf ligand.

Upon the addition of heat, the coordinated ligand is able reconfigure itself to cyclize by displacing the immediate equatorial oxygen, forming an intermediate with a N_{eq}–Rh/Rh–N_{ax} non-bridging bonds around a Rh centre, known as an *ax-eq* chelate species. Further energy is used to break the axial bond, and the previous axially bound nitrogen displaces the second Rh–O_{eq} bond of the leaving acetato ligand to form a chelate of the formamidinato functionality towards the Rh_2^{4+} core, known as an *eq-eq* species.

Under basic conditions, the second step is favoured by the increased nucleophilicity of the negatively charged formamidine backbone. In this way, the bi-substituted complexes are formed first and are selective to the *cisoid* species where the two dpf ligands are added *cis* to each other. This is due to O1 (3.628 Å) and O3 (2.811 Å), which are *cis* to each other, having shorter distance with N2, so less energy is needed to substitute at those positions. The tri-substituted and homoleptic complexes are formed by similar subsequent stepwise substitutions from the bi-substituted product. The coordination of the dpf ligand is limited to one axial site due to the increased steric bulkiness around the Rh centres, allowing for better lability of the acetato ligand leaving group.

2.10 Summary

A series of *N,N'*-bidentate formamidine ligands were prepared and fully characterise with various spectroscopic techniques. These ligands were reacted with the $[Rh(Cl)(COD)]_2$ to affording the bimetallic complexes of the type $[Rh(R\text{-}dpf)(COD)]_2$, where R-dpf is a *para* substituted bridging diphenylformamidine ligand with R = H, CH_3, F or CF_3. These were characterised fully according to their spectroscopies and structures elucidated. The hydroformylation activity of the complexes is discussed in Chapter 3. The formamidine ligands were also reacted with $[Rh_2(TfOAc)_4]$ and $[Rh_2(OAc)_4]$ to afford the homoleptic and mixed ligand dirhodium(II) complexes of the type $[Rh_2(R\text{-}dpf)4]$ and $[Rh_2(R\text{-}dpf)_x(OAc)_{4-x}]$ with x = 2, 3 or 4 and R = H, CH_3 or F. These were also fully characterised by various spectroscopic techniques and their structures elucidated. A mechanism for the formation of the mixed ligand dirhodium complexes is proposed based on an intermediate that was isolated. The activity of these dirhodium(II) complexes in the allylic oxidation of cyclohexene will also be discussed in Chapter 4.

2.11 References

20 F. A. Cotton, C. A. Murillo, S. E. Stiriba, X. Wang and R. Yu, *Inorg. Chem.*, 2005, **44**, 8223–8233.

21 A. M. Angeles-Boza, H. T. Chifotides, J. D. Aguirre, A. Chouai, P. K. L. Fu, K. R. Dunbar and C. Turro, *J. Med. Chem.*, 2006, **49**, 6841–6847.

22 F. A. Cotton, E. A. Hillard and C. A. Murillo, *J. Am. Chem. Soc.*, 2002, **124**, 5658–5660.

23 E. B. Boyar and S. D. Robinson, *Coord. Chem. Rev.*, 1983, **50**, 109–208.

27 J. L. Bear, B. Han, Z. Wu, E. Van Caemelbecke and K. M. Kadish, *Inorg. Chem.*, 2001, **40**, 2275–2281.

109 F. A. Cotton and T. R. Felthouse, *Inorg. Chem.*, 1981, **20**, 584–600.

110 R. H. Beer, W. B. Tolman, S. G. Bott and S. J. Lippard, *Inorg. Chem.*, 1991, **30**, 2082–2092.

111 F. A. Cotton, K. R. Dunbar and C. T. Eagle, *Inorg. Chem.*, 1987, **26**, 4127–4130.

112 G. Aullón, A. Lledós and S. Alvarez, *Inorg. Chem.*, 2000, **39**, 906–916.

113 C. Köcher and W. A. Herrmann, *J. Organomet. Chem.*, 1997, **532**, 261–265.

114 E. W. Abel, M. A. Bennett and G. Wilkinson, *J. Chem. Soc.*, 1959, 3178–3182.

115 O. Trhlíková, J. Zedník, H. Balcar, J. Brus and J. Sedláček, *J. Mol. Catal. A Chem.*, 2013, **378**, 57–66.

116 I. D. Kostas, *Inorganica Chim. Acta*, 2003, **355**, 424–427.

117 D. P. Kapusta, A. M. Kulakova and M. G. Khrenova, *Russ. J. Phys. Chem. A*, 2020, **94**, 945–950.

118 S. F. Bureiko, N. S. Golubev, S. Y. Kucherov and A. V. Shurukhina, *J. Mol. Struct.*, 2007, **844**–**845**, 70–76.

119 B. A. Dar, S. N. Ahmad, M. A. Wagay, A. Hussain, N. Ahmad, K. A. Bhat, M. A. Khuroo, M. Sharma and B. Singh, *Tetrahedron Lett.*, 2013, **54**, 4880–4884.

120 S. R. Beeren, S. L. Dabb, G. Edwards, M. K. Smith, A. C. Willis and B. A. Messerle, *New J. Chem.*, 2010, **34**, 1200–1208.

121 E. Leitmannová, J. Svoboda, J. Sedláček, J. Vohlídal, P. Kačer and L. Červený, *Appl. Catal. A Gen.*, 2010, **372**, 34–39.

122 A. A. Mohamed, *Coord. Chem. Rev.*, 2010, **254**, 1918–1947.

123 P. Piraino, G. Tresoldi and F. Faraone, *J. Organomet. Chem.*, 1982, **224**, 305–312.

124 P. Piraino, G. Bruno, F. Nicolo, F. Faraone and S. Lo Schiavo, *Inorg. Chem.*, 1985, **24**, 4760–4762.

125 S. A. Johnson, H. R. Hunt and H. M. Neumann, *Inorg. Chem.*, 1963, **2**, 960–962.

126 B. G. Anderson, D. Cressy, J. J. Patel, C. F. Harris, G. P. A. Yap, J. F. Berry and A. Darko, *Inorg. Chem.*, 2019, **58**, 1728–1732.

127 E. C. Taylor and W. A. Ehrhart, *J. Org. Chem.*, 1963, **28**, 1108–1112.

128 F. A. Cotton, P. Lei, C. A. Murillo and L. S. Wang, *Inorganica Chim. Acta*, 2003, **349**, 165–172.

129 C. W. Yeh, H. L. Hu, R. H. Liang, K. M. Wang, T. Y. Yen, J. Der Chen and J. C. Wang, *Polyhedron*, 2005, 24, 539–548.

130 A. A. Soliman, O. I. Alajrawy, F. A. Attabi, M. R. Shaaban and W. Linert, *Spectrochim. Acta - Part A Mol. Biomol. Spectrosc.*, 2016, **152**, 358–369.

131 F. A. Cotton, E. V. Dikarev, M. A. Petrukhina and S. E. Stiriba, *Inorg. Chem.*, 2000, **39**, 1748–1754.

132 E. Cristina Stanca-Kaposta, D. P. Gamblin, J. Screen, B. Liu, L. C. Snoek, B. G. Davis and J. P. Simons, *Phys. Chem. Chem. Phys.*, 2007, **9**, 4444–4451.

133 M. Handa, S. Nishiura, T. Masuda, N. Yano, M. Mikuriya and Y. Kataoka, *Chem. Pap.*, 2018, **72**, 841–851.

134 S. De Doncker, A. Casimiro, I. A. Kotze, S. Ngubane and G. S. Smith, *Inorg. Chem.*, 2020, **59**, 12928–12940.

135 N. N. Omosun and G. S. Smith, *Eur. J. Inorg. Chem.*, 2019, **2019**, 2558–2564.

136 S. Siangwata, S. Chulu, C. L. Oliver and G. S. Smith, *Appl. Organomet. Chem.*, 2017, **31**, 1–9.

137 N. N. Omosun, S. Ngubane and G. S. Smith, *Appl. Catal. A Gen.*, 2021, **610**, 117950.

138 P. Piraino, G. Bruno, G. Tresoldi, S. Lo Schiavo and P. Zanello, *Inorg. Chem.*, 1987, **26**, 91–96.

139 Y. Ide, T. Ikeue, Y. Kataoka, R. Inoue, M. Nakamura, D. Yoshioka, M. Mikuriya, T. Kawamoto and M. Handa, *J. Organomet. Chem.*, 2016, **803**, 92–103.

140 S. Y. Chow and L. R. Odell, *J. Org. Chem.*, 2017, **82**, 2515–2522.

141 E. M. Shustorovich, M. A. Porai-Koshits and Y. A. Buslaev, *Coord. Chem. Rev.*, 1975, **17**, 1–98.

142 J. C. A. Boeyens, F. A. Cotton and S. Han, *Inorg. Chem.*, 1985, **24**, 1750–1753.

143 V. M. Miskowski, W. P. Schaefer, B. Sadeghi, B. D. Santarsiero and H. B. Gray, *Inorg. Chem.*, 1984, **23**, 1154–1162.

144 J. L. Bear, C. L. Yao, R. S. Lifsey, J. D. Korp and K. M. Kadish, *Inorg. Chem.*, 1991, **30**, 336–340.

145 K. V. Catalan, J. S. Hess, M. M. Maloney, D. J. Mindiola, D. L. Ward and K. R. Dunbar, *Inorg. Chem.*, 1999, **38**, 3904–3913.

146 W. R. Osterloh, G. Galindo, M. J. Yates, E. Van Caemelbecke and K. M. Kadish, *Inorg. Chem.*, 2020, **59**, 584–594.

147 R. S. Lifsey, X. Q. Lin, M. Y. Chavan, M. Q. Ahsan, K. M. Kadish and J. L. Bear, *Inorg. Chem.*, 1987, **26**, 830–836.

148 K. Das, K. M. Kadish and J. L. Bear, *Inorg. Chem.*, 1978, **17**, 930–934.

149 R. R. Gagné, C. L. Spiro, C. A. Hamann, T. J. Smith, W. R. Thies and A. K. Shiemke, *J. Am. Chem. Soc.*, 1981, **103**, 4073–4081.

150 P. C. Maria and J. F. Gal, *J. Phys. Chem.*, 1985, **89**, 1296–1304.

151 C. Reichardt, *Angew. Chemie Int. Ed. English*, 1979, **18**, 98–110.

152 M. J. Kamlet, J. L. Abboud and R. W. Taft, *J. Am. Chem. Soc.*, 1977, **99**, 6027–6038.

153 R. Seeber and P. Zanello, *J. Chem. Soc. Dalt. Trans.*, 1985, 601–603.

154 R. Seeber, P. Piu, P. Piraino and P. Zanello, *Inorganica Chim. Acta*, 1989, **155**, 27–30.

155 J. J. Ziółkowski, M. Moszner and T. Glowiak, *J. Chem. Soc. Chem. Commun.*, 1977, 760–761.

156 T. Kawamura, M. Maeda, M. Miyamoto, H. Usami, K. Imaeda and M. Ebihara, *J. Am. Chem. Soc.*, 1998, **120**, 8136–8142.

157 R. D. Cannon, D. B. Powell, K. Sarawek and J. S. Stillman (née Lund), *J. Chem. Soc., Chem. Commun.*, 1976, 31–32.

158 F. A. Cotton, E. V. Dikarev and M. A. Petrukhina, *Angew. Chemie - Int. Ed.*, 2001, **40**, 1521–1523.

159 H. Miyasaka, C. S. Campos-Fernández, R. Clérac and K. R. Dunbar, *Angew. Chemie - Int. Ed.*, 2000, **39**, 3831–3835.

160 F. P. Pruchnik, A. Jutarska, Z. Ciunik and M. Pruchnik, *Inorganica Chim. Acta*, 2003, **350**, 609–616.

161 T. Yoshimura, K. Umakoshi and Y. Sasaki, *Inorg. Chem.*, 2003, **42**, 7106–7115.

Chapter 3

Catalysis: Hydroformylation of 1-octene

3.1 Introduction

Homogeneously catalysed reactions are known to display good catalytic activity and selectivity, despite being confounded by complications related to catalyst recovery and recycling. The use of bimetallic complexes in homogeneously catalysed reactions such as hydroformylation reaction has gained momentum.[137] This reaction involves the conversion of an olefin to an aldehyde in the presence of hydrogen and carbon monoxide and a metal catalyst (Scheme 3.27).[12,32,162–164] The aldehyde that is generated from the atom-economical hydroformylation reaction is frequently processed into valuable consumer products in the cosmetics, bulk and fine chemicals industries.[35,165,166]

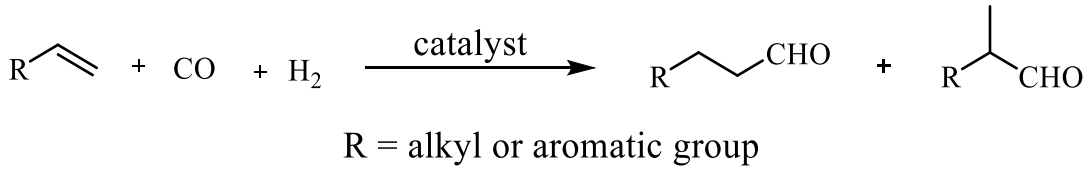

Scheme 3.27 Hydroformylation of olefins.

A major disadvantage of this process is characterised with competing side reactions, involving the isomerisation of the olefin as well as hydrogenation of the aldehydes which gives rise to alcohols.[10,78,167–170] Furthermore, selectivity (chemo- and regioselectivity) of a catalyst is one of the main factors that are considered in catalyst development and evaluation. A typical industrial hydroformylation catalyst possesses excellent chemoselectivity towards aldehydes, as well as excellent regioselectivity towards either linear or branched aldehydes, depending on the desired product.[166,171–173] Linear aldehydes are mostly utilised in the bulk and fine chemical industries where as the branched aldehydes have found use in the agrochemicals and pharmaceutical industries. Current industrial hydroformylation catalysts are based on cobalt [$Co_2(CO)_8$] and rhodium [$HRh(CO)(PPh_3)_3$] metal complexes. Rhodium-based metal complexes are generally preferred over other transition metals (Co, Ru and Ir) as hydroformylation catalysts due to their high activity and selectivity under milder reaction conditions.[32,174]

Naturally occurring metalloenzymes bearing two or more metals as active sites, for example, iron-sulfur proteins (ferredoxins) that catalyse biological redox processes, have the effect of improving the catalytic activity *via* cooperative interactions between the metals.[170,175] A typical example may involve one metal acting as the main catalytic centre whereas the other metal serves as an electron reservoir, stabilising the electron density around the catalytic centre. This has sparked interest in developing rhodium-based bimetallic complexes for hydroformylation in the hope that similar cooperativity may result in improved catalytic activity. From this, we were prompted to evaluate the effect of homobimetallic complexes in the hydroformylation reaction.[134,176]

In our laboratory, bimetallic rhodium complexes have been investigated and were shown to be catalytically active in the hydroformylation of 1-octene.[134,177] de Doncker *et. al.* demonstrated that homoleptic diphenylformamidine-based dirhodium(II) complexes are catalytically active in the hydroformylation of 1-octene. The use of the diphenylformamidine ligands engenders steric bulkiness around the metal centres.[134] Furthermore, Govender *et. al.* reported good catalytic activity in the hydroformylation of 1-octene using mixed valent bimetallic Rh(I,III) complexes.[177] As a result, the aforementioned studies have motivated us to design related Rh(I) bimetallic complexes of the type $[Rh(COD)(R\text{-}dpf)]_2$ bearing diphenylformamidinate ligands bridging the two Rh metals and 1,5-cyclooctadiene ligands chelated on each Rh metal. This should reduce steric bulkiness around the Rh metal whilst maintaining the active Rh(I) oxidation state to further improve on the results reported.

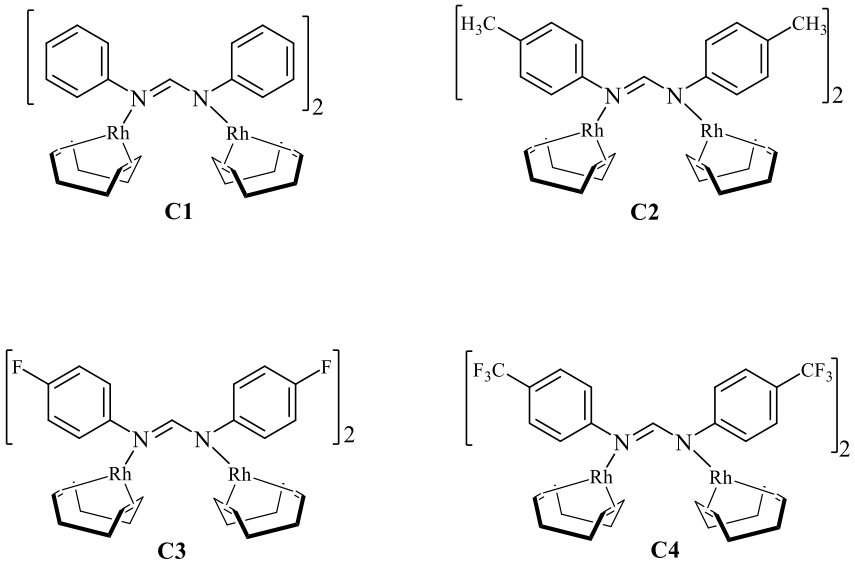

Figure 3.44 Bimetallic Rh(I) complexes **C1** – **C4** used in the hydroformylation of 1-octene.

The diphenylformamidine ligands bridging the two Rh(I) metal centres on complexes **C1** – **C4** (Figure 3.44) impart on the effect of a reduced steric bulkiness, so their evaluation as catalysts in the hydroformylation of 1-octene should have the potential to improve activity and chemoselectivity towards aldehydes.

3.2 Catalytic Evaluation of Bimetallic Rh(I) Complexes in the Hydroformylation of 1-octene

*3.2.1 Preliminary screening using precatalyst **C1***

A clean and dry 90 mL stainless steel pipe reactor that was equipped with a Teflon-coated magnetic stirrer bar. The reactor was loaded with 1-octene (2.25 mL) as a substrate, *n*-decane as an internal standard (204 mg, 1.43 mmol) and each of the bimetallic complexes **C1** – **C4** (2.87×10^{-3} mmol) in 5.00 mL toluene. The reactor was sealed, degassed with nitrogen three times, and pressurized with syngas (1:1, $CO:H_2$) at a desired pressure of 30 – 50 bar. The contents inside the reactor were heated to 55, 65, 75, 85 or 95 ^{o}C as chosen and stirred for 4 h. After which, the reaction mixture was cooled to room temperature, filtered and samples were collected and analysed by GC. The products were confirmed with respect to authentic *iso*-octenes (2- and 3-octene) and aldehydes (linear and branched).

The initial catalytic studies towards the optimum reaction conditions in the hydroformylation of 1-octene were performed with the unsubstituted bimetallic Rh(I) complex **C1** as the representative catalyst precursor (Figure 3.1). The effects of temperature (55 – 95 ^{o}C) and pressure (30 – 50 bar) were evaluated in the hydroformylation of 1-octene over 4 h as shown in Table 3.9.

Table 3.9 Activity evaluation and optimization of reaction conditions with **C1**.

Entry	Temperature (ºC)	Pressure (bar)	Conversion (%)	Aldehydes (%)	*Iso*-octenes (%)	TOF (h^{-1})	*n;iso*
1	55	30	9	71	29	38	1.7
2	65	30	29	75	25	123	2.0
3	75	30	41	70	30	179	2.2
4	85	30	97	67	33	407	1.8
5	95	30	99	58	42	337	1.9
6	55	40	13	78	22	66	1.7
7	65	40	20	80	20	91	2.2
8	75	40	55	75	25	251	2.0
9	85	40	98	79	21	500	1.7
10	95	40	99	76	24	466	1.5
11	55	50	11	82	18	54	1.5
12	65	50	25	85	15	121	1.7
13	75	50	54	79	21	268	1.9
14	85	50	95	84	16	451	1.7
15	95	50	99	79	21	472	1.5

The reactor was loaded with toluene (5 mL), substrate (0.574 mmol) and Rh–metal loading 2.87×10^{-3} mmol. The reactor was purged with nitrogen, followed by purging three times with syngas. The data was analysed using GC-FID. Conversion is referred to as olefins (includes iso-olefins) to aldehydes exclusively. Reactions were conducted for 4 hours.

3.2.1.1 Pressure Variation

An increase in pressure at constant temperature has no significant effect on the conversion of 1-octene, for example, as observed with entries 4, 9 and 14 at 85 ºC and syngas pressure of 30, 40 and 50 bar, respectively. On the other hand, a gradual increase in conversion is observed when temperature is increased at constant pressure, with near-quantitative conversion of 1-octene (99%) obtained at 95 ºC and 30 bar syngas pressure (entry 5). However, a decrease in chemoselectivity for aldehydes is observed when temperature is increased at constant pressure, from 71% aldehydes at 55 ºC / 30 bar to 58% aldehydes at 95 ºC / 30 bar. This is ascribed to the preferential temperature-promoted isomerisation of the substrate at high temperatures, leading to a build-up of iso-octenes in the system, from 29% (entry 1) to 42% (entry 5). This

process is complimentary to the formation of iso-octenes *via* the metal-hydride addition-elimination mechanism of the generally accepted Rh(I)-mediated hydroformylation catalytic cycle.[178,179]

3.2.1.2 Temperature Variation

A steady increase in the catalytic activity of **C1** is observed when temperature is increased at constant pressure, for example, from 53 h^{-1} (55 ^{o}C / 30 bar) to 602 h^{-1} (85 ^{o}C / 30 bar). It is worth mentioning that catalytic activity decreased when temperature was increased from 85 ^{o}C to 95 ^{o}C at constant pressure, attributed to the susceptibility of the olefin to isomerisation at high temperatures. This leads to a decrease in the quantity of aldehydes and consequently the TOF calculated based on ((mmol of aldehydes per mmol of Rh)/time). However, this decrease in activity was not observed at the highest temperature and pressure (95 ^{o}C / 50 bar) owing to the increased syngas pressure that has the effect of subduing the temperature-promoted isomerisation, effectively leading to the hydroformylation of the iso-octenes to aldehydes. Overall, moderate *n;iso* ratios were obtained throughout the optimisation study, with the best ratios obtained at the expense of conversion (entries 3 and 7). From this optimisation data, the best conditions were established at 85 ^{o}C and 40 bar syngas pressure, based on the good chemoselectivity for aldehydes (79%), near-quantitative conversion of the substrate (98%) and the high activity (500 h^{-1}). However milder conditions of 85 ^{o}C and 30 bar syngas pressure were chosen based on the closely similar results (entry 4 vs entry 9).

3.3 Ligand Substituent Effects, Mercury Poisoning and Product Distribution

3.3.1 Para-substitution electronic effects

The influence of the electron-donating (**C2**) and electron-withdrawing (**C3** and **C4**) substituents at the *para*-position was investigated at 85 ^{o}C and 30 bar syngas pressure (Table 3.10). A closer look at the results shows that the chemoselectivity for aldehydes interestingly increases in the order **C3 < C1** < **C2** < **C4** (entries 5, 1, 3 and 7 respectively). Similarly, the activity of the catalyst precursors increases in that order, with the precatalyst bearing the most electron-withdrawing substituent (**C4**) posting the best activity of 541 h^{-1}. Such activity can be ascribed to the inductively electron-withdrawing CF_3-group favouring the dissociation of the CO ligand and in turn facilitating stronger olefin coordination.[180] Moreover, this observation can be rationalised by the larger oxidation potential of **C4** (0.78 V vs Ag/AgCl) as discussed in section 2.8.1 of Chapter 2. In this case, the formed aldehydes easily dissociate from the

electron deficient Rh centres in order to stabilise this reduction in the charge density. Interestingly, **C3** has the lowest conversion (72%, entry 5) and activity (246 h^{-1}), ascribed to the competing mesomeric and inductive effects of the fluoride substituent on the metal centres. In essence, the trifluoromethyl group in **C4** is more electron-withdrawing, and hence a high potential is required to access the higher oxidation states. Due to this, the displacement of the formed products is facilitated by the poor interaction with the electron-deficient Rh centre. However, in **C3**, the inductive effect of the fluoride substituent begins to dominate in order to stabilise the deficiency in charge experienced by the Rh centres at higher oxidation states. In this case, the products have better interaction with the Rh centre and remain coordinated, impeding further coordination of the substrate.

Table 3.10 Aryl substituent effect and mercury-drop poisoning.

Entry	Complex	Conversion (%)	Aldehydes (%)	Iso-octenes (%)	Linear (%)	Branched (%)	TOF (h^{-1})	*n:iso*
1	**C1**	97	67	33	64	36	407	1.8
2	**C1+Hg**	91	58	42	69	31	331	2.2
3	**C2**	99	74	26	59	41	448	1.5
4	**C2+Hg**	93	62	38	66	34	342	2.0
5	**C3**	72	54	46	68	32	246	2.2
6	**C3+Hg**	18	55	45	72	28	63	2.6
7	**C4**	>99	91	9	50	50	541	1.0
8	**C4+Hg**	34	56	44	63	37	116	2.1

The reactor was loaded with toluene (5 mL), substrate (0.574 mmol) and Rh–metal loading 2.87×10^{-3} mmol. The reactor was purged with nitrogen, followed by purging three times with syngas. The data was analysed using GC-FID. Conversion is referred to as olefins (includes iso-olefins) to aldehydes exclusively. Reactions were conducted for 4 hours at 85 ºC and 30 bar CO: H_2. Note for entries 2, 4, 6 and 8, mercury drops were added.

3.3.2 Mercury drop test

The addition of mercury in the catalytic reactor creates an inactive amalgam between the mercury and the nanoparticles. A slight decrease in conversion is observed upon addition of a drop of mercury when **C1** and **C2** are used as catalyst precursors (entries 2 and 4), indicative

of the good stability of the complexes (Table 3.10). However, the conversion and activity show a drastic decline for catalyst precursors **C3** and **C4** (entries 6 and 8), suggesting that the catalytic performance of these two catalyst precursors is mediated by both homogeneous and heterogeneous particles.

3.3.3 Product distribution

Given the rather unique catalytic behaviour of **C3** and **C4** in the presence of mercury when compared to **C1** and **C2**, we were interested in probing further the substrate and product-distribution profiles of **C4** as a function of time in the hydroformylation experiments (Figure 3.45). The profile shows that the quantity of 1-octene present in the system reaches near-depletion at 2 h of reaction time.

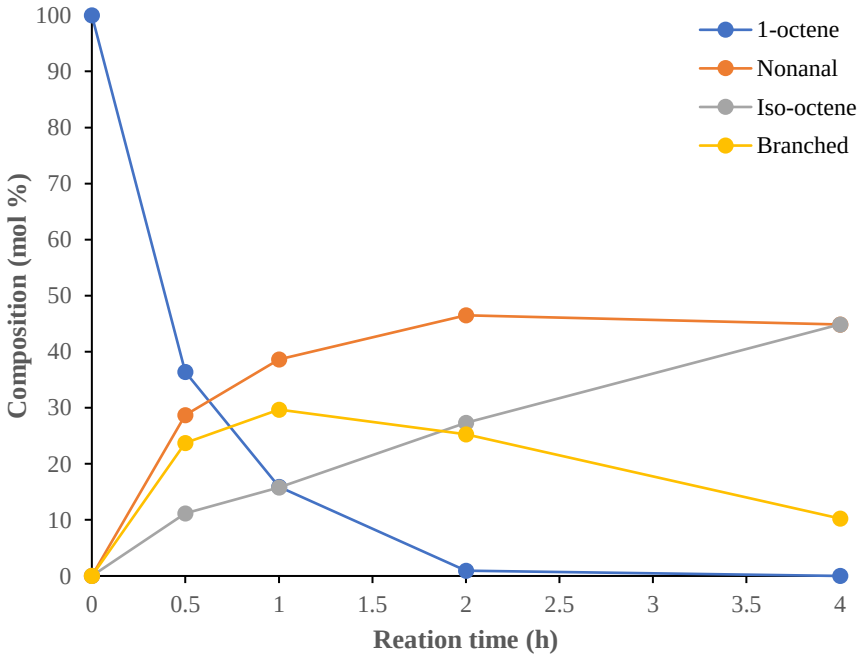

Figure 3.45 Percentage composition over 4 h using precatalyst **C4**, reaction performed at 85 ^{o}C and 30 bar.

Within the first 2 h, a gradual build-up of the linear aldehyde nonanal is observed, reaching a plateau at ca. 50 mol % in the system. Branched aldehydes are observed to increase in the system with time and this is ascribed to a combination of direct formation *via* the Markovnikov addition of the olefin during the catalytic cycle, and the hydroformylation of the isomeric products that are formed in the system. The latter is corroborated by the observed decrease of the isomers in the system from 1 h of reaction time, indicative of their conversion to branched aldehydes that are accumulating even well after 1-octene has been depleted in the system. At

this stage there exists no competition for the catalytic active sites between the depleted 1-octene and the *iso*-octenes present in the system.

Overall, the substrate and product-distribution profile studies with **C4** show that conversion of the iso-octenes to aldehydes accounts for the increase in branched aldehydes in the system post-substrate depletion after 2 h of the hydroformylation reaction. This sheds light towards possibly designing analogous catalyst precursors that could be fine-tuned towards good regioselectivity in the hydroformylation of olefins.

3.4 Summary

A series of dinuclear rhodium(I) complexes [Rh(COD)(R-dpf)]$_2$ (**C1** – **C4**) synthesised were found to be active as precatalysts in the hydroformylation of 1-octene. Conversion is similar between **C1** and **C2**, but lower with **C3** and higher with **C4**. The trifluoromethyl substituent is more selective towards total aldehydes with outstanding turn-over frequencies, hence more active of the series. Time studies with **C4** shows that isomerization of 1-octene is favoured as the reaction time is increased and the precatalyst is chemo-selective towards aldehydes, by converting the octene isomers to their respective aldehydes.

3.5 References

10 R. E. Harmon, S. K. Gupta and D. J. Brown, *Chem. Rev.*, 1973, **73**, 21–52.

12 B. Cornils, W. A. Herrmann and M. Rasch, *Angew. Chemie Int. Ed.*, 1994, **33**, 2144–2163.

32 G. D. Frey, *J. Organomet. Chem.*, 2014, **754**, 5–7.

35 G. T. Whiteker and C. J. Cobley, in *Organometallics as Catalysts in the Fine Chemical Industry*, 2012, vol. 42, pp. 35–46.

78 D. Singh, M. E. Rezac and P. H. Pfromm, *J. Am. Oil Chem. Soc.*, 2009, **86**, 93–101.

134 S. De Doncker, A. Casimiro, I. A. Kotze, S. Ngubane and G. S. Smith, *Inorg. Chem.*, 2020, **59**, 12928–12940.

137 N. N. Omosun, S. Ngubane and G. S. Smith, *Appl. Catal. A Gen.*, 2021, **610**, 117950.

162 A. E. C. Collis and I. T. Horvath, *Catal. Sci. Technol.*, 2011, **1**, 912–919.

163 D. J. Cole-Hamilton, *Scienc*, 2003, **299**, 1702–2706.

164 C. De Rumpa and S. Sumanta, *Res. Chem. Intermed.*, 2013, **39**, 3463–3474.

165 B. Cornils, *Org. Process Res. Dev.*, 1998, **2**, 121–127.

166 B. Cornils and E. G. Kuntz, *J. Organomet. Chem.*, 1995, **502**, 177–186.

167 M. E. Vol'pin and I. S. Kolomnikov, *Russ. Chem. Rev.*, 1969, **38**, 273–289.

168 K. A. Kumar, K. S. Shruthi, N. Naik and D. C. Gowda, *E-Journal Chem.*, 2008, **5**, 914–917.

169 C. Zhu, N. Yukimura and M. Yamane, *Organometallics*, 2010, **29**, 2098–2103.

170 D. G. H. Hetterscheid, S. H. Chikkali, B. deBruin and J. N. H. Reek, *ChemCatChem*, 2013, **5**, 2785–2793.

171 B. Cornils, in *Modern Solvent Systems in Industrial Homogeneous Ctalysis*, 1999, vol. 206, pp. 133–152.

172 B. Cornils, *J. Mol. Catal. A Chem.*, 1999, **143**, 1–10.

173 H. U. Blaser, A. Indolese and A. Schnyder, *Curr. Sci.*, 2000, **78**, 1336–1344.

174 R. Franke, D. Selent and A. Börner, *Chem. Rev.*, 2012, **112**, 5675–5732.

175 J. Przybyla-Toscano, L. Christ, O. Keech and N. Rouhier, *J. Exp. Bot.*, 2021, **72**, 2014–2044.

176 R. Gómez Arrayás, J. Adrio and J. C. Carretero, *Angew. Chemie Int. Ed.*, 2006, **45**, 7674–7715.

177 P. Govender, S. Ngubane, B. Therrien and G. S. Smith, *J. Organomet. Chem.*, 2017, **848**, 281–287.

178 C. P. Lenges and M. Brookhart, *Angew. Chemie Int. Ed.*, 1999, **38**, 3533–3537.

179 M. Vilches-Herrera, L. Domke and A. Börner, *ACS Catal.*, 2014, **4**, 1706–1724.

180 Y. Jiao, M. S. Torne, J. Gracia, J. W. Niemantsverdriet and P. W. N. M. Van Leeuwen, *Catal. Sci. Technol.*, 2017, **7**, 1404–1414.

Chapter 4

Catalysis: Allylic Oxidation of Cyclohexene

4.1 Introduction

The functionalisation of C–H bonds to oxidised products is an important transformation in organic chemistry towards the preparation of naturally occurring compounds.[181] These products have major applications in industries such as pharmaceuticals, cosmetics, plant and fine-chemicals.[35,166,171,173] One drawback is the high activation energy required to break the C–H bond.[40,181] As a result, harsh reaction conditions are usually employed to provide the system with enough energy to overcome the energy barrier.[182] As of recent times, the use of transition-metal catalysts has increased exponentially. This is due to the high reactivity of the transition-metal compounds, and they provide more energy at shorter reaction times, in this way desired products are obtained faster.

One example of a homogeneous process is the allylic oxidation of alkenes where an alkene functional group is converted to enones and enediones by functionalising the α-(C–H) bond adjacent to the C=C alkene bond (Scheme 4.28).[183] For example, the 1,4-enedione is found in a variety of bioactive natural products and is useful as a starting material in organic synthetic pharmaceutical drugs.[2,184,185] Due to the proximity of the alkene double bond to the C–H bond, the C–H bond is activated with a lower bond dissociation energy due to the possible resonance with the C=C double bond to stabilise the transition state.[40,182] As a result, allylic hydrogens are more susceptible to radical abstractions than proton abstractions, provided that no basic reagent is involved in the reaction.

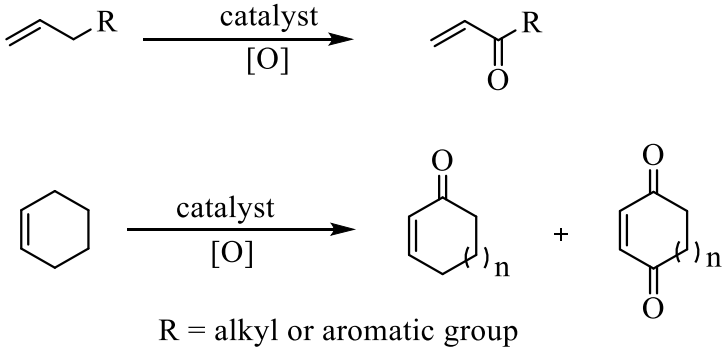

Scheme 4.28 Allylic oxidation of alkenes.

The products obtained from allylic oxidation have wide applications ranging from intermediates for the total synthesis of natural products, anticancer reagents, and flavouring constituents.[186–188] Strategies that have been adopted in the past lack regio- and stereoselectivity, and usually have overoxidation issues. Moreover, the assisting reagents were mainly based on Se or Cr oxides in stochiometric amounts, which gives rise to side products including oxides, enoles and diols.[45,189] Eco-friendly alternative methods based on the chemistry of Cu, Pd, and Rh have been reported with catalytic amounts of complexes.[45] The key is in the ability of the catalyst to undergo a 1-electron oxidation, in order to facilitate the radical reaction.[43,44] Ketones obtained by this method can be used as a valuable raw material for plant protection products or in pharmaceutical industry. Improvement of selectivity and efficiency of the reaction is carried out by developing new and more efficient catalytic systems.

Dirhodium(II) complexes such as the Du Bois catalyst,[190] the benzenedipropionic acid based $Rh_2(esp)_4$[191] and the caprolactamate complex $Rh_2(cap)_4$ [191] have been utilised as catalysts in the conversion of sulfide to sulfoxide and allylic products.[105,192,193] Furthermore, the use of $Rh_2(cap)_4$ as a catalyst could rapidly convert most olefins to their corresponding enones and diones in 1 h with 0.1 mol% catalyst loading.[103] Owing to their orbital arrangement of the dimetal core (Shown in Figure 1.5 of Chapter 1), these complexes are easily reduced and oxidised. The redox potentials are largely influenced by the electronics of the equatorially coordinated ligands. Enhancing the electron density around the Rh_2^{4+} core could provide easier access to the higher oxidation states of the metal centre involved in the catalytic mechanism. This can overcome the harsh reaction conditions linked with the promotion of products from this reaction.

The examples mentioned above have utilised bulky, bidentate ligands with both oxygen and nitrogen donor atoms simultaneously. Further to this, the ligands lack any conjugated π-electron system and accounts for their catalytic activity. These studies have motivated us to design dirhodium(II) complexes bearing diphenylformamidinate ligands with an elongated π-electron system. Precisely, homoleptic dirhodium(II) complexes of the type $[Rh_2(R\text{-}dpf)_4]$ are expected to allow for easier oxidation at the Rh metal centres due to the electron rich environments. Heteroleptic mixed ligand complexes of the type $[Rh_2(R\text{-}dpf)_x(OAc)_{4-x}]$ with x = 2 or 3 are expected to have less steric bulk due to the presence of the acetate ligands. This

chapter discusses the catalytic activity of these complexes in the allylic oxidation of cyclohexene.

4.2 Reported Mechanism of Dirhodium(II) Complexes in Allylic Oxidation

Based on reported mechanisms from literature,[102,103,194] we can postulate the mechanism for the allylic oxidation of cyclohexene using the homoleptic dirhodium(II) complex [$Rh_2(dpf)_4$] (Scheme 4.29). The reaction is initiated by the radical reaction between the oxidant TBHP and the complex, where an electron is abstracted from the HOMO π* orbitals, increasing its reactivity to form the hydroxy species labelled **2**. Another TBHP binds to the vacant axial site, followed by an H-migration to form H_2O which dissociates from the axial site forming the *tert*-butyl peroxide complex **3**. Simultaneously, the tert-butoxide radical reacts with another TBHP to generate the more basic *tert*-butyl peroxide intermediate **1**. The intermediate abstracts the α-proton from the cyclohexene substrate to generate the reactive cyclohexene radical **4**, which in turn binds to the reactive complex **3**. The subsequent reductive elimination of the *tert*-butyl peroxide from intermediate complex **3** regenerates the catalyst and cyclohexene *tert*-butyl peroxide **5**. This is then converted to the desired enone product by a reductive quenching to terminate the reaction, releasing *tert*-butanol.

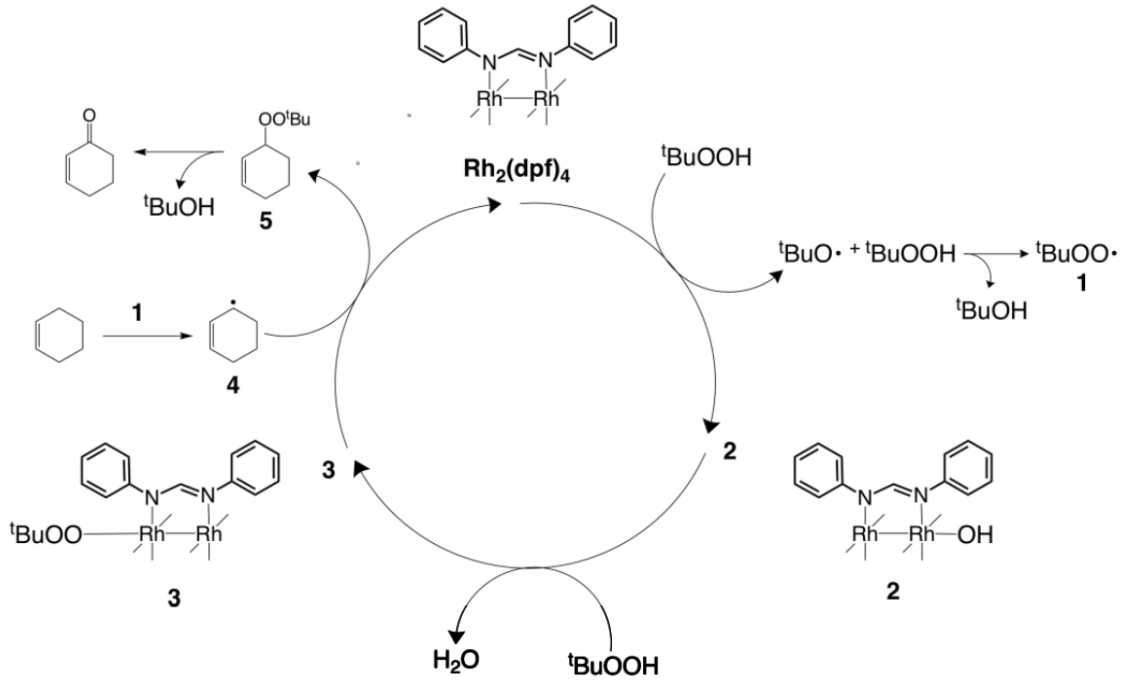

Scheme 4.29 Possible mechanism for the formation of cyclohexen-2-one using.

4.3 Solvent Variation with Dirhodium(II) Complexes in the Allylic Oxidation of Cyclohexene

4.3.1 Catalytic performance in DCM

The homoleptic diphenylformamidinate complexes (**C5** – **C7**) as well as the acetate containing mixed ligand heteroleptic complexes (**C8** – **C11**) were evaluated for their catalytic activity in the allylic oxidation of cyclohexene (Figure 4.46). The expectation is that combination of the formamidine ligands and the acetate ligands will favour the higher oxidation state Rh_2^{5+} of the core, which is the key intermediate involved in this reaction and should allow for easier formation of less bulky products.

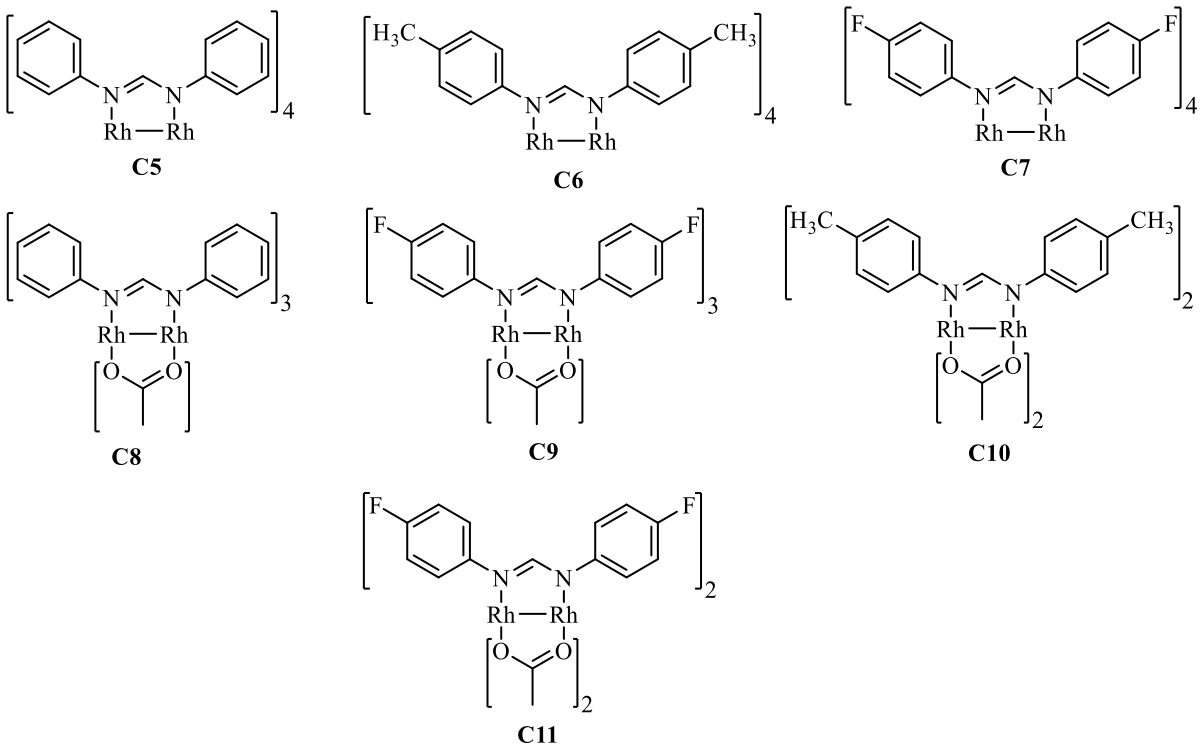

Figure 4.46 Dirhodium(II) complexes **C5** – **C11** used in the allylic oxidation of cyclohexene.

The reaction conditions were chosen based on previously reported procedures in literature, with slight modifications.[46,83,195] It has also been reported that T-Hydro (70% TBHP in water) is the more active oxidant over TBHP in *n*-decane,[31-32] For this reason, T-Hydro was chosen as the oxidant. Furthermore, it has been found that there is significant improvement in catalytic activity when the reactions are performed at the boiling point of the solvent. Due to this, we have chosen to run the reactions at the boiling point temperatures. The solvents of choice are DCM, THF and ACN due to their polarity, weakly coordinating and strongly coordinating

effects, respectively, at the axial sites of the dirhodium(II) complexes as well as their ability to stabilise the higher oxidation states, and Table 4.11 shows catalytic results in DCM.

Table 4.11 Activity evaluation in the allylic oxidation of cyclohexene in DCM[a]

Entry	Catalyst	Conversion (%)	Selectivity (%)			TON[b]
						
1	**C5**	58	77	14	9	138
2	**C6**	63	82	11	7	154
3	**C7**	80	84	9	7	194
4	**C8**	83	85	8	7	203
5	**C9**	91	86	8	6	228
6	**C10**	88	86	7	7	226
7	**C11**	92	86	8	6	229
			Parameter variation			
8[c]	**C7**	97	87	12	1	46
9[d]	**C7**	72	73	25	2	175
10[e]	**C7**	92	82	16	1	241
11[c]	**C9**	96	81	17	2	45
12[d]	**C9**	92	75	21	4	231
13[e]	**C9**	93	81	17	2	233
14[c]	**C11**	95	83	14	3	44
15[d]	**C11**	92	74	23	3	230
16[e]	**C11**	93	80	18	2	231

[a]Reaction conditions: T-Hydro (470 mg, 3.65 mmol) was added to a solution of cyclohexene (100 mg, 1.22 mmol), catalyst (0.1 mol %) and 10.0 mL of DCM. The reaction was stirred for 24 h at 40 ^{o}C. The products were identified and quantified using GC-FID. Values provided in the table are from three experiments, and the yields are averaged (+/- 1-4%). [b]Turnover number is calculated from the amount of cyclohexene reacted per amount of catalyst.[c]Reaction was performed with 0.5 mol% catalyst loading. [d]Reaction was performed with (784 mg, 6.09 mmol) of T-Hydro. [e]Reaction was stirred for 48 h.

In DCM, **C5** and **C6** are found to have the least conversion (58%, **C5**) and (63%, **C6**). In comparison to their acetate counterpart, there is significant increase in conversion upon the increase of the acetato ligands coordinated (**C5** vs **C8**) and (**C6** vs **C10**). This can be related to the relatively lower potential for the first oxidation $Rh_2^{4+/5+}$ compared to the homoleptic complexes and less steric hindrance by the dpf ligands related to the nature of the mixed

ligands. In comparison with the homoleptic complexes, the addition of the acetato ligands hinders the backdonation from the metal centres to the acetato ligand due to less σ* orbital of the dimetal core, which is destabilised and brings about easier oxidation. In this case, more of the active species of Rh_2^{5+} is generated.[103] The same trend is observed for **C7**, **C9** and **C11**. In all complexes, the reaction is chemoselective towards the 2-cyclohexen-1-one product. In the case of **C5**, the generation of O_2 which is needed to react with the radical of the substrate is much slower, hence less 2-cyclohexen-1-one is formed. In comparison with **C8**, the dimetal core of the reactive species is less electron deficient than in **C5** due to the presence of the acetato ligand. Since there is conjugation between the p-orbitals of the alkene (C=C) and carbonyl (C=O) functionalities of the 2-cyclohexen-1-one product, it therefore follows that the alkene functional group is more electron deficient. The interaction between this orbital and the Rh_2^{5+} core of **C8** is less favoured. This will propagate the dissociation of the product much faster than in **C5** where the interaction is more stable. The formation of 2-cyclohexen-1-ol is favoured by the reduction event that is present in **C5** – **C7**. The formation of *cis*-1,2-cyclohexanediol could not be propagated by these complexes.

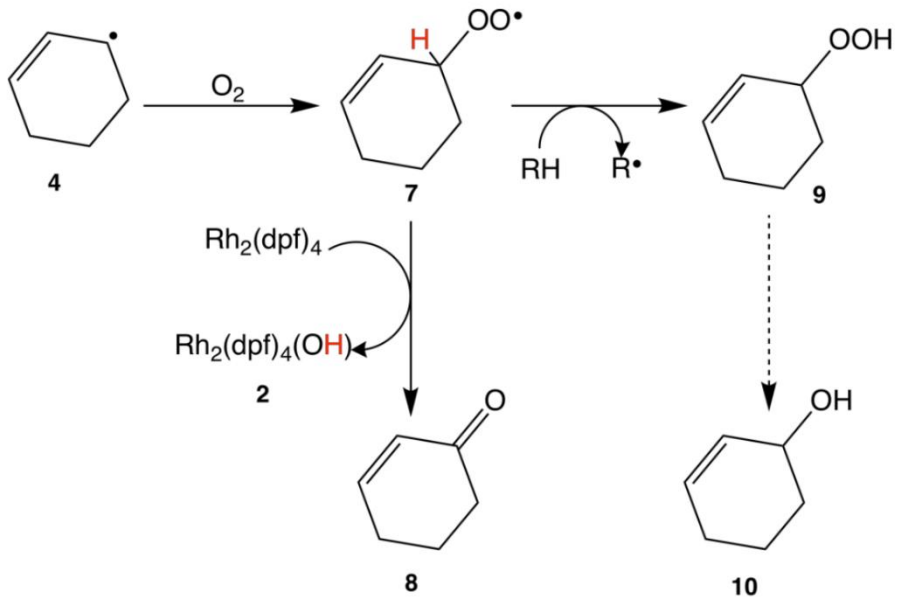

Scheme 4.30 Propagation of cyclohexene radical leading to the enone (**8**) and enol (**10**).

The initially formed allylic radical **4** reported earlier in Scheme 4.2 can react with the highly reactive *tert*-butyl peroxide complex **3** (also in Scheme 4.2),[198] while also undergoing a side reaction by trapping the dioxygen formed as by product during the formation of di-*tert*-butyl peroxide **9** (Scheme 4.30). This peroxide intermediate **9** is then reduced to form the enol product **10**. On the other hand, the intermediate **7** undergoes a Russel's chain termination mechanism which gives the enone product **8**.[199] The formation of the ketone should be favoured

over the alcohol in the presence of the catalyst which traps the intermediate **7**. The cleavage of the O–O bond and a hydrogen transfer should lead to the formation of the oxidised catalyst **2** and ketone **8**.

4.3.2 Reaction parameter variations

The catalyst loading was increased from 0.1 mol% to 0.5 mol% (Table 4.11, entries 8, 11, and 14). As a result, the conversion of cyclohexene **C7** (entry 8), **C9** (entry 11) and **C11** (entry 14) was observed to increase. This was expected because increasing the catalyst loading increases the number of Rh metal centre sites available to interact with the substrate. As such, more cyclohexene undergoes radical abstraction to produce the active radical species. Surprisingly, at this high catalyst loading, the complexes become inactive much faster as attested to by the decrease in the TON (< 46, entries 8, 11 and 14). For **C7**, the amount of 2-cyclohexen-1-one in the system is slightly higher compared to the 84% found when using 0.1 mol% catalyst loading (Table 4.1, Entry 3), while also increasing the amount of 2-cyclohexen-1-ol. This can be related to the rate of formation of the reactive *tert*-butyl peroxyether complex which leads to more 2-cyclohexen-1-one, that is forming faster. In comparison, the amount of 2-cyclohexen-1-ol in the system increases for **C9** (Entry 11) and **C11** (Entry 14) as the increase in the peroxide radical is compensated by the peroxide intermediate and easier reduction facilitated by the acetato ligands.

The increase in the amount of TBHP added to the system (from 3 eq. to 5 eq.) leads to a decrease in the conversion with **C7**, from 80% to 72% (Entry 9) with no significant change with **C9** and **C11**. Furthermore, there is also an increase of 2-cyclohexen-1-ol in the system. The excess TBHP reacts with the unused catalyst in the reaction mixture. This increase the concentration of the active Rh_2^{5+} species in the reaction, which in turn increases the formation of the hydrogen peroxide intermediate which is reduced to the enol product.

Doubling the time increases the conversion of the substrate, with the greatest difference observed for **C7** (Entry 10, 92 vs 80%). The increase in the time allows for more collisions between the cyclohexene and the complexes, which causes the system to absorb enough energy to overcome the reaction barrier. Over longer periods, the less more electron rich complexes (**C9** and **C11**) with three and two acetato ligands, respectively, induce more production of the reactive peroxide species that is easily converted to the hydrogen peroxide intermediate. Due to the electron rich environment, there is favourable reduction of the hydrogen peroxide intermediate to the enol product. Consequently, the formation of the enone is inhibited.

4.3.3 Catalytic performance in THF

Table 4.12 shows the catalytic activity complexes in the allylic oxidation of cyclohexene in THF at 66 ^{o}C. There is slight increase in conversion when using THF with the homoleptic complexes **C5** – **C7**. Evidently, there is no formation of 2-cylohexen-1-ol. This indicates that all the dirhodium *tert*-butyl peroxyether fully converts the cyclohexenyl radical to 2-cyclohexen-1-one at a faster rate, as the reduction process is not favourable in THF, hence lower TON values in THF compared to DCM.

Table 4.12 Activity evaluation in the allylic oxidation of cyclohexene in THF.[a]

Entry	Catalyst	Conversion (%)	Selectivity (%)			TON[b]
						
1	**C5**	63	86	0	14	150
2	**C6**	64	88	0	12	158
3	**C7**	60	98	0	2	147
4	**C8**	61	75	0	25	148
5	**C9**	64	78	0	22	162
6	**C10**	68	76	0	24	176
7	**C11**	62	79	0	28	154

[a]Reaction conditions: T-Hydro (470 mg, 3.65 mmol) was added to a solution of cyclohexene (100 mg, 1.22 mmol), catalyst (0.1 mol %) and 10.0 mL of THF. The reaction was stirred for 24 h at 66 ^{o}C. The products were identified and quantified using GC-FID. Values provided in the table are from three experiments, and the yields are averaged (+/- 1-5%). [b]Turnover number is calculated from the amount of cyclohexene reacted per amount of catalyst.

The electron rich complexes are more active, as the more reactive higher oxidation states are easily stabilised by the electron donating substituents (Entry 2, **C6**) and (Entry 10, **C10**). For the mixed ligand complexes **C8** – **C11**, there is slight decrease in the conversion from DCM to THF. This is explained by the favourable interaction between the oxygen atom of THF and the dimetallic core. As the degree of coordination by the acetato ligand is increased from 0 to 1 and 2, the steric hindrance is reduced. This allows for easy coordination of the THF ligand, which destabilises the HOMO π^* orbitals of the dimetallic core, making the core more susceptible to electron abstraction and increasing the concentration of the active Rh_2^{5+} species.

4.3.4 Catalytic activity in ACN

In ACN (Table 4.13), there is almost complete conversion obtained. The strongly coordinating ACN cause the charge distribution between the two Rh metals of the dirhodium core to be uneven. In this case, the uncoordinated Rh will have increased ability for reduction, so more 2-cylohexen-1-ol is able to form in comparison to THF. The formation of 2-cylohexen-1-ol reduces the amount of 2-cyclohexen-1-one in the system and induces a slow formation of the cyclohexene oxide.

Table 4.13 Activity evaluation in the allylic oxidation of cyclohexene in ACN.[a]

Entry	Catalyst	Conversion (%)	Selectivity (%)			TON[b]
			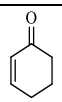	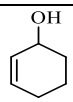		
1	**C5**	98	75	7	18	233
2	**C6**	98	89	8	2	240
3	**C7**	98	90	8	2	239
4	**C8**	98	89	8	2	241
5	**C9**	98	91	7	2	247
6	**C10**	99	91	7	2	241
7	**C11**	99	90	8	2	247

[a]Reaction conditions: T-Hydro (470 mg, 3.65 mmol) was added to a solution of cyclohexene (100 mg, 1.22 mmol), catalyst (0.1 mol %) and 10.0 mL of ACN. The reaction was stirred for 24 h at 82 °C. The products were identified and quantified using GC-FID. Values provided in the table are from three experiments, and the yields are averaged (+/- 1-2%). [b]Turnover number is calculated from the amount of cyclohexene reacted per amount of catalyst.

For the mixed ligand heteroleptic complexes **C8** – **C11**, the reason is more chemoselective to the ketone product. This is explained by the favourable interaction between the nitrogen donor atom of ACN and the dimetallic core. Furthermore, an increase in the degree of coordination by the acetato ligand from 0 to 1 and 2, the steric hindrance is reduced. The rate of coordination of acetonitrile increases and the HOMO π* orbitals of the dimetallic core is destabilised as mentioned in section 1.2.2 of Chapter 1, making the core more susceptible to electron abstraction and increasing the concentration of the active Rh_2^{5+} species at a faster rate. This in turn gives higher TON (>240).

Catino *et. al.* reported that the dirhodium(II) caprolactamate complex $[Rh_2(cap)_4]$ achieves a selectivity of 33 % in DCM with 5 eq. of TBHP with 1 mol% catalyst loading in the allylic

oxidation of 1-acetylcyclohexene.[103] The addition of 50 mol% K_2CO_3 in the reaction improves the reaction to 80%, and decreasing the catalyst loading by 10-fold, 78% selectivity is achieved in 1 h. However, using the same conditions with cyclohexene, moderate selectivity (60%) of 2-cyclohexen-1-one is obtained, while no activity is achieved in THF and ACN.[103] In our case we have managed to design high performing catalysts (**C9** and **C11**) that can achieve selectivity towards 2-cyclohexen-1-one with 86% (and TON of 228 and 229, respectively) in DCM, with less TBHP (3 eq.). This can be rationalised by the lower oxidation potentials ($E_{1/2}$ = -110 and 30 mV vs Ag/AgCl, respectively) over 55 mV for $[Rh_2(cap)_4]$, so the easier oxidation in **C9** and **C11** permits for better reactivity. Given that these two complexes had the highest oxidation potentials among the series of the complexes in the study, we have found that these complexes have better activity compared with $[Rh_2(cap)_4]$.

Our complexes are also catalytically active in THF and ACN, while $[Rh_2(cap)_4]$ is inactive in these solvents. These complexes also outperform the oxygen based dirhodium tetraacetate $[Rh_2(OAc)_4]$ and dirhodium perfluorobutyrate $[Rh_2(pfb)_4]$ complexes, which afford < 33% of the ketone. The reactivity is limited by the difficulty in the first oxidation, with $E_{1/2}$ = 1170 and 1800 mV, respectively.[148,200] It is our belief that there are benefits in reducing the degree of coordination of the bulk dpf ligands with the acetate ligands. However, not all the dpf ligands should be replaces as this provide for me electron density towards the dirhodium core, raising the HOMO π^* orbital in energy. It is our expectation that these complexes would be active in various substituted cyclohexenes, as shown by Catino *et. al.*, but still requires more evaluation.

3.4 Summary

The homoleptic and mixed ligand dirhodium(II) complexes $[Rh_2(R\text{-}dpf)_x(OAc)_{4-x}]$ (**C5** – **C11**, where R is H, CH_3 or F), bearing diphenylformamidinate ligands with x = 2, 3 or 4 synthesised were evaluated and found to be active catalysts in the allylic oxidation of cyclohexene. In DCM, the mixed ligand complexes (**C8** – **C11**) are more active due to more stabilisation of the higher Rh_2^{5+} oxidation state. In THF, there is no formation of 2-cyclohexen-2-ol. With ACN, there is near quantitative conversion, resulting from the strong coordination of acetonitrile that causes uneven charge distribution between the two Rh metals, allowing for easier reduction. The complexes become more active in ACN as the higher oxidation state species are more favoured.

3.5 References

2 P. T. Anastas and J. C. Warner, *Green Chemistry: Theory and Practice*, Oxford University Press, New York, 1998.

31 R. F. Heck and D. S. Breslow, *J. Am. Chem. Soc.*, 1961, **83**, 4023–4027.

32 G. D. Frey, *J. Organomet. Chem.*, 2014, **754**, 5–7.

35 G. T. Whiteker and C. J. Cobley, in *Organometallics as Catalysts in the Fine Chemical Industry*, 2012, vol. 42, pp. 35–46.

40 J. Wencel-Delord, T. Dröge, F. Liu and F. Glorius, *Chem. Soc. Rev.*, 2011, **40**, 4740–4761.

43 J. T. Groves, G. A. McClusky, R. E. White and M. J. Coon, *Biochem. Biophys. Res. Commun.*, 1978, **81**, 154–160.

44 J. T. Groves, T. E. Nemo and R. S. Myers, *J. Am. Chem. Soc.*, 1979, **101**, 1032–1033.

45 K. Srinivasan and S. Perrier, *J. Mol. Catal.*, 1986, **36**, 297–317.

46 A. L. García-Cabeza, R. Marín-Barrios, F. J. Moreno-Dorado, M. J. Ortega, G. M. Massanet and F. M. Guerra, *Org. Lett.*, 2014, **16**, 1598–1601.

83 K. Chen, P. Zhang, Y. Wang and H. Li, *Green Chem.*, 2014, **16**, 2344–2374.

103 A. J. Catino, R. E. Forslund and M. P. Doyle, *J. Am. Chem. Soc.*, 2004, **126**, 13622–13623.

166 B. Cornils and E. G. Kuntz, *J. Organomet. Chem.*, 1995, **502**, 177–186.

171 B. Cornils, in *Modern Solvent Systems in Industrial Homogeneous Ctalysis*, 1999, vol. 206, pp. 133–152.

173 H. U. Blaser, A. Indolese and A. Schnyder, *Curr. Sci.*, 2000, **78**, 1336–1344.

181 M. C. White, *Synlett*, 2012, **23**, 2746–2748.

182 S. J. Blanksby and G. B. Ellison, *Acc. Chem. Res.*, 2003, **36**, 255–263.

183 Q. Zhou, *Angew. Chemie Int. Ed.*, 2016, **55**, 5352–5353.

184 U. S. E. P. Agency, Basics of Green Chemistry, https://www.epa.gov/greenchemistry/basics-green-chemistry#definition, (accessed 11 February 2019).

185 C. Masters, *Homogeneous Transition-metal Catalysis: A Gentle Art*, Chapman and Hall, 19981.

186 E. E. Robinson and R. J. Thomson, *J. Am. Chem. Soc.*, 2018, **140**, 1956–1965.

187 G. Garg, L. K. Forsberg, H. Zhao and B. S. J. Blagg, *Chem. A Eur. J.*, 2017, **23**, 16574–16585.

188 K. Uehara, J. Watanabe, Y. Mogi and Y. Tsukioka, *J. Biosci. Bioeng.*, 2017, **123**, 333–341.

189 K. B. Sharpless and R. F. Lauer, *J. Am. Chem. Soc.*, 1972, **94**, 7154–7155.

190 C. G. Espino, K. W. Fiori, M. Kim and J. Du Bois, *J. Am. Chem. Soc.*, 2004, **126**, 15378–15379.

191 M. P. Doyle, L. J. Westrum, W. N. E. Wolthuis, M. M. See, W. P. Boone, V. Bagheri and M. M. Pearson, *J. Am. Chem. Soc.*, 1993, **115**, 958–964.

192 D. Wang, D. Kuang, F. Zhang, Y. Liu and S. Ning, *Tetrahedron Lett.*, 2014, **55**, 7121–7123.

193 Y. Wang, Y. Wang and Y. Kuang, *Chem. Commun.*, 2015, **51**, 5852–5855.

194 H. Choi and M. P. Doyle, *Org. Lett.*, 2007, **9**, 5349–5352.

195 Y. L. Su, L. De Angelis, L. Tram, Y. Yu and M. P. Doyle, *J. Org. Chem.*, 2020, **85**, 3728–3741.

196 D. Bogdal and M. Lukasiewicz, *Synlett*, 2000, **2000**, 143–145.

197 S. Dworakowska, U. Pisarek, S. Bednarz and D. Bogdał, 11–13.

198 F. A. Chavez and P. K. Mascharak, *Acc. Chem. Res.*, 2000, **33**, 539–545.

Chapter 5

Experimental procedures

5.1 General details

The anhydrous reagents and salts used were purchased from Sigma Aldrich and were used without any further purification. Solvents purchased from Kimix were distilled and stored with drying agents before use. Nuclear magnetic resonance (NMR) spectra were recorded using either a Bruker X-400 (^{1}H at 400 MHz, ^{13}C at 101 MHz and ^{19}F at 337 MHz) or a Varian Mercury 300 (^{1}H at 300 MHz and ^{13}C at 75 MHz) spectrometers at room temperature. The chemical shifts reported were determined using solvent signal as the reference. Coupling constants are reported in Hz and chemical shifts are reported in ppm. Infrared (IR) absorptions were measured using a Perkin-Elmer Spectrum 100 FT-IR spectrometer with KBr pellets. The absorption band frequencies are reported in cm^{-1}. Electron Spray Ionisation Mass Spectrometry (ESI-MS) was carried out on a Waters API Quattro instrument in both the positive and negative modes. Melting points have been determined using a Buchi melting-point B-540 apparatus. Cyclic voltammetry was performed with a three-electrode system using an Epsilon Eclipse voltammetric analyzer. A glassy carbon electrode was used as a working electrode. A Pt wire was used as a counter electrode and an Ag/AgCl solution was used as the reference electrode. The electrode was separated from the bulk of the solution by a fritted glass bridge containing the non-aqueous solvent with TBAP as the supporting electrolyte. The solvent was saturated with N_2 gas prior to taking measurements. Measurements were carried out with a scan rate of 0.1 $V.s^{-1}$ unless otherwise stated. The experiments were performed in degassed CH_2Cl_2, THF or CH_3CN containing 0.1 M TBAP as a supporting electrolyte. $[Rh(COD)Cl]_2$,[120] $[Rh_2(OAc)_4]$,[201] and $[Rh_2(TfOAc)_4]$[201] starting materials were synthesised following previously reported literature procedures.

5.2 General preparation of ligands

The *para*-substituted *N,N*'-diphenylformamidine ligands **L1** – **L4** were prepared following a previously reported literature procedure.[127] Triethyl orthoformate (1.87 mL, 11.3 mmol), *para*-substituted aniline (2.05 mL, 22.5 mmol), with R = H, Me, F or CF_3 and glacial acetic acid (32.17 μL, 0.56 mmol) were added in a dry two neck round bottom flask equipped with a stirrer bar and a condenser. The feint yellow mixture was heated to reflux at 145 – 148 °C for 18 h under a nitrogen atmosphere. The resulting brown reaction mixture was removed from the heat and allowed to cool down to room temperature. The resulting brown crude solid was dissolved in minimum hot dichloromethane and cooled to 0 °C on an ice bath. The contents were removed, quickly filtered by gravity, washed with cold petroleum ether and dried *in vacuo*.

5.2.1 N,N'-diphenylformamidine ligand ***L1***

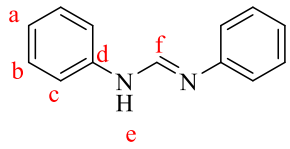

Yield: (1.09 g, 49 %). **Appearance**: thin-white crystals. **M.P.**: 139 – 141 °C. **^{1}H NMR** ($CDCl_3$, δ_{ppm}): 8.20 (s, 1H, H_f), 7.31 (t, $^3J_{H\text{-}H}$ = 7.88 Hz, 4H, H_b), 7.04 – 7.11 (m, 6H, $H_{a,c}$). **^{13}C{^{1}H} NMR** ($CDCl_3$, δ_{ppm}): 149.6 (C_f), 145.3 (C_d), 129.5 (C_b), 123.5 (C_a), 119.2 (C_c). **FT-IR** (KBr, ν_{cm}^{-1}): 3304 (br m, N–H), 2847 (w, C–H), 1581 (m, C=N), 1485 (s, C=C_{Ar}). **ESI-MS** (*m/z*): 197.1082 ($[M + H]^+$, 100 %) (calcd. 197.1079).

5.2.2 N,N'-Di-(4-methyl)phenylformamidine ***L2***

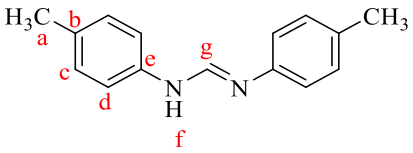

Yield: (1.34 g, 53 %). **Appearance**: pale-white crystals. **M.P.**: 141 – 143 °C. **^{1}H NMR** ($CDCl_3$, δ_{ppm}): 8.18 (s, 1H, H_g), 7.12 (d, $^3J_{H\text{-}H}$ = 8.08 Hz, 4H, H_d), 6.95 (d, $^3J_{H\text{-}H}$ = 8.24 Hz, 4H, H_c), 2.34 (s, 6H, H_a). **^{13}C{^{1}H} NMR** ($CDCl_3$, δ_{ppm}): 149.5 (C_g), 142.9 (C_e), 132.8 (C_b), 130.0 (C_d), 119.1 (C_c), 20.9 (C_a). **FT-IR** (KBr, ν_{cm}^{-1}): 3302 (br m, N–H), 2912 (w, C–H), 2854 (w, C–H), 1668 (m, C=C), 1608 (m, C=N), 1485 (s, C=C_{Ar}), 1312. **ESI-MS** (*m/z*): 225.1387 ($[M + H]^+$, 100 %) (calcd. 225.1392).

*5.2.3 N,N'-Di-(4-fluoro)phenylformamidine **L3***

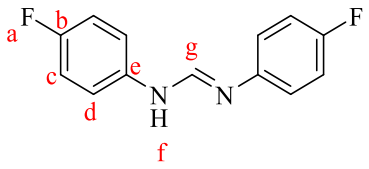

Yield: (1.22 g, 47 %). **Appearance**: white crystals. **M.P.**: 145 – 147 °C. **^{1}H NMR** ($CDCl_3$, δ_{ppm}): 8.05 (s, 1H, H_g), 6.99 (d, $^{3}J_{H\text{-}H}$ = 7.76 Hz, 8H, $H_{c,d}$). **^{13}C{^{1}H} NMR** ($CDCl_3$, δ_{ppm}): 160.8 (C_e), 158.4 (C_b), 150.0 (C_g), 120.8 (d, $^{3}J_{C\text{-}F}$ = 7.40 Hz, C_d), 116.2 (d, $^{2}J_{C\text{-}F}$ = 22.61 Hz, C_c). **^{19}F{^{1}H} NMR** ($CDCl_3$, δ_{ppm}): -120.2 (F_a). **FT-IR** (KBr, ν_{cm}^{-1}): 3174 (br m, N–H), 2852 (w, C–H), 1601 (m, C=N), 1497 (s, C=C_{Ar}). **ESI-MS** (*m/z*): 233.0887 ([M + H]$^{+}$, 100 %) (calcd. 233.0890).

*5.2.4 N,N'-Di-(4-trifluoromethyl)phenylformamidine **L4***

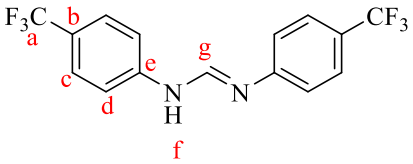

Yield: (1.06 g, 49 %). **Appearance**: white-needle crystals. **M.P.**: 155 – 158 °C. **^{1}H NMR** ($CDCl_3$, δ_{ppm}): 8.19 (s, 1H, H_g), 7.59 (d, $^{3}J_{H\text{-}H}$ = 8.40 Hz, 4H, H_c), 7.15 (d, $^{3}J_{H\text{-}H}$ = 8.25 Hz, 4H, H_d), 5.10 (s, 1H, H_f). **^{13}C{^{1}H} NMR** ($CDCl_3$, δ_{ppm}): 162.1 (C_e), 158.9 (C_b), 147.9 (C_g), 127.0 (d, $^{3}J_{C\text{-}F}$ = 3.52 Hz, C_c), 119.1 (C_d), 114.4 (C_a). **^{19}F{^{1}H} NMR** ($CDCl_3$, δ_{ppm}): -62.0 (F_a). **FT-IR** (KBr, ν_{cm}^{-1}): 3174 (br m, N–H), 2852 (w, C–H), 1608 (m, C=N), 1490 (s, C=C_{Ar}). **ESI-MS** (*m/z*): 333.0927 ([M + H]$^{+}$, 100 %) (calcd. 332.2650).

5.3 Preparation of bimetallic rhodium(I) complexes

The bimetallic Rh(I) complexes were synthesised following a known procedure with minor changes.[123] **L1** – **L4** (2 eq.) of each of the respective ligand and potassium tert-butoxide (171 mg, 1.52 mmol) were added to a clean, dry round bottom flask with a side arm. The flask was purged with nitrogen before anhydrous toluene (10 mL) was added. The contents were stirred vigorously for 2 h. To this solution, $[Rh(COD)Cl]_2$ (250 mg, 0.51 mmol) dimer was added. The resulting orange solution was stirred at room temperature for 24 h. A bright orange precipitate was filtered under vacuum, washed with *n*-hexane and dried *in vacuo*.

5.3.1 N,N'-Diphenylformamidine-(1,5)-cyclooctadiene dimer complex ***C1***

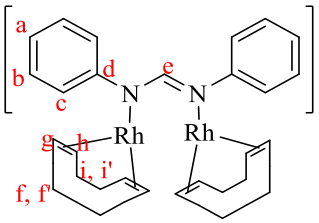

Yield: (412 mg, 61 %). **Appearance**: orange solid. **M.P.**: 216 – 218 ºC. **^{1}H NMR** ($CDCl_3$, δ_{ppm}): 7.30 (t, $^{3}J_{Rh\text{-}H}$ = 2.16 Hz, 2H, H_e), 7.19 – 7.25 (m, 16H, $H_{b,c}$), 6.99 (t, ^{3}J = 8.33 Hz, 4H, H_a), 4.40 (m, 4H, H_h), 3.85 (m, 4H, H_g), 2.92 – 2.95 (m, 4H, $H_{i'}$), 2.53 – 2.58 (m, 4H, $H_{f'}$), 1.92 (q, $^{3}J_{H\text{-}H}$ = 5.56 Hz, 4H, H_i), 1.79 (q, $^{3}J_{H\text{-}H}$ = 5.68 Hz, 4H, H_f). **^{13}C{^{1}H} NMR** ($CDCl_3$, δ_{ppm}): 165.2 (C_e), 152.6 (C_d), 128.4 (C_b), 125.0 (C_c), 122.9 (C_a), 84.2 (C_g), 75.6 (C_h), 31.3 (C_f), 30.9 (C_i). **FT-IR** (KBr, ν_{cm}^{-1}): 2936 (w, C–H), 2878 (w, C–H), 1610 (w, C=C_{COD}), 1550 (m, C=N), 1505 (m, C=C_{Ar}).

5.3.2 N,N'-Di-(p-tolyl)formamidine-(1,5)-cyclooctadiene dimer complex ***C2***

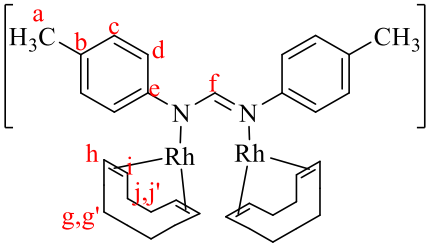

Yield: (441 mg, 51.4 %). **Appearance**: brown solid. **M.P.**: 214 – 216 ºC. **^{1}H NMR** ($CDCl_3$, δ_{ppm}): 7.25 (m, 2H, H_f), 7.00 – 7.18 (m, 16H, $H_{c,d}$), 4.37 (m, 4H, H_i), 3.85 (m, 4H, H_h), 2.91 (m, 4H, $H_{j'}$), 2.54 (m, 4H, $H_{g'}$), 2.30 (s, 12H, H_a), 1.90 (q, $^{3}J_{H\text{-}H}$ = 5.97 Hz, 4H, H_j), 1.78 (q, $^{3}J_{H\text{-}H}$ = 5.94 Hz, 4H, H_g). **^{13}C{^{1}H} NMR** ($CDCl_3$, δ_{ppm}): 164.9 (C_f), 150.1 (C_e), 132.1 (C_b), 128.9 (C_d), 124.9 (C_c), 84.0 (C_h), 75.4 (C_i), 31.3 (C_j), 30.9 (C_g), 20.9 (C_a). **FT-IR** (KBr, ν_{cm}^{-1}): 2912 (w, C–H), 2874 (w, C–H), 1613 (m, C=C_{COD}), 1560 (m, C=N), 1498 (C=C_{Ar}). **ESI-MS** (*m/z*): 868.2279 ($[M + H]^+$, 100 %) (calcd. 868.798).

5.3.3 N,N'-Di-(4-fluoro)phenylformamidine-(1,5)-cyclooctadiene dimer complex ***C3***

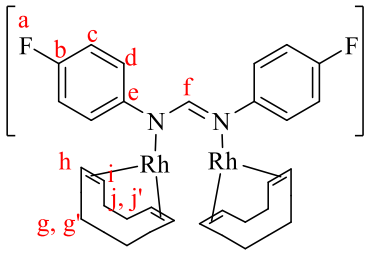

Yield: (550 mg, 66.8 %). **Appearance**: orange solid. **M.P.**: 230 – 233 °C. **^{1}H NMR** ($CDCl_3$, δ_{ppm}): 1.80 (q, $^{3}J_{H\text{-}H}$ = 5.82 Hz, 4H, H_g), 1.93 (q, $^{3}J_{H\text{-}H}$ = 6.57 Hz, 4H, H_j), 2.51 – 2.53 (m, 4H, $H_{g'}$), 2.92 (m, 4H, $H_{j'}$), 3.77 (m, 4H, H_h), 4.35 (m, 4H, H_i), 6.93 (t, $^{3}J_{H\text{-}F}$ = 6.08 Hz, 8H, H_c), 7.19 (m, 10H, $H_{d,f}$). **^{13}C{^{1}H} NMR** ($CDCl_3$, δ_{ppm}): 165.1 (C_f), 159.4 (d, $^{1}J_{C\text{-}F}$ = 243.07 Hz, C_b), 148.4 (C_e), 133.2 (C_j), 132.98 (C_g), 125.7 (C_d), 115.1 (d, $^{3}J_{C\text{-}F}$ = 21.79 Hz, C_c), 84.6 (C_h), 75.9 (C_i). **^{19}F{^{1}H} NMR** ($CDCl_3$, δ_{ppm}): -120.94 (F_a). **FT-IR** (ATR, $\nu_{cm^{-1}}$): 2872 (w, C–H), 2837 (w, C–H), 1604 (m, C=C_{COD}), 1564 (m, C=N), 1489 (C=C_{Ar}).

5.3.4 N,N'-Di-(4-trifluoromethyl)phenylformamidine-(1,5)-cyclooctadiene dimer complex ***C4***

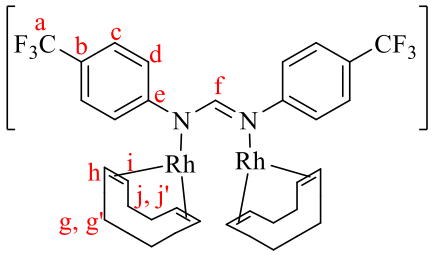

Yield: (349 mg, 61.6 %). **Appearance**: orange solid. **M.P.**: 210 – 213 °C. **^{1}H NMR** ($CDCl_3$, δ_{ppm}): 7.31 – 7.53 (m, 18H, $H_{c,d,f}$), 4.41 (m, 4H, H_i), 3.85 (m, 4H, H_h), 2.95 (m, 4H, $H_{j'}$), 2.57 (m, 4H, $H_{g'}$), 1.97 (q, $^{3}J_{H\text{-}H}$ = 5.27 Hz, 4H, H_j), 1.85 (q, $^{3}J_{H\text{-}H}$ =5.57 Hz, 4H, H_g). **^{13}C{^{1}H} NMR** ($CDCl_3$, δ_{ppm}): 165.6 (C_f), 155.0 (C_e), 126.7 (C_b), 126.0 (C_c), 124.6 (C_d), 85.1 (C_h), 76.7 (C_i), 79.1 (d, $^{1}J_{C\text{-}F}$ = 13.26Hz, C_a), 30.8 (C_j), 30.6 (C_g). **^{19}F{^{1}H} NMR** ($CDCl_3$, δ_{ppm}): -62.02 (F_a). **FT-IR** (KBr, $\nu_{cm^{-1}}$): 2939 (w, C–H), 2872 (w, C–H), 1610 (C=C_{COD}), 1551 (m, C=N), 1505 (m, C=CAr). **ESI-MS** (*m/z*): 1084.1407 ($[M]^+$, 100 %) (calcd. 1084.678).

5.4 Preparation of homoleptic dirhodium(II) complexes

L1 — L3 (10 eq.) of each respective ligand was melted at 149 °C in a clean, dry Schlenk tube.[122] After 30 mins, $[Rh_2(OTfAc)_4]$ (202 mg, 0.31 mmol) precursor was added to the ligand melt and the mixture was stirred with heat under nitrogen for 24 h. The reaction mixture was cooled

to room temperature resulting in a black crude precipitate. The precipitate was dissolved in hot methanol and filtered under vacuum. A green solid precipitate was dried *in vacuo*.

5.4.1 Tetrakis(N,N'-diphenylformamidinato)dirhodium(II) complex ***C5***

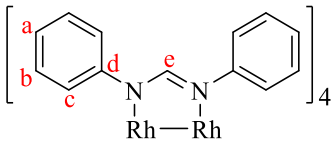

Yield: **(**253 mg, 83 %). **Appearance**: green solid. **M.P.**: 389 – 393 ºC. **^{1}H NMR** ($CDCl_3$, δ_{ppm}): 7.80 (s, 4H, H_e), 7.08 (t, $^{3}J_{H\text{-}H}$ = 7.58 Hz, 16H, H_b), 6.97 (t, $^{3}J_{H\text{-}H}$ = 7.26 Hz, 8H, H_a), 6.70 (d, $^{3}J_{H\text{-}H}$ = 7.60 Hz, 16H, H_c). **^{13}C{^{1}H} NMR** ($CDCl_3$, δ_{ppm}): 162.85 (C_f), 151.02 (C_d), 128.94 (C_b), 124.40 (C_c), 123.42 (C_a). **FT-IR** (KBr, ν_{cm}^{-1}): 1621 (C=N), 1571 (C=C_{Ar}). **ESI-MS** (*m/z*): 987.1862 ([M + H]$^{+}$, 100 %) (calcd. 987.8230).

5.4.2 Tetrakis(N,N'-di-4-methylphenylformamidinato)dirhodium(II) complex ***C6***

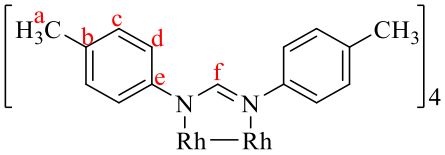

Yield: **(**289 mg, 87 %). **M.P.**: 402 – 405 ºC. **^{1}H NMR** ($CDCl_3$, δ_{ppm}): 7.68 (s, 4H, H_g), 6.88 (d, $^{3}J_{H\text{-}H}$ = 8.00 Hz, 16H, H_d), 6.59 (d, $^{3}J_{H\text{-}H}$ = 8.12 Hz, 16H, H_c), 2.23 (s, 24H, H_a). **^{13}C{^{1}H} NMR** ($CDCl_3$, δ_{ppm}): 162.3 (C_g), 148.8 (C_e), 132.5 (C_b), 129.4 (C_d), 124.3 (C_c), 20.9 (C_a). **FT-IR** (KBr, ν_{cm}^{-1}): 1622 (C=N), 1587 (C=C_{Ar}). **ESI-MS** (*m/z*): 1099.3120 ([M + H]$^{+}$, 100 %) (calcd. 1099.0310).

5.4.3 Tetrakis(N,N'-di-(4-fluoro)phenylformamidinato)dirhodium(II) complex ***C7***

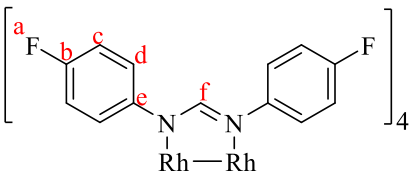

Yield: (276 mg, 80 %). **Appearance**: green solid. **M.P.**: 391 – 393 ºC. **^{1}H NMR** ($CDCl_3$, δ_{ppm}): 7.69 (t, $^{3}J_{Rh\text{-}H}$ = 3.22 Hz, 4H, H_g), 6.82 (t, $^{3}J_{H\text{-}F}$ = 8.53 Hz, 16H, H_c), 6.53 (dd, $^{3}J_{H\text{-}H}$ = 8.80 Hz; $^{4}J_{H\text{-}F}$ = 4.76 Hz, 16H, H_d). **^{13}C{^{1}H} NMR** ($CDCl_3$, δ_{ppm}): 162.7 (C_g), 160.0 (d, $^{1}J_{C\text{-}F}$ = 244.23 Hz, C_b), 146.7 (C_e), 125.3 (d, $^{3}J_{C\text{-}F}$ = 7.95 Hz, C_d), 115.9 (d, $^{2}J_{C\text{-}F}$ = 22.83 Hz, C_c). **^{19}F{^{1}H}**

NMR ($CDCl_3$, δ_{ppm}): -119.4 (F_a). **FT-IR** (KBr, ν_{cm}^{-1}): 1615 (C=N), 1581 ($C=C_{Ar}$). **ESI-MS** (*m/z*): 1130.1064 ($[M + H]^+$, 100 %) (calcd. 1130.7510).

5.5 Preparation of mixed-ligand dirhodium(II) complexes

$[Rh_2(OAc)_4]$ (251 mg, 0.57 mmol) was stirred in 90 mL chlorobenzene at 136 °C for 1 h under nitrogen. A solution containing stoichiometric amounts of respective ligand **L1 – L3** (336 mg, 1.71 mmol) and triethylamine in 10 mL chlorobenzene was added dropwise to the stirring solution. The resulting purple solution was refluxed under nitrogen for 24 h.[126] The reaction mixture was removed from heat and cooled to room temperature, followed by filtration under vacuum. The filtrate was concentrated under reduced pressure and subjected to silica gel column chromatography for purification using ethyl acetate/hexane (40:60) as the eluent.

5.5.1 Acetato-tris(N,N'-diphenylformamidinato)dirhodium(II) complex ***C8***

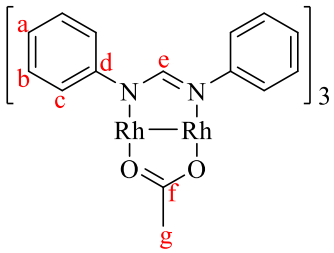

Yield: (115 mg, 67 %). **M.P.**: 282 – 284 °C. **Appearance**: dark green solid. **^{1}H NMR** ($CDCl_3$, δ_{ppm}): 8.14 (t, $^3J_{H\text{-}H}$ = 3.04 Hz, 8H, $H_{f'}$), 7.56 (t, $^3J_{Rh\text{-}H}$ = 4.18 Hz, 1H, H_f), 7.21 (t, $^3J_{H\text{-}H}$ = 7.68 Hz, 8H, $H_{b'}$), 7.07 (d, $^3J_{H\text{-}H}$ = 7.68 Hz, 8H, $H_{c'}$), 6.70 (t, $^3J_{H\text{-}H}$ = 7.10 Hz, 4H, $H_{a'}$), 6.86 (t, $^3J_{H\text{-}H}$ = 7.38 Hz, 4H, H_b), 6.80 (t, $^3J_{H\text{-}H}$ = 7.06 Hz, 2H, H_a), 6.57 (d, $^3J_{H\text{-}H}$ = 7.52 Hz, 4H, H_c), 2.07 (s, 3H, H_g). **^{13}C{^{1}H} NMR** ($CDCl_3$, δ_{ppm}): 162.1 (C_f), 150.6 ($C_{e'}$), 149.6 (C_e), 129.2 ($C_{b'}$) 128.9 ($C_{d'}$), 128.7 (C_b), 124.4 (C_d), 123.8 (C_c), 123.3 (C_a), 123.1 ($C_{a'}$), 122.6 ($C_{c'}$). **FT-IR** (KBr, ν_{cm}^{-1}): 3031 (w, C–H), 1616 (s, C=O), 1567 (m, C=N), 1486 (m, C=N), 1433 (m, $C=C_{Ar}$). **ESI-MS** (*m/z*): 850.0944 ($[M + H]^+$, 100 %) (calcd. 850.6190).

5.5.2 Acetato-tris(N,N'-di-4-fluorophenylformamidinato)dirhodium(II) complex ***C9***

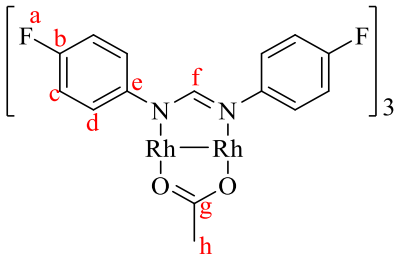

Yield: (274 mg, 70 %). **Appearance**: dark green solid. **M.P.**: 274 – 277 °C. **^{1}H NMR** ($CDCl_3$, δ_{ppm}): 7.93 (br s, 2H, $H_{f'}$), 7.45 (br s, 1H, H_f), 6.90 – 6.96 (m, 16H, $H_{c',d'}$),2.10 (s, 3H, H_h), 6.62 (t, $^{3}J_{H\text{-}F}$ = 8.40 Hz, 4H, H_c), 6.47 (dd, $^{3}J_{H\text{-}H}$ = 8.16; $^{4}J_{H\text{-}F}$ = 4.72 Hz, 4H, H_d). **^{13}C{^{1}H} NMR** ($CDCl_3$, δ_{ppm}): 186.1 (C_g), 163.1 (C_f), 162.7 ($C_{f'}$), 160.8 ($C_{b'}$), 158.4 (C_b), 146.5 ($C_{e'}$), 145.6 (C_e), 124.7 (d, $^{3}J_{C\text{-}F}$ = 7.24 Hz, C_d), 124.0 (d, $^{2}J_{C\text{-}F}$ = 6.35 Hz, $C_{d'}$), 116.3 (d, $^{3}J_{C\text{-}F}$ = 22.46 Hz, $C_{c'}$), 115.6 (d, $^{2}J_{C\text{-}F}$ = 22.40 Hz, C_c), 24.3 (C_h). **^{19}F{^{1}H} NMR** ($CDCl_3$, δ_{ppm}): -119.6 (F_a), -119.7 ($F_{a'}$). **FT-IR** (KBr, ν_{cm}^{-1}): 2923 (w, C–H), 2855 (w, C–H), 1614 (s, C=O), 1578 (m, C=N), 1494 (m, C=N), 1423 (m, C=C_{Ar}). **ESI-MS** (*m/z*): 958.0374 ($[M + H]^+$, 100 %) (calcd. 958.5710).

5.5.3 Diacetato-bis(N,N'-diphenylformamidinato)dirhodium(II) complex ***C10***

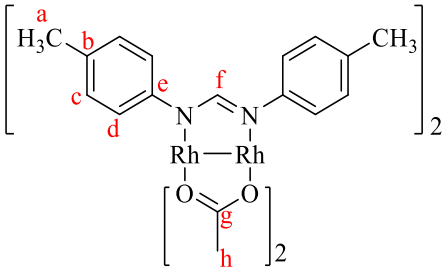

Yield: (141 mg, 61 %.) **Appearance**: shiny green crystals. **M.P.**: 265 – 267 °C. **^{1}H NMR** ($CDCl_3$, δ_{ppm}): 7.51 (t, $^{3}J_{Rh\text{-}H}$ = 3.36 Hz, 2H, H_f), 6.97 (d, $^{3}J_{H\text{-}H}$ = 7.96 Hz, 8H, H_d), 6.91 (d, $^{3}J_{H\text{-}H}$ = 8.04 Hz, 8H, H_c), 2.28 (s, 12H, H_a), 2.08 (s, 6H, H_h). **^{13}C{^{1}H} NMR** ($CDCl_3$, δ_{ppm}): 186.7 (C_g), 165.6 (C_f), 148.0 (C_e), 133.2 (C_b), 129.7 (C_d), 124.2 (C_c). **FT-IR** (KBr, ν_{cm}^{-1}): 2921 (w, C–H), 2858 (w, C–H), 1594 (s, C=O), 1584 (m, C=N), 1503, (m, C=N), 1425 (m, C=C_{Ar}). **ESI-MS** (*m/z*): 770.0757($[M + H]^+$, 100 %) (calcd. 770.5220).

5.5.4 Diacetato-bis(N,N'-di-4-fluorophenylformamidinato)dirhodium(II) complex ***C11***

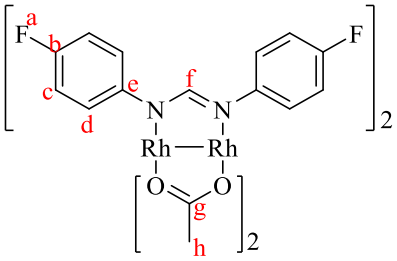

Yield: (139 mg, 60 %). **Appearance**: dark green solid. **M.P.**: 222 – 226 °C. **^{1}H NMR** ($CDCl_3$, δ_{ppm}): 7.40 (t, $^{3}J_{Rh\text{-}H}$ = 4.00 Hz, 1H, H_f), 6.80 – 6.96 (m, 16H, $H_{c',d'}$), 2.08 (s, 6H, H_h). **^{13}C{^{1}H} NMR** ($CDCl_3$, δ_{ppm}): 187.0 (C_g), 166.0 (C_f), 159.9 (d, $^{1}J_{C\text{-}F}$ = 244.23 Hz, C_b), 146.3 (C_e), 24.1 (C_h), 125.7 (d, $^{3}J_{C\text{-}F}$ = 7.54 Hz, C_c), 115.7 (d, $^{2}J_{C\text{-}F}$ = 22.40 Hz, C_d). **^{19}F{^{1}H} NMR** ($CDCl_3$, δ_{ppm}): -119.1 (F_a). **FT-IR** (KBr, ν_{cm}^{-1}): 2924 (w, C–H), 2853 (w, C–H), 1612 (s, C=O), 1584 (m, C=N), 1493 (m, C=N), 1432 (m, C=C_{Ar}). **ESI-MS** (*m/z*): 786.9843 ($[M + H]^+$, 100 %) (calcd. 786.3820).

5.6 Single crystal X-ray diffraction

Single-crystal X-ray diffraction data were collected on a Bruker D8 Venture diffractometer using graphite-monochromated Mo-Kα radiation (λ = 0.71073 Å). Data collection was carried out at 100(2) K. Temperature was controlled by an Oxford Cryostream cooling system (Oxford Cryostat). Cell refinement and data reduction were performed using the program SAINT. The data were scaled, and absorption correction performed using SADABS. The structure was solved by direct methods using SHELXS-97 and refined by full-matrix least-squares methods based on F^2 using SHELXL-97 and using the graphics interface program X-Seed. The programs X-Seed and POV-Ray were used to prepare molecular graphic images. All non-hydrogen atoms were refined anisotropically. All hydrogen atoms were placed in idealised positions and refined in riding models with U_{iso} assigned 1.2 times U_{eq} of their parent atoms and the C-H bond distances were constrained to 0.95 Å for CH and 0.99 Å for CH_2. Some of the CF_3 moieties were disordered and the positions of the fluorine atoms were refined with fractional site occupancy factors.

*5.6.1 Preparation of a single crystal of complex **C1***

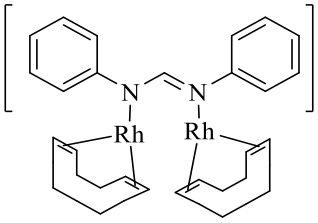

complex **C1** (10 mg) was dissolved in 1.00 mL of distilled dichloromethane in a glass vial. To the concentrated solution was 0.5 mL of *n*-hexane was added. The resulting heterogeneous mixture was sealed and cooled to 0 ^{o}C overnight. Holes were punched on the lid of the vial and the solution allowed to slowly diffuse at room temperature. An orange single crystal of **C1** was obtained after 2 days.

*5.6.2 Preparation of a single crystal of complex **C4***

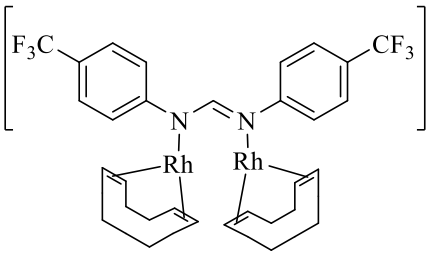

Complex **C4** (10 mg) was dissolved in 1.00 mL of distilled dichloromethane in a glass vial. To the concentrated solution was 0.5 mL of *n*-hexane was added. The resulting heterogeneous mixture was sealed and cooled to 0 ^{o}C overnight. Holes were punched on the lid of the vial and the solution allowed to slowly diffuse at room temperature. An orange single crystal of **C4** was obtained after 2 days.

*5.6.3 Preparation of a single crystal of complex **C5***

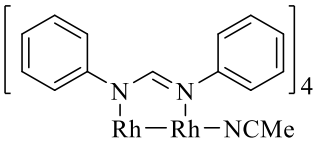

Complex **C5** (10 mg) was dissolved in 2.00 mL of anhydrous acetonitrile in a glass vial. The vial was sealed and purged with nitrogen while stirring at room temperature for 15 mins. The solution was left to slowly diffuse overnight. A red single crystal of [**C5(CH$_3$CN)**] adduct was obtained the next day.

*5.6.4 Preparation of a single crystal of complex **C8***

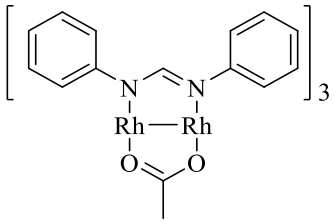

Complex **C8** (10 mg) of was dissolved in 1.00 mL of dichloromethane in a glass vial. To the concentrated solution was 0.5 mL of *n*-hexane was added. The resulting heterogeneous mixture was sealed and cooled to 0 ^{o}C overnight. Holes were punched on the lid of the vial and the solution allowed to slowly diffuse at room temperature. A green single crystal of **C8** was obtained after 5 days.

*5.6.5 Preparation of single crystals of complex **C10***

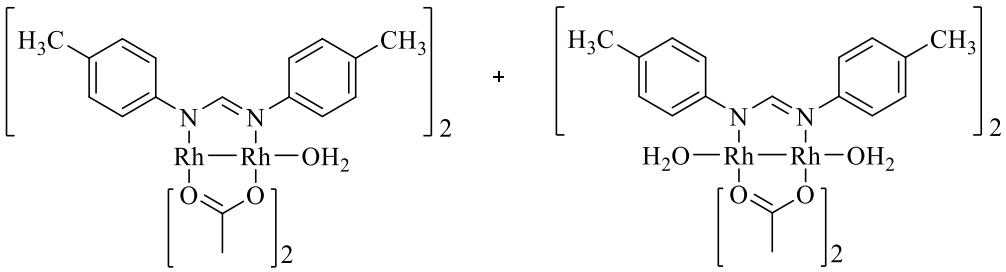

(blue) (red)

Complex **C10** (10 mg) was dissolved in 1.00 mL of dichloromethane in a glass vial. To the concentrated solution was 0.5 mL of *n*-hexane was added. The resulting heterogeneous mixture was sealed and cooled to 0 ^{o}C overnight. Holes were punched on the lid of the vial and the solution allowed to slowly diffuse at room temperature. A blue single crystal of [**C10(H_2O)**] adduct and a red single crystal of [**C10(H_2O)$_2$**] adduct were obtained from the same solution after 5 days upon.

5.7 Preparation of catalytic reactions

5.7.1 General procedure for hydroformylation

A clean and dry 90 mL stainless steel pipe reactor that was equipped with a Teflon-coated magnetic stirrer bar. The reactor was loaded with 1-octene (2.25 mL, 7.17 mmol) as a substrate, *n*-decane as an internal standard (204 mg, 1.43 mmol) and each of the bimetallic complexes **C1** – **C4** (2.87×10^{-3} mmol) in 5.00 mL toluene. The reactor was sealed, degassed with nitrogen three times, and pressurised with syngas (1:1, $CO:H_2$) at a desired pressure of 30 – 50 bar. The contents inside the reactor were heated to 55, 65, 75, 85 or 95 ^oC, stirred for 4 h. The reaction mixture was cooled to room temperature, filtered and samples were quantified by GC-FID. The products were confirmed with respect to authentic *iso*-octenes and aldehydes.

5.7.2 General procedure for allylic oxidation

Cyclohexene (100 mg, 1.22 mmol, 1.00 eq.) and each of the respective dirhodium(II) complexes **C5** – **C10** were dissolved in 4.00 mL solvent (DCM, THF or MeCN) in 25 mL carousel tubes equipped with stirrer bars and an inflating balloon. To this, tert-butyl hydroperoxide (70% in water) (471 mg, 3.66 mmol, 3.00 eq.) solution in 1.00 mL of the similar solvent was added. The reaction mixture was stirred vigorously at respective boiling point of the temperature for 24 h. The resulting reaction mixture was cooled to room temperature and small samples were taken for analysis of reaction products by use of GC analysis by comparison with authentic samples. Peak area of each signal was recorded, with the linear fit of the calibration standard curves used to estimate the concentration for each component.

5.8 References

122 A. A. Mohamed, *Coord. Chem. Rev.*, 2010, **254**, 1918–1947.

123 P. Piraino, G. Tresoldi and F. Faraone, *J. Organomet. Chem.*, 1982, **224**, 305–312.

126 B. G. Anderson, D. Cressy, J. J. Patel, C. F. Harris, G. P. A. Yap, J. F. Berry and A. Darko, *Inorg. Chem.*, 2019, **58**, 1728–1732.

127 E. C. Taylor and W. A. Ehrhart, *J. Org. Chem.*, 1963, **28**, 1108–1112.

Chapter 6

Overall Summary and Future Recommendations

6.1 Overall Summary

A series of *N,N'*-bidentate diphenylformamidine ligands **L1** – **L4** were synthesised. The ligands were characterised using various spectroscopic and analytical techniques, which was in agreement to what is reported in literature. These ligands were reacted with the dimeric rhodium precursor $[Rh(COD)Cl]_2$ to produce a series of bimetallic Rh(I) complexes **C1** – **C4** of the type $[Rh(R\text{-}dpf)(COD)]_2$ bearing the bridging diphenylformamidinate ligands, R = H, CH_3, F or CF_3 at the *para* positions. The ligands were also reacted with rhodium trifluoroacetate precursor $[Rh_2(TfOAc)_4]$ to afford the homoleptic complexes **C5** – **C7** of the type $[Rh_2(R\text{-}dpf)_4]$, with bridging diphenylformamidinate ligands, where R = H, CH_3 or F at the *para* positions. The ligands were also reacted with rhodium acetate precursor $[Rh_2(OAc)_4]$ to afford the mixed ligand heteroleptic complexes **C8** – **C11** of the type $[Rh_2(R\text{-}dpf)_x(OAc)_{4-x}]$, bearing bridging diphenylformamidinate ligands with x = 2 or 3 and R = H, CH_3 or F at the *para* positions. These complexes were fully characterised using spectroscopic analytical techniques.

The bimetallic Rh(I) complexes were evaluated as catalysts in the hydroformylation of 1-octene. These were found to be active as catalysts in the hydroformylation reaction. These complexes posed near quantitative conversion, with the highest observed for C2 and C4. Furthermore, the complexes are chemoselective towards aldehydes over the octene isomers. The highest chemoselectivity is observed for C4. These observations are attributed to the electron deficiency of the Rh metal centres upon oxidation due to the withdrawing trifluoromethyl substituent. In such a case, there is unfavourable interactions between the metal orbitals and the p orbitals of the acyl group of the aldehyde products, so the aldehyde product dissociate faster to regenerate the ground state Rh(I) complexes. Contrary to this, C3 has both mesomeric and inductive effects due to the fluoride group, and the mesomeric effect is more dominant at higher oxidation states, which stabilises the interaction with the acyl group, slowing the dissociation of the aldehyde products. Nonanal is generally more favourable over the branched aldehydes due to the bulkiness of the ligands.

The homoleptic and mixed ligand heteroleptic Rh(II) complexes were evaluated as catalysts in the allylic oxidation of cyclohexene. These were found to be active as catalysts for the allylic oxidation reaction with 0.1 mol% catalyst loading and 3 eq. of TBHP. The catalysis was evaluated in dichloromethane, tetrahydrofuran and acetonitrile. In dichloromethane, the mixed ligand complexes were found to be the best complexes for conversion. High selectivity is observed towards 2-cyclohexen-1-one over 2-cyclohexen-1-ol and cyclohexene oxide. Independent increase in catalyst loading, reaction time or amount of oxidation improves the conversion, however the reactivity of the catalyst is reduced with a 0.5 mol% catalyst loading based on the lower turnover numbers. In tetrahydrofuran, the conversions and turnover numbers are slightly lower compared to dichloromethane, due to the unfavourable axial interaction of the oxygen donor atom. In acetonitrile, the conversions are improved to near quantitative with higher turnover numbers and better chemoselectivity towards 2-cyclohexen-1-one. This is due to the stabilising effect of the higher oxidation states by acetonitrile

6.2 Future Recommendations

The utilisation of bimetallic rhodium complexes in catalysis is on a steep increase as researchers are seeking for an ideal catalyst to be used for industrial purposes. This work has contributed to the design of suitable candidates of bimetallic rhodium catalysts with uses in hydroformylation and allylic oxidation. These complexes pose good catalytic activity and selectivity in different solvents. This is supported by their easy in oxidation to generate the higher oxidation state reactive species, with lower oxidation potentials. There is great benefit in utilising ligands with a conjugated π-electron system, which affects the stabilisation of charge. Substituents with more electron-withdrawing or electron-donating strengths can thus be used to fulfil this purpose. The combination of the ligands with non-bulky ligands such as acetates greatly improves the activity. The complexes can also be evaluated for their catalytic activity in hydroformylation and allylic oxidation of other substrates, to increase their scope in reactivity. Theoretical investigations are required to determine if the monosubstituted dirhodium(II) complexes can be formed. This can be done by calculating energies of the complexes based on their degree of substitution. An energy profile can then be used to predict the energy and stability of the monosubstituted complexes. The ligands can be altered to make the complexes more water soluble. This can be done by adding sulfonate substituents. Performing the catalytic reactions in water is in line with the principles of green chemistry.

Appendix A

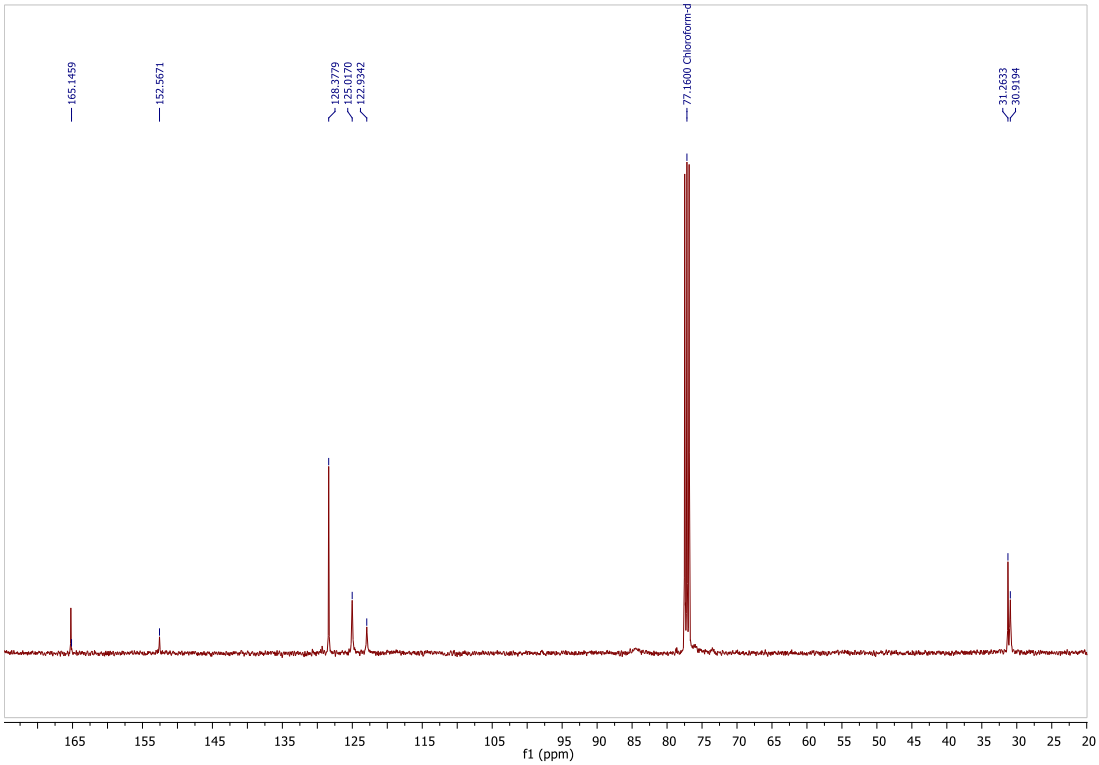

Appendix A-1 $^{13}C\{^{1}H\}$ NMR of **C1** in $CDCl_3$.

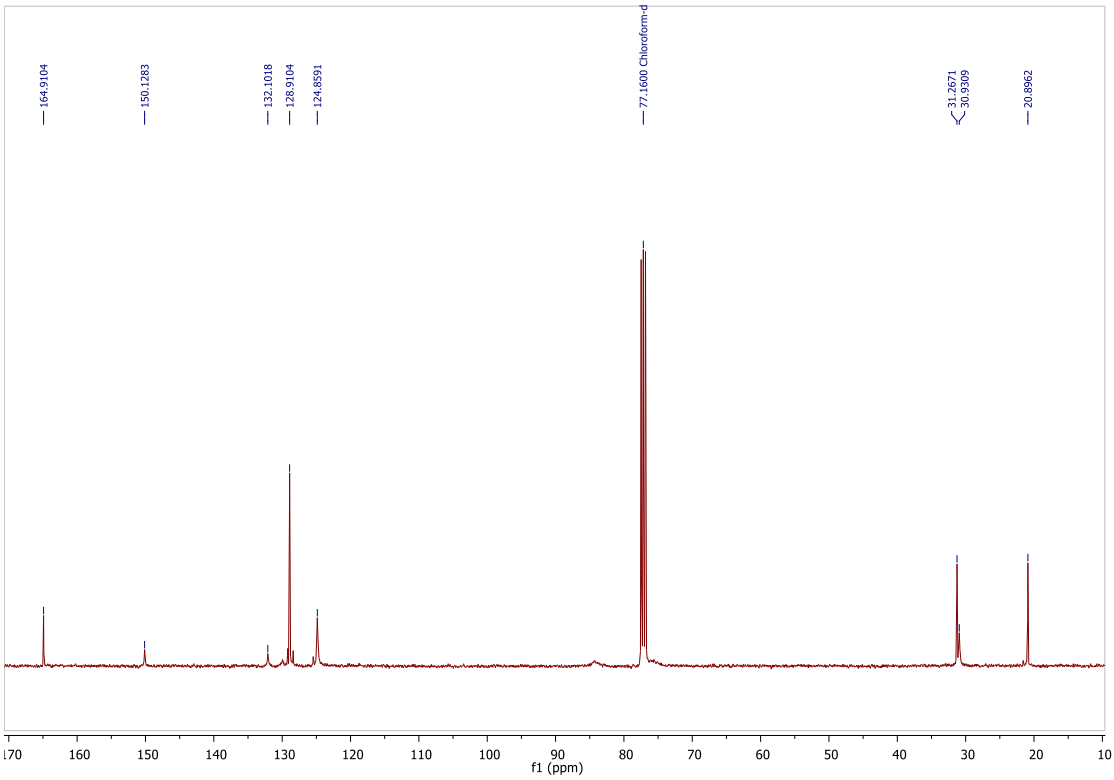

Appendix A-2 $^{13}C\{^{1}H\}$ NMR of **C2** in $CDCl_3$.

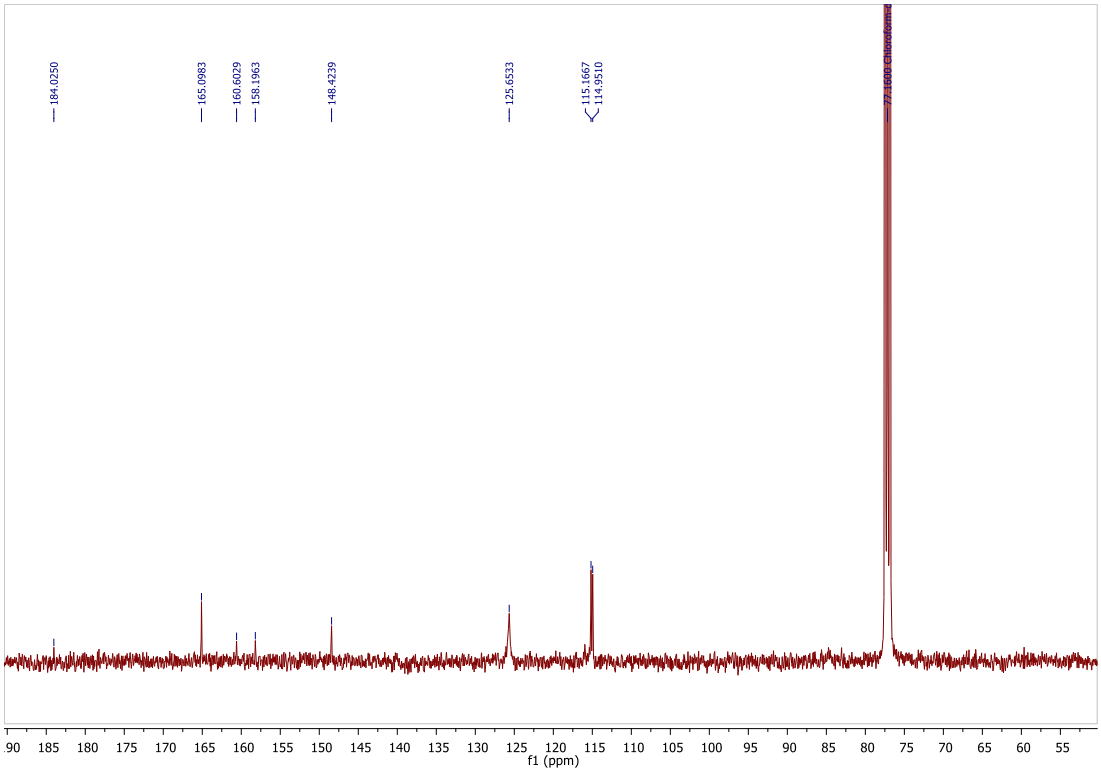

Appendix A-3 $^{13}C\{^{1}H\}$ NMR of **C3** in $CDCl_3$.

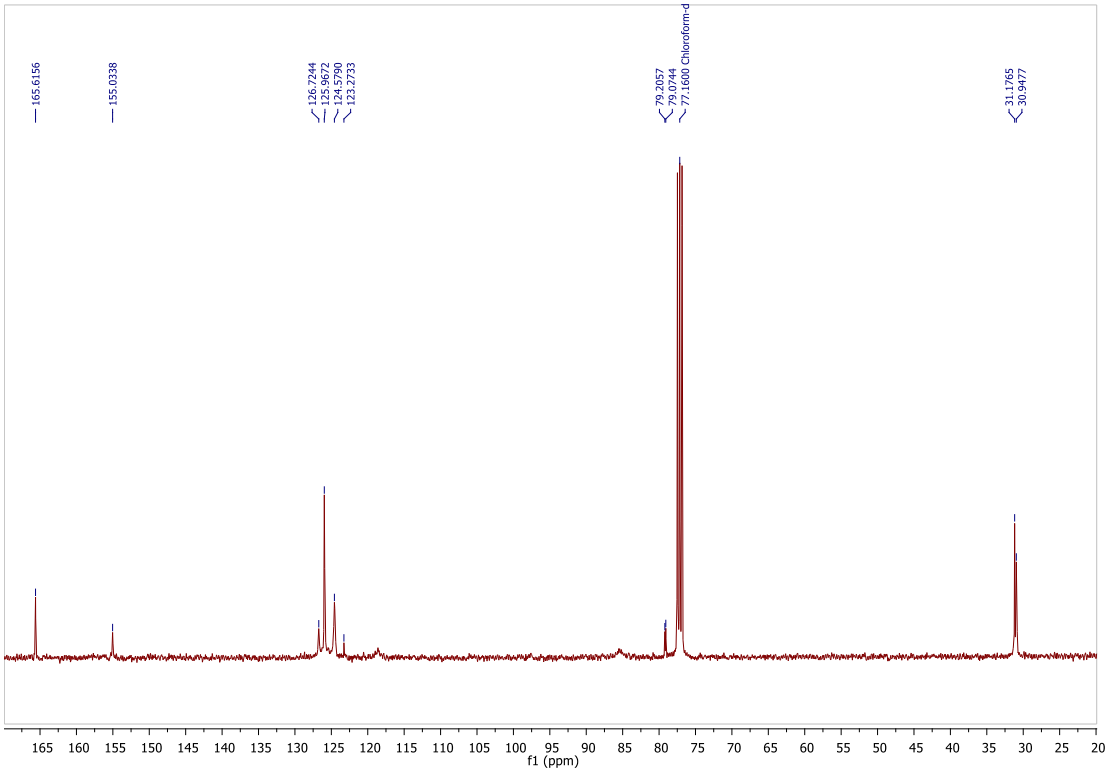

Appendix A-4 $^{13}C\{^{1}H\}$ NMR of **C4** in $CDCl_3$.

Appendix B

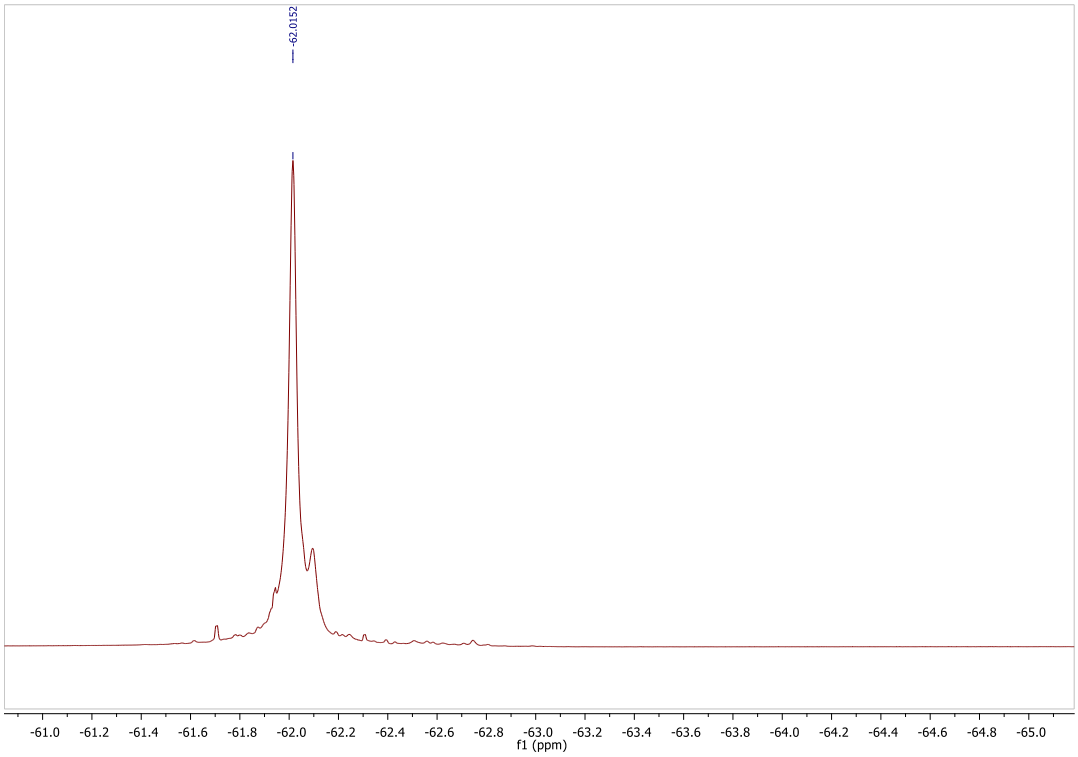

Appendix B-1 ^{19}F NMR of **C4** in $CDCl_3$.

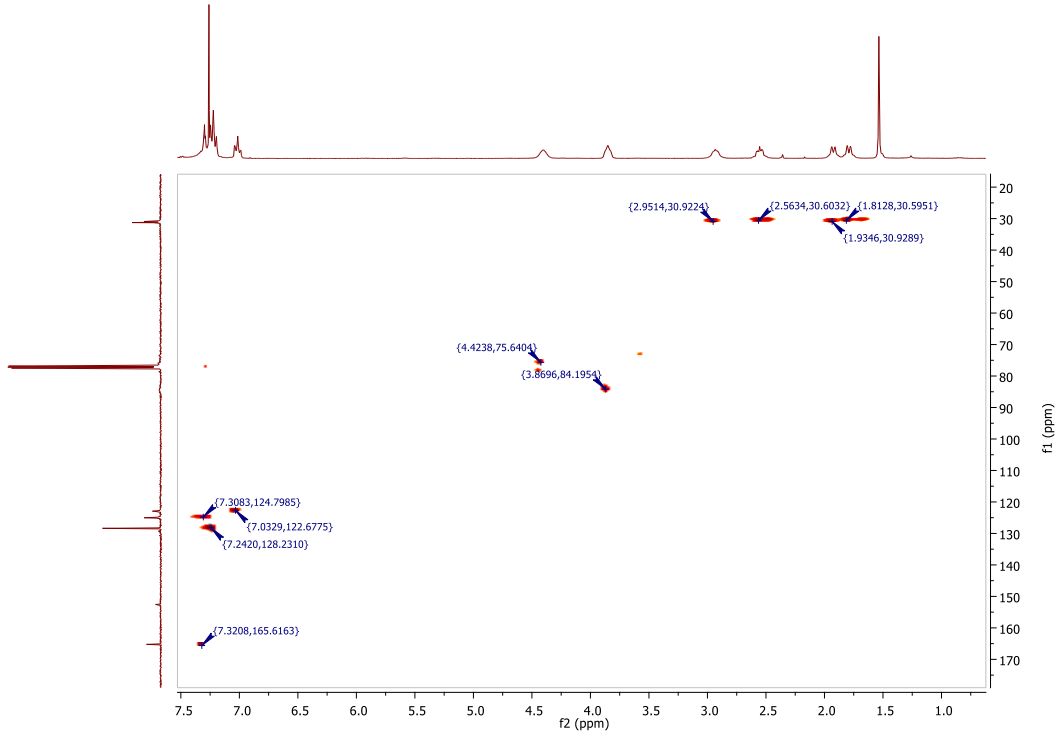

Appendix B-2 HSQC of **C1** in $CDCl_3$.

Appendix C

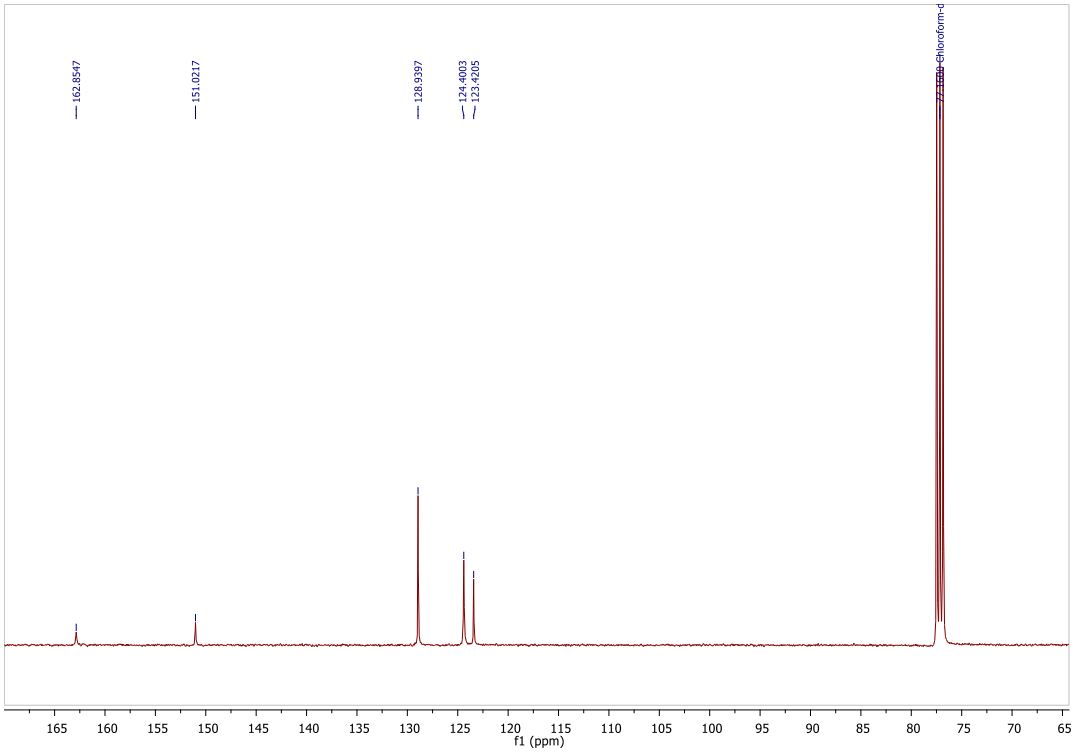

Appendix C-1 $^{13}C\{^{1}H\}$ NMR of **C5** in $CDCl_3$.

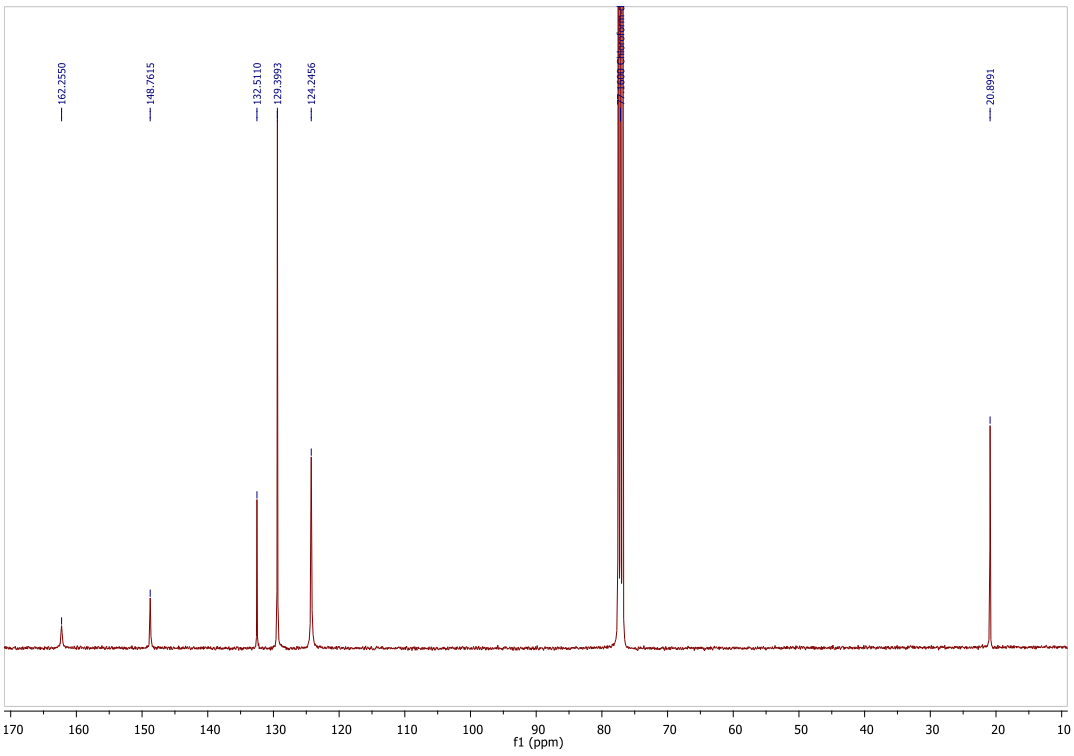

Appendix C-2 $^{13}C\{^{1}H\}$ NMR of **C6** in $CDCl_3$.

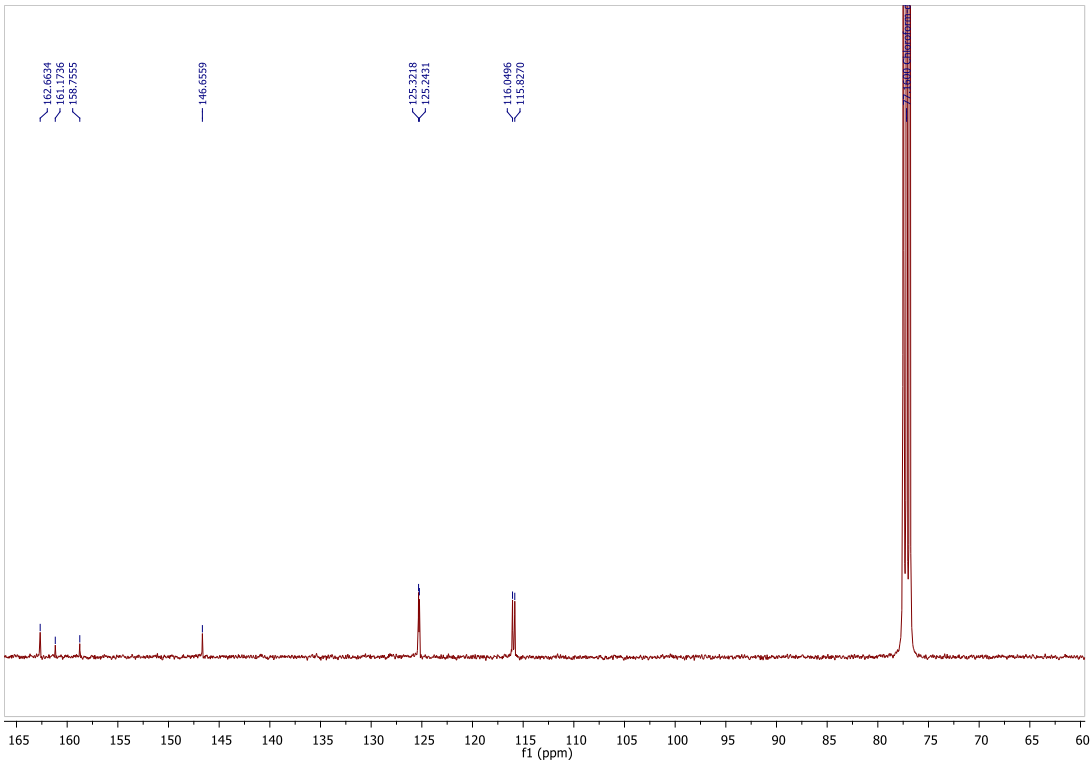

Appendix C-3 $^{13}C\{^{1}H\}$ NMR of **C7** in $CDCl_3$.

Appendix D

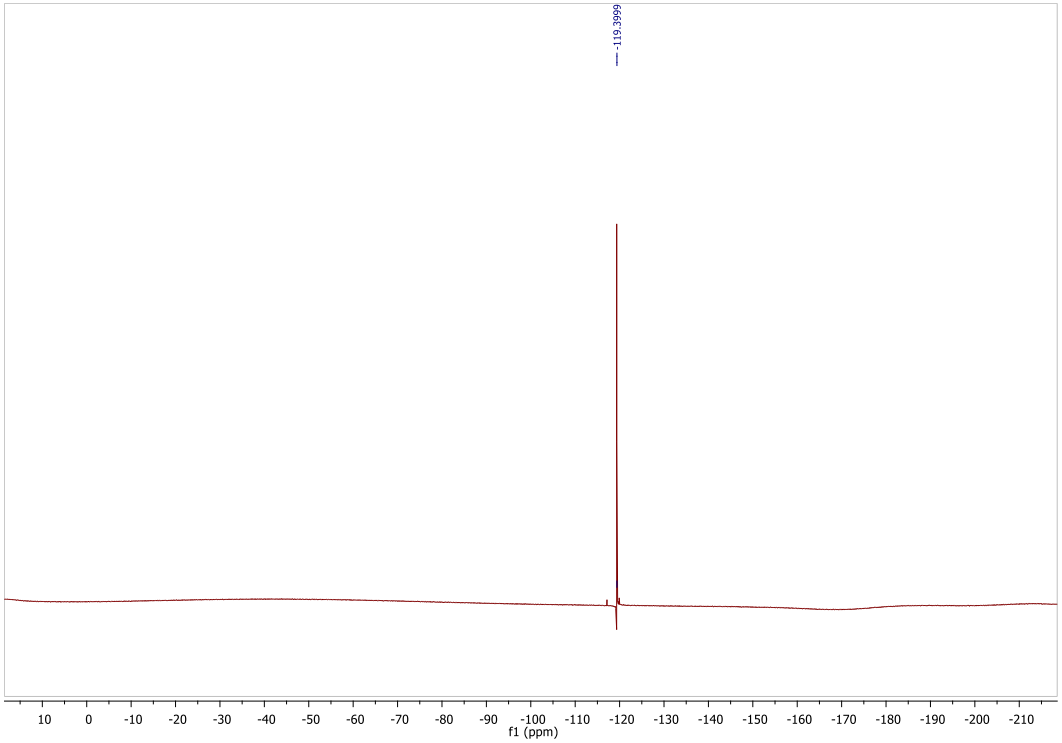

Appendix D-1 ^{19}F NMR of **C7** in $CDCl_3$.

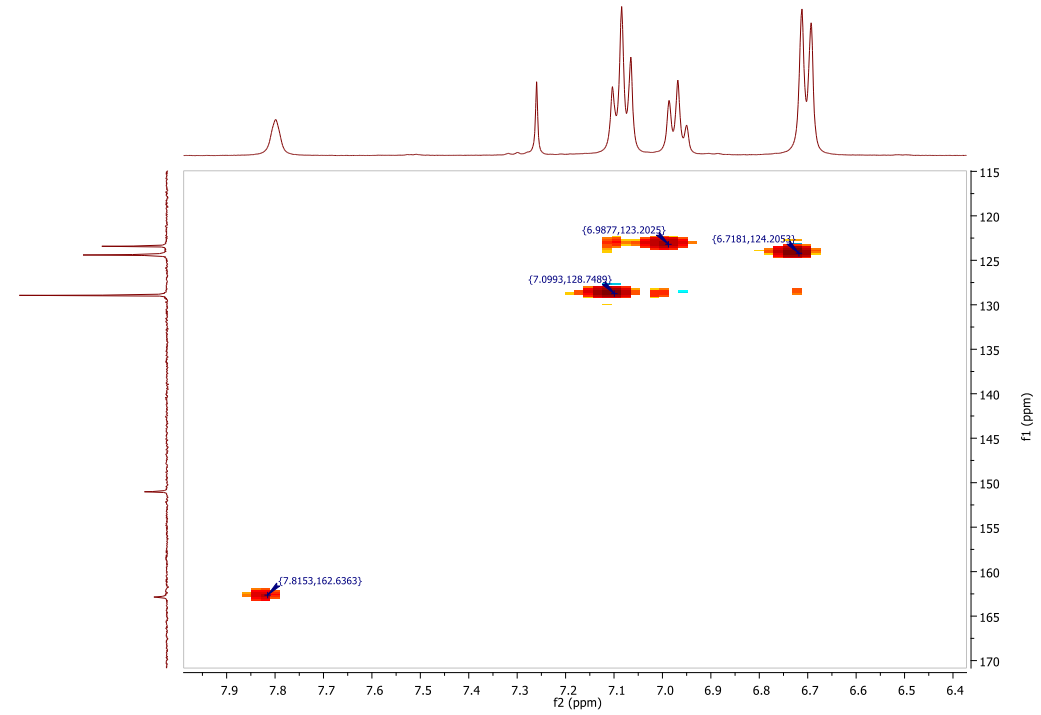

Appendix D-2 HSQC of **C5** in $CDCl_3$.

Appendix E

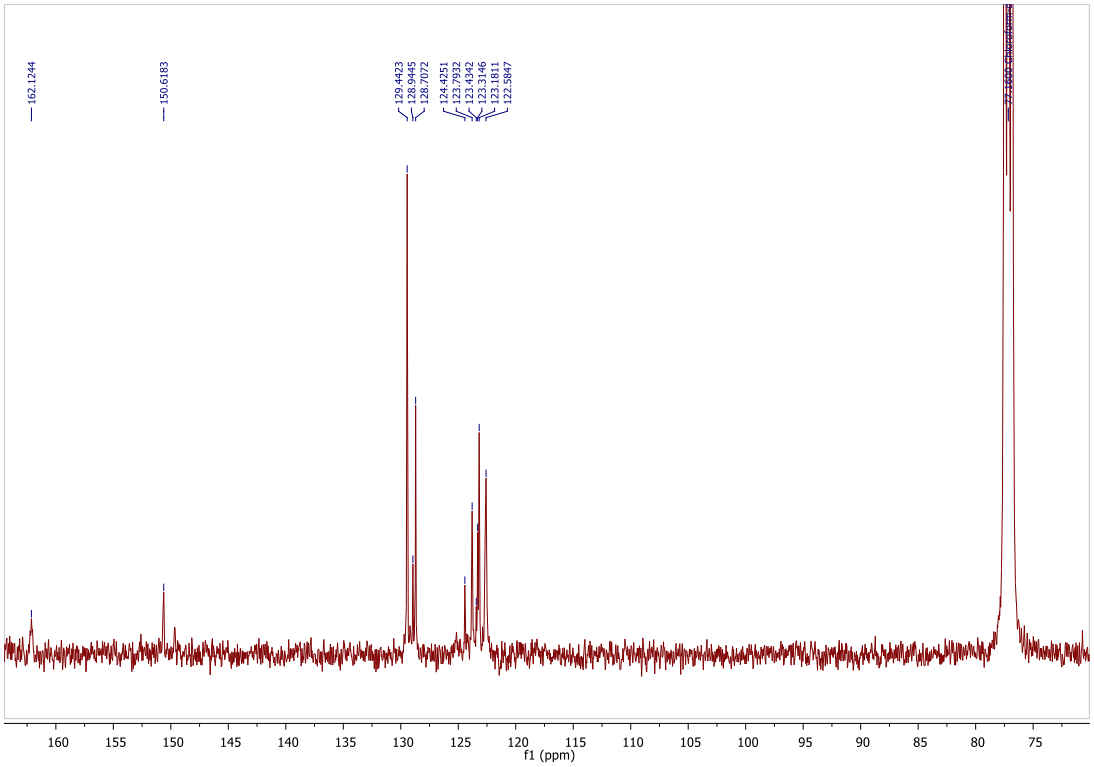

Appendix E-1 $^{13}C\{^{1}H\}$ NMR of **C8** in $CDCl_3$.

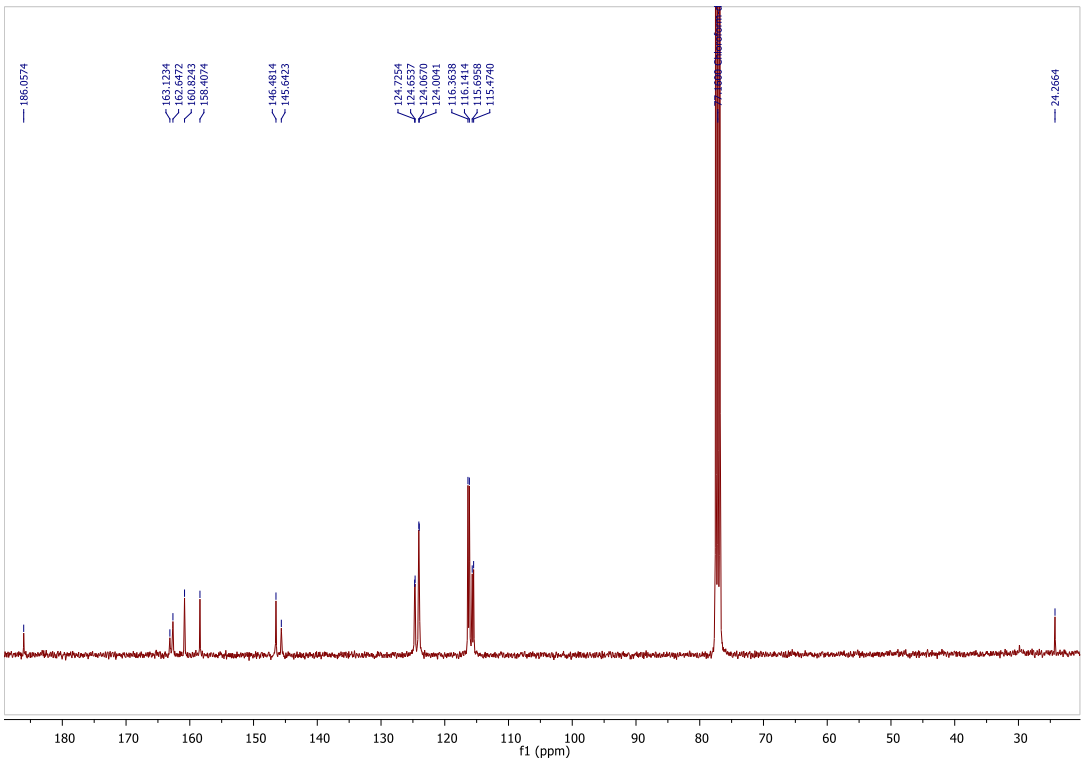

Appendix E-2 $^{13}C\{^{1}H\}$ NMR of **C9** in $CDCl_3$.

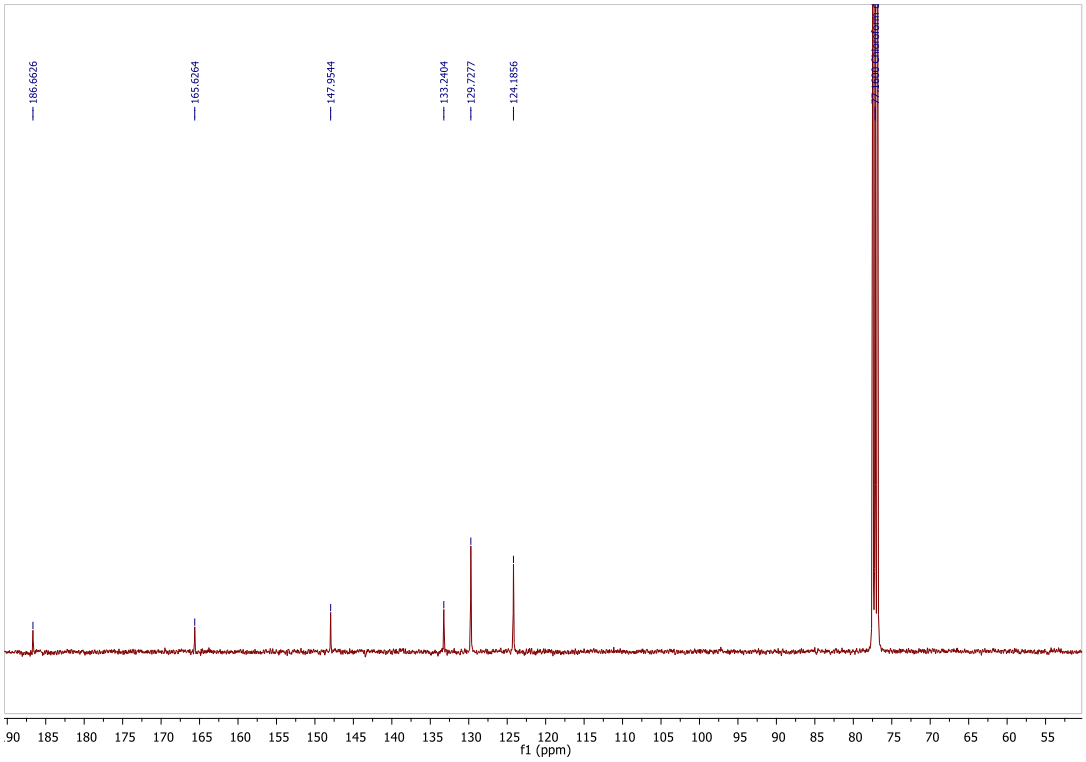

Appendix E3 $^{13}C\{^{1}H\}$ NMR of **C10** in $CDCl_3$.

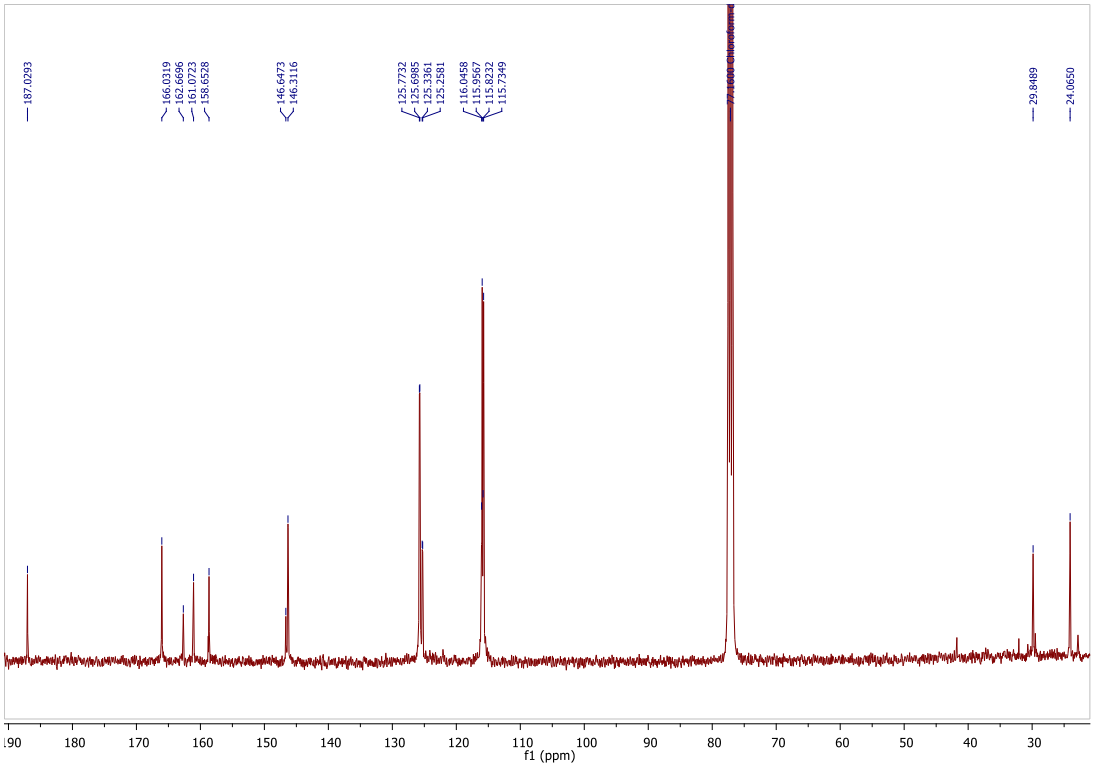

Appendix E4 $^{13}C\{^{1}H\}$ NMR of **C11** in $CDCl_3$.

Appendix F

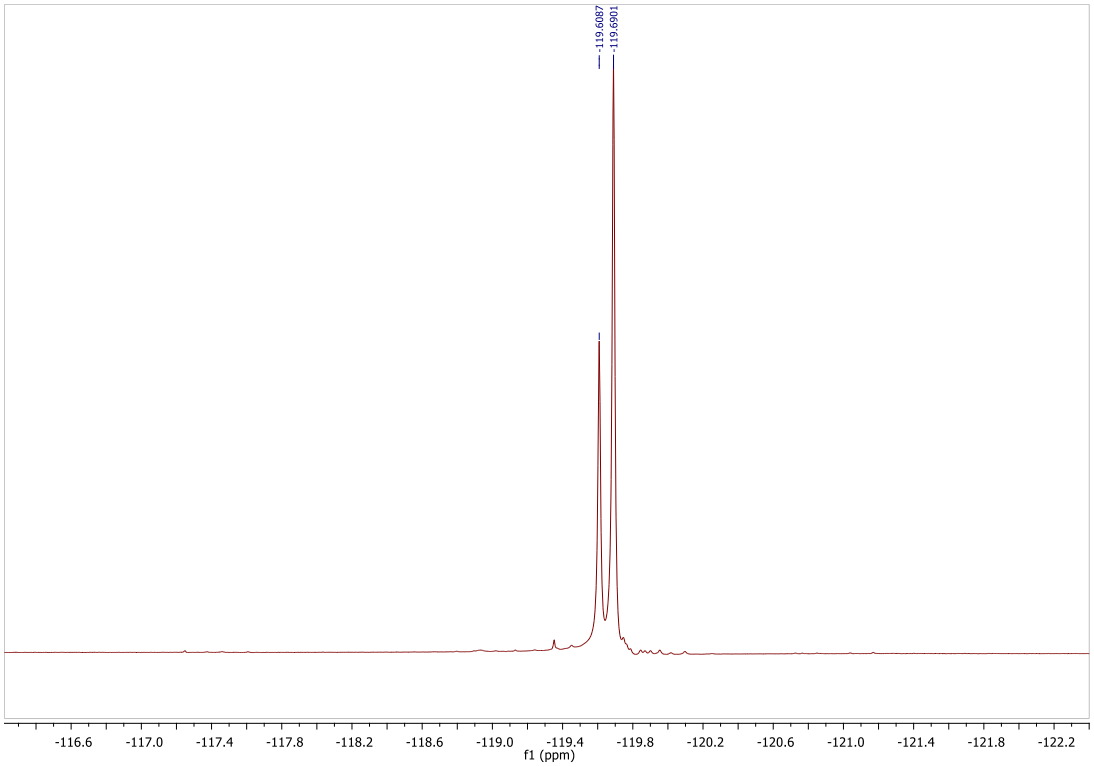

Appendix F-1 ^{19}F NMR of **C9** in $CDCl_3$.

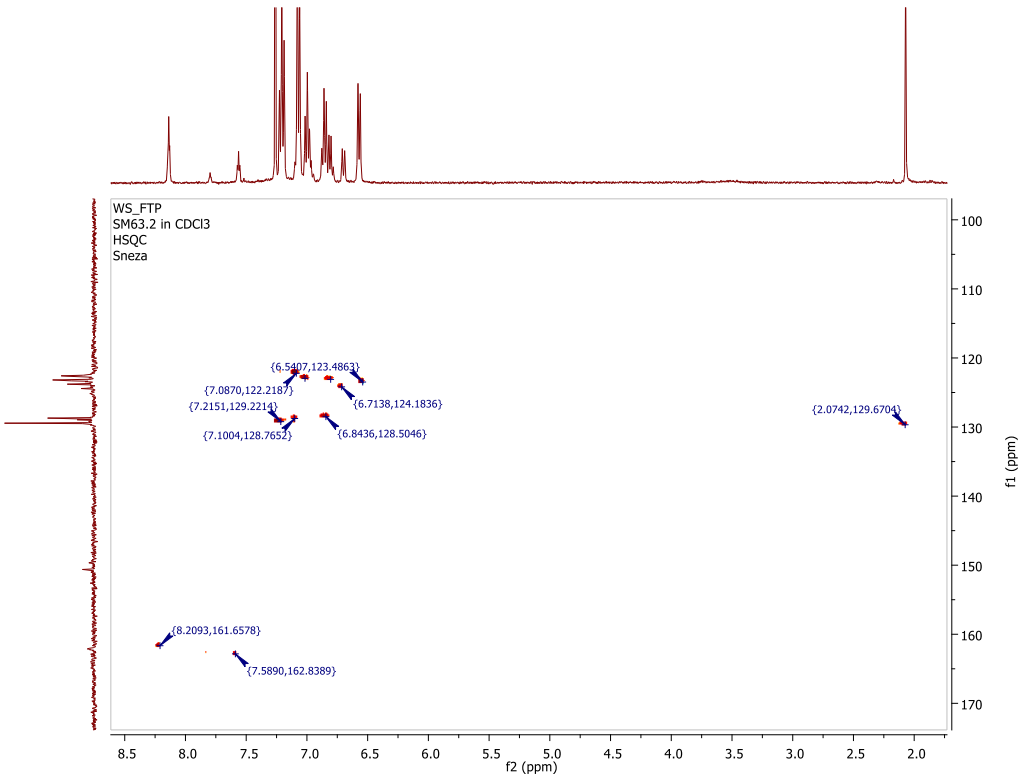

Appendix F-2 HSQC of **C8** in $CDCl_3$.